Experimental investigation of flame propagation through stratified mixture field

Saravanan Balusamy

École Doctorale – S.P.M.I.I.

THÈSE

Présentée par

Saravanan BALUSAMY

Pour l'obtention du grade de

Docteur de l'Institut National des Sciences Appliquées de Rouen

Discipline:	Physique
Spécialité:	Energétique
Formation Doctorale:	Sciences Physiques, Mathématiques et de l'Information pour l'Ingénieur
Laboratoire d'Accueil:	UMR-CNRS-6614-CORIA

Etude expérimentale de la propagation de flammes dans un mélange stratifié

Le 22 Octobre 2010

Membres du Jury

Rapporteurs:

Dany ESCUDIÉ	Directrice de Recherche CNRS, CETHIL, Lyon
Epaminondas MASTORAKOS	Professeur, Cambridge University

Examinateurs:

Marc BELLENOUE	Professeur à l'ENSMA, Poitiers
António PIRES DA CRUZ	Ingénieur, Institut Français du Pétrole, Paris
Luc VERVISCH	Professeur, INSA de Rouen

Directeurs de thèse:

Armelle CESSOU	Chargée de Recherche CNRS, CORIA, Rouen
Bertrand LECORDIER	Chargé de Recherche CNRS, CORIA, Rouen

Dedicated to
the supreme cause,
my parents,
and my sister.

Acknowledgments

Firstly, I would like to express my gratitude to my advisors Dr. Armelle CESSOU and Dr. Bertrand LECORDIER. I wish to thank them for their relentless support and their valuable guidance throughout my four years of thesis work. I am indebted to their inspiration, expertise and commitment. I owe all my success to them.

I would like to thank the ANR (Agence Nationale de la Recherche) and the CNRS, for their financial support to this work through the MESOPTI-CO2 program, in collaboration with the GSM (Groupment Scientifigue Moteurs).

I would like to thank Dr. Michel Ledoux, Director of UMR 6614-CORIA laboratory and his successor Dr. Mourad Boukhalfa for the excellent working conditions of this wonderful laboratory. I would like to thank also the staff members of this laboratory for their help to the many administrative formalities of my work and stay in this beautiful country.

I wish to thank all the members of the jury for their valuable suggestions and made my thesis defense one of my most memorable days.

I am indebted to the gentlemen of the workshop, who were able to understand my broken French and helped me to transform my drawings into products of experiment set-up. I wish to thank Benjamin, Jacky, Ludovic, Bruno, Thierry, Philippe and Yves for their wonderful assistance. A special thanks to Benjamin to transfer my CATIA designs into physical constructs.

I wish to thank Gilles Godard for his valuable assistance to setup the hot wire anemometry experiment.

A special thanks to Prof. Ramesh and Dr. Ganesan, who have introduced me to the CORIA laboratory.

I would like to thank Céline Tournebize, Florient Frat, Nathalie Pasquier, Corine Lacour, Amath Lo, Altug Yavuz and all other members of CORIA laboratory. Hearty thanks to Arnab, Subbu, Siva, Selvam, Suresh, Preetha and Mukesh.

I would like to thank my beloved parents (Mr. Balusamy and Mrs. Kasthuri Balusamy) and my beloved sister (Ms. Vadivu) for being a source of constant moral courage and inspiration.

Summary

Stratified mode of combustion in practical applications increases their fuel efficiency and reduces CO_2 emissions. However, a better control of stratified combustion requires deeper knowledge about the propagation of flame through stratified mixture field. So, in order to understand the stratified combustion and to provide quantitative data for the numerical modeling, the propagation of propane-air flames through stratified mixture field under laminar and turbulent flow condition in a constant volume combustion chamber is investigated. Simultaneous PIV/PLIF measurement techniques have been utilized to calculate combined velocity and equivalence ratio field of flame propagation. The flow of propane-air mixture is seeded with olive oil particles and anisole vapor, illuminated by combined PIV/PLIF laser sheets and emitted Mie scattering signal is collected by CCD camera and emitted fluorescence signal is collected by ICCD camera. The acquired images are then post-processed to measure combined flow and scalar fields of combustion. The interference of one technique on other technique are verified and successfully eliminated. All the parameters of experimental set-up are optimized to produce quantitative data with low uncertainty and the accuracy of measurements are improved with new post-processing tools developed in this work.

In the first part of study, turbulent stratified flame propagation in a constant volume combustion chamber is investigated. An axi-symmetrical injection setup has been developed to realize stratified mixture field and its parameters are optimized to achieve rich mixture condition at the point of ignition. The evolution of velocity of jet at the entrance of combustion chamber is measured by hot wire anemometry. The flame is spark-ignited and its propagation through stratified mixture is acquired by simultaneous PIV/PLIF techniques. In order to isolate stratification effect from flow turbulence, the flame propagations through six different homogeneous mixtures with same aerodynamic conditions are also acquired. From the acquired images, combined velocity and equivalence ratio fields are measured and flame fronts are extracted with sub-pixel resolution by a new extraction tool. From the extracted flame fronts, global parameters of all the cases are calculated and compared. The local flame speed, local equivalence ratio and local fresh gas velocity around the flame fronts are measured for all the cases. The local values of stratified flames are conditioned by local equivalence ratio and conditioned values are compared with that of equivalent homogeneous cases to understand the effect of stratification on the enhancement of flame propagation.

The second part of study is focused on the developments of local measurements of flame speed and fresh gas velocity in order to investigate laminar stratified flames quantitatively. So in this part, two original methods have been developed to deduce the local flame speed and local fresh gas velocity from pair of PIV images. The local flame speed is measured from the distance between two successive flame front positions. The local fresh gas velocity near the flame front is extracted from the maximum of the normal velocity profile, located within $1\ mm$ ahead of the flame front. To achieve the required spatial resolution, a new algorithm based on interrogation window reshaping technique has been developed which takes into account the flow and flame front topologies. The accuracy and reliability of the new methods have been evaluated from two complementary approaches based respectively on synthetic images of particle and on the well-established configuration of outwardly propagating spherical flames.

The final part of this study is the investigation of laminar stratified flame propagation in a constant volume combustion chamber. For that, a unique injection setup has been developed to achieve controllable as well as repeatable laminar stratified mixture field inside a constant volume combustion chamber. The injection system is optimized to realize very low flow with very high degree of stratification. The flame is then spark-ignited and its propagation through stratified mixture is acquired by using simultaneous PIV/PLIF measurement techniques. The flame propagations through three different stratified fields with same aerodynamics are acquired to know the effect of degree of stratification on flame propagation. From the particle images, the local flame speed, local fresh gas velocity and local laminar burning velocity are calculated by using new PIV algorithms developed in the second part of this work. The local variables of all three stratified cases are then conditioned based on local equivalence ratio of $\phi = 0.6$ and compared with each other in order to know the influence of degree of stratification on memory effect and relaxation time of stratified flames. The experimental data gathered in this study provides a useful validation set for stratified combustion models.

Keywords: Stratified combustion, Local laminar burning velocity, PIV, PLIF, Propane-Air, Memory effect, Adaptive interrogation window scheme, Local fresh gas velocity, Axi-symmetrical injection, Hot wire anemometry, Flame front extraction

Contents

Chapter 1

Introduction

1.1 Fossil fuel combustion and pollution

Since the start of industrial revolution, we developed the ability to harness power of fossil fuels, which eventually influenced our day-to-day life. At the beginning of 18^{th} century, coal is used to fire the steam engines and coal gas is used as gas lights. Then, transportation sector started to expand with the application of steam engines and further accelerated by the invention of internal combustion engines powered by gasoline and diesel oils. Today, energy produced from the combustion of fossil fuels cover almost 85% of global energy demand [Brown (2006)]. The usage of fossil fuel is continuously increasing with the development of emerging economies and with rise of human population. But the burning of fossil fuels produces lot of harmful emissions and

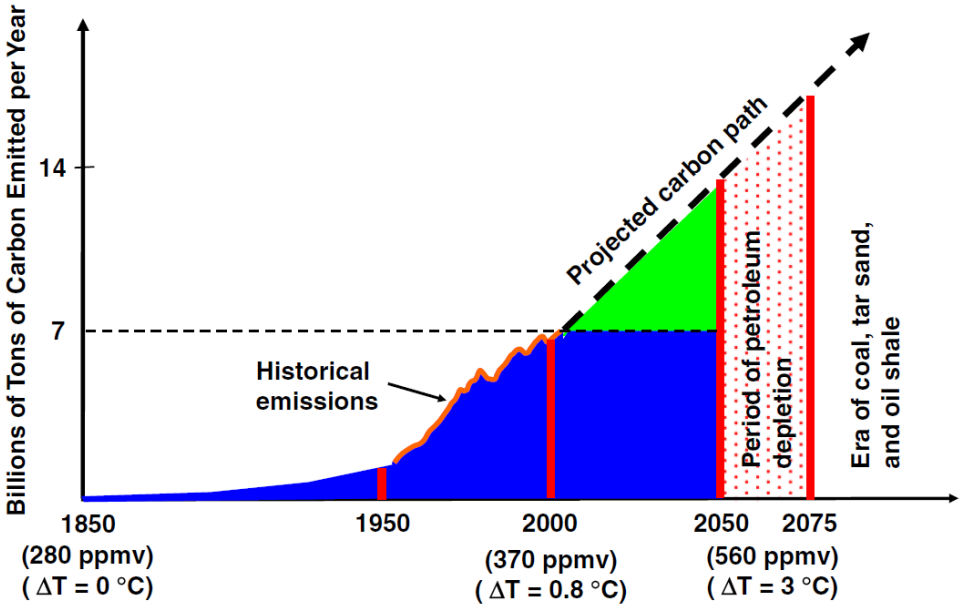

Figure 1.1: Projections of fossil fuel availability and CO_2 emissions. Figure taken from Law (2007)

our unsustainable addiction to the consumption of fossil fuel started to impact the environment of the Earth. Among the pollutants, greenhouse gases (GHG) plays a crucial role in controlling the

temperature of Earth's atmosphere. One of the major greenhouse gases is carbon dioxide (CO_2). The historical and projection of CO_2 emissions after start of industrial revolution is shown in Fig. 1.1. The global mean surface temperature is increased 0.8 °C during the period 1850 to 2000 and projected to increase around 3 °C if that current pattern of fossil fuel consumption is continued. This high global temperature could affect the delicate balance of nature of Earth and could lead to catastrophic situations. So it is important to reduce the fossil fuel consumption, cut down the emissions and to find alternative energy sources within another two or three decade.

At present, transportation sector consumes around 25% of world's fossil fuel supplies, burning them in internal combustion engines and gas turbines, and produces lot of greenhouse gas emissions. The historic and future predictions of CO_2 emissions by different mode of transportation is shown in Fig. 1.2. It clearly shows that the road transportation sector is the major contributor of CO_2 emissions in to the atmosphere. Since the level of emission is proportional to the consumption, it is important to improve the fuel efficiency of automobiles. So the top priorities of vehicle

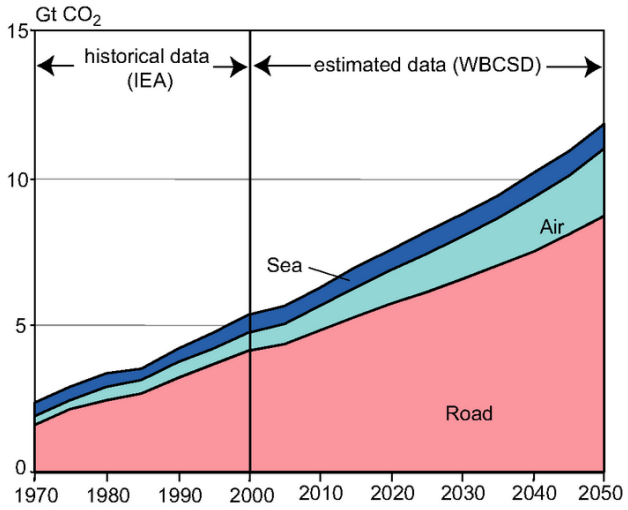

Figure 1.2: CO_2 emissions by different modes of transportation (source IPCC Fourth Assessment Report: Climate Change 2007)

manufacturers are increasing the fuel efficiency and reducing the emissions to zero level. Recent research and developments focus on new strategies to control the combustion and to reduce the emission. One such technology is the gasoline direct injection (GDI) engines which offers more fuel efficiency and lower CO_2 emissions than conventional petrol engines [Zhao et al. (1999), Alkidas (2007)].

1.2 Gasoline direct injection engines

Mitsubishi was the first gasoline direct injection engine manufacturer who introduced the GDI engines to the Japanese market in 1996 and to the European market in 1997 [Iwamoto (1997)]. This was followed by manufacturers throughout the world due to its improved efficiency compared to port-fuel-injected (PFI) engines. The major difference between GDI engine and PFI engine is the way of preparing fuel-air mixture inside a combustion chamber. In the PFI engine, fuel is injected

into the intake manifold which partially evaporates and mixes with throttled air flowing to the cylinder during intake stroke. This injection strategy indirectly controls the fuel-air mixture condition and that leads to cold starting problem, fuel wall wetting, incomplete burning and higher emissions. Those problems can be avoided by direct injection of fuel inside the cylinder. In GDI engine, fuel is directly injected inside the combustion chamber like diesel engine which helps to provide precise control on fuel-air mixture condition at each cylinder based on the requirements. The main advantages of GDI engines over PFI engines are the elimination of pumping loss, charge cooling effect, higher volumetric efficiency, higher compression ratio, lower octane requirement, improved transient response of engine, faster cold starting and lower CO_2 emissions [Zhao et al. (1999)].

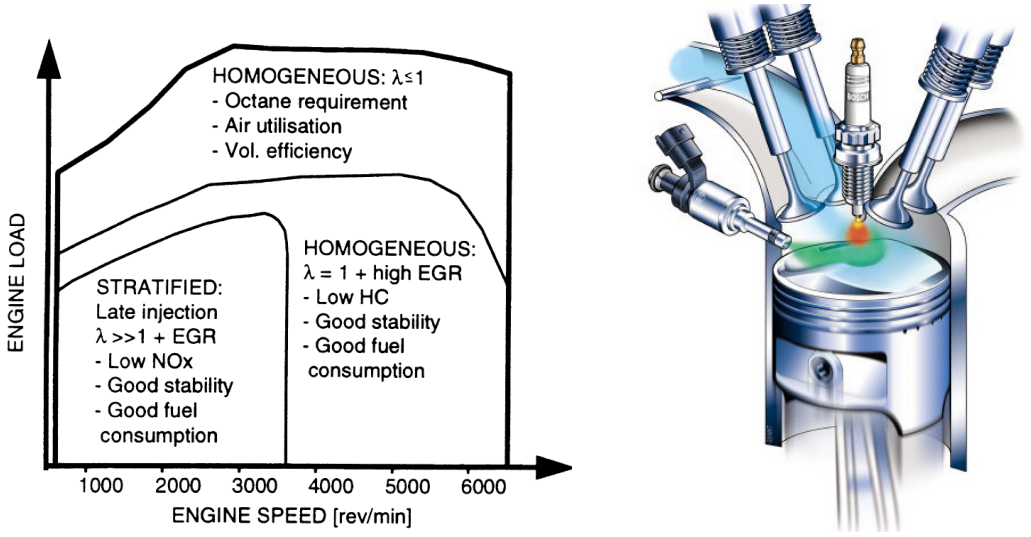

(a) GDI engine operating map (Zhao et al. (1999))

(b) Ford 3.5L EcoBoost engine

Figure 1.3: Gas direct injection engine

One example of GDI engine operating regimes is shown in Fig. 1.3. The potential of GDI engine is realized by advanced combustion strategies which switch the engine operating condition from homogeneous regime to stratified combustion regime whenever possible. Under low engine load and low engine speed conditions, the engine operates in the stratified mode by delayed injection. In this mode, the overall mixture is lean but the mixture is rich around the spark plug at the time of ignition, which ensures the combustion. This strategy results in less fuel consumption and lower CO_2 emissions. Under normal load conditions, the engine operates in the homogeneous mode by injecting the fuel during intake stroke. This homogeneous combustion mode of GDI engine is also effective due to the direct injection which improves the overall performance of engine.

In GDI engine, fuel-air mixing strategy plays a key role in determining the performance of engine. Three major strategies have been developed as shown in Fig. 1.4. Spray guided systems are realized by a special arrangement where the spark plug and injector are located close together. The equivalence ratio around the spark plug is controlled by the spray penetration so the distribution of fuel-air mixture depends on the spray characteristics. The performance of spray guided system is affected by spark plug wetting, shortened spark plug life, high cost of resistant materials and so on. The wall guided system relies on the shape of piston crown in order to

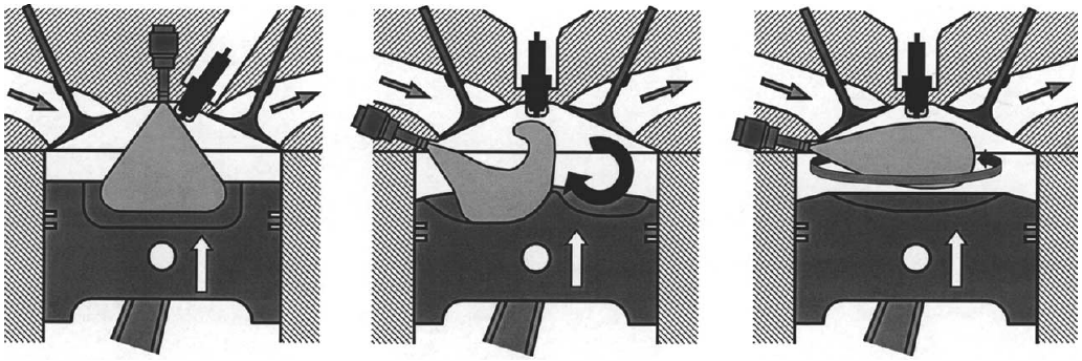

Figure 1.4: Classification of GDI combustion systems: spray-guided (left), wall-guided (middle) and flow-guided (right) system. [Hentschel (2000)]

achieve the rich mixture around the spark plug. The piston crown is shaped like bowls to direct the flow toward the spark plug. This creates tumble motion inside the plane which reduces the wall wetting effect by directing the hot flow toward the wall which promotes the evaporation of fuel droplets. The wall guided system is intensively used due to its advantages over spray guided system. In the flow guided system, the fuel spray is guided to the spark plug by air motion. The inlet valves are designed in such a way that they create an air flow that rotates around the spark plug. The problem with this strategy is the fuel deposit on the wall due to centrifugal force of air motion. So in all the methods either fuel flow or air flow pattern plays a key role in achieving the stratification of mixture field around the spark plug. An optimum GDI engine needs precise control of fuel-air mixture around the spark plug which depends upon various parameters of injection system, cylinder and piston geometries, valve timings, engine operating conditions. Therefore, potential advantages of GDI engines are constrained by the difficulties in controlling the stratified mixture around spark plug, complexity of injection and combustion controlling systems needed for smooth operation, and so on [Zhao et al. (1999)].

1.3 Background

The stratified combustion mode of GDI engine improves the fuel efficiency and reduces CO_2 emissions significantly. However, to achieve the benefits of stratified combustion, the engine configuration must be able to generate favorable stratified mixture condition around the spark plug, otherwise knock and misfire can occur. Indeed, numerical simulation tools can be very helpful to optimize the engine design parameters but the selection of desired mixture conditions around the spark plug for different engine operating conditions is difficult and that requires deeper knowledge about the stratified combustion. Actually, stratified combustion is very complex one where the flame front propagates through non homogeneous mixture field and subjected to various turbulent scales. Unlike premixed flames, stratified flames exhibit memory effect which means the characteristics of propagation is affected by the burned products of previous timings of propagation. This memory effect combined with flow-flame interactions and complex engine geometries make the stratified combustion very difficult to model. So it is necessary to investigate the stratified combustion and to develop experimental database for further improvements of GDI engine technology.

1.4 Objectives of this study

The main objective of this experimental study is to investigate the stratified flame propagation in simplified configuration in order to understand the stratified combustion and to provide useful data for the numerical simulations. Quantitative analysis of combustion parameters can be very helpful in that regard and those parameters can be measured from the flow and scalar fields of flame propagation [Pasquier et al. (2007)]. So, one of the main tasks of this study is to measure the combined flow and scalar fields of flame propagation by utilizing simultaneous PIV/PLIF measurement techniques.

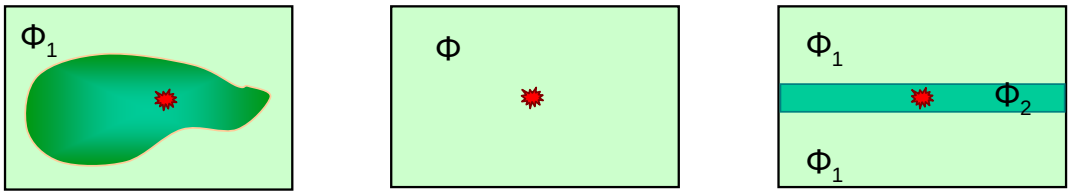

(a) Case 1: Turbulent stratified combustion

(b) Case 2: Laminar premixed combustion

(c) Case 3: Laminar stratified combustion

Figure 1.5: Case studies.

The main aim of this study is to analyze the flame propagation through stratified mixture field under laminar and turbulent flow conditions. So the work is divided into three cases (Fig. 1.5) as given below:

1. To achieve a turbulent stratified mixture field inside a constant volume combustion chamber and to analyze the flame propagation through stratified and equivalent homogeneous mixture fields in order to gain the knowledge of stratification effect on flame propagation.

2. To develop a direct experimental approach to measure the local instantaneous laminar burning velocity of stretched premixed flames in order to extend the application of this approach to the laminar stratified flames.

3. To establish a laminar stratified mixture field inside a constant volume combustion chamber and to investigate the flame propagation through different stratified mixture fields in order to know the effect of degree of stratification on flame propagation.

1.5 Outline of the thesis

The present thesis is organized into eleven chapters.

Chapter 2 contains a brief summary about the fundamentals of laminar premixed combustion, turbulent combustion and the partially premixed combustion. A literature review about the experimental and numerical investigations on stratified flame propagation is provided.

Chapter 3 gives a brief introduction of experimental configurations used in this work.

Chapter 4 describes the principle of PIV technique, its subsystems and the post-processing schemes used to measure the velocity vector field. The uncertainty and spatial resolution of velocity measurements are provided.

Chapter 5 describes the PLIF technique, its subsystems and the fluorescent tracer used in this work. The new LIF image error correction algorithm for the measurement of equivalence ratio field is presented. The uncertainty and spatial resolution of equivalence ratio measurements are provided.

Chapter 6 describes the way of combining the PIV and PLIF techniques in order to achieve the simultaneous measurement of velocity and equivalence ratio field of flame propagation.

Chapter 7 provides the details of axi-symmetrical injection setup developed for the preparation of turbulent stratified mixture field inside a constant volume combustion chamber. The velocity and equivalence ratio of stratified mixture field at the time and position of ignition are presented.

Chapter 8 analyzes the turbulent flame propagation through stratified and homogeneous mixture fields. The global and local variables of stratified and homogeneous flames are measured and the results are compared in order to gain knowledge of effect of stratification on flame propagation.

Chapter 9 introduces a new direct experimental approach developed for the measurement of local instantaneous laminar burning velocity of stretched flames. Two original methods for the measurement of local flame speed and local fresh gas velocity near flame front are presented. The validations of new methods are provided.

Chapter 10 provides the details of injection setup used for the realization of laminar stratified jet inside a constant volume combustion chamber. The flame propagations through three different stratified mixture fields with same flow conditions are analyzed. The local variables are calculated by using new PIV algorithms. The local conditioned velocities of three different stratified cases are compared in order to know the effect of degree of stratification on flame propagation.

Chapter 11 contains a summary of the different tasks carried out in this work and the relevant conclusions drawn from each task. In the end, some possible research perspectives are suggested.

Chapter 2

Literature review on stratified combustion

Abstract. *The combustion of fossil fuels converts the chemical energy into heat, but also produces lot of pollution. The need to reduce emission and fuel consumption motivates the scientific research community to develop new technologies. One such technology is the direct injection gasoline engine which uses stratified combustion strategy for the part load operations. This stratified mode of combustion is complex and the optimization of its various parameters requires more fundamental understanding of the flame propagation through spatially non-homogeneous mixture conditions. The characteristics of the stratified combustion depend strongly on the local variations of mixture and also on the length-scale of these variations. In this chapter, the basic parameters of combustion process such as laminar burning velocity, flame stretch rate, turbulent burning velocity and turbulent premixed combustion regimes are reviewed. The effects of equivalence ratio on the burning velocity, wrinkling of flame front due to the turbulence and the flame front instabilities are discussed. Few experimental and numerical investigations on the stratified combustion are reviewed.*

2.1 Introduction

The combustion of fossil fuels produces energy that meets almost 85% of global energy demand. But the combustion process produces lot of greenhouse gases too, which are impacting the climate of earth [Brown (2006)]. So, the most important concern is to minimize the emissions as well as improve the efficiency of the combustion processes. A lot of interesting solutions have been developed in the automobile sector which contributes major part of fossil fuel usage. The recent developments are homogeneous charged compression ignition engines and direct injection gasoline engines [Zhao et al. (1999, 2003)]. The direct injection gasoline engine technology helps to realize low fuel consumption as well as low CO_2 emissions [Takagi (1998), Zhao et al. (1999), Alkidas (2007)]. But the design parameters of direct injection engine need to be optimized for the maximum benefits [Duclos et al. (1999)]. In that regard, computational fluid dynamics (CFD) tools play a key role in optimizing the various parameters like piston crown shape, injector location, spray parameters, spark plug orientation and so on. However, numerical modeling requires

fundamental understanding of the complex combustion processes happening inside the combustion chamber [Barlow (2007)]. Experimental investigations on the simplified configurations can be very useful to understand the fundamental combustion process [Dégardin et al. (2006), Pasquier et al. (2007), Anselmo-Filho et al. (2009)]. This chapter covers some of the basic concepts of combustion and more about the partially premixed flame propagation in laminar and turbulent flow conditions to examine the availability of data to understand the stratified combustion.

2.2 Laminar premixed combustion

The combustion can be classified as premixed and non-premixed combustion based on the fuel and air mixing process. In the premixed mode of combustion, the fuel and air are mixed prior to entering the flame front zone. So in this mode, the flame propagation is more like a wave phenomena and the most important parameter is the laminar burning velocity [Law (2006)]. This laminar burning velocity is related to the physico-chemical properties of the fuel-air mixture, therefore many of the premixed flame characteristics such as extinction, flashback, blow-off and turbulent burning velocity can be computed from the laminar burning velocity.

2.2.1 Structure of laminar premixed flame

The conceptual structure of planar laminar flame is shown in Fig. 2.1. The two important zones of premixed flame are the preheat zone and the reaction zone. All the chemical processes are take place in the reaction zone where the fresh mixture burns and produces high temperature which is around $2000K$ for the hydrocarbon fuels. This high temperature continuously heats up the chemically inert premixed zone. Typical value of flame front thickness (δ_l) which comprises both reaction and premixed zone is around 0.1 to $1mm$ [Law (2006)].

The preheat zone thickness of flame front can be related to the properties of fuel-air mixture by the following expression [Lecordier (1997)]:

$$\delta_p = \frac{\lambda}{\rho C_p S_L^0} \tag{2.1}$$

where λ is the thermal conductivity of mixture, C_p is the specific heat, ρ is the mass density of fresh mixture and S_L^0 is the planar laminar burning velocity. The reaction zone thickness (δ_r) can be related to the preheat zone thickness (δ_p) by:

$$\delta_r = \delta_p/\beta \tag{2.2}$$

where β is Zeldovich number which is in the order of 10. The thickness of preheat zone and the laminar burning velocity can be related to the chemical time scale as:

$$\tau_c = \delta_p/S_L^0 \tag{2.3}$$

The important characteristic dimensions of laminar premixed flames are δ_p, δ_r and τ_c, very essential for the modeling of turbulent combustion.

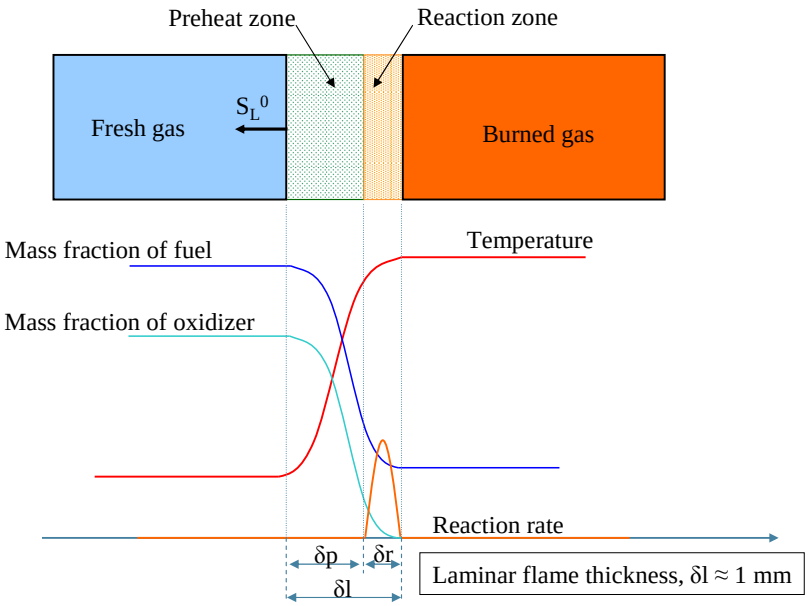

Figure 2.1: Planar laminar premixed flame structure.

2.2.2 Planar laminar burning velocity

The velocity of a perfect one-dimensional, planar, adiabatic, unstrained and steady flame is defined as the planar laminar burning velocity. The first theoretical analysis of planar laminar burning velocity is proposed by Mallard and Le Chatelier in 1886. Further works are carried out by Zeldovich, Frank-kamenetskii, Semenov and Clavin [Glassman (1987)]. The theoretical prediction of laminar burning velocity is expressed as [Clavin (1985)]:

$$S_L^0 \propto \frac{\rho_b}{\rho_u}\sqrt{\frac{D_{th}}{\beta^{n+1}\tau_r}} \tag{2.4}$$

where ρ_b is the density of burned gas, ρ_u is the density of fresh gas region, D_{th} is the heat diffusivity of reactive mixture, β is Zeldovich number, n denotes the reaction order of the limiting component and τ_r is the chemical reaction time. The above expression also indicates the relationship between the laminar burning velocity and the equivalence ratio of mixture. The measurement of planar laminar burning velocity is very difficult due to the practical limitations to achieve adiabatic, unstrained, steady laminar flame. So, various experimental configurations have been developed to calculate the laminar burning velocity from the global measurements. The different methods and the accuracy of measurements are given in the next section.

2.3 Influence of flame stretch rate

The important configurations that have been used for the laminar burning velocity measurements are flat counter-flow flames [Egolfopoulos et al. (1989)], spherically propagating flames in a combustion vessel [Stone et al. (1998)] and flat adiabatic stabilized flames [Bosschaart and De Goey

(2004)]. Few experimental results obtained from those configurations for the propane/air mixture at atmospheric pressure and ambient temperature conditions are shown in Fig. 2.2. In general, the maximum laminar burning velocity is predicted at around $\phi = 1.0$. But there are differences in the magnitude of laminar burning velocities due to the assumptions used for the calculation, stretch effects on the flame propagation and the presumed values of fuel-air properties.

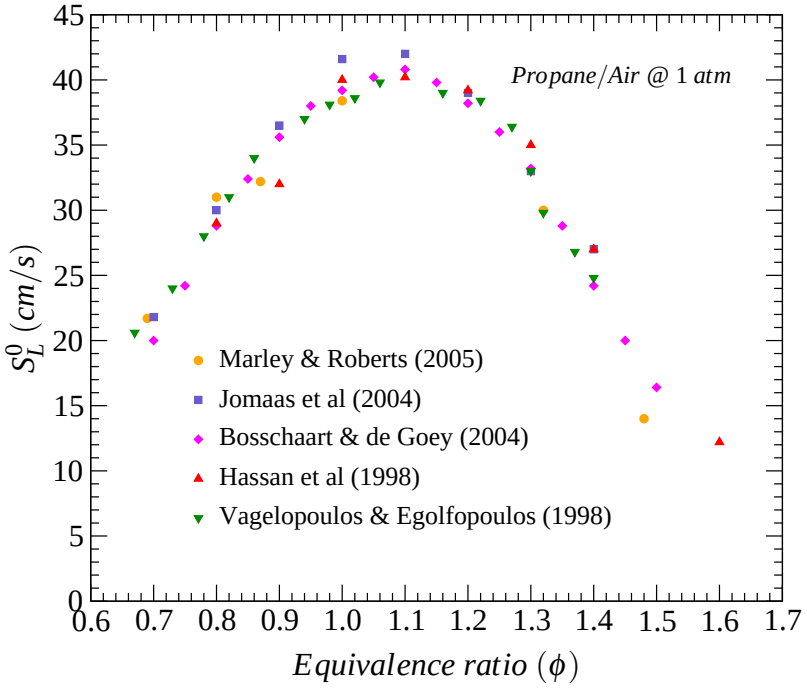

Figure 2.2: Influence of equivalence ratio on the propagation of planar laminar flame.

The influence of stretch rate on the flame propagation is well explained by Bradley et al. (1996). The flame stretch rate, k, is defined as the fractional rate of change of an area element on a flame surface [Williams (1985)]:

$$k = \frac{1}{A}\frac{dA}{dt} \tag{2.5}$$

where A is the area of the surface element of flame. The total flame stretch rate is the combination of stretch rate due to the curvature (k_c) and stretch rate due to the flow field aerodynamic strain (k_s) [Bradley et al. (1996)].

$$k = k_c + k_s \tag{2.6}$$

Locally, flame front is stretched due to the interaction between flame propagation and flow expansion, which induces local variations in the flame temperature and the mass burning rate. So, a strong relationship exists between local flame speed and the local flame stretch rate and any experimentally measured value of the laminar burning velocity should be associated with their corresponding stretch rate [Clavin (1985)]. That means the experimental configuration must provide a well defined relationship between the flame stretch rate and the flame propagation.

2.4 Spherical flame configuration

Among the different experimental configurations, spherical outwardly propagating flame at constant pressure has an advantage of continuous variation of stretch during the flame propagation, so that the unstretched laminar burning velocity can be obtained through a linear extrapolation to zero stretch with some assumptions [Markstein (1964)].

The general expression of flame stretch rate (Eqn. 2.5) can be simplified for the case of spherically symmetrical flames propagating outward at constant pressure from a central ignition point source [Clavin (1985)] as:

$$k = \frac{2}{r}\frac{dr}{dt} = \frac{2}{r}S_b \tag{2.7}$$

where S_b is the flame speed and r is the radius of flame front as shown in Fig. 2.3.

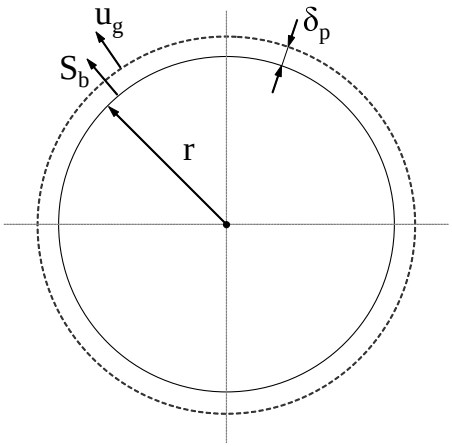

Figure 2.3: Description of the structure of spherically expanding laminar flame front.

The flame speed of a spherical outwardly propagating flame at constant pressure is related to the flame stretch rate through a linear relationship, in the limit of a moderate stretch and far from the extinction limit [Clavin (1985)],

$$S_b(k) = S_b^0 - L^b \cdot k \tag{2.8}$$

where S_b^0 is the unstretched flame speed and L^b is the burned gas Markstein length. The unstretched laminar burning velocity is then deduced from the unstretched flame speed by considering mass continuity at zero stretch.

$$u_{s_b}^0 = S_b^0/(\rho_u/\rho_b) \tag{2.9}$$

where, (ρ_u/ρ_b) is the ratio of the unburned and burned gas densities assuming adiabatic combustion at constant pressure.

The fresh gas velocity u_g near the preheat zone of flame front can be related to the laminar burning velocity by the following expressions [Bradley et al. (1996)]:

$$u_{n_r}(k) = \frac{-\rho_b}{\rho_b - \rho_u} u_g(k) \tag{2.10}$$

$$u_{n_r}(k) = u^0_{n_r} - L^{nr} \cdot k \tag{2.11}$$

where $u^0_{n_r}$ is the unstretched laminar burning velocity and L^{nr} is the Markstein length in the fresh gas region.

The laminar burning velocity can also be determined directly as the difference between the local flame speed S_b and the local fresh gas velocity u_g as a function of flame stretch rate [Bradley et al. (1996), Lecordier (1997)]

$$u_n(k) = S_b(k) - u_g(k) \tag{2.12}$$

$$u_n(k) = u^0_n - L^n \cdot k \tag{2.13}$$

where, u^0_n is the unstretched laminar burning velocity at zero stretch and L^n is the Markstein length in the fresh gas region.

Markstein length can be expressed in the non-dimensional form, as a Markstein number (Ma) by normalizing the length by planar flame front thickness (δ_l):

$$Ma^n = L^n/\delta_l \tag{2.14}$$

The Markstein lengths and Markstein numbers are very useful parameters to analyze the flame front instabilities [Gu et al. (2000)].

2.5 Flame front instabilities

The flame front can be regarded as a boundary which separates the fresh gas mixture from the burned products. During the combustion, the burned products expand and the coefficient of expansion (Θ) is defined as the ratio of fresh gas mixture density (ρ_u) to the burned gas density (ρ_b) [Bychkov and Liberman (2000)]. It varies from 5 to 10 for most of laboratory flames. This expansion of burned products is strongly coupled with fuel flow which leads to the different kind of flame front instabilities.

2.5.1 Hydrodynamic instabilities

The general structure of flame front is wrinkled in many experimental configurations because of hydrodynamic instability, first studied by Darrieus and Landau (DL theory). All the flame propagations in gaseous mixtures are subjected to this hydrodynamic instability due to the expansion of burned products [Bychkov and Liberman (2000)]. The streamlines of wrinkled flame fronts are completely different from planar flame front propagation. The deflection in the streamlines develops convective fluxes inside the flame in the direction tangential to the tilted front as shown in Fig. 2.4. Also, the deflection of the streamlines induces a hydro-dynamic perturbation in the upstream and downstream flow. In the convex part, the streamlines are converging in the burned gases and the reverse happens for the concave part [Clavin (1985)]. The expansion and contraction of stream-tubes introduce a pressure gradient which amplifies the flame propagation. So the initial perturbation in the flame front grows rapidly in time and further wrinkles the flame front, leads to

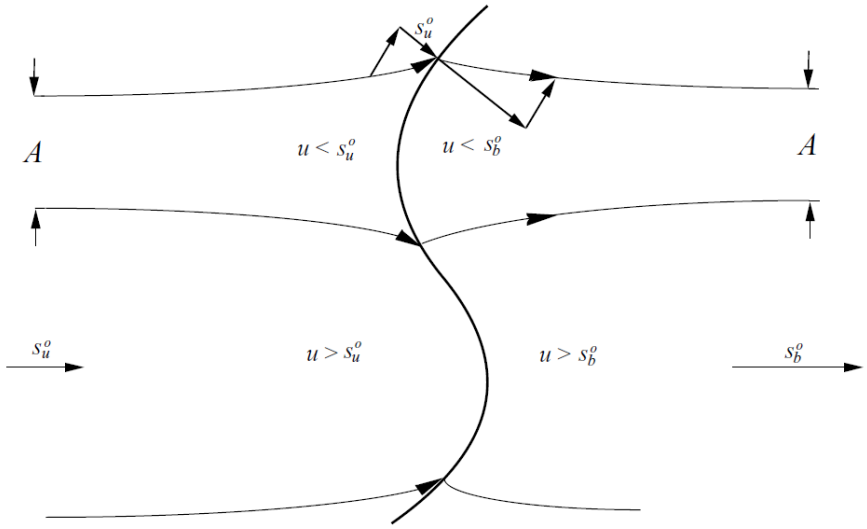

Figure 2.4: Modifications of streamlines produced by wrinkling of flame front (Clavin (1985)).

the DL instability. Experimental investigations of DL instability have shown that the characteristic length scale of instability is at least twice the order of flame front thickness [Bychkov and Liberman (2000)]. The solution for the DL instability has been developed by taking into account the thermal conduction and fuel diffusion [Clavin (1985)].

2.5.2 Thermo-diffusive instabilities

In the case of premixed flames, even though the fuel diffusion is not controlling the burning rate but still it is an important factor when the fuel diffusion is stronger than thermal conduction. Actually, it can lead to the thermal instabilities of flame front. For a wrinkled flame front, the diffusive fluxes of mass and heat are not only in the normal direction of flame front, but also present in the tangential direction of flame front as shown in Fig. 2.5.

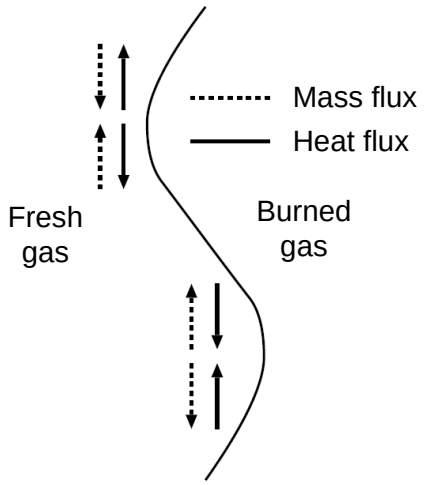

Figure 2.5: Thermo-diffusive instabilities (Clavin (1985)).

Transverse diffusion fluxes of mass and heat are opposite and modify the local temperature of combustion. In the convex part of upstream side flame front, the diffusion flux of heat has a tendency to reduce the temperature whereas the diffusion of mass increases the total amount of chemical energy to be released. The inverse phenomenon happens in the concave part of flame front.

The competition between thermal diffusivity (α) and mass diffusivity (D) for a particular species (k) can be understood well by analyzing its Lewis number (Le_k).

$$Le_k = \alpha / D_k \tag{2.15}$$

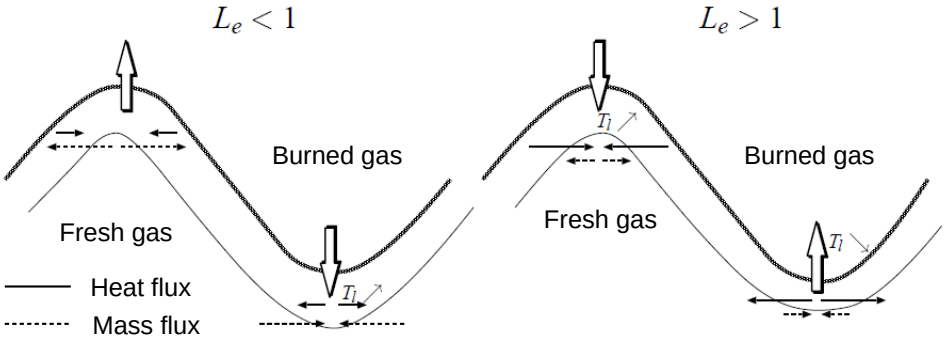

Figure 2.6: Stabilizing or destabilizing effect of Lewis number ($L_e \neq 1$) (Law (1989)).

The effect of Lewis number on the stabilization of flame front is shown in Fig. 2.6. For the case of Lewis number less than unity, reactants diffuse faster than heat which increases the local temperature at convex front and reduces at concave front. The outcome of this effect is the increase of flame speed at convex and vice versa at concave front. The opposite phenomenon happens for the case of Lewis number greater than unity. So for the fuels having $Le > 1$ becomes stable and for the fuels having $Le < 1$ becomes unstable even without the presence of turbulent flow.

2.6 Laminar partially premixed combustion

The laminar burning velocity is strongly coupled with equivalence ratio of mixture and the stability of the flame front is related to the Lewis number which is again based on the fuel-air mixture. So the variation of laminar burning velocity as well as the stability of flame front can be accessed from the equivalence ratio of mixture for the homogeneous combustion. But there are applications where the fuel-air mixture is partially premixed. Combustion of stratified fuel-air mixtures is common in many applications where the behavior of flame propagation are entirely different from that of homogeneous case. These applications need experimental and numerical investigations of partially premixed flames to improve the combustion efficiency and to reduce the pollutions.

Few experimental [Ra (1999), Galizzi and Escudie (2006), Kang and Kyritsis (2007a, 2009)] and numerical [Pires Da Cruz et al. (2000), Marzouk et al. (2000)] investigations have been un-

dertaken to study the laminar flame propagation through spatially non homogeneous mixture conditions. The major findings that have been proposed from the investigations are the widening of flammability limits, enhanced or reduced flame propagation through stratified mixture and modification of inner structure of flame. The stratified flames exhibit memory effect which enhances the flame propagation through very lean mixture field. So the estimation of local variables needs information of flame history which adds further complication to the numerical simulation. Some details of experimental and numerical investigations are described in this section.

2.6.1 Experimental investigations

A detailed experimental analysis of laminar stratified flame propagation was carried out by Ra (1999) using a constant volume combustion vessel (Fig. 2.7). He investigated the flame propagation from rich methane-air mixture (M_1) to lean mixture (M_2) using high speed camera together with Schlieren technique. The mixtures were separated by a soap bubble and the rich mixture inside the soap bubble was ignited by a laser beam. He also carried out numerical calculations using one dimensional HCT code. He concluded that the flame propagation in stratified charge shows

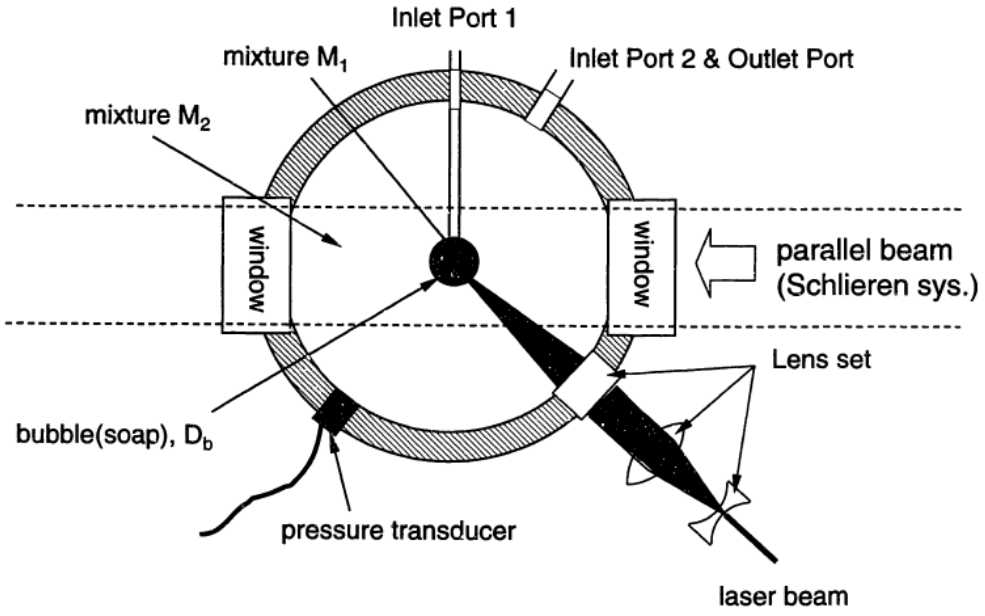

Figure 2.7: Experimental setup for the laminar stratified flame propagation (Ra (1999)).

memory effects so that flame propagates faster from rich to much leaner region. He reported that the hotter burned gas temperature in richer region back supports the flame propagation in leaner conditions. He insisted that the flame modeling should consider the previous burned gas temperature and end gas state.

Samson (2002) investigated the laminar flame propagation through stratified propane-air mixture field using PIV, OH and CH chemiluminescence and PLIF techniques. He examined the propagation of flame along the direction of mixture stratification by using OH and CH chemiluminescence images (Fig. 2.8) and observed oval shape of flame front for stratified cases and decrease of reaction rate with decrease of local equivalence ratio.

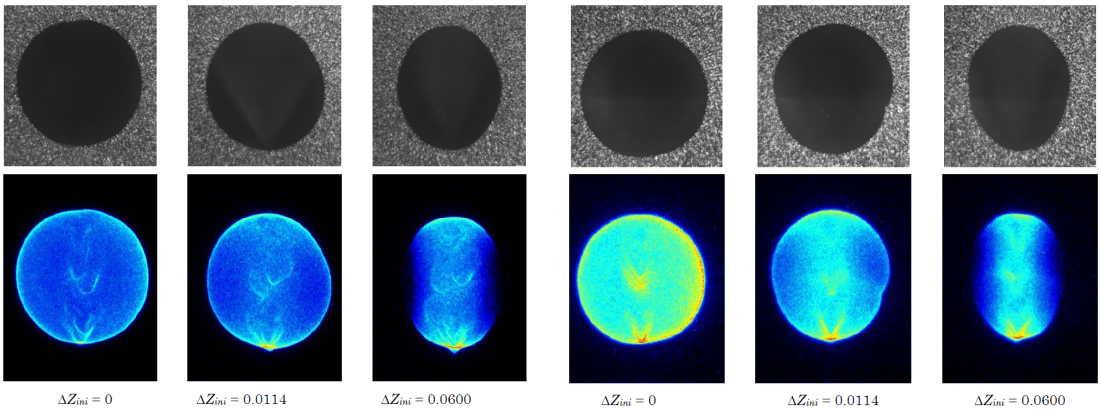

(a) OH chemiluminescence (b) CH chemiluminescence

Figure 2.8: Simultaneous tomography and chemiluminescence images for three different stratifications at 6 ms after ignition (Samson (2002)).

Another interesting experimental investigation was performed by Galizzi and Escudie (2006) on an oblique laminar flame front propagating in a stratified mixture. They investigated methane-air flame propagation using techniques: PIV, laser tomography, CH^* chemiluminescence, LDA, thermocouple measurements, and CH_4 concentration by NDIR method. One example of homogeneous and stratified flame is shown in Fig. 2.9. Their conclusions are: increase of flame speed

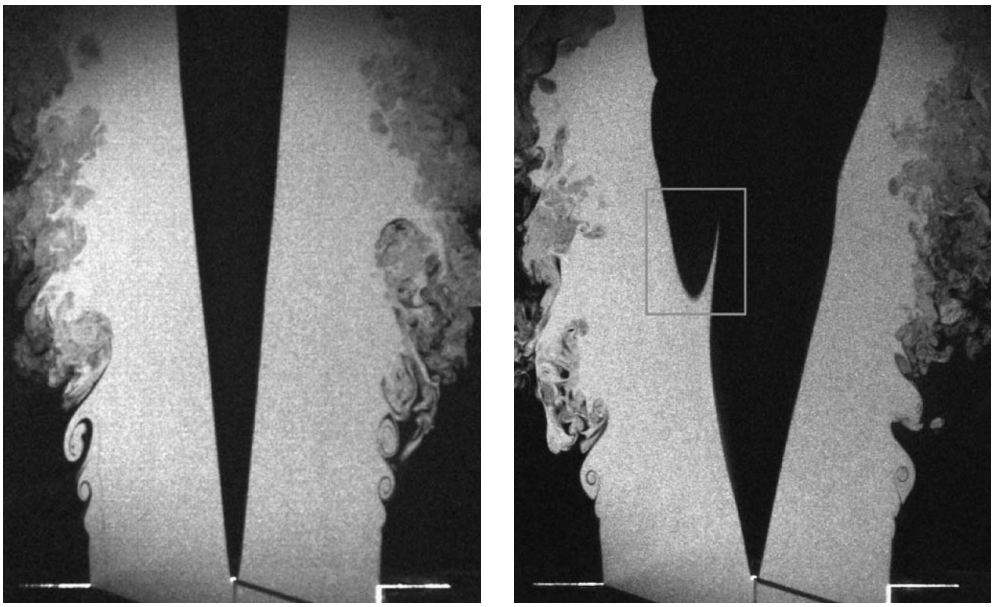

(a) Homogeneous flame. (b) Stratified flame.

Figure 2.9: Propagation of V-shaped flame front in homogeneous and stratified mixtures (Galizzi and Escudie (2006)).

in the stratified case, influence of parallel stratification on the oblique flame propagation and the formation of peninsula shape in stratified mixture region due to the evolution of parallel to normal propagation of flame front.

Dégardin et al. (2006) was conducted a simultaneous measurement of temperature and mixture fraction of V-shaped laminar flame using PLIF and Rayleigh scattering techniques. Their experimental setup is shown in Fig. 2.10. They stabilized a V-shaped flame on a heated rod at the exit of convergent section. By using injection ramps, they were able to generate different stratified mixture conditions. They measured simultaneous temperature and mixture fraction field of methane-air flame and from that they calculated the flame front thickness. From their

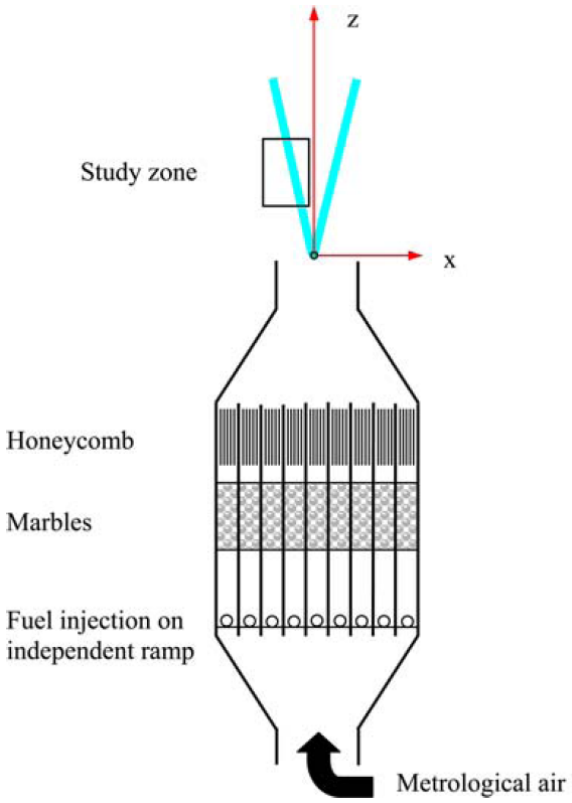

Figure 2.10: Laminar stratified V-shaped flame propagation (Dégardin et al. (2006)).

experimental results, they concluded that the flame thickness of the stratified flames becomes quasi-independent of the local methane mole fraction with decreasing equivalence ratios. But for the homogeneous flames, the flame thickness strongly increases with a decreasing equivalence ratio.

Kang and Kyritsis (2007a,b, 2009) have developed a controllable way to achieve the mixture stratification based on a diffusive-convective balance. They investigated methane-air mixtures using PLIF and line-Raman imaging techniques. The details of their combustion chamber and the stratified mixture profiles are shown in Fig. 2.11. They concluded that the flames propagating in the stratified cases are faster, can reach as much as a factor of two compared to the adiabatic flame speed corresponding to the local equivalence ratio. The heat input from the burned gas dominates the flame propagation over the decrease of equivalence ratio of mixture that means back supported as pointed out by other studies [Ra (1999)].

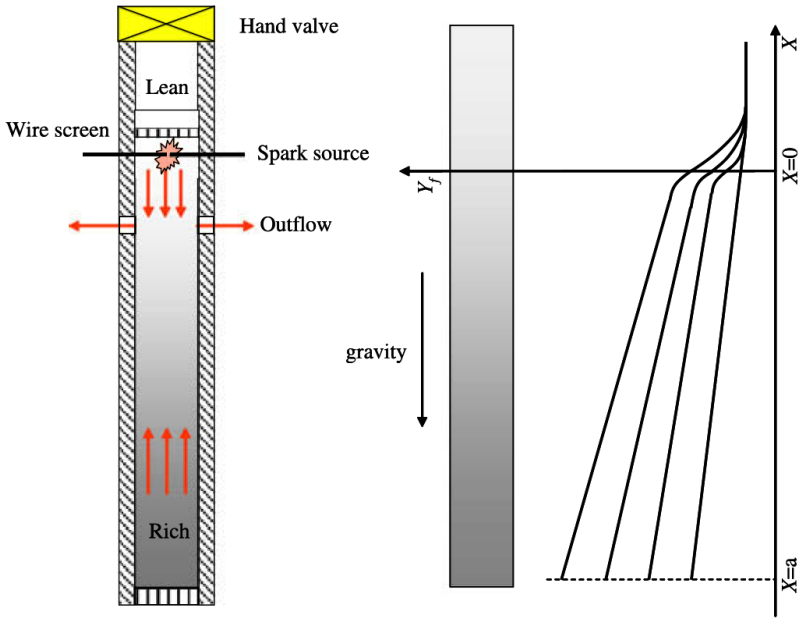

Figure 2.11: Combustion chamber for stratified flame propagation (Kang and Kyritsis (2009)).

2.6.2 Numerical investigations

The numerical simulations on stratified combustion modeling are few due to the complexity of this kind of combustion. Freely propagating laminar methane/air flames through spatially stratified mixture were modeled by Pires Da Cruz et al. (2000). They studied the propagation of flame through four different stratified configurations. One of their results of flame propagation from stoichiometric to lean mixture is shown in Fig. 2.12.

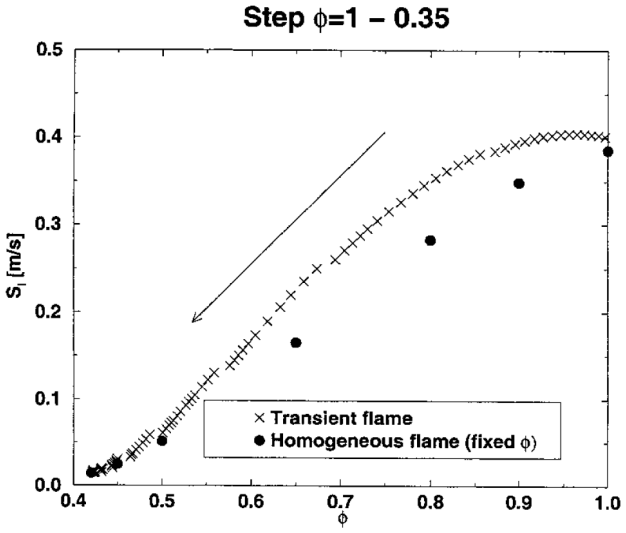

Figure 2.12: Comparison of laminar burning velocities through Stoichiometric to lean mixture (Pires Da Cruz et al. (2000)).

They observed difference in laminar burning velocity between homogeneous and stratified combustion. From their observations, the stratified flame exhibits faster propagation and the lower

flammability domain of methane-air flame is extended from $\phi = 0.5$ to $\phi = 0.42$. They also observed higher burned gas temperatures in the stratified case which attributes to the faster fuel decomposition and faster flame propagation. They reported that the memory effect of flame front which propagates from rich mixture to lean mixture plays a key role in the stratified combustion.

Another interesting numerical simulation was carried out by Marzouk et al. (2000) on unsteady strained flame propagation through stratified mixture. They concluded that the flame speeds in the stratified cases are faster than their equivalent homogeneous conditions and can burn into mixtures lower than flammability limit. They suggested that the high temperature in the rich region acts as a temperature reservoir which back supports the flame propagation and broadens in the lean side.

So far the available experimental and numerical results indicated the different behavior of stratified flame propagation compared to the equivalent homogeneous conditions. But the exact nature of combustion and the important factors that govern the flame propagation are still not clearly understood and needs further quantitative investigation of stratified flame propagation in well established experimental configurations so that measurements can help to improve the modeling of combustion.

2.7 Turbulent combustion

The turbulent combustion covers the majority of combustion applications such as gas turbines and internal combustion engines. The understanding and modeling of turbulent combustion are major challenge to the combustion research community for many decades. There are considerable improvements in the area of non-premixed and premixed turbulent combustion research. However, partially premixed turbulent combustion is not well understood yet. Few experimental and numerical investigations have been carried out to understand the stratified flame propagation. This section covers some of the important topics of turbulent premixed combustion and the next section covers few experimental and numerical investigations on the partially premixed turbulent combustion.

2.7.1 Turbulent burning velocity

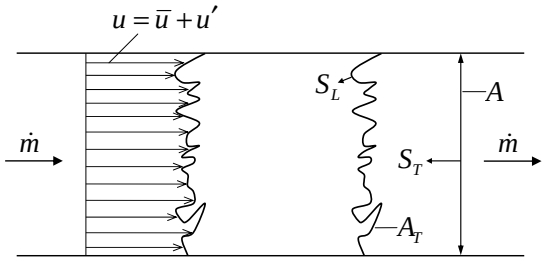

Figure 2.13: An idealized normal premixed flame in a duct with constant flow velocity.

A schematic representation of turbulent flame front in a duct with constant flow velocity is shown in Fig. 2.13. The mass flux $\dot{m}$ through the instantaneous turbulent flame surface area A_T can be

equated to the mass flux through the cross-sectional area A by the following expression [Peters (2000)]:

$$\dot{m} = \rho_u S_L A_T = \bar{\rho_u} S_T A \tag{2.16}$$

where S_L is the laminar burning velocity, S_T is the turbulent burning velocity and ρ_u is the unburned mixture density. By assuming constant density, the above expression can be modified as:

$$\frac{S_T}{S_L} = \frac{A_T}{A} \tag{2.17}$$

This ratio of turbulent to laminar burning velocity can be expressed as [Poinsot and Veynante (2005)]:

$$\frac{S_T}{S_L} \approx 1 + \left(\frac{u'}{S_L}\right)^n \tag{2.18}$$

where u' is the RMS of the velocity fluctuations and n is the adjustable exponent varies between 0.5 to 1.0. A more detailed correlation between the turbulent burning velocity and laminar burning velocity for a real wrinkled flame propagation can be expressed as [Driscoll (2008)]:

$$\frac{S_T}{S_L^0} = f\left(\frac{u'}{S_L^0}, \frac{l}{\delta_l}, Ma_T, \frac{W}{l}, \; or \; \frac{t}{(l/u')}\right) \tag{2.19}$$

where S_L^0 is the unstretched laminar burning velocity, l is the stream-wise integral scale, δ_l is the unstretched laminar flame thickness, W is the burner or chamber size and Ma_T is the turbulent Markstein number.

Driscoll (2008) reviewed three kind of turbulent burning velocities which are global consumption speed, local consumption speed and local displacement speed. For a spherical flame front propagation, local displacement speed is the appropriate turbulent burning velocity. The definition of local displacement speed is given below:

$$S_{T,LD} = (V_{flame} - V_{gas})_{LE} \cdot n_{LE} \tag{2.20}$$

where V_{flame} is the velocity of flame in the laboratory reference, V_{gas} is the velocity of fresh gas at the leading edge (LE) of flame front and n is the normal vector. In this work the local turbulent burning velocity is measured based on the Eqn. 2.20.

2.7.2 Turbulent premixed combustion regimes

Turbulent premixed combustion can be categorized based on their important characteristics like integral length scale, turbulent kinetic energy and dissipation rate. Turbulent combustion diagram in terms of length and velocity scale ratios have been proposed by Barrere (1974), Bray (1980), Borghi (1984), Williams (1985), Peters (1988), Abdel-Gayed et al. (1989). In the combustion diagram, various combustion regimes may be identified by the length (l_t/δ) and velocity scale ratios (u'/S_L) as shown in Fig. 2.14. The important dimensionless numbers in the diagrams are Damköhler number (Da), Reynolds number (Re_t) and Karlovitz number (Ka).

The Damköhler number Da is defined as the ratio of integral time scale (τ_t) to the chemical time scale (τ_c).

$$Da = \frac{\tau_t}{\tau_c} = \frac{l_t}{u'}\frac{S_L}{\delta} \tag{2.21}$$

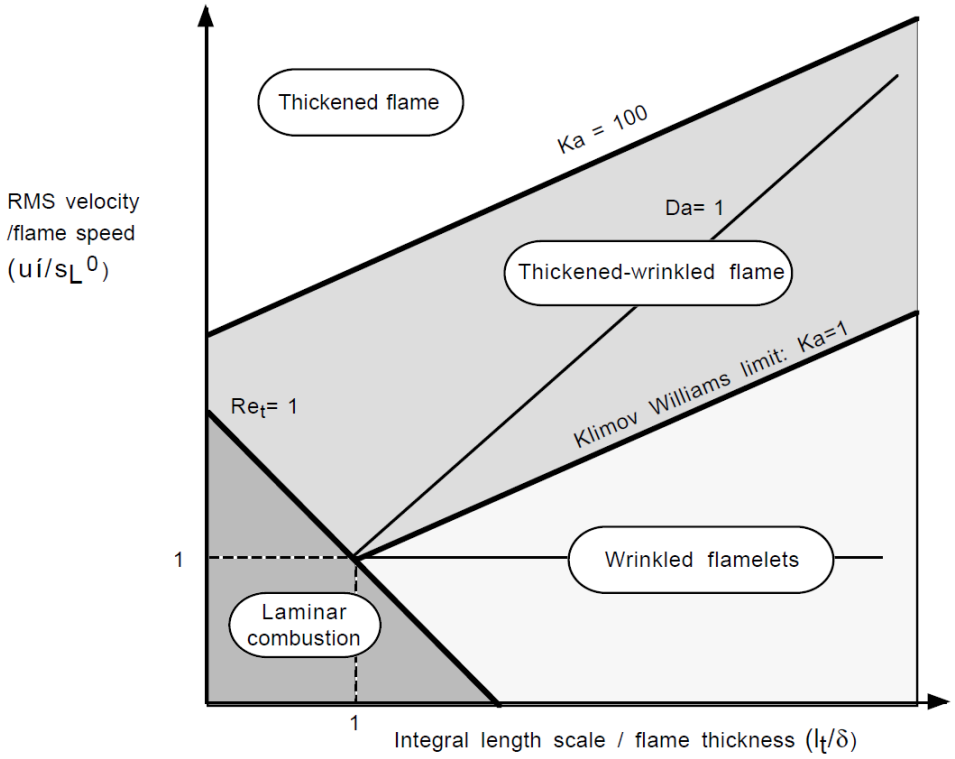

Figure 2.14: Modified turbulent combustion diagram proposed by Peters (Peters (1999)).

where l_t is the integral length scale, u' is the RMS of velocity fluctuations and δ is the thickness of laminar flame.

The Karlovitz number Ka is the comparison of chemical time scale to the Kolomogrov (smaller eddies) time scale (τ_k).

$$Ka = \frac{\tau_c}{\tau_k} = \left(\frac{u'}{S_L}\right)^{3/2} \left(\frac{\delta}{l_t}\right)^{1/2} \tag{2.22}$$

The turbulence Reynolds number is defined as:

$$Re_t = \frac{u'}{S_L}\frac{\delta}{l_t} \tag{2.23}$$

The three non-dimensional numbers are related as:

$$Re_t = Da^2 Ka^2 \tag{2.24}$$

The turbulent premixed combustion can be divided into three regimes using the Damköhler and Karlovitz number [Poinsot and Veynante (2005)]. The three combustion regimes are thin wrinkled flame or flamelet regime, thickened-wrinkled flame regime and thickened flame regime.

Thin wrinkled flame or flamelet regime is shown in Fig. 2.15. In this regime, the flame is thinner than all the turbulent scales ($Re_t > 1, Da < 1 \; and \; Ka < 1$). This regime can be further divided into two regions, based on the velocity ratio u'/S_L.

- Wrinkled flamelet regime ($u' < S_L$): Flame speed is more than speed of turbulent motion. The flow eddies cannot wrinkle the flame up to flame interactions.

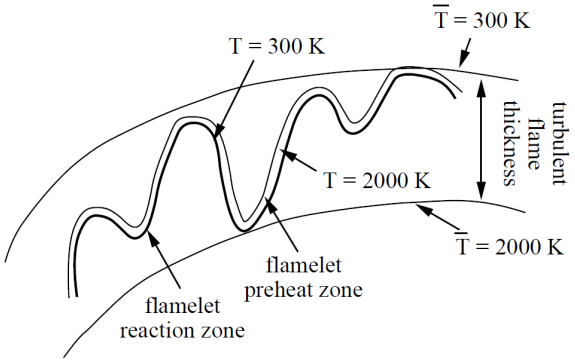

Figure 2.15: Flamelet (Thin wrinkled flame) regime (Poinsot and Veynante (2005)).

- Corrugated flamelet regime ($u' > S_L$): Turbulent motion velocities are dominating the flame speed and wrinkles the flame front up to the flame interactions.

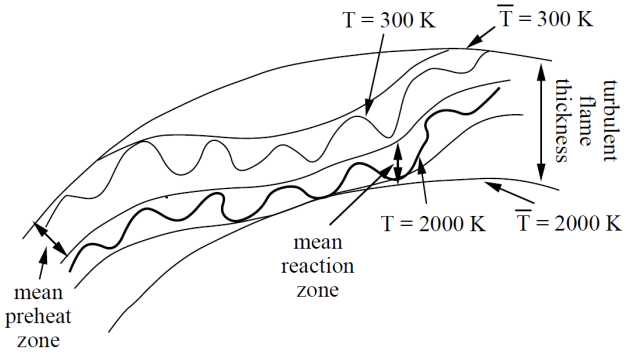

Figure 2.16: Thickened-wrinkled flame regime (Poinsot and Veynante (2005)).

Thickened-wrinkled flame regime is plotted in the Fig. 2.16. This combustion regime is identified by $Re_t > 1, Da > 1 \; and \; Ka > 1$. In this type of flames, the chemical time scale is larger than Kolomogrov time scale but smaller than turbulent time scale so the eddies can penetrate the flame front. The flame front is in wrinkled shape and possibly large eddies can quench the flame locally.

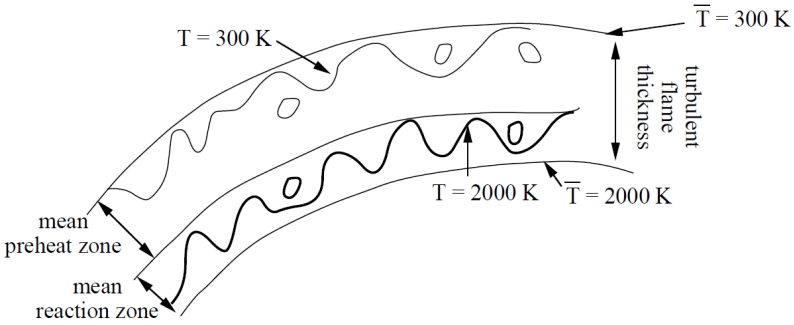

Figure 2.17: Thickened flame regime (Poinsot and Veynante (2005)).

Thickened flame regime is characterized by $Re_t > 1, Da < 1 \; and \; Ka > 1$. The graphical representation of this regime is shown in Fig. 2.17. $Da < 1$ indicates that chemistry is slower than

turbulence and this regime is also called as well stirred reactor. So the mixing is faster and the overall reaction rate is limited by the chemistry.

2.7.3 Turbulent flow effects on flame propagation

The combustion regime of flame propagation in direct injection engine is in the flamelet regime [Haworth et al. (2000)]. So the turbulent flame front can be viewed as an ensemble of small laminar flame elements. The different types of turbulence affect the structure of flame front and enhance the wrinkling of flame front. The three main interactions, identified by Pope [Pope (1988)] are shown in Fig. 2.18.

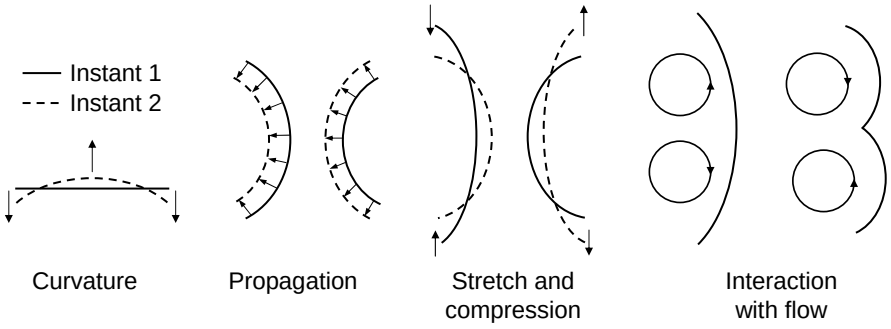

Figure 2.18: Turbulent flow effects on flame propagation (Pope (1988), Haworth and Poinsot (1992)).

The first kind of interaction is related to the aerodynamics, where flame front is stretched by the normal stress acting on its surface (bending). The second type of interaction is related to the propagation of curved flame front. The surface of the flame front could increase or decrease depends upon the initial curvature and the direction of propagation (Huygens principle). The third kind of interaction is linked with tangential motion of flow field with respect to the flame front. So depending upon the direction of velocity gradient, the flame surface could be compressed or stretched. The influence of vortex pair is also shown in Fig. 2.18. It can change the curvature of flame front and can modify the strain rate depending upon the direction of vortex pair.

Therefore the turbulence together with hydrodynamic and thermo-diffusive instabilities may destabilize the flame propagation depending upon the local flow and mixture field conditions (effect of Lewis number).

2.8 Turbulent partially premixed combustion

Turbulent partially premixed combustion is gaining more attention because of its presence in practical applications such as direct injection gasoline engines and gas turbines. In direct injection gasoline engines, charge stratification helps to sustain the flame propagation in the overall lean mixtures and thereby reduces the fuel consumption and emissions. However, stratification also introduces cycle to cycle variations and the delicate control of combustion process requires more fundamental understanding of flame propagation through spatially non-homogeneous mixture. As discussed earlier, laminar flame propagation through stratified mixture is different from the homo-

geneous cases and the prediction of their burning velocity needs information of flame history. The additional turbulence makes the turbulent stratified combustion much more complex. So far, few experimental and numerical investigations have been undertaken on the partial premixed turbulent flames which are reviewed in this section.

2.8.1 Experimental investigations

Cho and Santavicca (1993), Santavicca (1995) carried out an experimental study of the effect of incomplete fuel-air mixing on spark-ignited flame kernel growth in turbulent propane-air mixtures at atmospheric pressure and 300K conditions. In their work, the flow characteristic was measured by LDV, rms fluctuation of equivalence ratio was measured by NO_2-based LIF and flame kernel growth was measured by high speed laser shadowgraphy. They evaluated the effect of incomplete fuel-air mixing in terms of the flame kernel growth rate, cyclic variations in the flame kernel growth, and the rate of misfire. They concluded that the fluctuation in the local equivalence ratio

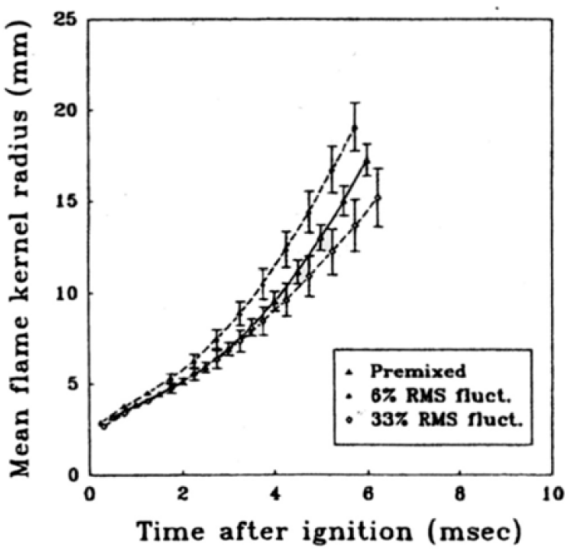

Figure 2.19: Evolution of mean flame kernel radius (Cho and Santavicca (1993)).

causes wrinkling and distortion of the flame kernel surface. The wrinkling of flame kernel surface increases with increase of RMS fluctuation of fuel-air equivalence ratio. They observed more cyclic variations in the non-homogeneous case compared to the homogeneous case as shown in Fig. 2.19.

Zhou et al. (1998) conducted an experimental investigation of flame propagation through stratified mixture field with different turbulence levels. They varied the mean equivalence ratio of the propane-air mixture from $\phi = 0.7$ on the lean side to $\phi = 1.6$ on the rich side and they tried different levels of turbulence intensity in the combustion chamber. They observed increase of wrinkling with inhomogeneity as shown in Fig. 2.20. They measured the flame propagation for the different level of turbulence and inhomogeneity and noted that the flame propagation in stratified mixture is faster than homogeneous cases. They constructed a map of flame propagation as a function of mixture condition and degree of inhomogeneity as shown in Fig. 2.20.

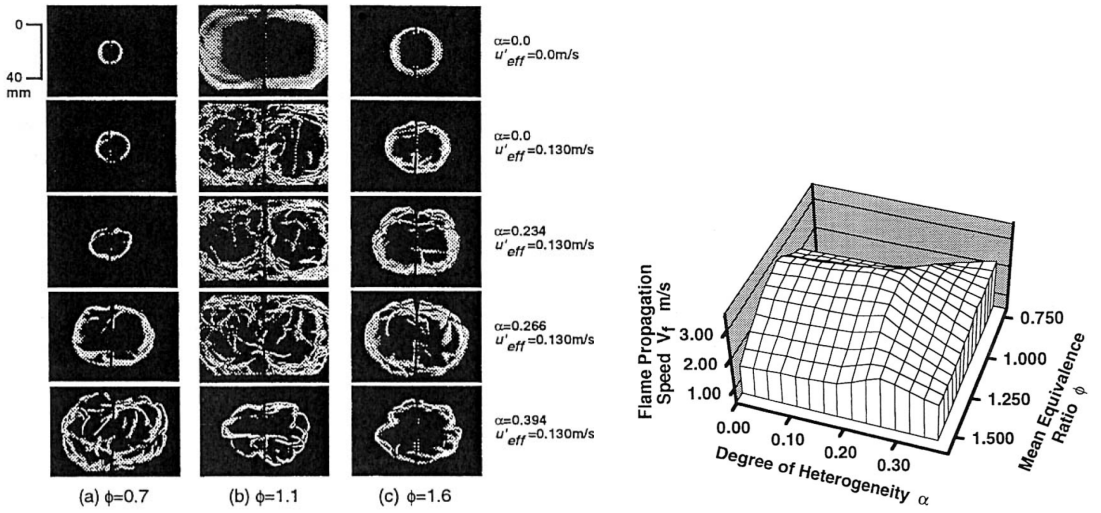

(a) Effect of mixture fluctuation on the flame folding (b) Variation of flame speed

Figure 2.20: Experimental investigation of stratified flame propagation (Zhou et al. (1998)).

Samson (2002) investigated the turbulent flame propagation through stratified propane-air mixture field using tomography and PLIF technique. He studied the effect of stratification on flame front curvature by comparing the results of stratified flames with equivalent homogeneous conditions. He concluded that the stratified flames are similar in size with homogeneous cases and no increase of flame wrinkling with stratification.

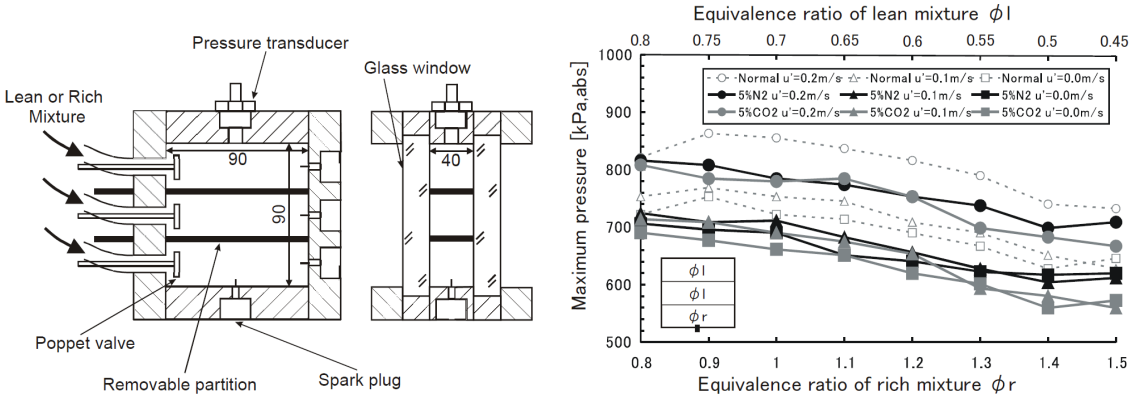

(a) Experimental setup. (b) Variation of maximum pressure.

Figure 2.21: Experimental setup and maximum pressure of homogeneous and stratified flames (Moriyoshi and Morita (2003)).

Moriyoshi and Morita (2003) examined a simplified stratified charge conditions with changing initial turbulence intensity, degree of mixture charge stratification, and kinds of fuels in order to understand the stratification features. Their experimental setup is shown in Fig. 2.21. The combustion chamber has two partitions and two poppet valves in each volume to generate a tumble-like flow for turbulence and the mixture was ignited at the center of chamber. They measured the velocity in the middle of volume using LDV. They measured the gas pressure using pressure transducer. The maximum pressure for the various mixture stratification conditions and turbulence

levels is shown in Fig. 2.21. They observed increase of maximum pressure with initial turbulence and decrease of maximum pressure with extension of charge stratification. They concluded that the effect of lean-side mixture is stronger than of rich-mixture in stratified conditions.

Pasquier et al. (2007) carried out a fundamental investigation of flame propagation through turbulent stratified propane-air mixture field. They measured two-dimensional velocity and equivalence ratio field of flame propagation using simultaneous PIV and PLIF measurement techniques. They achieved mixture stratification by an axi-symmetrical injection of pure propane into a constant volume chamber which was already filled with lean homogeneous mixture ($\phi = 0.6$). The mixture was spark ignited at a point close to the stoichiometric condition and they observed the free flame propagation. One example of instantaneous velocity and equivalence ratio of stratified

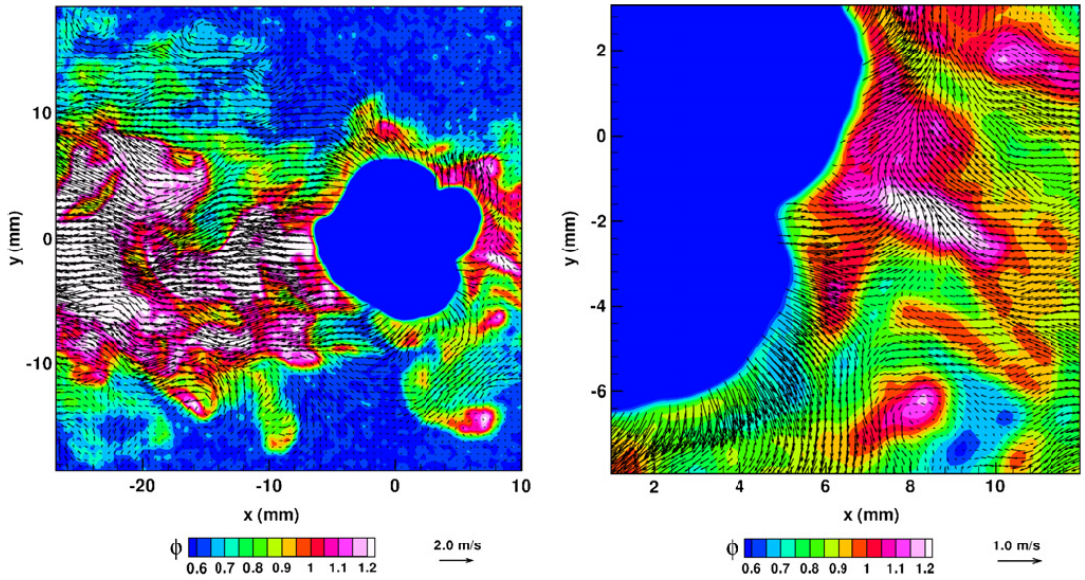

Figure 2.22: Instantaneous velocity and equivalence ratio field of turbulent stratified flame propagation (Pasquier et al. (2007)).

flame propagation is shown in Fig. 2.22. In their configuration, the flame was subjected to small scale and large scale variations of mixture field. They compared the global parameters such as mean flame radius, mean flame propagation, pressure rise, and flame front asymmetry of homogeneous and stratified flame conditions. They also compared the conditioned local burning velocities of stratified flames with results of homogeneous flames at different instances. They concluded that the local turbulent burning velocity may increase or decrease depending upon the local mixture fraction and mixture distribution along the flame front.

Robin et al. (2008) performed both experimental and numerical studies on the partially premixed combustion with strong equivalence ratio gradients. They measured flame temperature and fuel mole fraction of turbulent V-shaped methane-air flame using simultaneous Rayleigh scattering and acetone PLIF techniques. From the temperature measurements, they deduced the flame thickness and analyzed the relationship between flame stretch and flame thickness for homogeneous and stratified mixture conditions. They concluded that the increase of flame stretch leads to a decrease of normalized flame thickness. They observed that for a same mean equivalence ratio condition, stratified flames are thinner than equivalent homogeneous conditions. They also did

numerical modeling of turbulent reactive flows of partial premixed combustion. From their results of numerical simulations, they described the mean structure of stratified flames and the evolution of the mean chemical reaction rate for different partially premixed conditions.

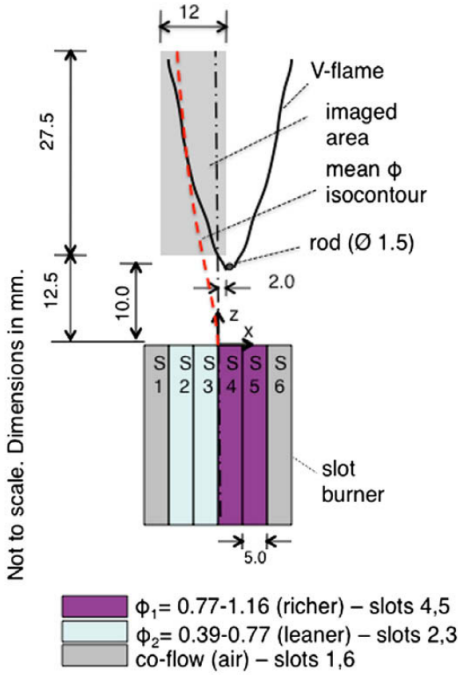

Figure 2.23: Experimental setup of turbulent stratified V-flame (Anselmo-Filho et al. (2009)).

Anselmo-Filho et al. (2009) studied premixed and stratified methane-air V-flames at a mean equivalence ratio of 0.77, within low turbulent intensity. They utilized acetone PLIF technique for the measurement of mixture fraction of cold field and OH PLIF for the measurement of flame front position. Their experimental setup is shown in Fig. 2.23. They measured flame brush thickness, flame surface density (FSD) and flame curvature of both premixed and stratified flame propagation. They concluded that the stratification increases the FSD above the premixed flame in all cases. There is a little variation of flame brush thickness with stratification. The distribution of flame curvature in stratified flames is broader and more symmetric than premixed cases. They suggested that the FSD and flame curvature effects may be attributed to the differential rates of propagation of lean and rich mixture pockets.

2.8.2 Numerical investigations

Numerical simulations of partially premixed flames focus either on the direct injection engine configurations or on the simple configurations. Some of the numerical modeling approaches and their findings are reviewed in this section.

Hélie and Trouvé (1998) studied the spark-ignited turbulent flame propagation through a partially premixed mixture by using direct numerical simulations. They described the combustion process takes place in two stages, first stage is the premixed flame propagation and the second stage is the non premixed combustion which consumes all the excess fuel and oxidizer left behind the premixed front (Fig. 2.24). In their simulations, they used different degrees of scalar inhomo-

geneity around mean stoichiometric conditions. They tried to study the effect of partial premixing on both turbulent flame topology and the mean reaction rate and the way to include the information to the flamelet models. They concluded that the partial premixing has a net negative impact on the overall mean premixed reaction rate. They proposed modifications to the coherent flame

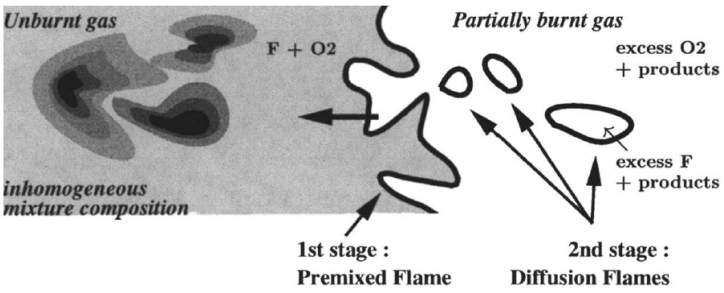

Figure 2.24: Turbulent flame propagation into non homogeneous reactants (Hélie and Trouvé (2000)).

model (CFM) to account the effects of variable mixture strength on primary premixed flame and the formation of non premixed flame propagation in their work [Hélie and Trouvé (2000)]. From their findings, they concluded that the non-homogeneity tends to have a net negative impact on the turbulent flame speed close to the stoichiometric conditions and opposite for the flammability limits where the non-homogeneity in that conditions tends to have a net positive impact on the turbulent flame speed.

Haworth et al. (2000) performed numerical simulations of turbulent propane-air flames propagating into regions of non-homogeneous mixture. They considered the part load, low speed gasoline direct injection (GDI) engine operating conditions as their initial conditions of model. Their simulations included complex chemical kinetics, realistic molecular transport, and fully resolved hydrodynamics. Their schematic representation of flame propagation through non-homogeneous mixture is shown in Fig. 2.25.

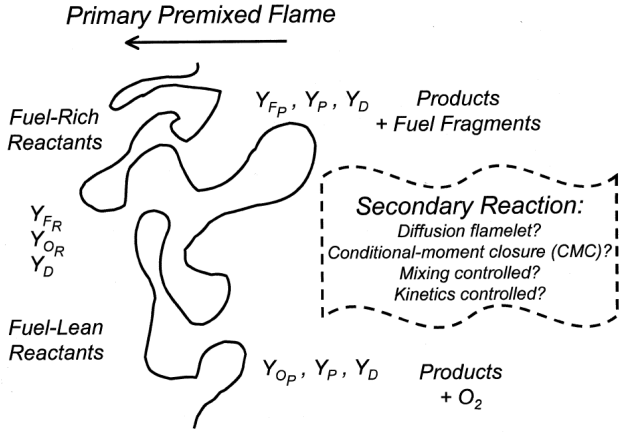

Figure 2.25: Turbulent stratified flame propagation (Haworth et al. (2000)).

Their findings of primary heat release rate shown that for the non-homogeneous case, the global heat release is initially higher than equivalent homogeneous case and later adjusts to the reactant non-homogeneity and finally drops to lower level than homogeneous case. They

concluded that the differences in global heat release rate and flame area between homogeneous and non-homogeneous cases are very minimal. They suggested that the combustion occurs in two stages. The first stage consumes all the primary fuel and produces most of the heat release and in this stage the combustion takes place in the laminar premixed flamelet regime. Next is the secondary stage, which consumes fuel fragments from rich zones, oxidizer from lean zones and this secondary stage is governed by the turbulent mixing and the kinetics of CO_2 production.

Jiménez et al. (2002) carried out a direct numerical simulations (DNS) of combustion in globally lean non-homogeneous propane-air mixtures with initial conditions close to the part load, low speed GDI operating conditions. Their simulation is based on the flamelet models that includes detailed transport, thermodynamics, chemistry and thermal NO production. They studied the propagation of initial lean laminar flame in the homogeneous and non-homogeneous turbulent mixture configurations which are shown in the Fig. 2.26. In that figure, white represents $\phi = 0$ and black represents $\phi = 2.0$ and the gray scale represent intermittent values. The thin black line corresponds to the stoichiometric line and the vertical lines represent the initial laminar flame. They reported substantial differences in the heat release rate between homogeneous and non-

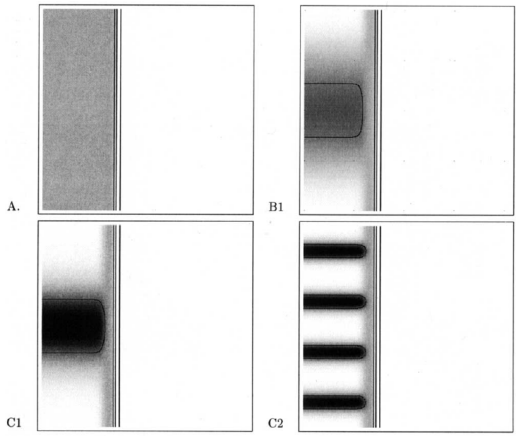

Figure 2.26: Initial spatial distribution of equivalence ratio field (Jiménez et al. (2002)).

homogeneous cases. They found a strong influence of the PDF of mixture distribution and shown that appropriate distribution can lead to more than 60% efficiency gain. They concluded that the spatial distribution of the non-homogeneity is an important factor to determine the wrinkling of flame and found more NO concentration in the non-homogeneous case.

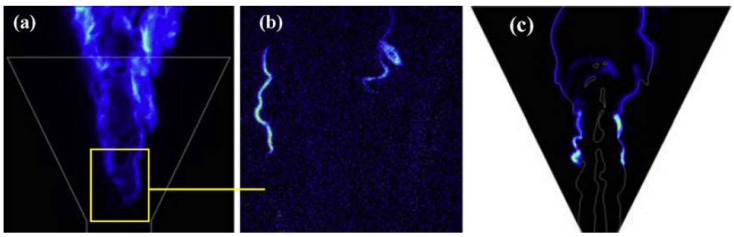

Figure 2.27: Comparison of experimental and LES results (Li et al. (2009)).

Li et al. (2009) investigated the structure and dynamics of a turbulent partially premixed methane/air flame in a conical burner using laser diagnostics and large-eddy simulations (LES).

They utilized CH and CH_2O PLIF techniques to examine the flame structure and a high speed video for the chemiluminescence imaging. They studied the flame structure using LES based on a two-scalar flamelet model, with the mixture fraction for the mixing field and level-set G-function for the partially premixed flame front propagation. Their experimental setup and their experimental and numerical results are shown in Fig. 2.27. They detected thin CH layers in the cone and above the cone by PLIF measurements and they found similar results from LES results. From the LES results, they found a shear layer formed by large scale vortices, which effectively stabilized the triple flame front. They found similar results from the chemiluminescence and CH PLIF results. Their work shows the effectiveness of using experimental and numerical investigations to understand complex combustion phenomena.

2.9 Summary on stratified combustion

A summary of few experimental and numerical findings from the literature are given below:

- The flammability limits are extended by the presence of rich mixtures in the lean mixture field.
- The stratified flame propagation and their flame structure are different from equivalent homogeneous conditions.
- The stratified flames exhibit memory effect.
- The correlation of burning velocity versus flame stretch rate from homogeneous cases cannot be applicable to the stratified flames.
- The heat input of burned gases back supports the flame propagation through lean stratified mixture field.
- The heat release rates of stratified flames are more than equivalent homogeneous cases.
- The flame front wrinkling may increase or decrease with increase of non-homogeneity of mixture field.
- The local turbulent burning velocity depends on the distribution of mixture field along the flame front.
- The modeling of stratified combustion needs time history of flame propagation and variation of mixture field.

So from the literature survey, it becomes clear that further investigations are needed to improve the fundamental understanding of stratified combustion. For that, quantitative information are needed such as local flame temperature, local equivalence ratio distribution, time history of flame propagation, velocity field, heat release rate and so on. But simultaneous measurements of all the parameters are not possible with current technologies. Nevertheless, it can be possible to measure few of them by combining the optical techniques such as PIV, PLIF, Rayleigh scattering and Raman scattering. In this work, simultaneous measurements of velocity and equivalence ratio field have been realized by using PIV/PLIF techniques.

2.10 Conclusion

In this literature review, some of the basics of combustion process are covered in order to understand more about the partially premixed flames. Also, the measurement of laminar burning velocity, the effect of flame stretch, link between equivalence ratio and laminar burning velocity and flame front instabilities are discussed. The turbulent burning velocity, turbulent premixed combustion regimes and the wrinkling of flame front due to turbulence are described. Some of the experimental and numerical investigations of partially premixed flame propagation in laminar and turbulent flows are reviewed. From the literature review, we understood that further investigation in the partially premixed flame propagation is needed to provide some useful data sets for the numerical modeling as well as for the fundamental understanding of the stratified combustion. So our main objective of this work is to investigate the stratified flame propagation in laminar and turbulent flow conditions by using optical diagnostic techniques.

Chapter 3

Experimental configuration

The main objective of this work is to investigate the flame propagation through stratified mixture field in order to improve the understanding of stratified combustion and to provide useful validation datasets for numerical simulation. So, experimental investigations have been carried out in a simplified configuration of constant volume combustion chamber by using optical diagnostics techniques.

In this work, two different experimental configurations have been developed to realize laminar and turbulent stratified mixture condition inside the combustion chamber. Then flame is spark-ignited at the center of a stratified mixture and the propagation of flame through stratified mixture field is investigated by using combined PIV/PLIF measurement techniques. In the first configuration, turbulent mixture field is generated by an axi-symmetric injection of rich propane-air mixture into the combustion chamber which is already filled with lean homogeneous mixture. After that, unsteady flame propagation through turbulent stratified mixture field is observed by simultaneous PIV/PLIF techniques. In order to isolate the stratification effect from the influence of turbulence, flame propagations through six different turbulent homogeneous mixture fields are also investigated. In the second experimental configuration, laminar stratified mixture field is realized by a unique injection setup based on the balancing of vacuum pressure inside the combustion chamber. Then, flame propagation through stratified mixture field is analyzed by simultaneous PIV/PLIF techniques. In order to understand the effect of degree of stratification on propagation of flame, laminar flame propagations through three different stratified mixture fields are analyzed.

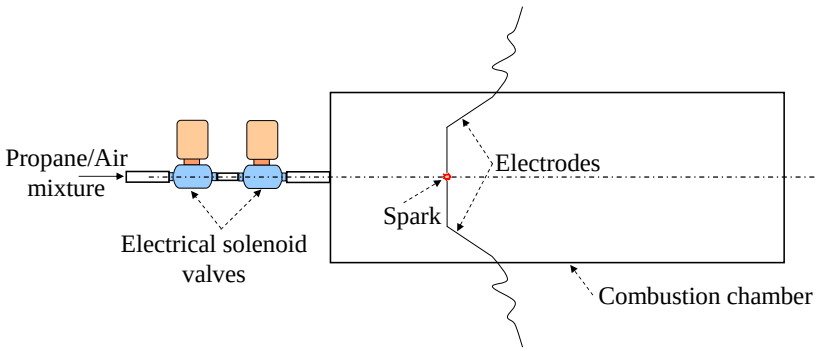

Figure 3.1: A simplified representation of experimental configuration.

The constant volume combustion chamber utilized in this work is a rectangular chamber, which is equipped with three quartz windows in order to provide optical access to the laser diagnostic techniques. Inside the combustion chamber, turbulent stratified mixture field is realized by using axi-symmetrical injection unit which mainly consists of electrical solenoid valves as shown in Fig. 3.1. At the center of combustion chamber, two thin electrodes are placed to spark-ignite the mixture. The location of ignition is fixed along the axis of injection and close to one end of the combustion chamber. After the spark-ignition, the propagation of flame through stratified mixture field is investigated by simultaneous acquisition of PIV and PLIF images of flame propagation. For that, the fuel-air mixture is seeded with oil particles and fluorescent tracer, illuminated by laser sheets and the emitted signals are collected from within investigation area (shown in Fig. 3.2) by PIV/PLIF techniques. In order to measure combined velocity and scalar field of flame propagation, two PIV images are acquired within time delay of Δt and one PLIF image is acquired in between them. The acquired two-dimensional images are then post-processed in order to measure the velocity field from PIV image pair and equivalence ratio field from PLIF image.

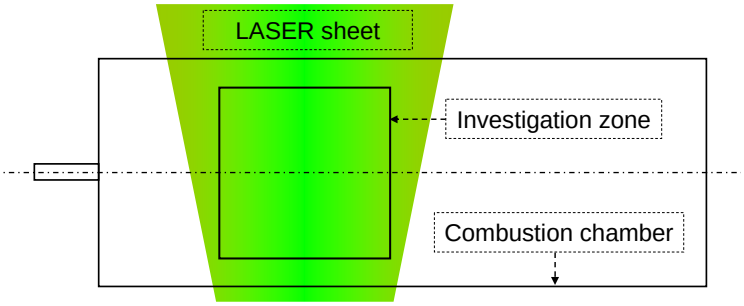

Figure 3.2: Position of investigation area in the combustion chamber.

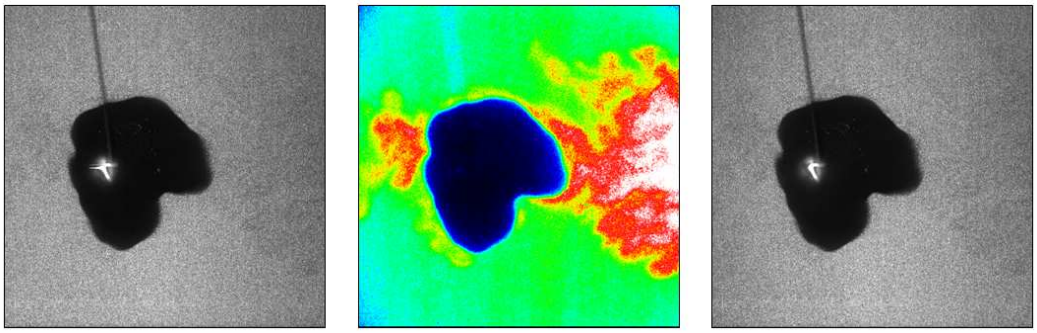

Figure 3.3: Acquired PIV and PLIF images of turbulent stratified flame propagation.

One example of simultaneously acquired PIV image pair with PLIF image of turbulent stratified flame propagation is shown in Fig. 3.3. In those particle images, the fresh gas region is represented by Mie scattering signals from seeding particles and the burned region is represented by the absence of seeding particles which are burned through very sharp temperature gradient

of flame front. In the PLIF image, the fluorescence signals are varying proportional to the local equivalence ratio of mixture and the burned region is represented by low level signals of background noises due to the absence of fluorescent tracer which is completely burned through flame front. From the acquired PIV and PLIF images, the velocity field and the equivalence ratio field of turbulent flame propagations are computed by post-processing tools.

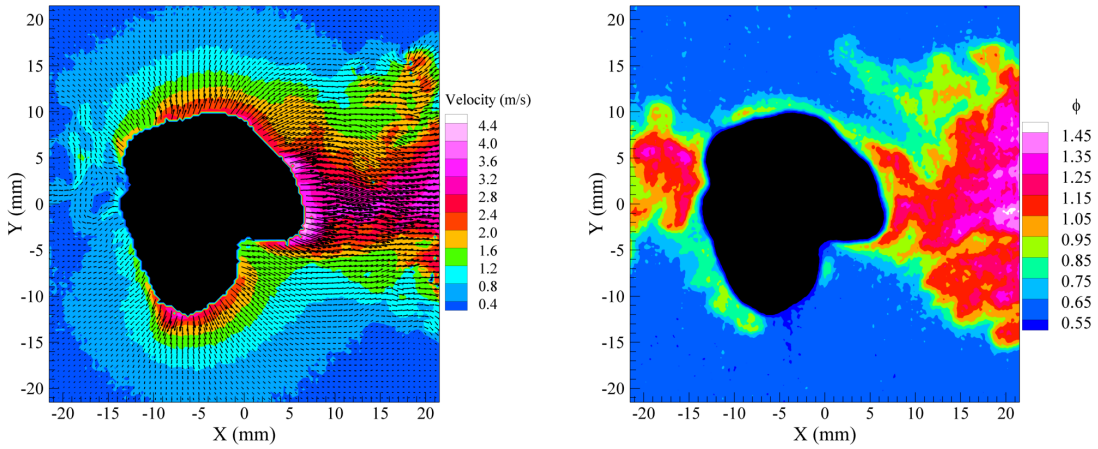

(a) Velocity field (b) Equivalence ratio field

Figure 3.4: Instantaneous flow and scalar field of turbulent stratified flame propagation.

The computed instantaneous velocity and equivalence ratio field of turbulent stratified flame propagation is shown in Fig. 3.4. From the combined quantitative measurement of flow and scalar fields, local flame speed, local fresh gas velocity, local curvature and local equivalence ratio around the flame fronts are measured. Then local curvature and local burning velocity are conditioned by the local equivalence ratio of stratified flames and the conditioned datasets are compared with that of equivalent homogeneous flames in order to understand the effect of stratification on flame propagation.

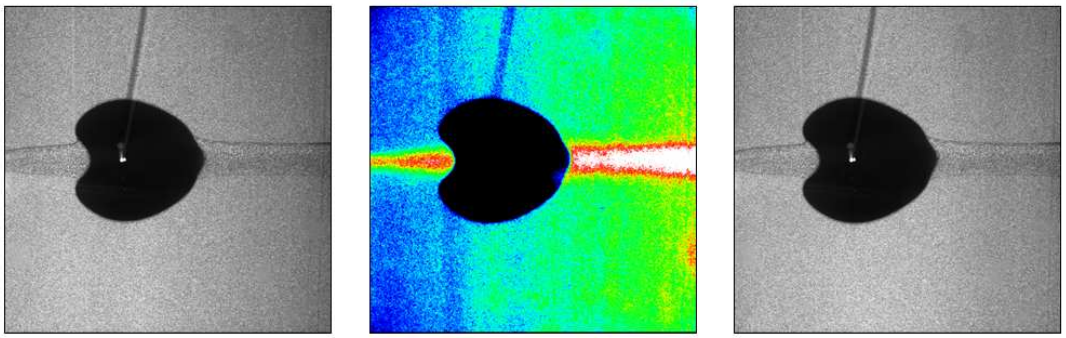

PIV image at t PLIF image at $t+\Delta t/2$ PIV image at $t+\Delta t$

Figure 3.5: Acquired PIV and PLIF images of laminar stratified flame propagation.

We have also investigated the stratified flame propagation under laminar flow condition. One example of acquired PIV/PLIF images of laminar stratified flame propagation is shown in Fig. 3.5.

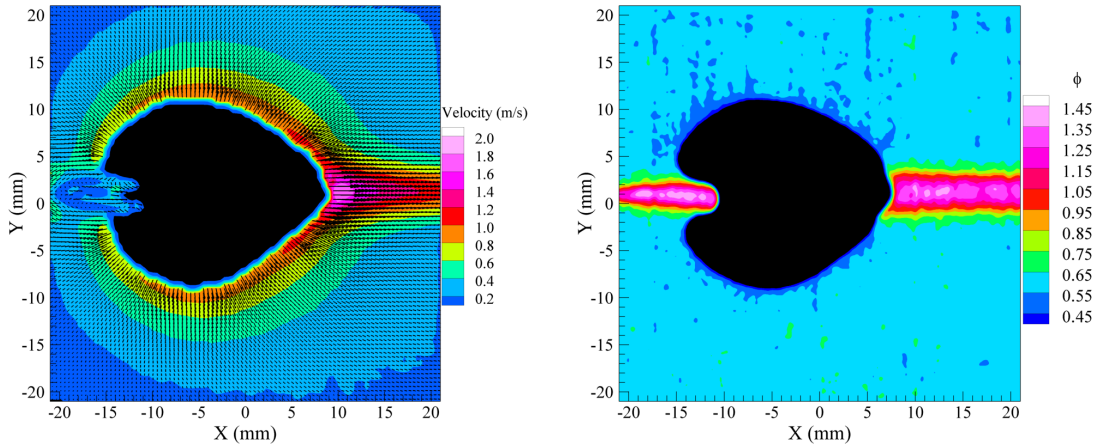

(a) Velocity field

(b) Equivalence ratio field

Figure 3.6: Instantaneous flow and scalar field of laminar stratified flame propagation.

From those simultaneous PIV and PLIF images, the combined velocity and equivalence ratio field of laminar flame propagation are calculated by post-processing tools and the final quantitative flow and scalar fields are shown in Fig. 3.6. Also from the PIV image pair, local flame speed, local fresh gas velocity and local laminar burning velocity of stratified flame are measured by new PIV approaches developed in this work. After that, to compare three different stratified cases, the measured local variables are sampled from the regions where the flame fronts are propagating through lean mixture of within moderate stretch range. The conditioned local variables of three cases are then compared in order to know the effect of degree of stratification on flame propagation.

The following chapters explain in detail the optical diagnostic tools used in this work, post-processing tools, the combined PIV/PLIF setup and the accuracy and spatial resolution of velocity and equivalence ratio measurements. The later chapters explain the stratified combustion in laminar and turbulent flow conditions.

Part I

Optical Diagnostics

Chapter 4

Particle image velocimetry

Abstract. *Particle image velocimetry (PIV) is used to measure quantitative, two dimensional velocity field. In this technique, the observation area or the fluid under investigation is seeded with small particles, illuminated by laser sheet, which forms an image and that is recorded by a digital camera. The displacements between the two successive recorded images are then computed by a statistical method. Finally the measurement is obtained from the displacement and time delay between the two images. This chapter focuses on the principle of PIV measurement, evaluation of velocity vectors and the masking technique to eliminate spurious vectors from the velocity field. The uncertainty and spatial resolution of velocity measurements are given.*

4.1 Introduction

Particle image velocimetry is a non intrusive technique developed for the quantitative measurement of two-dimensional velocity field of flow under investigation. In a typical PIV technique, the flow under investigation is seeded with small particles that can follow the flow and illuminated by thin laser sheet so that only particles in that plane are acquired by using high resolution digital camera. Nd:YAG (Neodymium-doped Yttrium Aluminium Garnet, $Nd : Y_3Al_5O_2$) lasers with double cavity package is widely used for PIV measurements [Adrian (2005)]. This double pulsed laser illuminates the flow twice within short time. The scattered signals are captured by high resolution CCD (charge-coupled device) camera that can store the first image fast enough to be ready for the second exposure within few nanoseconds. The acquired PIV image pair is then post-processed in order to measure the velocity field. The accuracy of velocity measurement is depends upon both the quality of particle images and the post-processing techniques. The quality of particle images are affected by various parameters such as seeding particles density, energy variations of laser pulses, noises in the image recordings and so on. Therefore, a careful attention has been given to the experimental conditions to achieve accurate measurements. This chapter explains the principle of PIV and covers the subsystems of PIV setup used in this work. This chapter also describes the calculation of velocity field using post-processing scheme, data validation tool to remove the spurious vectors from the velocity field. Also, in this work, a unique masking technique has been developed for the removal of spurious vectors from the velocity fields of flame propagation. Finally, the uncertainty and spatial resolution of velocity field measurements are provided.

4.2 Principle

The basic principle of PIV is to measure the two dimensional velocity field of flow under investigation by measuring the displacement of small particles added to the flow, which are recorded in the PIV images. The experimental setup of a typical PIV system (Fig. 4.1) consists of particle generator to seed the flow, pulsed laser unit to illuminate the particles twice, optics to expand laser beam into thin laser sheet, CCD camera for double frame/single exposure PIV recording and a synchronizer to control the timing of camera and laser unit.

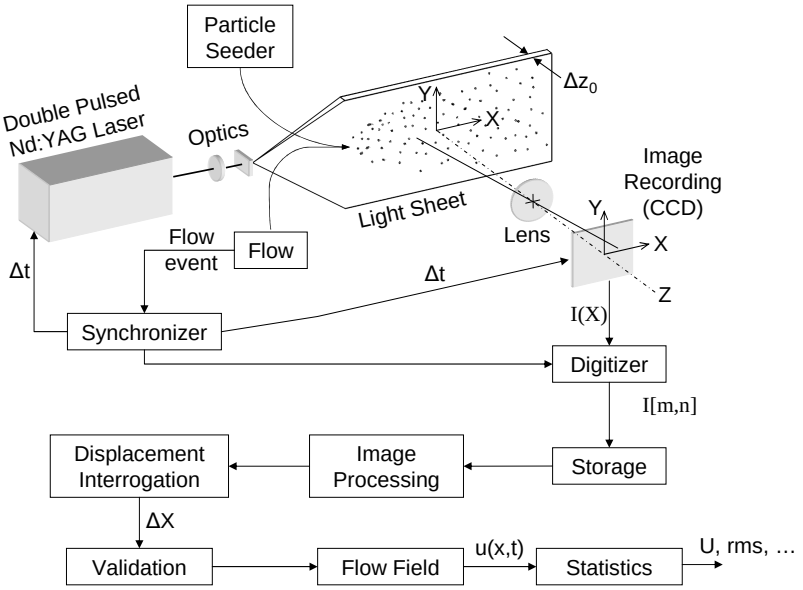

Figure 4.1: Typical particle image velocimetry system [Adrian (2005)].

The recorded PIV images are then evaluated to obtain the velocity field. The principle of evaluation is to divide the image into small subareas called “interrogation windows" and the displacement of particles in the window between first and second illumination is determined for each interrogation window by cross-correlation method [Lecordier (1997), Raffel et al. (2007)]. Then the velocity vector is calculated from the displacement taking into account the time delay between the two illuminations and the magnification of image. The complete two dimensional velocity map is achieved by repeating this process to all the interrogation windows. The computed velocity field is further analyzed by a data validation tool to remove the spurious vectors in the velocity map.

4.3 PIV subsystems

PIV measurement can be split into two parts: first part is related to the acquisition of images while the second part is the post-processing of recorded images to compute the velocity field. The standard PIV acquisition system consists of several subsystems, namely: flow seeding unit, flow illumination, imaging and recording. Each subsystem is explained one by one in this section.

4.3.1 Flow seeding unit

The seeding of flow is very critical to the accuracy of PIV measurement. The particles must meet the following requirements [Westerweel (1993)]:

- The particles added to the fluid should follow the motion exactly.
- The particles should not alter the flow or combustion process.
- The particles should have sufficient light scattering efficiency.

In general, liquid particles have been utilized for the gaseous medium due to their higher scattering efficiency [Raffel et al. (2007)]. We tried olive oil, silicone oil and DEHS (Di Ethyl Hexyl Sebacate) and observed the same signal levels so we decided to use olive oil in this work because of its easy availability.

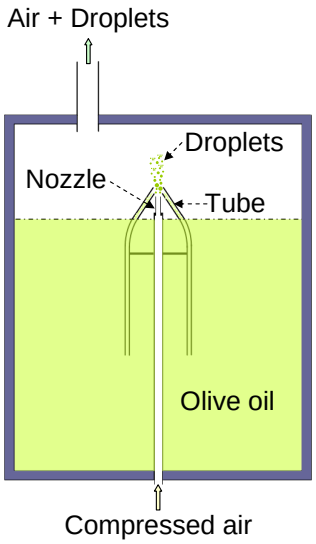

Figure 4.2: Olive oil particles generator.

In this work, micro-metric olive oil particles are produced by using a particle generator. In this generator, compressed air with 4 to 5 bar pressure is forced through a nozzle whose diameter is around 1 mm. A small tube partially immersed in the olive oil is placed adjacent to the nozzle tip, so that when compressed air exists the nozzle, it creates a low pressure and that sucks oil through tube and produces small droplets by shear mechanism. Two small tubes are used to generate more particles. The generated droplets size varies between 1 to 5 μm. Homogeneous distribution of seeding particles is achieved for high quality PIV recordings in order to obtain velocity field with high accuracy. The mass fraction of olive oil introduced in air flow is kept low to ensure there has no effect on the combustion process [Lecordier (1997)].

4.3.2 Flow illumination

In this work, a double cavity Nd:YAG laser (TwinsUltra, Quantel) delivering pulses of 30 mJ at a wavelength of 532 nm has been utilized to illuminate the micro-metric olive oil particles. It provides

two identical laser pulses and the duration of illumination is $7\ ns$ which "freeze" the motion of the particles. The maximum repetition rate is $20\ Hz$. The laser unit is shown in Fig. 4.3. The laser sheet is created by the association of 3 lenses: one spherical lens of $1\ m$ focal length, one cylindrical lens of $-25\ mm$ focal length and one cylindrical lens of $+150\ mm$ focal length. With the combination of lenses, the laser sheet keeps thin along with several centimeters and close to its minimum thickness of $800\ \mu m$. The positions of lenses are optimized to form the minimum laser sheet thickness at the center of the combustion chamber.

4.3.3 Acquisition of images

PIV images must have sufficient spatial resolution with reasonable signal-to-noise ratio and this could be achieved by high resolution CCD cameras. An interline CCD camera (Hamamatsu C9300-505) has been used, which provides a $12\ bit$ image pair of 2048×2048 pixels. The CCD camera is shown in Fig. 4.3.

(a) Laser. (b) CCD camera.

Figure 4.3: LASER and CCD camera unit.

This CCD digital camera can operate in both single and dual readout mode and the frame rates are 6 and 11 frames per second respectively. Peltier cooling of camera drastically reduces dark current and thereby increases signal-to-noise ratio. The camera can acquire pair of images with minimum time delay of $200\ ns$. The camera is mounted with a Nikkor lens of $135\ mm$ focal length ($f/d_{max} = 2$) which provided $4.4 \times 4.4\ cm^2$ field of view. An interferential pass-band filter ($532 \pm 5\ nm$) is used to reject the flame chemiluminescence signals.

4.4 PIV evaluation

The second part of PIV measurement is the computation of velocity field from the acquired PIV image pairs. The most common PIV evaluation method is cross-correlation scheme which is a statistical analysis of two singly exposed particle images [Westerweel (1993), Raffel et al. (2007)]. In a PIV image pair, the second image is acquired after a short time so the positions of particles in the second image have moved relative to that of first image according to the local flow condition. So the flow velocity can be measured by calculating the straight-line displacement of the localized groups of particles between image pair. This can be accomplished by applying cross-correlation

method to the interrogation windows sampled from first and second images. The cross-correlation function is formulated as [Raffel et al. (2007)]:

$$R_{II}(x,y) = \sum_{i=-K}^{K} \sum_{j=-L}^{L} I(i,j)I'(i+x, j+y) \tag{4.1}$$

Where I and I' are the intensity values extracted from the first and second interrogation windows respectively. For each sample shift (x, y), the sum of the products of all overlapping pixel intensities is calculated which produces one cross-correlation value $R_{II}(x, y)$ that represents the degree of match between two interrogation windows. So in the cross-correlation plane, the position of peak value of cross-correlation estimates the displacement of localized particle groups. The size of interrogation window is in the order of 16 to 64 pixels and to find the displacement of whole image would require substantial computation process. However, the entire process can be speeded up by using Fourier transform function [Raffel et al. (2007)]. The main principle of cross-correlation scheme based on Fourier Transforms is shown in Fig. 4.4. In that scheme, the

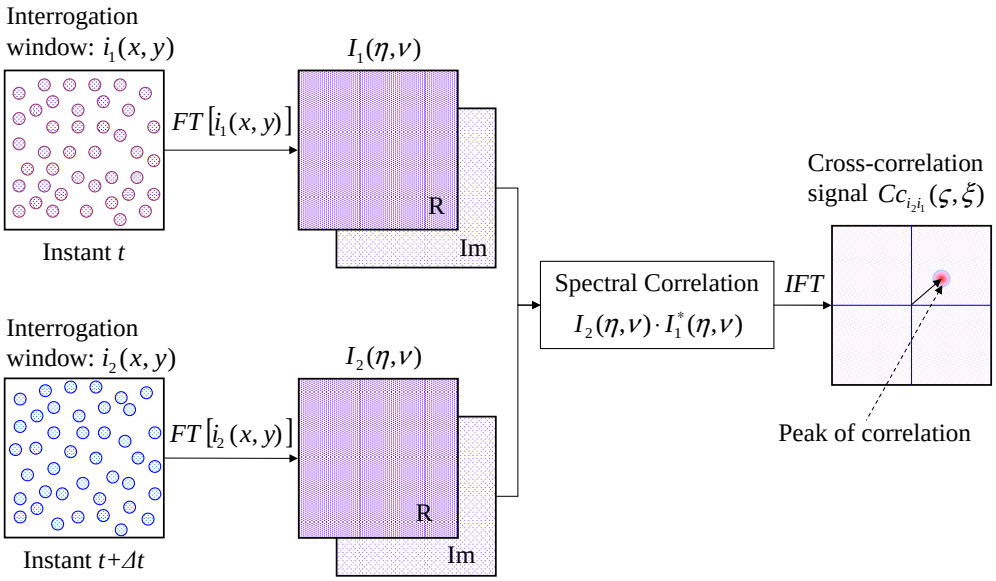

Figure 4.4: Analysis of double frame/single exposure recordings: cross correlation method [Lecordier (1997)].

recorded images are subdivided into interrogation windows which contain the position of particles at time t and $t + \Delta t$. Next, the real and imaginary parts of interrogation windows are calculated by using the Fourier transformation. After that, the spectral correlation is carried out, which is the complex conjugate multiplication of two Fourier transforms I_1 and I_2. Then, the resulting Fourier coefficients are inversely Fourier transformed to produce the cross-correlation plane where the peak of correlation represents the displacement between the two interrogation windows. The position of peak of correlation is then calculated from the correlation plane with sub-pixel resolution [Lecordier (1997)]. Finally, the velocity vector is obtained from the estimated displacement along with time delay (Δt) and the magnification of image. The whole velocity field is then calculated by repeating the above procedure for all the interrogation windows.

4.5 Measurement of velocity field

In this work, the PIV technique is utilized to measure the velocity field of stratified flame propagation through laminar and turbulent flows. So we need a PIV evaluation scheme which can provide accurate measurements in both laminar and turbulent flow configurations. The accuracy of velocity measurement primarily depends on the quality of acquired images, because of all the information regarding the flow field are represented by the intensity and locations of seeding particles in the recorded images. To acquire good quality of particle images, it is very important to control the experimental parameters such as density of seeding particles, uniform distribution of seeding particles, identical illumination of first and second pulses of laser, optical collection of signals without distortion, filtration of flame chemiluminescence and no window fouling.

The size of interrogation window also plays a critical role on the accuracy as well as spatial resolution of measurements. For a given flow condition, the optimum size of interrogation window is selected based on various factors such as time delay between the image pairs, distribution of seeding particles, laser energy and so on. Thus, progressively the accurate velocity vector field has been obtained after optimizing both experimental as well as PIV evaluation parameters.

The PIV evaluation scheme used in this work was developed by Lecordier and Trinité (2003). It is a sub-pixel iterative approach and the principle of this approach is based on a predictor/corrector method. It first predicts the displacement using a conventional PIV evaluation scheme explained in section 4.4. Then it corrects the measurement by progressively shifting the windows fraction of pixels until reaching zero displacement. Also during the correction step, the window sizes are modified and rotated to increase the spatial resolution. This algorithm measures the velocity field accurately with high spatial resolution and takes computer time only 3 times longer than conventional PIV approach. More details about the algorithm are available in the literature [Lecordier (1997), Lecordier et al. (2001), Lecordier and Trinité (2003)].

4.5.1 Data validation

The computed velocity vector field may contain some spurious vectors. The spurious vectors are abnormal vectors by magnitude and direction compared to the neighbor vectors [Westerweel (1994)]. The spurious vectors are originated from various sources such as seeding variation, higher velocity gradient, fluctuations in laser energy, window fouling and so on. The spurious vectors in the velocity field can be eliminated by using a suitable data validation tool.

The validation tool utilized in this work was developed by Lecordier and Trinité (2003). The parameters used in the validation tool are signal-to-noise ratio (SNR), maximum magnitude of vector and maximum permissible standard deviation of mean and median tests (size 5×5 pixels). First, the experimental parameters and the interrogation window size are optimized by comparing the percentage of spurious vectors with different flow conditions. Finally, the interrogation window size is fixed to 20×20 pixels and time delay between two images is fixed to $60\ \mu s$ for turbulent case and $200\ \mu s$ for laminar case. One example of instantaneous velocity field calculated from the axi-symmetrical turbulent jet is shown in Fig. 4.5. The velocity field of jet contains less than 0.1% of spurious vectors before validation and those vectors are removed by the validation tool.

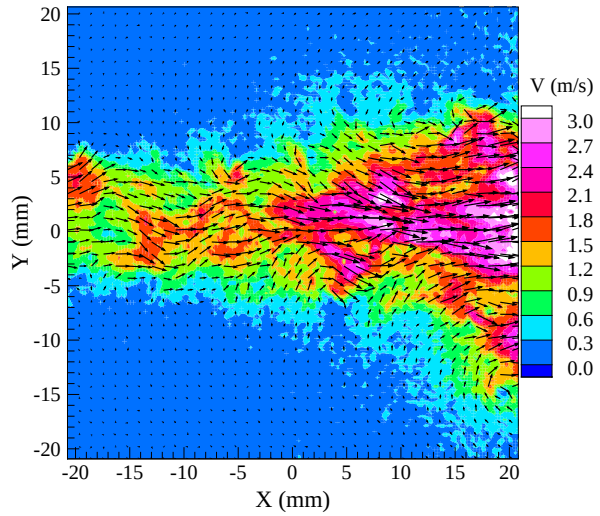

Figure 4.5: Instantaneous velocity vector field of turbulent jet.

4.5.2 Masking technique

In this work, we need to measure the local fresh gas velocity very close to the flame front for the investigation of flame propagation through stratified mixture field. One example of instantaneous velocity field of turbulent flame propagation is shown in Fig. 4.6. It contains more than 1.0% of

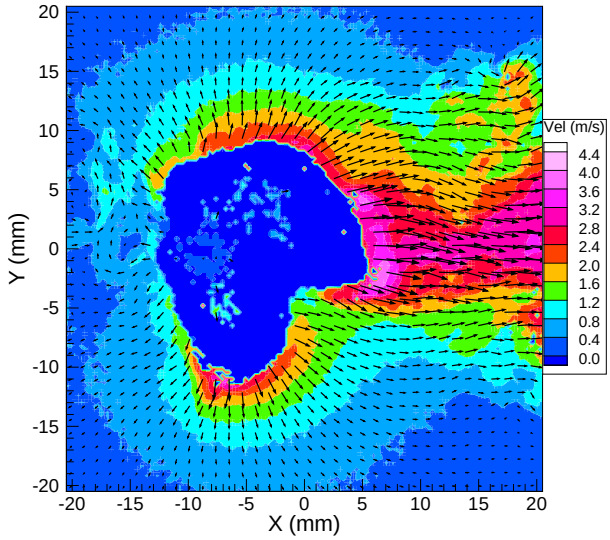

Figure 4.6: Instantaneous velocity vector field of flame propagation.

spurious vectors in the burned gas region and the validation tool fails to remove them because mean and median tests cannot identify those vectors in the burned gas region. These spurious vectors near the flame fronts could introduce error in fresh gas velocity measurements and must be eliminated. This can be achieved by isolating the vectors in the burned gas region from the measurements. But the main difficulty is that the burned regions are varying with each PIV image pair of flame propagation. In order to solve this problem, we have developed a unique technique using mask image of burned region.

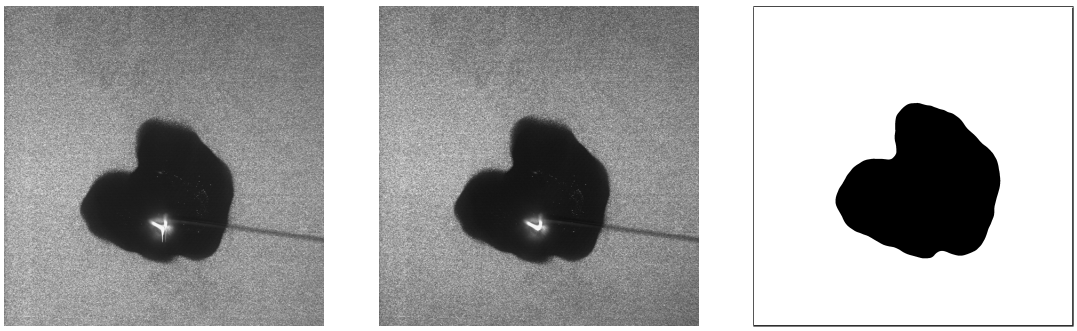

(a) First image (b) Second image (c) Binary image

Figure 4.7: One example of PIV image pair with binary image.

Mask image is a binary image, in that the burned region is represented by 0 level and fresh gas region is represented by level 1. The boundary of the burned gas region is the flame front contour. The extraction of flame front contour from particle image is explained in the appendix (§ A). One example of PIV image pairs with binary image is shown in Fig. 4.7. The binary image is created based on the flame front contour of the first image of PIV image pair.

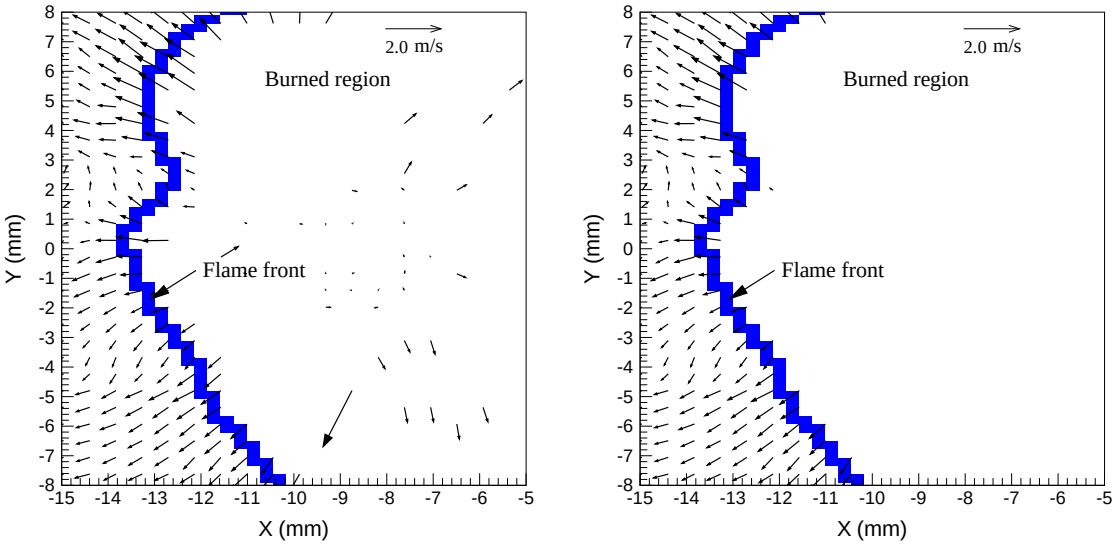

(a) Closer view of velocity field before masking (b) Closer view of velocity field after masking

Figure 4.8: Spurious vectors elimination by masking technique.

The principle of masking technique is that the vectors in the burned gas region are identified by mask image and those vectors are then omitted in the final validated velocity vector field. A closer observation of velocity field near burned region before and after the corrections are shown in Fig. 4.8. It clearly shows the elimination of spurious vectors near the flame front by masking technique. Indeed, the percentage of spurious vectors in the velocity field is reduced to less than 0.1% after the application of masking technique.

4.6 Precision of PIV measurements

The spatial resolution and the uncertainty of PIV measurements are very important parameters especially for the turbulent combustion studies [Lecordier et al. (2001), Lavoie et al. (2007)]. The spatial resolution gives an idea of the smallest turbulent scale that can be measured and the uncertainty is related to the statistical error in the measurements.

For the PIV uncertainty measurement, we followed the procedure given by Foucaut et al. (2004). The principle is to acquire particle images of no-flow condition and applying the same post processing schemes of real measurements to calculate the standard deviation of velocity field. The same parameters of real experimental conditions such as the time delay between images, field of view, laser energy, seeding density and synchronization are used for the image acquisition. Then the velocity field and their fluctuations are calculated by using interrogation windows of size 20×20 with 50% overlapping. The measured fluctuation in the velocity field of zero motion is $0.04\ m/s$. Thus we can measure the velocity field with an uncertainty of $\pm\ 0.04\ m/s$ and any fluctuation below than $\pm\ 0.04\ m/s$ cannot be considered.

The spatial resolution of PIV measurements is also calculated based on the study of Foucaut et al. (2004). The velocity vector field is measured by cross-correlation technique using interrogation windows. Therefore the PIV measurement is like a low pass filtering of actual velocity field and the spatial resolution is related to the size of interrogation window [Wereley and Meinhart (2001)]. Foucaut et al. (2004) expressed an relation between the spatial resolution and the size of interrogation window based on the cut off frequency calculated at $-3\ dB$ (corresponds to 50% of unattenuated value) as:

$$f_c = 2.8/X \tag{4.2}$$

where X is the size of interrogation window and f_c is the cut off frequency in 1/pixel. In this work, the cut off frequency is $0.14/pixel$ and the corresponding spatial resolution is $160\ \mu m$. So the minimum possible turbulent scale that can be measured by our experimental setup is $160\ \mu m$ with an uncertainty of $\pm\ 0.04\ m/s$.

4.7 Summary and conclusions

Particle image velocimetry technique provides two dimensional, quantitative velocity vector fields. This technique is very useful in understanding the complex turbulent flow fields. In this work, PIV technique is implemented for the analysis of laminar and turbulent combustion studies. This chapter explained the experimental setup and the basic principle of PIV evaluation scheme. The advanced PIV algorithm used for the velocity field measurement along with the validation tool used for the removal of spurious vectors are also discussed. The experimental and PIV evaluation parameters such as time delay between the image pair, magnification, seeding density, interrogation window size are optimized in order to achieve the velocity measurements with less than 1% spurious vectors. A masking technique is implemented for the removal of spurious vectors in the combustion studies. Our PIV technique can measure the velocity field with an uncertainty of $\pm\ 0.04\ m/s$ and with spatial resolution of $160\ \mu m$. In conclusion, we can now investigate the laminar and turbulent flow fields by using the PIV technique.

Chapter 5

Planar laser induced fluorescence

Abstract. *Laser induced fluorescence (LIF) is a highly selective and sensitive technique for detecting minor species in the combustion processes. In this technique, the molecules are populated to the excited states by absorption of laser radiation and after a certain lifetime, the molecules relax back to the ground states by emitting fluorescence signals. The fluorescence signals are then captured using an intensified CCD camera. In the linear regime of LIF, the fluorescence signals are proportional to the relative concentrations of the excited molecules which enable this technique to measure the equivalence ratio. In this chapter, the experimental setup, LIF subsystems, calibration techniques, measurement errors, their sources and corrections are described. The uncertainty and spatial resolution of LIF measurements are finally provided.*

5.1 Introduction

Laser induced fluorescence is an optical diagnostic tool widely used for detecting minor species like $OH, NO, CH, ...$ in combustion processes and also used for the measurements of temperature, velocity and pressure [Eckbreth (1998), Cessou (2006)]. LIF technique can be extended to two-dimensional measurements by expanding the laser beam into a thin laser sheet and recording the fluorescence signal by an intensified CCD camera. This extended two-dimensional measurement is called as planar LIF (PLIF). In this work, PLIF technique has been utilized to measure the

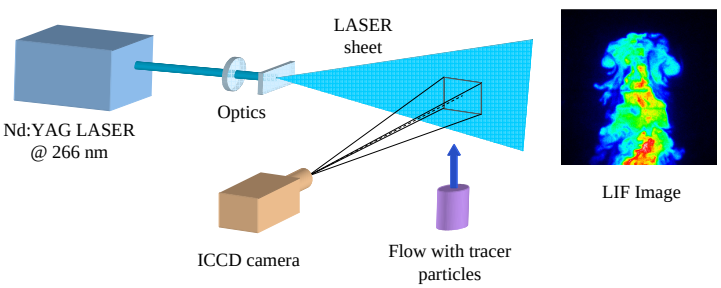

Figure 5.1: Typical experimental setup for a planar laser induced fluorescence.

equivalence ratio field. For that, fuel is doped with fluorescent tracer proportional to the fuel flow

rate. Then the tracer in the flow is illuminated by a laser light sheet (Fig. 5.1) whose wavelength is chosen to excite tracer molecules to higher energy state. A fraction of these excited molecules emit fluorescence signal and the rest of them return to the ground state by transferring excess of energy through non-radiative decay processes like collisional quenching or inter-crossing system. The emitted fluorescence signals from tracer molecules are proportional to the equivalence ratio of mixture and the laser intensity. Therefore, quantitative measurement of equivalence ratio is realized by calibrating the acquired fluorescence signal with known mixture and laser intensity. The acquired PLIF images are affected by noise from various sources, so the images are post-processed by a new image correction technique in order to improve the accuracy of measurements. This chapter covers the experimental setup, details of calibration of signal, new post-processing scheme for image error correction and the spatial resolution of equivalence ratio measurements.

5.2 Principle of LIF

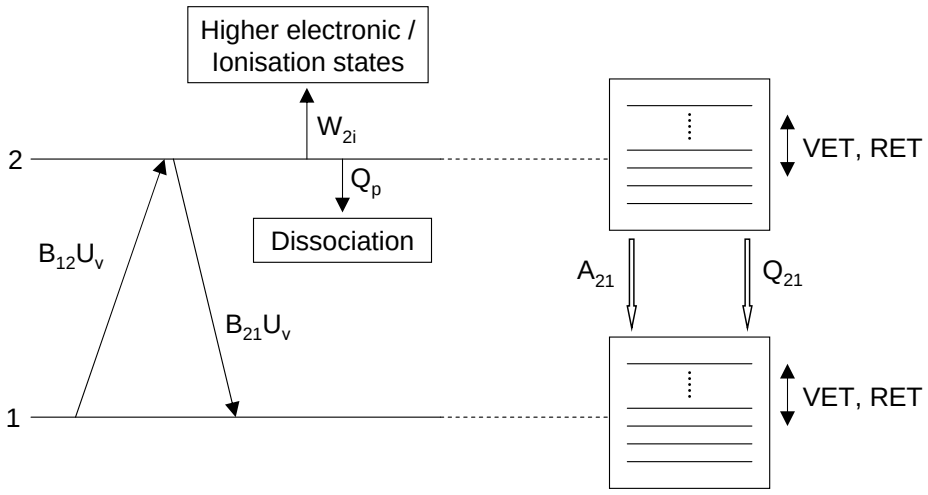

Figure 5.2: Principle of laser induced fluorescence (Hanson et al. (1990)).

The theoretical background of laser induced fluorescence is schematically shown in Fig. 5.2 [Hanson et al. (1990)]. The theoretical principle of LIF can be simplified by considering two-level scheme where molecules in the lower electronic energy state 1 are excited by laser absorption $(B_{12}U_\nu)$ which populates the upper electronic state 2. The upper energy state is depopulated through many ways:

- The molecule can return to the ground state by stimulated emission $(B_{21}U_\nu)$
- The molecules can be excited to higher electronic or ionization states (W_{2i})
- The molecules can loss energy due to dissociation (Q_p)
- The molecules can transfer its excited electron to other molecules by collisional quenching (Q_{21})

- The molecules can return to ground state by spontaneous emission of fluorescence (A_{21})

More details on the principle of LIF can be found in the references [Hanson et al. (1990), Eckbreth (1998), Cessou et al. (2000)].

5.3 Linear regime of LIF

In the case of two-levels model of fluorescence emission, the population of excited molecules N_2 can be described by the following equation [Cessou et al. (2000)]:

$$N_2(t) = \frac{N_0 U_\nu B_{12}}{(B_{12}+B_{21})U_\nu + A_{21} + Q_{21}} \left[1 - e^{-[(B_{12}+B_{21})U_\nu + A_{21} + Q_{21}]t}\right] \tag{5.1}$$

where $A_{21}, B_{12}, B_{21}, Q_{21}$ are Einstein coefficients, N_0 is the population of molecules at fundamental level and U_ν is the spectral energy density of laser beam. The fluorescence signal intensity can be expressed as:

$$S_f = h\nu \frac{\Omega}{4\pi} V N_0 \frac{B_{12}}{B_{12}+B_{21}} \frac{A_{21}}{1 + \frac{U_{\nu sat}}{U_\nu}} \tag{5.2}$$

where $h\nu$ is the photon energy, Ω is the solid angle of collection, V is the interaction volume and $U_{\nu sat}$ is the saturation intensity. For the case of lower laser intensities, which means $U_\nu \ll U_{\nu sat}$, the Eqn. 5.2 becomes:

$$S_f = h\nu \frac{\Omega}{4\pi} V N_0 B_{12} U_\nu \frac{A_{21}}{A_{21} + Q_{21}} \tag{5.3}$$

Thus fluorescence signal is proportional to the number of molecules N_0 and the laser intensity U_ν. But it is still affected by collisional quenching rate Q_{21} which depends upon temperature, pressure and concentration of species.

5.4 FARLIF

The fluorescence signal is affected by quenching rate and the quantitative measurement of concentration becomes difficult in some conditions. But, if the quenching rate is higher than spontaneous emission $(A_{21} \ll Q_{21})$, then the fluorescence signal becomes:

$$S_f = h\nu \frac{\Omega}{4\pi} V B_{12} U_\nu A_{21} \frac{N_0}{Q_{21}} \tag{5.4}$$

Thus the fluorescence signal is proportional to ratio of population of molecules in fundamental level to the Einstein coefficient of collisional quenching:

$$S_f \propto \frac{N_0}{Q_{21}} \tag{5.5}$$

Consider that the fluorescent tracer added to the fuel is chosen to be quenched by oxygen. Also, consider that the N_0 is proportional to the fuel concentration and collisional quenching rate is proportional to the oxygen concentration. Then, the Eqn. 5.5 can be expressed as:

$$S_f \propto \frac{Fuel}{O_2} \propto Equivalence\ ratio \tag{5.6}$$

Therefore, the equivalence ratio (ϕ) can be measured directly from the fluorescence signal for a given conditions of temperature, pressure and laser intensity. This technique is called as fuel-air ratio LIF (FARLIF) [Reboux et al. (1996)]. This measurement technique needs a fluorescent tracer with strong collisional quenching by oxygen molecules.

5.5 Choice of a tracer

Aromatic tracers are widely used for fuel-air ratio measurements because of their strong quenching by oxygen [Schulz and Sick (2005)]. The choice of aromatic tracer is very critical and important, must be taken based on criteria given below:

- The oxygen molecule must be the major collisional quenching contributor.
- The variation of fluorescence signal must be linear with the variation of laser energy and equivalence ratio.
- Good fluorescence yield is important.
- The emission spectrum must be shifted from absorption spectrum in order to avoid reflections from elastic scattering at the wavelength of laser.
- The tracer must have same thermo physical properties as the fuel so that it can mix well with fuel and can adequately represent the fuel concentration.
- The tracer should be not toxic.

Pasquier-Guilbert (2004) carried out a detailed analysis of choice of tracer by using an optical cell and found that anisole was a suitable tracer for the mixture of propane-air. The absorption and emission spectra of anisole are shown in Fig. 5.3. Some important properties of anisole are listed in the table 5.1. In that table, L_0 is the fluorescence intensity of solution in the absence of

CAS No.	100-66-3
Molecular Weight (g/mol)	108.14
Chemical Formula	$C_6H_5OCH_3$
Appearance	Clear, colorless liquid
Boiling Point	156°C
Melting Point	-37°C
Flash Point	52°C
Autoignition temperature	475°C
Vapor Density	3.72
Vapor Pressure (mmHg)	10 @ 42°C
L_0/L	1.54

Table 5.1: Anisole properties.

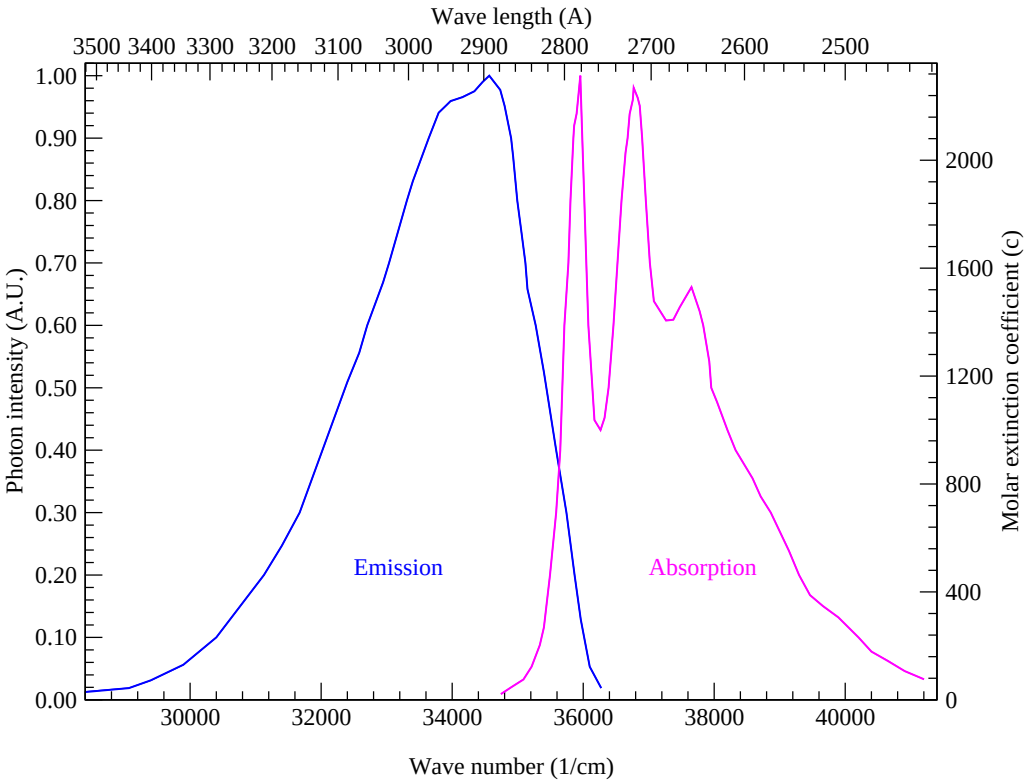

Figure 5.3: Emission and absorption spectra of anisole (Berlman (1971)).

air and L is the fluorescence intensity of same solution in the presence of air [Berlman (1971)]. The autoignition temperature of propane in air is around 450 - 504°C [Glassman (1987)] and the autoignition temperature of anisole is very close to propane. This similarity provides an advantage that tracer also disappears with fuel in the burned region which enables to visualize the burned region and to identify the flame front in the combustion images.

5.6 LIF subsystems

A typical LIF system (shown in Fig. 5.1) consists of several subsystems which are listed below:

1. A tracer unit which adds molecular tracer to fuel, proportional to the fuel flow rate.
2. A LASER unit to excite the fluorescent tracer.
3. An optical unit to create thin laser sheet.
4. An ICCD camera unit to capture the fluorescence signal.
5. UV filter to remove elastic and Mie scattering signals.
6. A synchronization unit to control the timing of laser and camera unit.

5.6.1 Tracer unit

The function of tracer unit is to add the fluorescent tracer proportional to the fuel flow rate. In this work, anisole is used as tracer for the propane-air mixture. A small concentration of anisole vapor

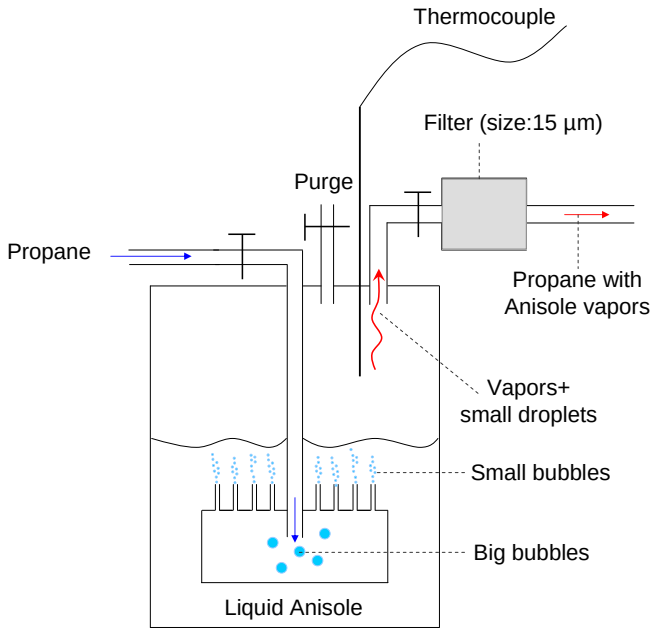

Figure 5.4: LIF tracer unit.

is added to propane by using a bubbler system as shown in Fig. 5.4. In that system, propane is used as a carrier gas and the flow rate of anisole vapor is controlled by the carrier gas flow rate [Boer (1995)]. The flow rate of propane was initially controlled by a thermal mass flow meter

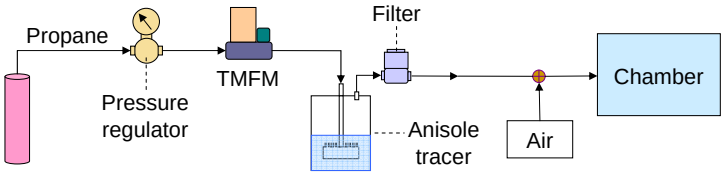

(a) Flow configuration 1.

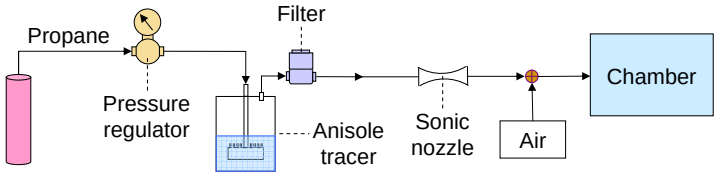

(b) Flow configuration 2.

Figure 5.5: Flow configuration of tracer.

(TMFM) as shown in Fig. 5.5. But the quantity of anisole vapor added to the propane flow rate varied significantly in that configuration due to the fluctuation of pressure inside the tracer unit

caused by the downstream conditions. In order to avoid this problem, another configuration has been utilized (Fig. 5.5). In this configuration, a sonic nozzle is fixed in between tracer unit and chamber. The flow rate of propane with anisole vapor through the sonic nozzle is controlled by the upstream pressure of propane. The advantage of sonic nozzle is that the flow rate is not affected by the downstream conditions. For a particular gas, the critical mass flow rate in the sonic nozzle is directly proportional to the stagnation pressure in the upstream [Bignell (2000)]. The calibration of the sonic nozzle is carried out by passing known quantities of propane at different pressures. The flow rate of propane is measured using a soap bubble meter. Finally, a linear relationship between the flow rate and the upstream pressure is obtained. This calibration process is frequently carried out to ensure correct functioning of sonic nozzle. The quantity of anisole vapor added to propane is very low due to its higher fluorescence yield ($L_0/L = 1.54$) so that it can be considered to have a negligible effect on the equivalence ratio of propane-air mixture.

5.6.2 LIF laser unit

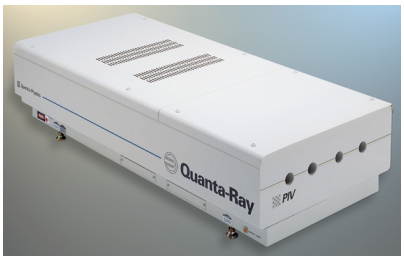

Figure 5.6: QuantaRay laser unit.

In our case, anisole vapor in the fuel-air mixture is excited by fourth harmonic of a Nd:YAG laser. The laser is a QuantaRay PIV 400 manufactured by Spectra Physics. The repetition rate of laser is $10\ Hz$ and the output energy is $100\ mJ$ at $266\ nm$ wavelength with fluctuations of around 5%. The duration of laser pulse is $8\ ns$. The residual fundamental and second harmonic laser beams are filtered out by specially coated UV mirrors.

5.6.3 Laser sheet formation

The laser sheet is formed by the combination of spherical and cylindrical lenses. A Dichroic mirror is used to optically combine the PIV laser beam with LIF laser beam. The minimum laser sheet thickness is around $400\ \mu m$, which is created by the association of one spherical lens of $1\ m$ focal length, one cylindrical lens of $-25\ mm$ focal length and one cylindrical lens of $+150\ mm$ focal length.

5.6.4 ICCD camera

The fluorescence signal is collected by an intensified CCD (ICCD) camera. The ICCD camera is a Roper Scientific PIMAX 512 manufactured by Princeton Instruments. The pixel format is 512×512 and the available pixel rates are $100\ KHz$ and $1\ MHz$ with a gating speed of $2\ ns(FWHM)$. The objective used in this work is a 100 F/2.8 type CERCO 2178 UV lens manufactured by EADS

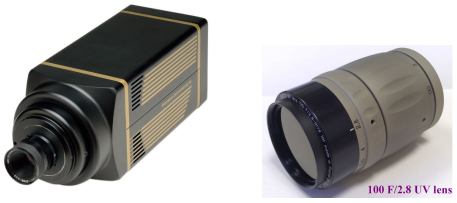

(a) ICCD camera. (b) UV objective.

Figure 5.7: ICCD camera and objective.

SODERN. The overall diameter of objective is $\phi\ 66\ mm$ and F-stop range is $F/2.8\ to\ F/8$. The field of view of LIF image is around $4.4 \times 4.4\ cm^2$.

5.6.5 Filter

The fluorescence signal emitted by the anisole tracer is broadband and situated around $350\ nm$ [Fig. 5.3]. Furthermore this range of wavelengths needs to be isolated from the laser excitation wavelength ($266\ nm$) and also from the Mie scattering wavelength ($532\ nm$). A Dichroic mirror is used to separate the Mie scattering signal from fluorescence signal. The laser wavelength signal is removed by a long-pass $266\ RazorEdge$ filter manufactured by Semrock. The diameter of filter is $25\ mm$. Due to its smaller size compared to the objective, it is placed in between UV objective and ICCD camera.

5.6.6 Synchronization unit

The synchronization unit used in this work comprises of timing generators, logic gates and oscilloscopes. The laser is operated by an external signal of fixed frequency ($10\ Hz$) with an option of shifting the frequency within $\pm 10\%$ of the operating frequency.

5.7 Calibration of fluorescence signal

Theoretically, in the linear regime of LIF operation, the fluorescence signal is proportional to the ratio of local population of molecules illuminated by the laser sheet to the collisional quenching rate (Eqn. 5.5). This collisional quenching rate depends upon the collisional partners and in our case oxygen is the major collisional partner [Pasquier-Guilbert (2004)]. So the fluorescence signal acquired from the PLIF image is proportional to the laser energy and the fuel-air ratio which determines local population of tracer molecules and quenching rate. Thus the first step of equivalence ratio measurement is to calibrate the fluorescence signal with known mixture and laser energy so that we can find a linear relationship between the fluorescence signal and the equivalence ratio.

One example of PLIF image of a homogeneous mixture is shown in Fig. 5.8. The spatial variation of signal level is related to factors such as vignetting effect [Ferrier et al. (1993)], inhomogeneity of laser profile, optical collection effect and so on. These variations could affect

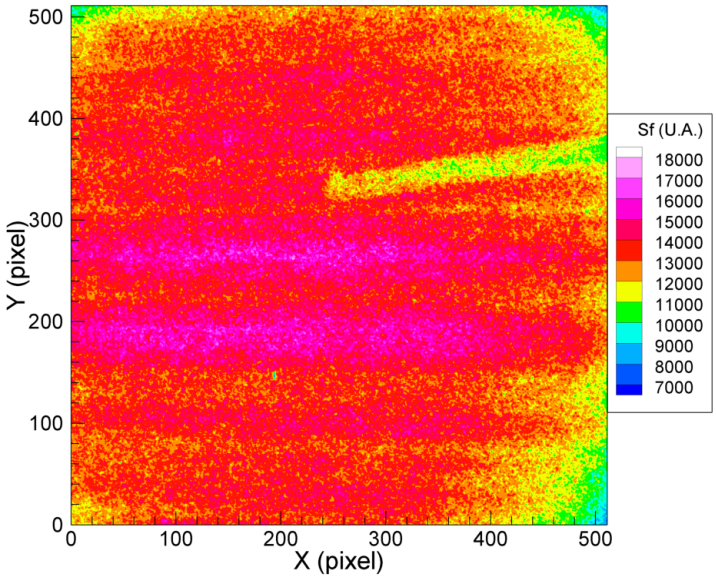

Figure 5.8: Fluorescence image of homogeneous mixture field.

the equivalence ratio measurement. But the first checking point is the linearity of mean fluorescence signal with respect to the equivalence ratio at a given laser intensity. So we carried out the calibration procedure before doing any post-processing of images.

First, the combustion chamber is filled with propane-air mixture of known equivalence ratio and one hundred consecutive images are acquired. The mean and standard deviation of one hundred consecutive images are shown in Fig. 5.9. During the acquisition, the instantaneous

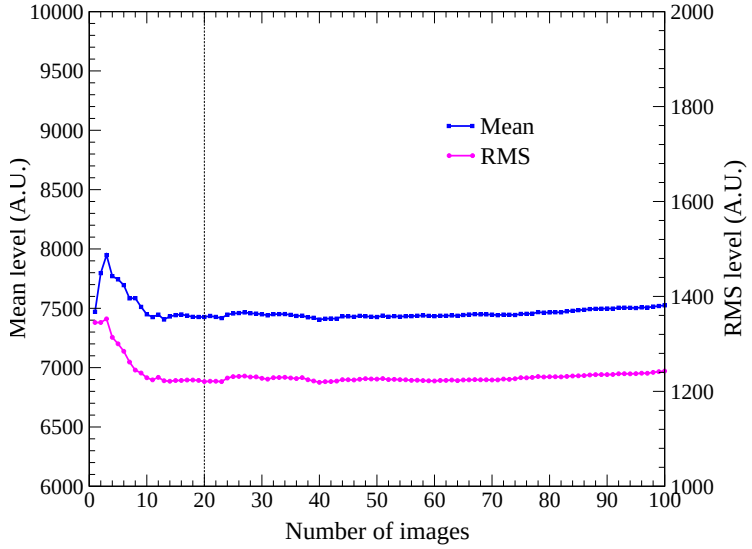

Figure 5.9: Mean and rms of ICCD images of homogeneous mixture.

energy of the laser beam is measured by using an energy meter located on the path of reflected beam from the spherical lens (Fig. 5.10). The procedure is repeated for the range of equivalence ratios varying from $\phi = 0.6$ to $\phi = 2.0$. Finally, the combustion chamber is filled with air alone

and one hundred images are acquired to compensate the background noise comprises of black noise of ICCD camera and diffusion of light. Then the background and energy corrected mean fluorescence signal level of each image is measured by the following expression:

$$S_f(i) = (I(i) - \overline{I_b}) * E_r/E_i \tag{5.7}$$

where I is the mean fluorescence signal level of whole image, $\overline{I_b}$ is the mean fluorescence signal of one hundred background images, E_r is the reference energy and E is the instantaneous energy.

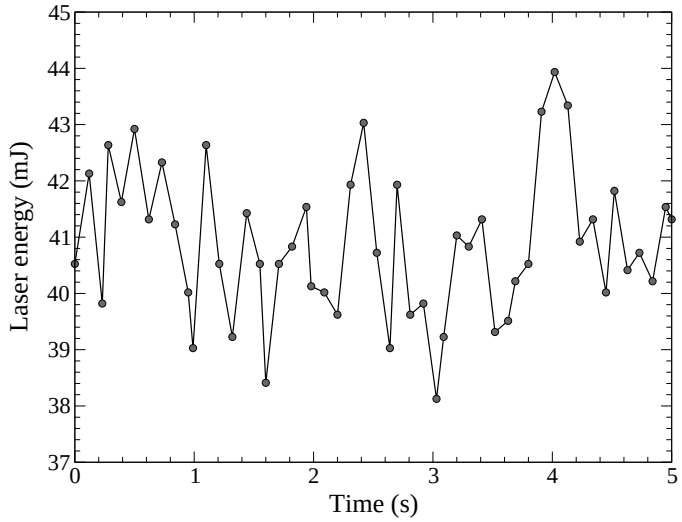

Figure 5.10: Instantaneous laser energy.

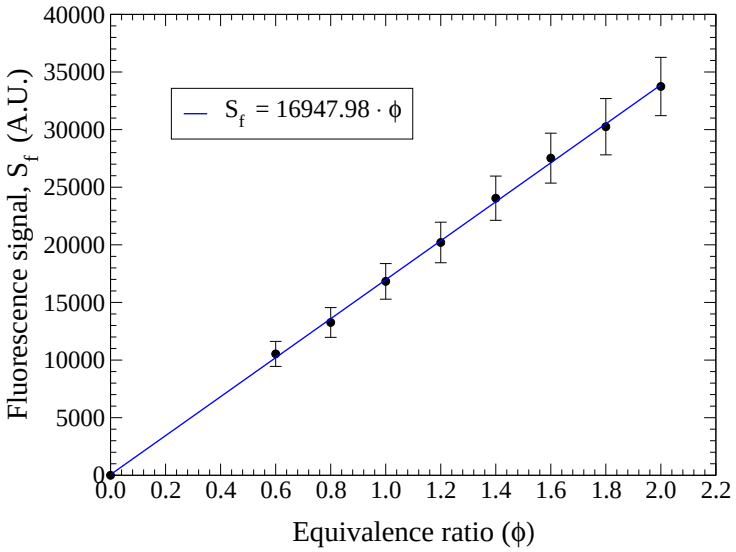

Figure 5.11: FARLIF calibration curve.

The variation of corrected fluorescence signal level as a function equivalence ratio is shown in Fig. 5.11. The fluorescence signal shows a very good linearity with equivalence ratio. This lin-

earity confirms that despite the assumption of two-level scheme, fluorescence signal from anisole vapor allows the quantified measurement of equivalence ratio and also indicates that the quantity of anisole added to the propane is well controlled. The increase of fluctuations with equivalence ratio is due to increase of noise level with signal level. The next section focuses on the source of noises and their elimination by post-processing techniques.

5.8 Measurement of Equivalence ratio

The raw PLIF images need to be post-processed in order to accurately measure the local equivalence ratio and for that we must understand the factors which influence the inhomogeneity of fluorescence signal. So the mean profiles of raw images are analyzed first. The mean horizontal and vertical full binning profiles of 20 raw images are shown in Fig. 5.12. The mean horizon-

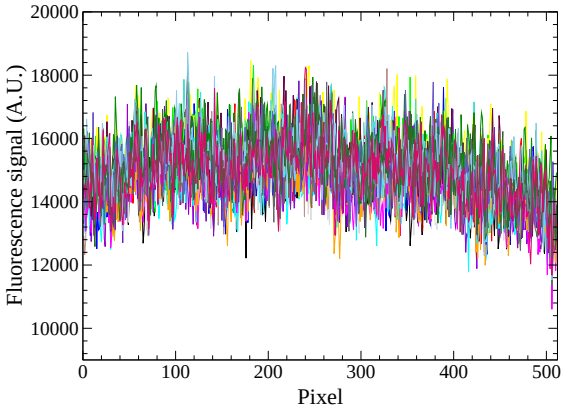

(a) Mean horizontal profiles.

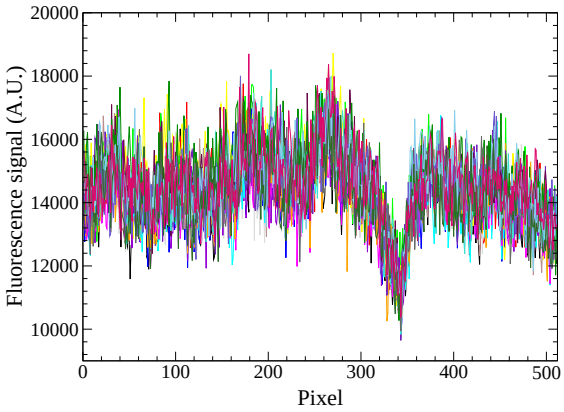

(b) Mean vertical profiles.

Figure 5.12: Horizontal and vertical profiles of 20 raw images.

tal profiles are showing a typical pattern where the signal levels are lower at right and left sides compared to the central region of profiles and this could be related to the vignetting effect. The variations in the mean vertical profiles could be related to the inhomogeneity of laser profile. The

presence of electrode in the combustion chamber also affects the vertical profiles as we can see the sudden drop in the fluorescence signals around 320 pixels in the mean vertical profiles.

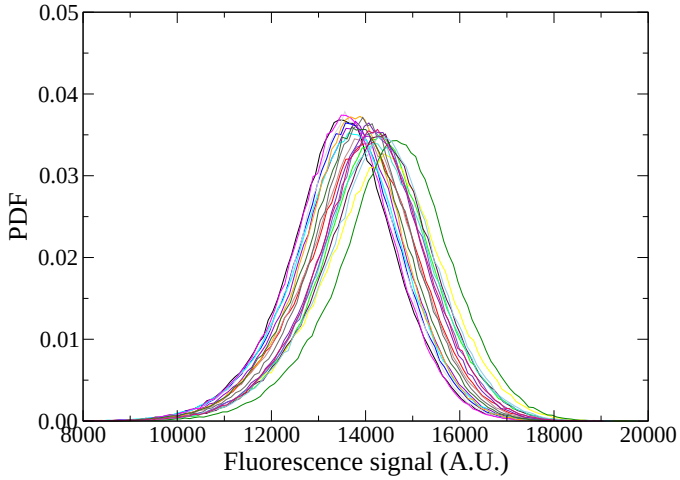

Figure 5.13: PDF of raw images.

The probability of distribution of signals collected from 20 images is shown in Fig. 5.13. The distribution is slightly non-symmetrical and wide on the lower levels of signal. Though images are acquired for the same homogeneous mixture condition, there is no perfect overlapping of distribution due to the shot-to-shot variation of laser energy, variation in the laser energy profile and random noises introduced by various sources. These sources of noises and their elimination are given in the next sections.

5.8.1 Sources of error

There are multiple factors contributing to the variations of signal level. The important sources of errors are listed below:

- Errors due to inhomogeneity of laser profile
- Errors due to shot-to-shot variation of laser energy
- Errors introduced by the collecting optics
- Errors originated from the ICCD camera
- Errors originated from the mixture preparation

Laser profile:
The fluorescence signal level is directly proportional to the intensity of laser (Eqn.5.3). The local energy distribution in the laser sheet is a critical factor because that can affect the local measurement of equivalence ratio. Therefore homogeneous distribution of energy across the laser beam is very essential for accurate local measurements. Any inhomogeneity in laser profile over time can become source of errors.

Laser stability:
The shot-to-shot variations of laser energy are another source of error. This error could be eliminated by correcting the signal level by instantaneous laser energy. The measurement of instantaneous laser energy can be realized by using external devices such as photomultiplier or by calculating from the small region of acquired image.

Optical collection:
The optical collection system also introduces errors to the measurement due to the vignetting effect, wrong alignments and the distortion produced by the optical windows. The fluorescence signal level could be also affected by the window fouling effect.

Camera:
The ICCD camera unit converts the incident light signal into electric charge, amplifies the charge, converts the charge to voltage signal, and digitizes the signal and stores as an image on a computer. These various stages introduce both random and systematic noises to the acquired image.

Mixture preparation:
The mixture preparation of propane-air could introduce error as a difference between the measured value and the true value of equivalence ratio and this error cannot be corrected by post-processing of images. But the perfect linearity observed between the mean fluorescence signal and the equivalence ratio ensures proper mixture preparation in our work.

5.8.2 Error correction

The systematic errors imposed on a fluorescence image can be eliminated by the post-processing scheme explained in this section. The local fluorescence intensity $I_F(x, y, i)$, which is proportional to the local equivalence ratio $\phi(x, y, i)$ of image acquired from two-dimensional laser sheet, can be expressed as [Shan et al. (2004)]:

$$I_F(x, y, i) = g[I_L(x, y, i), S(x, y)]\phi(x, y, i) + b \cdot I_L(x, y, i) + I_{dark}(x, y, i) \tag{5.8}$$

where i is image number, $g[I_L(x, y, i), S(x, y)]$ is the unknown function of local laser intensity $I_L(x, y, i)$ and $S(x, y)$ is the pixel by pixel optical transfer function of the imaging system. The fluorescence signal from the interference of laser illumination is represented by $b \cdot I_L(x, y, i)$. The dark noise of CCD camera is represented by $I_{dark}(x, y, i)$. The background noise is the summation of diffusion signal and the dark noise.

$$I_{back}(x, y, i) = b \cdot I_L(x, y, i) + I_{dark}(x, y, i) \tag{5.9}$$

Since intensity of the background noise is small compared to the fluorescence signal, background noise is assumed independent of the shot-to-shot variation of the laser energy. Also, rms of dark noise of the camera is negligible compared with other sources of uncertainty, the background noise can be eliminated by acquiring an average image of mixture with zero equivalence ratio.

$$I_{back}(x, y, i) \simeq b \cdot \overline{I_L(x, y)} + \overline{I_{dark}(x, y)} = \overline{I_{back}(x, y)} \tag{5.10}$$

Thus,

$$I_F(x, y, i) = g[I_L(x, y, i), S(x, y)]\phi(x, y, i) + \overline{I_{back}(x, y)} \tag{5.11}$$

If we consider that the laser sheet profile is conserved from one shot to another, then

$$I_L(x,y,i) = P(x,y)\cdot < I_L > (i) \tag{5.12}$$

where P(x,y) is the laser sheet profile and $< I_L >$ is the spatial average of the laser energy. This assumption gives,

$$I_F(x,y,i) - \overline{I_{back}(x,y)} = S(x,y)\cdot P(x,y)\cdot < I_L > (i)\cdot \phi(x,y,i) \tag{5.13}$$

By acquiring the average fluorescence signal of a homogeneous mixture,$\phi(x,y,i) = \phi_{ref}$, the determination of the influence of the spatial response of the camera and the laser sheet profile can be determined.

$$\overline{I_{ref}(x,y)} - \overline{I_{back}(x,y)} = S(x,y)\cdot P(x,y)\cdot \overline{< I_L >}\cdot \phi_{ref} \tag{5.14}$$

The equivalence ratio field is then given by

$$\phi(x,y,i) = \phi_{ref}\cdot \frac{\overline{< I_L >}}{< I_L > (i)}\cdot \frac{I_F(x,y,i) - \overline{I_{back}(x,y)}}{\overline{I_{ref}(x,y)} - \overline{I_{back}(x,y)}} \tag{5.15}$$

The shot to shot correction factor is,

$$R_i = \frac{\overline{< I_L >}}{< I_L > (i)} \tag{5.16}$$

The correction factor is calculated from the mean signal level of region of interest (ROI) of mean reference and instantaneous image as given below:

$$R_i = \frac{\phi_i}{\phi_{ref}}\cdot \frac{\overline{I_{ref_{roi}}}}{\overline{I_{F_{roi}}}} \tag{5.17}$$

The equation 5.15 becomes,

$$\phi(x,y,i) = \frac{I_F(x,y,i) - \overline{I_{back}(x,y)}}{\overline{I_{ref}(x,y)} - \overline{I_{back}(x,y)}}\cdot R_i\cdot \phi_{ref} \tag{5.18}$$

The correction procedure is schematically shown in Fig. 5.14 and the examples of final corrected images at different equivalence ratios are shown in Fig. 5.15. The mean reference image is taken at $\phi = 1.2$ for the LIF image correction. The vignetting effect is completely removed in the final corrected images by the correction procedure. But the spatial variations along Y direction are not completely removed. Among the examples of final corrected images (Fig. 5.15), $\phi = 1.0$ is having least spatial variations and $\phi = 1.8$ is having highest spatial variations. That clearly shows the increase of spatial variation with increase of difference between the equivalence ratios of raw and reference images utilized for the correction. Also the spatial variations are dominant in Y direction and this point is further illustrated by the mean vertical and horizontal profiles shown in Fig. 5.16. At $\phi = 1.2$, there is no variation in the mean profiles. That means the correction scheme works well when the reference images are taken with same mixture conditions of raw images and becomes worse when the differences are more. The distributions of equivalence ratio

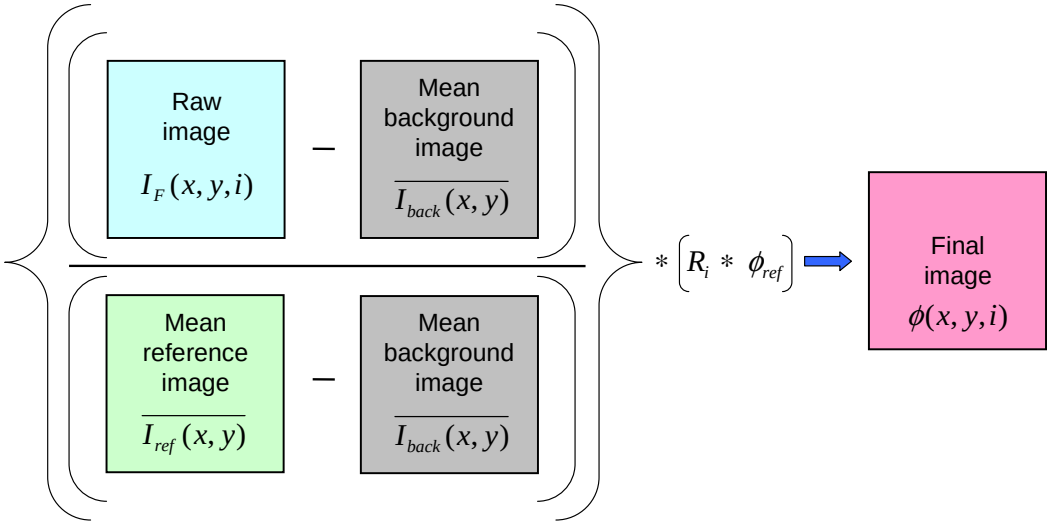

Figure 5.14: LIF image error correction procedure.

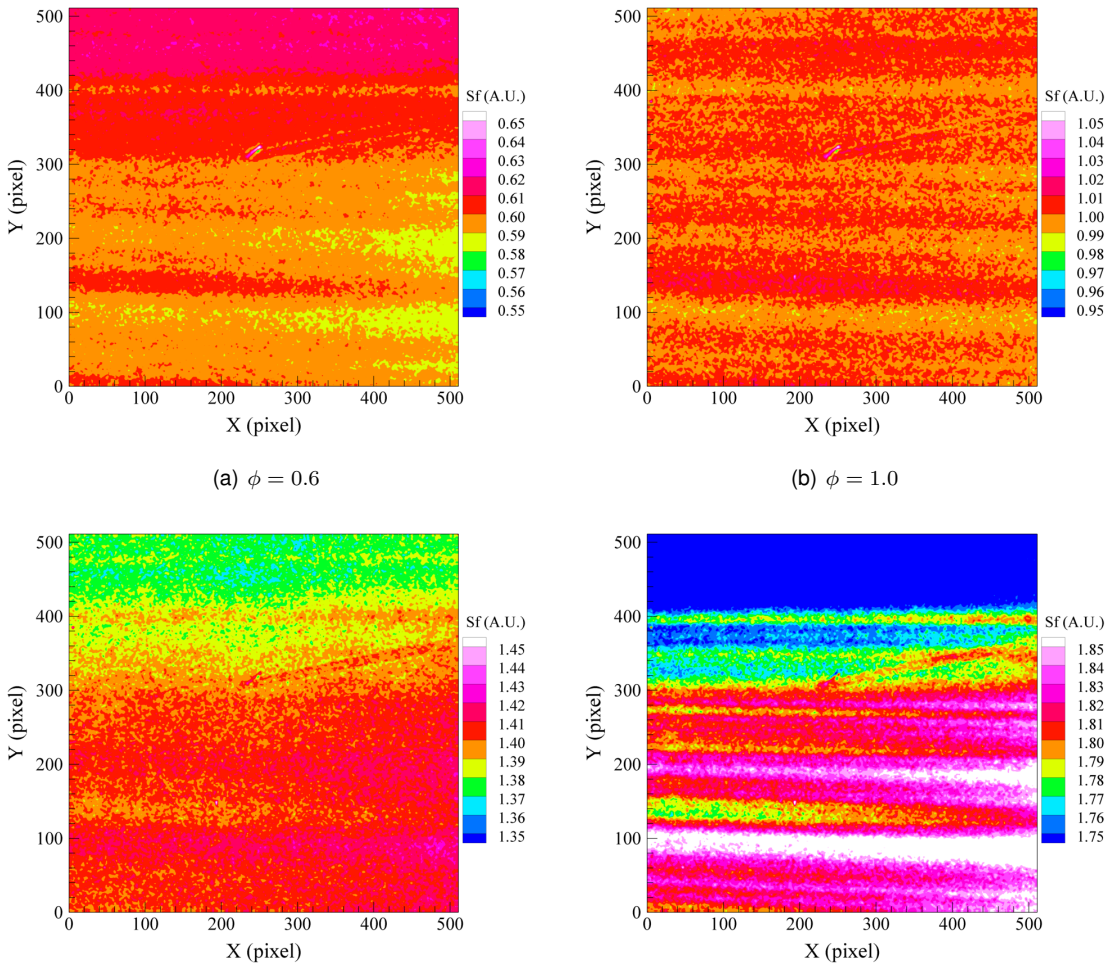

(a) $\phi = 0.6$

(b) $\phi = 1.0$

(c) $\phi = 1.4$

(d) $\phi = 1.8$

Figure 5.15: Examples of corrected images.

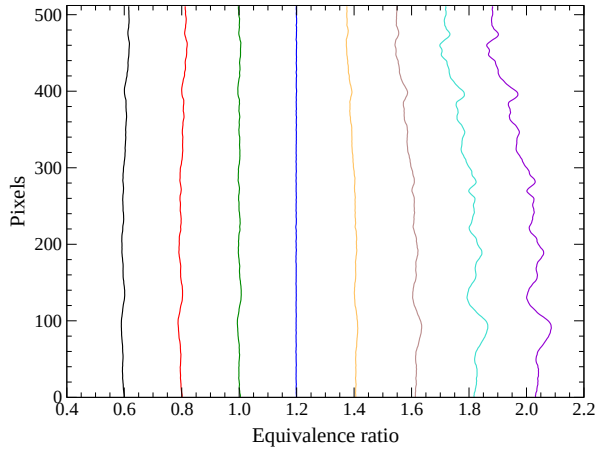

(a) Vertical profiles

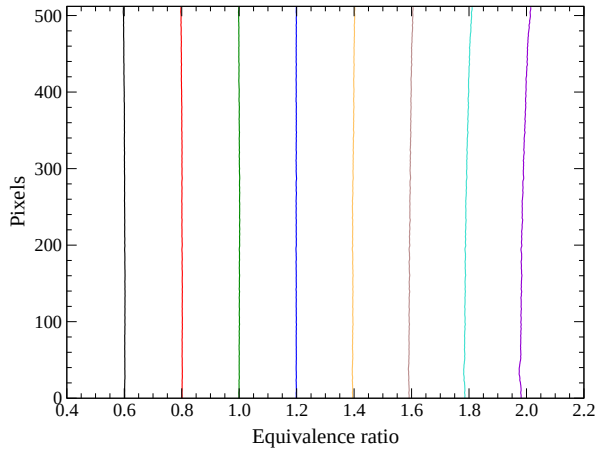

(b) Horizontal profiles

Figure 5.16: Mean horizontal and vertical profiles of corrected images.

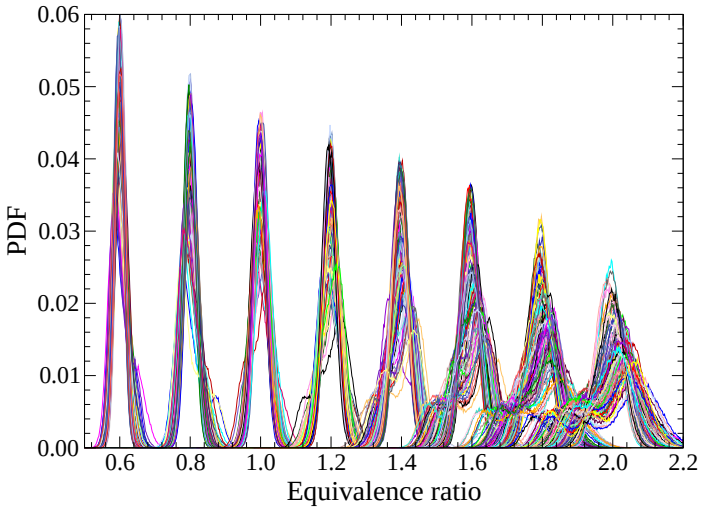

Figure 5.17: PDF of corrected images.

for different corrected images are shown in Fig. 5.17. The distributions are almost symmetric up to $\phi = 1.2$ and becomes more and more non symmetric with increase of equivalence ratio. Indeed, the distribution of each case changes with different reference images and even for same mixture condition, the distribution changes with reference images taken at different times. All those observations indicate that the correction procedure cannot be applicable when the raw and reference images are taken at different time or at different mixture conditions.

5.8.3 Novel correction technique

The spatial variation of laser beam over a period of time affects the local measurement of equivalence ratio because of normalization of raw image by reference image taken at a different time. This spatial variation effect cannot be eliminated by the standard correction scheme. So, a novel scheme has been developed based on the mean vertical laser beam profiles extracted from the instantaneous raw image and mean reference image.

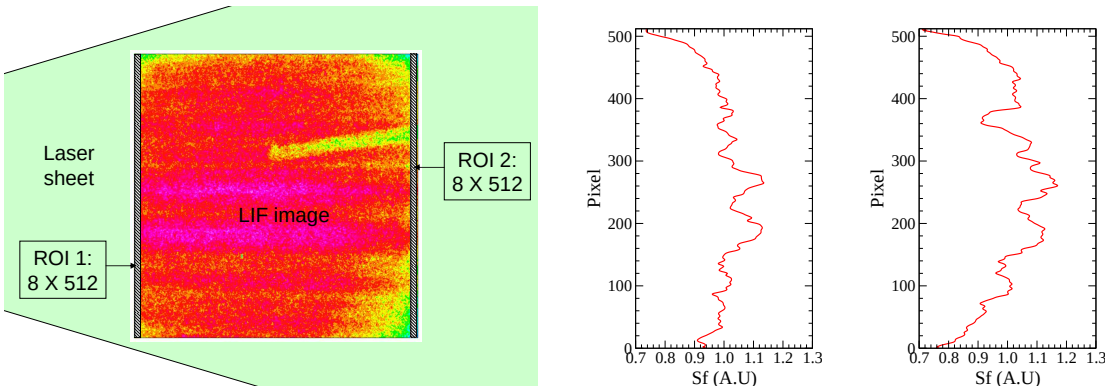

(a) Raw image (b) Mean profile 1 (c) Mean profile 2

Figure 5.18: Mean vertical profiles from the ROI region of image.

In our configuration, the laser beam has been passing from left to right of image shown in Fig. 5.18. Therefore, the instantaneous spatial distribution of laser energy for each image can be calculated from the mean vertical profiles of region of interest (ROI) from the left and right side of image. One example of mean vertical profiles calculated from first and second ROI are shown in Fig. 5.18. The left and right side mean vertical profiles are not having similar variation of fluorescence signals along Y direction due to the vignetting effect, presence of electrodes and laser sheet expansion along X direction. But the normalization of raw image by mean reference image can eliminate those interferences except the laser sheet profile shot-to-shot variation. However, the laser beam variation can be included in to the correction scheme by computing the laser profile image based on the ROI profiles. So the basic principle of our new scheme is to normalize each image by its own laser profile image before applying the standard correction procedure.

The principle of new correction technique is depicted in Fig. 5.19. The first step of our new technique is to calculate sample and reference image respectively from raw and mean reference images subtracted by mean background images. Then their corresponding laser profile images are computed from their ROI profiles. After that, sample and reference images are normalized by their own computed laser profile images and that eliminates the effect of temporal variation of

laser sheet profile. Next normalized sample image is divided by the normalized reference image in order to eliminate the vignetting effect, presence of electrodes and other systematic errors. Finally, the output image is multiplied by the shot-to-shot correction factor.

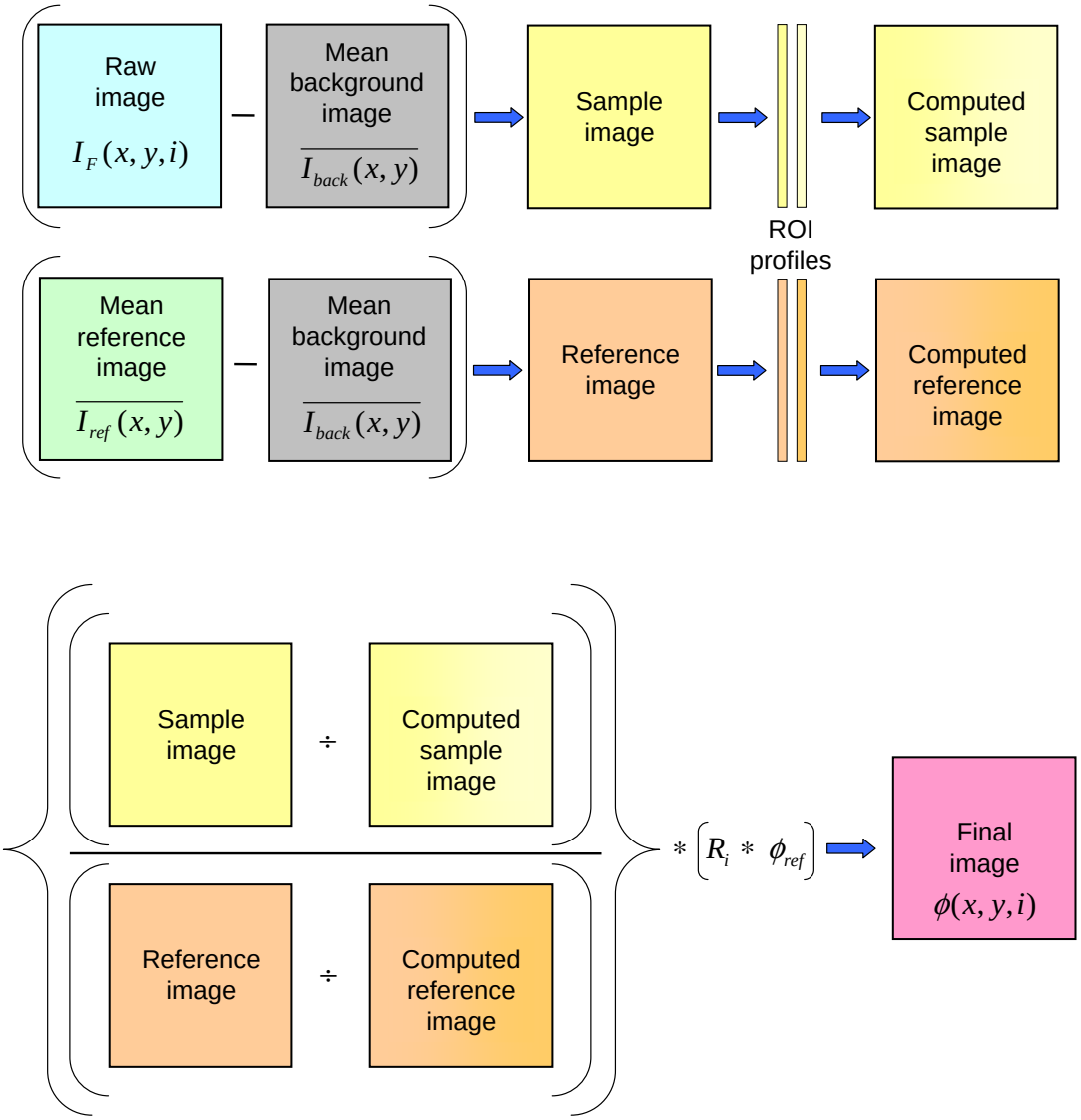

Figure 5.19: Novel correction technique.

One example of computed laser profile images of reference and sample image are shown in Fig. 5.20. These images are constructed from their ROI profiles by using a linear fit of the signal between the left and right side mean vertical profiles. The computed laser profile images shows clear difference between the sample and reference image, which causes spatial variation in the final image because of normalization of raw image by mean reference image in standard correction technique. But by normalizing the sample and reference images by their own computed laser profile images eliminate this laser beam profile effect. One example of normalized sample and reference image are shown in Fig. 5.21. The spatial variation of fluorescence signal in the

normalized sample image is similar with normalized reference image. This normalized image also shows the presence of electrodes at top right corner of image, vignetting effect in top and bottom of image and variation of signal along X direction especially in the right end of image due to the diffusion of light. So by dividing the normalized sample image by normalized reference image eliminates all those systematic errors. Few examples of final corrected images by the new

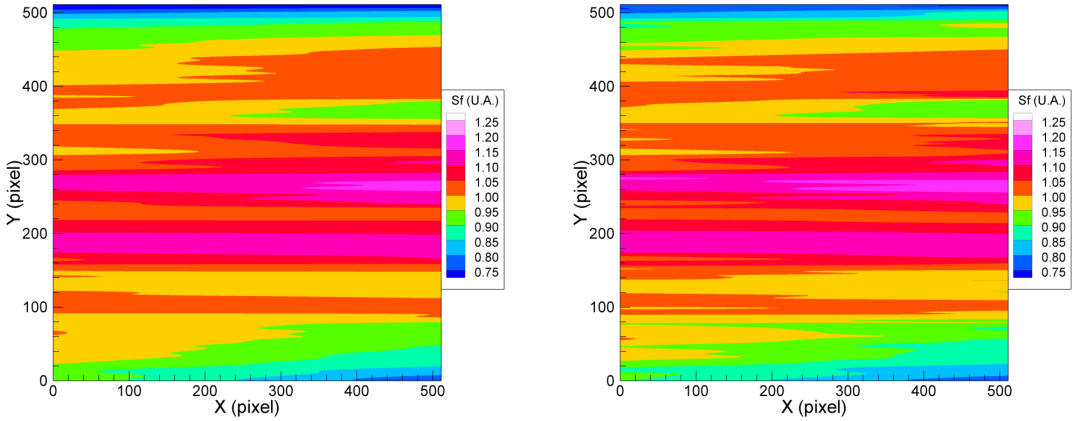

(a) Computed reference image. (b) Computed sample image.

Figure 5.20: Computed reference and sample images.

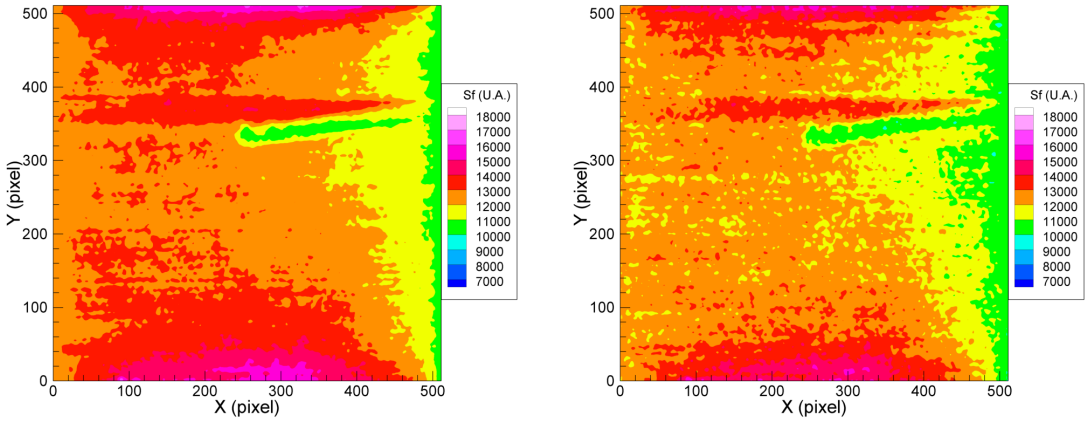

(a) Normalized reference image. (b) Normalized sample image.

Figure 5.21: Profile corrected reference and sample images.

technique are shown in Fig. 5.22. The spatial variations in the vertical direction are eliminated by the new technique. However, final corrected images show a small residual spatial variation in the horizontal direction which is related to the increase in diffusion of signals from the windows with equivalence ratio and the new technique cannot correct those variations. Nevertheless, the reference images are acquired with mixture conditions closer to the combustion images so that diffusion of light is almost same for both reference and raw images. The overall spatial variations of final images are very much lower than the finale images calculated by the standard correction technique.

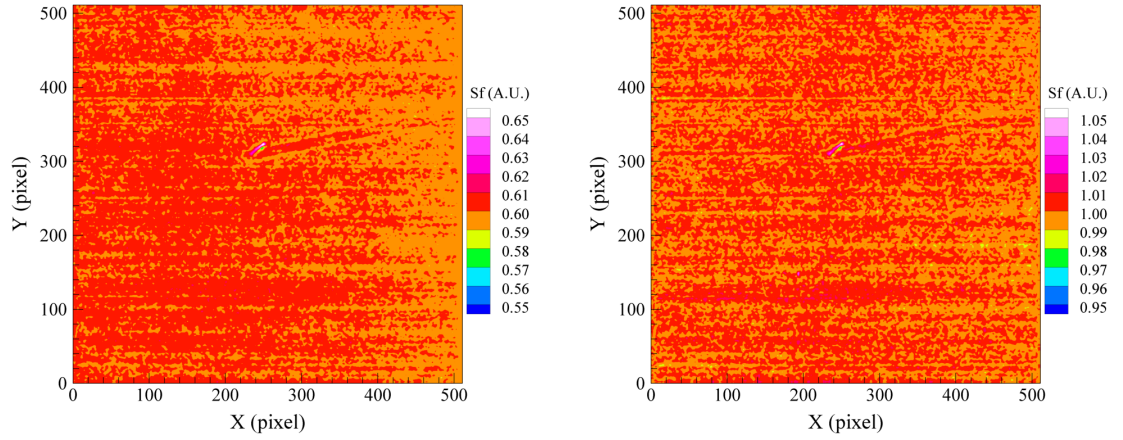

(a) $\phi = 0.6$

(b) $\phi = 1.0$

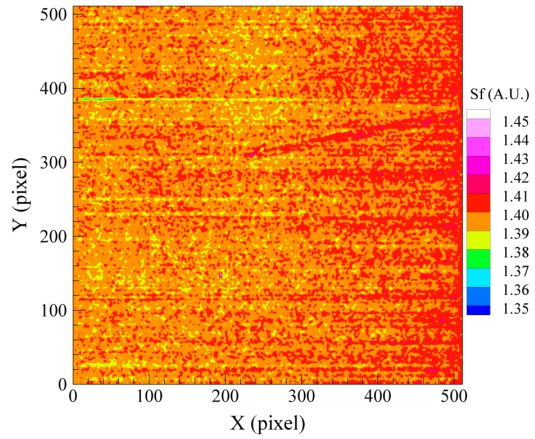

(c) $\phi = 1.4$

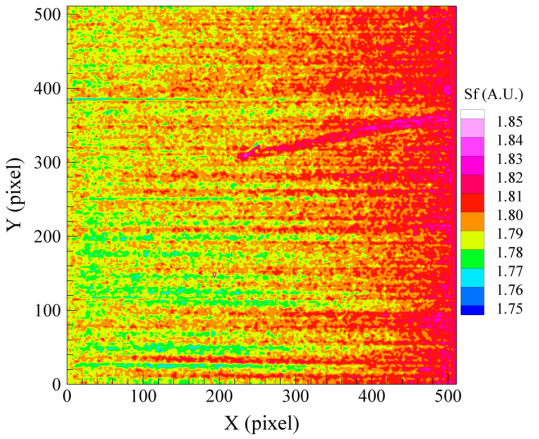

(d) $\phi = 1.8$

Figure 5.22: Examples of corrected images by novel technique.

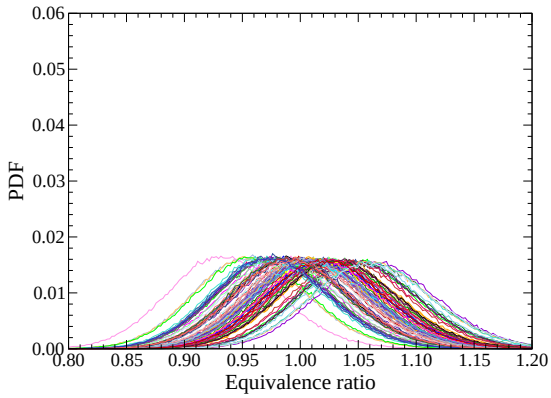

(a) PDF of Laser sheet profile corrected images.

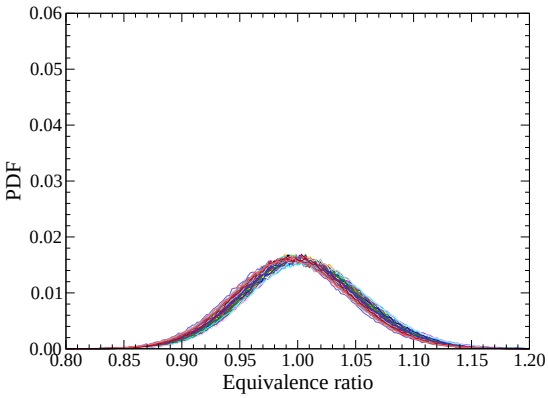

(b) PDF of shot-to-shot laser energy variation corrected images.

Figure 5.23: PDF of images.

Now we would like to show the results of intermediate steps of LIF image error correction procedure. The distributions of equivalence ratio of one hundred images calculated from their final images before and after the shot to shot correction are shown in Fig. 5.23. The dispersions are almost same and their shift from the true value ($\phi = 1.0$) clearly indicates the effect of shot to shot laser energy variation on the measured values. A perfect overlapping is observed after the shot-to-shot correction.

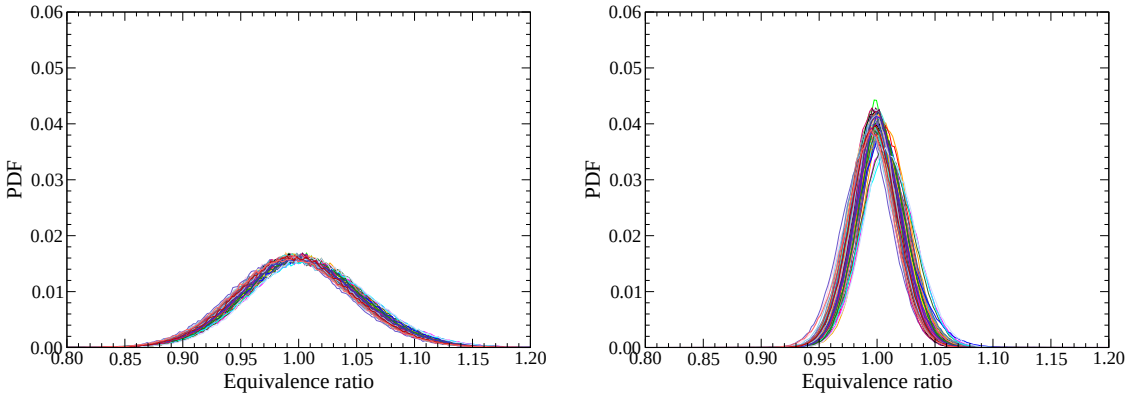

(a) PDF of images without filtration.

(b) PDF of images after filtration.

Figure 5.24: PDF of median and Gaussian filtered images.

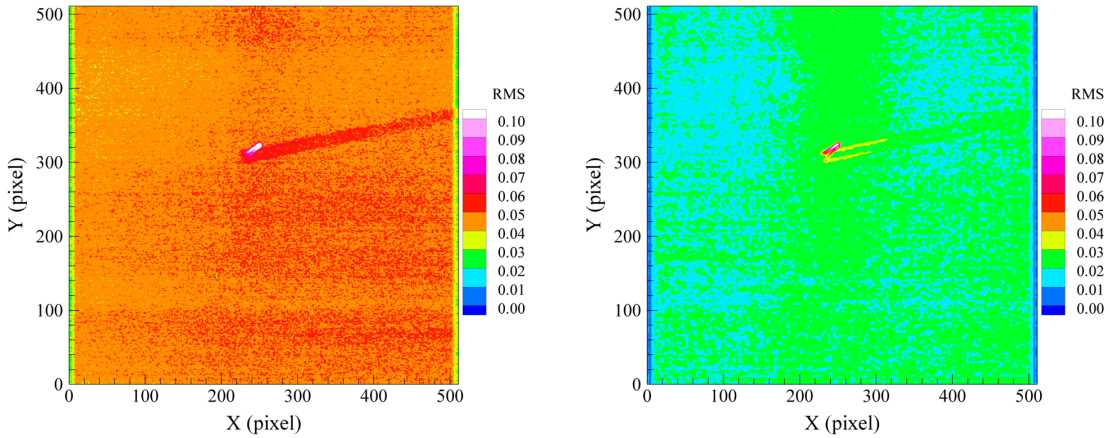

(a) RMS of 20 images without filtration.

(b) RMS of 20 images with filtration.

Figure 5.25: Fluctuations of 20 images.

The precision of measurements can be improved by removing random noises in the images using median and Gaussian filter schemes. But the filtration could decrease the spatial resolution of measurements. So the size of filter has been optimized based on the variation of fluctuation and spatial resolution with respect to different filter sizes. The optimization process is explained in the next section. The images are filtered by applying two times of median filter of size 3×3 pixels and one time of Gaussian filter of size 5×5 pixels. The distributions of equivalence ratio of images before and after the filtration are shown in Fig. 5.24. The dispersions of filtered images

are lower than the unfiltered images which clearly indicate the improvement in the precision of measurements. The comparison of fluctuations of images with and without filtration is shown in Fig. 5.25. The dispersion is reduced globally in the filtered images.

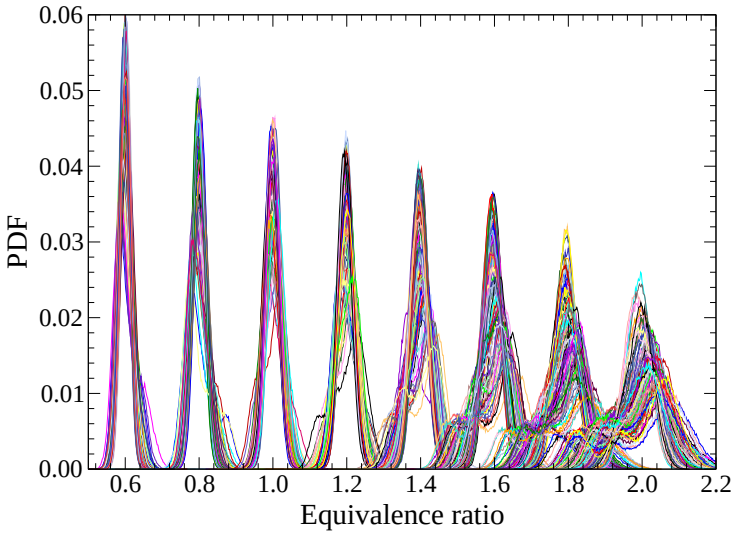

(a) Standard correction procedure

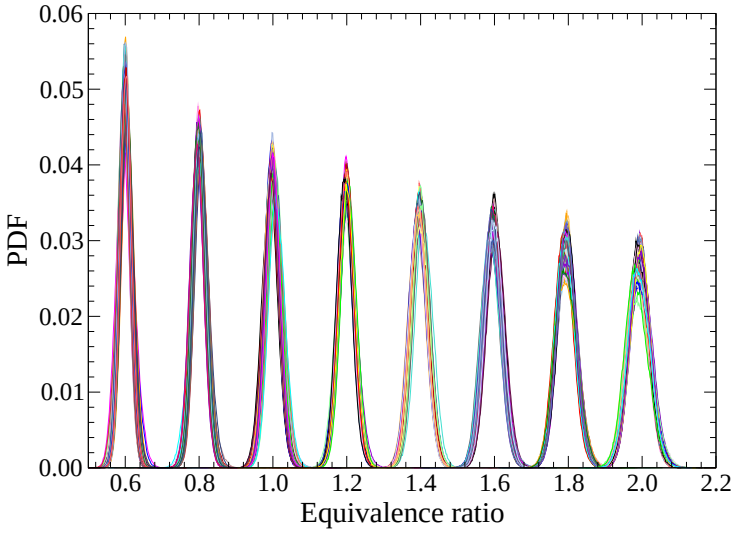

(b) New correction technique

Figure 5.26: PDF of corrected images of homogeneous mixtures taken at different equivalence ratios.

The distributions of equivalence ratio for different corrected images by new technique are shown in Fig. 5.26. The distributions are symmetric for all the equivalence ratios. For each homogeneous mixture conditions, equivalence ratio at the peak of distribution is perfectly matches with actual value and the dispersions are very small compared to the results obtained by the standard correction procedure. The dispersions of PDF curves increase with equivalence ratio due to the increase of noise to the signal level with equivalence ratio.

The comparison of equivalence ratios measured from raw images and final images with and without profile corrections are shown in Fig. 5.27. As expected, the fluctuations are smaller in corrected images and even smaller with profile corrected images which shows that the precision of measurement is improved by the new correction technique. A summary of LIF correction steps with fluctuations are given in Table 5.2. The fluctuations ($\pm\ \sigma$) are reduced from around 10% to around 2% by the correction process. So the uncertainty in the equivalence ratio measurement is around $\phi = \phi_{measured} \pm 2\%$ at $\phi = 1.0$.

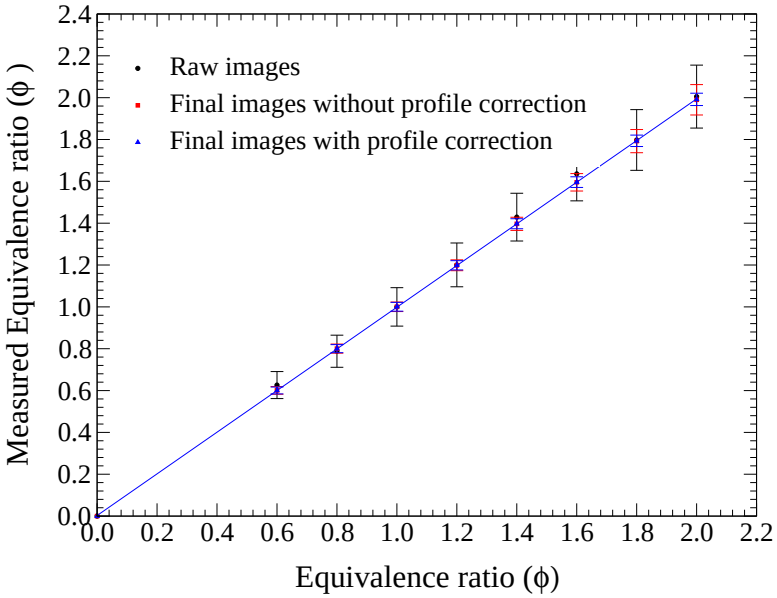

Figure 5.27: FARLIF calibration curve.

LIF Image correction stages	**rms at** $\phi = 1.0$
Raw images	$\pm$ 10.61 %
Laser sheet corrected images	$\pm$ 5.75 %
Pulse energy corrected images	$\pm$ 5.09 %
Filtered images	$\pm$ 2.10 %

Table 5.2: Fluctuations at different stages of LIF image correction.

5.9 Precision of LIF measurement

As explained earlier, the variation of fluorescence signal level in the raw image is contributed by various error sources (§ 5.8). Even though new correction technique eliminates all the systematic errors, it cannot remove the random noises imposed on the image which varies pixel-to-pixel. For the random noises, median filter is an effective tool which could eliminate noise without affecting the gradient of signal. Median filter is a non-linear filter which replaces the middle value of 2D array by their median value. By combining the median filter with Gaussian filter, it is possible to

remove the random noises and smooth the image for better precision. But the spatial resolution of measurement decreases with increase of filter size. So the filter size needs to be optimized for good precision with reasonable spatial resolution.

Spatial resolution of numerical filter:

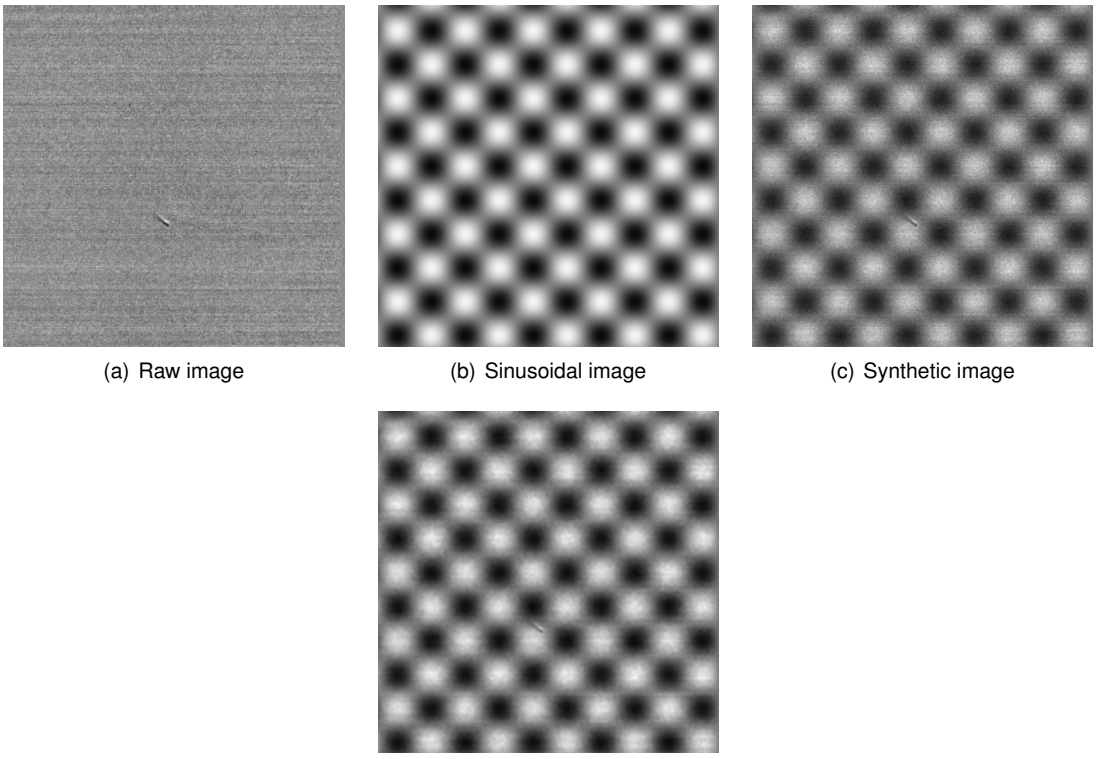

(a) Raw image (b) Sinusoidal image (c) Synthetic image

(d) Filtered image

Figure 5.28: Filtration of synthetic image.

We have developed a method for the measurement of spatial resolution of the numerical filter applied by using synthetic images. The principle of method is to create a two-dimensional sinusoidal image, convolute that image with profile corrected raw image, then apply the filter and measure the ratio of amplitudes of filtered and synthetic image as a function of frequency. Examples of raw image, sinusoidal image, convoluted synthetic image and filtered image are shown in Fig. 5.28. Here the raw image is one of the instantaneous images taken at $\phi = 1.0$ homogeneous mixture condition so that it represents the same kind of randomness of real images. The formula used to generate the two-dimensional synthetic images is given below:

$$I_{Syn}(x,y) = 2 \cdot I_{Raw}(x,y) + I_{Raw}(x,y) \cdot cos\left(\frac{2\pi}{T}x + \frac{\pi}{180}\phi_x\right) \cdot cos\left(\frac{2\pi}{T}y + \frac{\pi}{180}\phi_y\right) \tag{5.19}$$

where $I_{Syn}(x,y)$ is the intensity of convoluted image, $I_{Raw}(x,y)$ is the intensity of raw image, T is the period of sinusoidal wave, ϕ_x, ϕ_y are the phases in X and Y directions. The phase is taken as 45°. The frequency of image is reciprocal of period, that is, frequency $f = 1/T$.

The imposed and filtered profiles are shown in Fig. 5.29. Here M3 represents median filter of size 3×3, M5 represents median filter of size 5×5 and similarly G3, G5 represent Gaussian

filters of size 3×3 and 5×5. The combinations of filters tried in this work are M3G5, M3M3G5, M5G5 and M5M5G5.

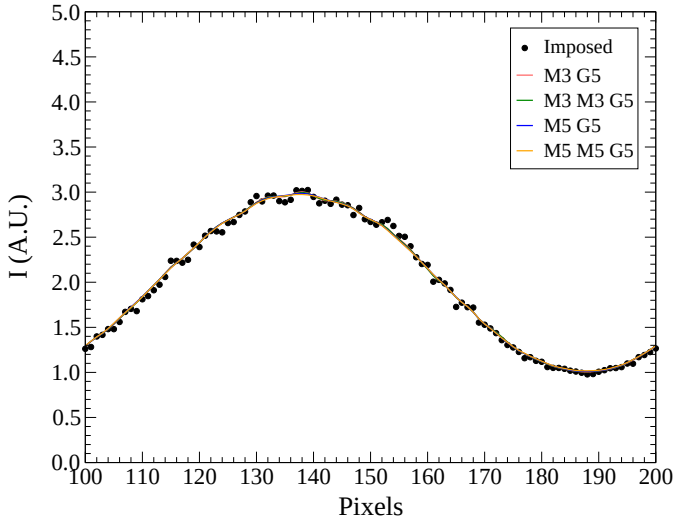

(a) Frequency = 0.01/pixel

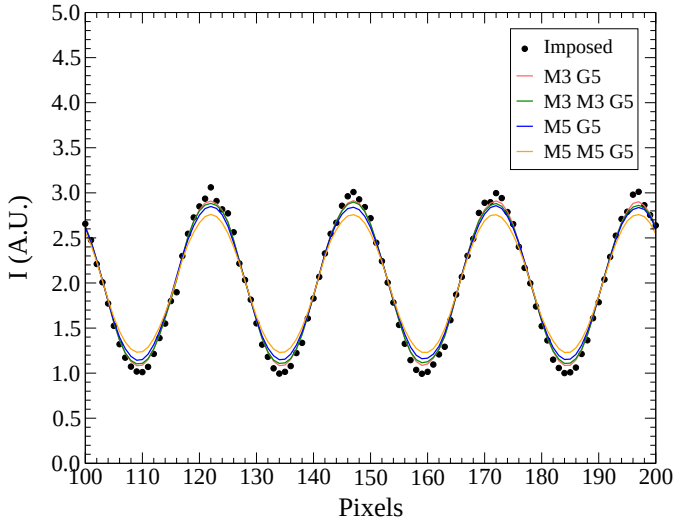

(b) Frequency = 0.04/pixel

Figure 5.29: Imposed and filtered profiles at different frequencies.

The mean amplitudes of synthetic and filtered images are calculated and their ratios versus the frequency are shown in Fig. 5.30. The limiting resolution at 10% of amplitude is deduced from this graph. The values of limiting resolution increases with filter size and number of filtrations as expected.

The fluctuations of equivalence ratio measurement for the homogeneous mixture conditions are shown in Fig. 5.31. The fluctuations are coming down with increase of filter size as well as number of filtering but the reduction is small compared to the drop in limiting resolution. So we have chosen $M3M3G5$ filtration scheme which removes random noises as shown in Fig. 5.29 with reasonable limiting resolution.

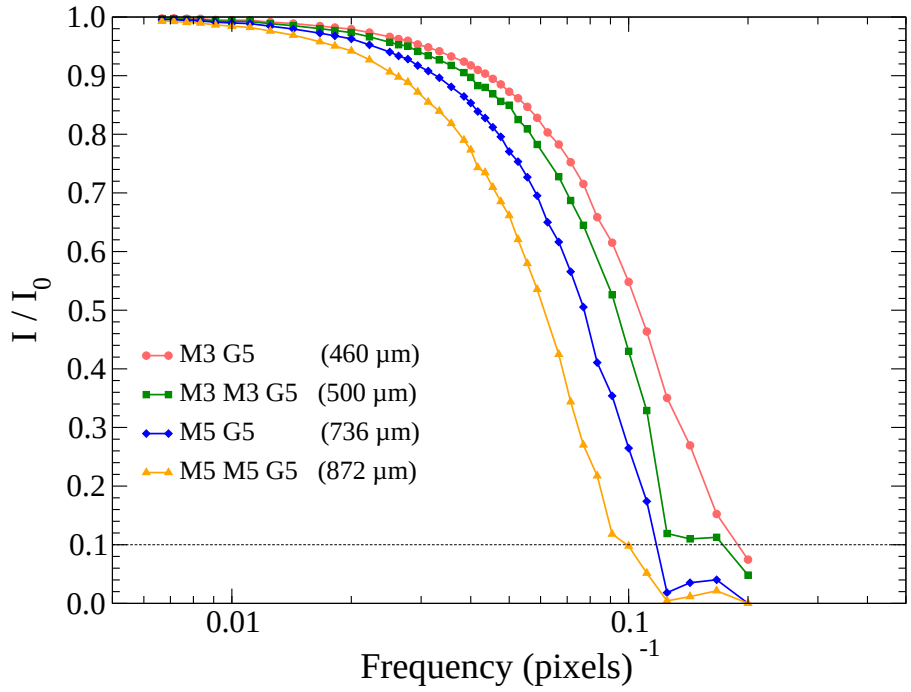

Figure 5.30: Spectra of filtered images.

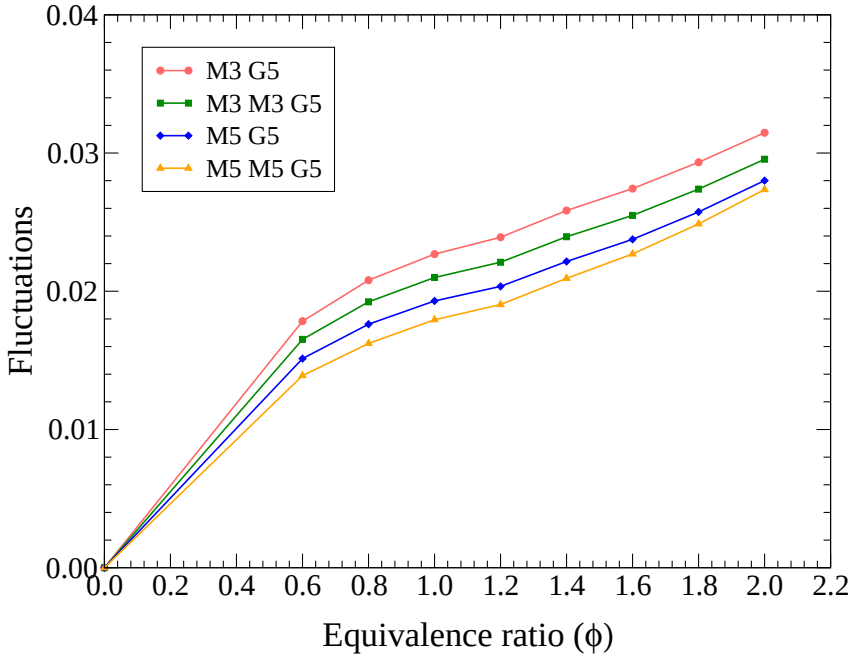

Figure 5.31: Fluctuations of equivalence ratio measurement.

Spatial resolution based on edge response:

The above method focused mainly on the optimization of numerical filter size by taking into account only the random noises of PLIF images. The cut-off frequency of the numerical filter could be smaller or higher than the cut-off frequency of optical collection system. So it could be interesting to measure the spatial resolution of collection system in order to compare them with that of numerical filter. Therefore, in this work, we have measured the spatial resolution of optical collection system from their edge response [Smith (1997)].

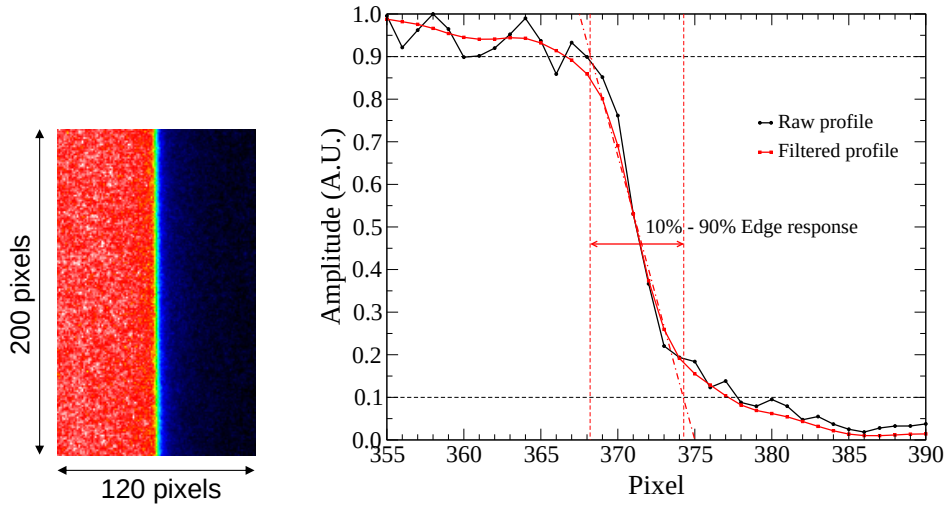

(a) Closer view of PLIF image

(b) Profile of edge

Figure 5.32: Edge response

In order to measure the spatial resolution, a sharp edge is placed in the path of laser sheet and that produced an edge in acquired PLIF image as shown in Fig. 5.32. Then local intensity values across the edge are measured from the PLIF image and one example of such a profile extracted from raw and filtered images are shown in Fig. 5.32. The $M3M3G5$ filtration scheme is used to filter the PLIF images. In the raw profile, we can clearly see the fluctuations in amplitude due to the random noises and diffusion of signal at lower amplitude range and those fluctuations are eliminated in filtered profile. To know the spatial resolution, we have to measure the distance required for the edge response to rise from 10% to 90%. But due to the local fluctuation in amplitude, it is not possible to measure the edge based on local values. So a linear fit is applied to the slope of edge and from that fitted line, the edge response is measured as shown in Fig. 5.32.

The edge response of both raw and filtered images are measured at different vertical positions and then their mean and standard deviation are calculated, which are given in Fig. 5.33. The limiting resolution of raw and filtered images are around $409\ \mu m$ and $444\ \mu m$, respectively. That means the limiting resolution of optical collection system is around $410\ \mu m$. The small difference in resolution between raw and filtered images indicates that the effect of numerical filtration on edge response is small, but the precision of measurement is improved by the filtration scheme. So the spatial resolution of equivalence ratio measurement which included both optical system as well as numerical filtration process is $444\ \mu m$ for an investigation area of $45 \times 45\ mm^2$ with an uncertainty of $\pm 2\%$ at $\phi = 1.0$.

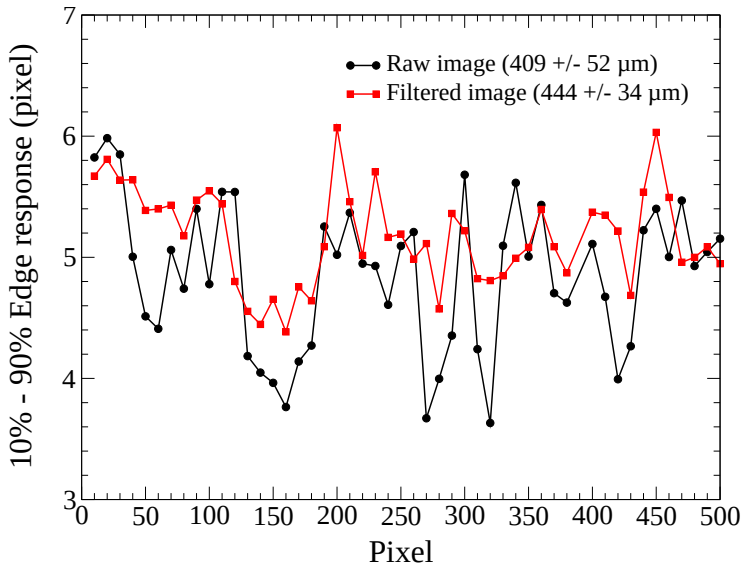

Figure 5.33: Variation of edge response along the length of PLIF image.

5.10 Summary and conclusions

Fluorescent tracer	$Anisole$
Laser excitation wavelength	$266\ nm$
Image size (pixel)	512×512
Linearity range	$\phi = 0.6\ to\ 2.0$
Uncertainty ($\pm\ \sigma$)	$\pm\ 2\ \%\ @\ \phi = 1.0$
Spatial resolution	$444\ \mu m$

Table 5.3: Parameters of LIF technique for equivalence ratio measurement.

Laser induced fluorescence is a highly useful technique for the quantitative measurement of equivalence ratio of non-reactive and reactive mixture conditions. The basic principle of LIF is reviewed in this section. The need of tracer for the equivalence ratio measurement and the important criteria of tracer selection are discussed. The experimental setup of LIF measurements are discussed with great detail. The procedure for the calibration of fluorescence signal, inhomogeneity of LIF images and possible sources of error are explained. A novel image error correction technique has been developed in this work based on the instantaneous profiles. The various stages of post-processing of new technique and the improvements achieved in each steps are explained with examples. Finally, the spatial resolution of LIF measurement using synthetic images is described. The relationship between precision and spatial resolution of measurements with filtration process are explained. The experimental setup of LIF technique used in this work allows us to measure the equivalence ratio with an uncertainty of $\pm 2\%$ at $\phi = 1.0$ with spatial resolution of $444\ \mu m$.

Chapter 6

PIV/PLIF system

Abstract. *In this work, simultaneous measurements of velocity and equivalence ratio are performed by using PIV/PLIF techniques. For that, both PIV and LIF laser beams are combined by optics. The fuel-air mixture is seeded with fluorescent tracer and oil particles in order to acquire fluorescent signal from tracer and Mie scattering signal from particles. The emitted signals are separated by beam splitter and acquired by CCD and ICCD cameras. Laser units and cameras are operated by a dedicated synchronization unit. Optical filters are utilized to eliminate the interference between PIV and LIF measurements. This chapter explains the experimental setup, synchronization of optical techniques, interference between the two techniques and elimination of them.*

6.1 Introduction

The main objective of this experimental work is to understand the stratified combustion phenomena at the fundamental level and to provide some valuable data for the development and validation of numerical simulations. The characteristic of stratified combustion depends strongly on the flow-chemistry interactions and simultaneous measurements of flow and scalar field is very much essential for the better understanding of this complex combustion process [Frank et al. (1996), Barlow (2007)]. Simultaneous PIV/PLIF measurement techniques are gaining popularities due to their compatibility and the usefulness of data generated by the combined measurements [Pasquier et al. (2007)]. So in this work, both techniques are utilized to measure velocity and equivalence ratio fields. In this chapter, we are going to discuss about the way of combining two measurement techniques, interferences between them and elimination of interferences.

6.2 Experimental setup

The principles of PIV and PLIF techniques, their experimental arrangements and their subsystems are discussed already in the previous chapters. Those two systems are combined in this work in order to perform simultaneous velocity and equivalence ratio measurements. The combined experimental configuration is shown in Fig. 6.1. In that configuration, two separate lasers are used. PIV measurements are carried out by using the second harmonic of a double-cavity Nd:YAG

laser (Quantel TwinsUltra) and PLIF measurements are carried out by using the fourth harmonic of a Nd:YAG laser (Quantaray Spectra-Physics). The two laser beams are optically combined by a Dichroic mirror ($T = 0.99$ @ $532\ nm$, $R = 0.95$ @ $266\ nm$) and the overlapped laser sheets are formed by the combination of spherical ($f = 1m$) and cylindrical lenses ($f = -25mm, f = +100mm$). Typical thickness of PIV and LIF laser sheets at the entrance of combustion chamber are $800\ \mu m$ and $400\ \mu m$ respectively. A mechanical shutter is placed in the optical path which helps to prevent continuous illumination of chamber in order to avoid damaging the structure of anisole as previously observed by Pasquier-Guilbert (2004) and allows the laser beam only at the time of acquisition.

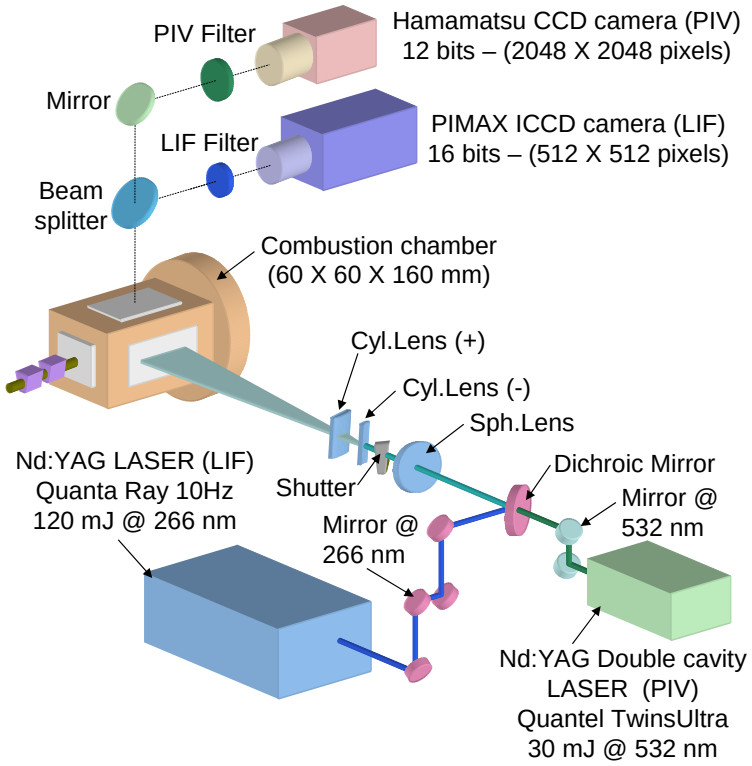

Figure 6.1: Experimental configuration for simultaneous PIV/PLIF measurements.

The fuel is seeded with anisole vapor proportional to the fuel flow rate and air is seeded with olive oil particles. The emitted fluorescence signal in the UV range and Mie scattering signal in the visible range are collected at right angles to the laser sheet. Fluorescence signal is separated from Mie scattering signal by a high pass Dichroic sheet which is transparent to the Mie scattering signal reflects the fluorescence signal towards ICCD camera. Fluorescence signal is filtered by a long pass filter and the filtered signal (spectral range 275-350 nm) is collected by an ICCD camera with a gate width of $2\ ns$. Mie scattering signal is reflected towards CCD camera by a mirror. An interferential pass-band filter ($532 \pm 5\ nm$) in front of CCD camera rejects the flame chemiluminescence from Mie scattering signal and the filtered signal in the visible range is acquired by a CCD camera.

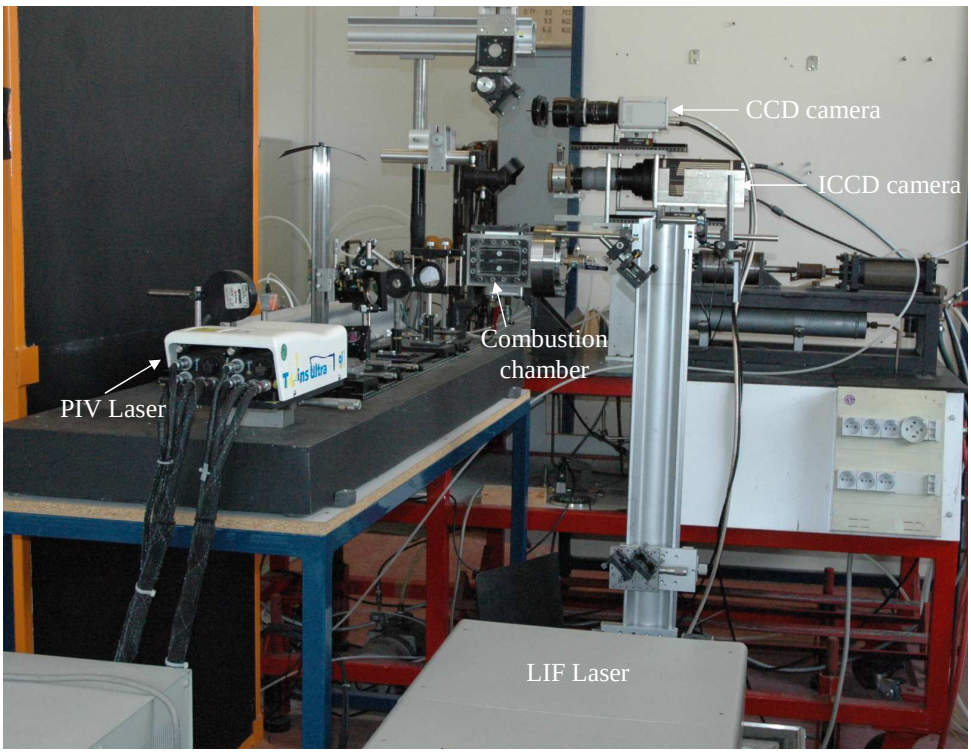

Figure 6.2: Photograph of experimental configuration.

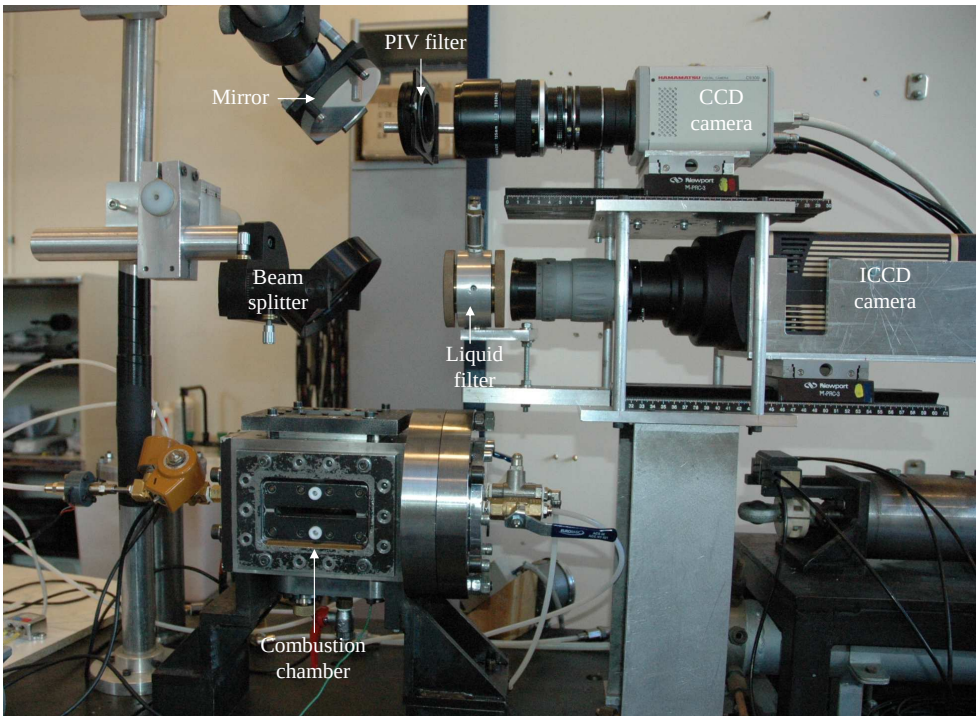

Figure 6.3: Photograph of image acquisition units.

6.3 Synchronization

In our turbulent stratified combustion studies, the flow events are unsteady and non repeatable. But the LIF laser needs to be operated with fixed frequency. So the main objective of synchronization unit is to combine the unsteady flow or combustion events with laser diagnostics. Figure 6.4 shows the timings of various elements of PIV/PLIF systems. In that diagram, the initiating signal based on the unsteady flow event is represented by a trigger signal and all the timings are synchronized with this trigger signal. The PIV system requires five input signals, two for the flash lamps, two for Q switches and one for CCD camera. The LIF system requires three input signals, one for the flash lamp, one for Q switch and one for ICCD camera.

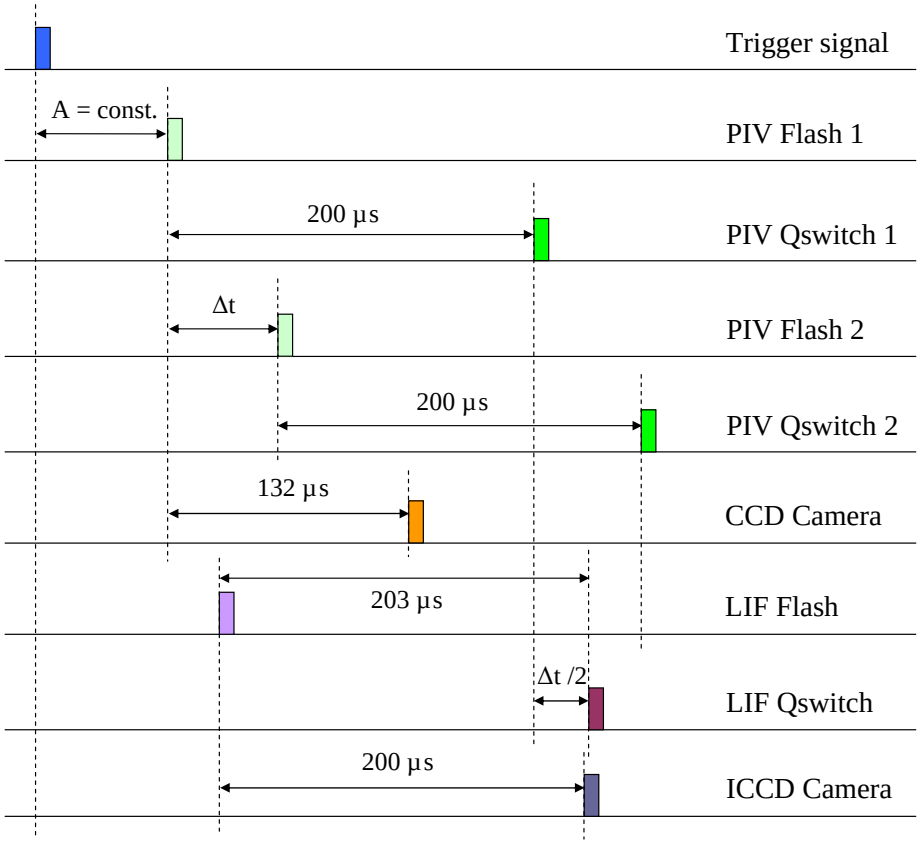

Figure 6.4: Synchronization of PIV with PLIF systems.

For the velocity measurement, we have to acquire two images with a time delay Δt between them. In order to perform simultaneous PIV/PLIF measurement, the PLIF image is taken at time $\Delta t/2$ from the first PIV image. In the case of PIV laser, the optimum time delay between flash lamp and Q switch is $200\ \mu s$. For LIF laser, the optimum time delay is $203\ \mu s$ between flash and Q switch. Both PIV and LIF laser are operated at fixed frequency of $10\ Hz$. The CCD camera is operated in dual mode and the acquisition event is initiated after $132\ \mu s$ from first flash of PIV. The ICCD camera needs an advance Q switch pulse which is delivered after $200\ \mu s$ from LIF flash timing. So the only variable is time delay Δt which will be optimized based on the average flow velocity and the magnification factor of image.

6.4 Image calibration

The CCD camera captures two images with known time delay between them and the ICCD camera captures one fluorescence image in between the two PIV images. One example of CCD and ICCD images are shown in Fig. 6.5.

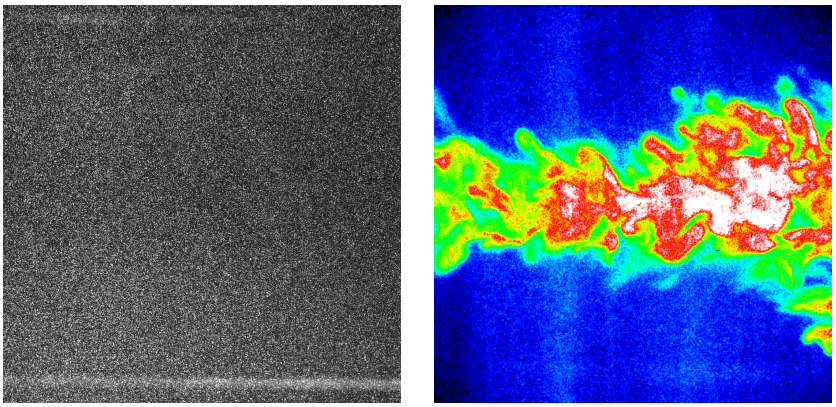

(a) CCD image. (b) ICCD image.

Figure 6.5: Sample CCD and ICCD images.

In order to convert the flow and scalar field results from pixel dimensions to millimeter dimensions, the captured images need to be calibrated with reference scale images (shown in Fig. 6.6). These reference images are obtained by placing a reference scale exactly in the same plane of laser sheet. In the reference scale, some symbols are marked and the position of those symbols in CCD and ICCD images are matched for the combined PIV/PLIF measurements. From the acquired images, conversion factors are calculated by applying linear fit to the counted pixels between the lines as a function of distances between the lines. Finally the measurements are transformed to the millimeter dimensions by using those conversion factors.

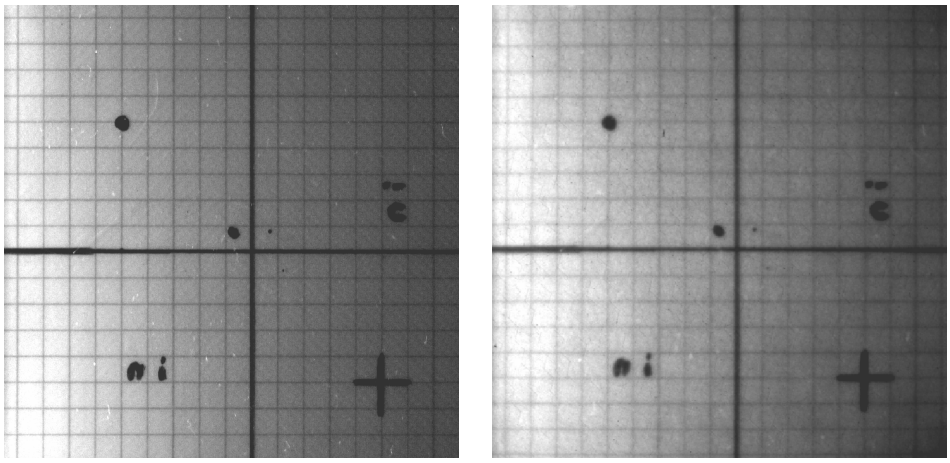

(a) CCD image. (b) ICCD image.

Figure 6.6: CCD and ICCD images of reference scale.

6.5 Interference between PIV and LIF measurements

As explained earlier, the fuel-air mixture is seeded with anisole vapor and olive oil particles for the simultaneous measurements. But this could introduce some interferences between the two measurement techniques.

Interference of LIF tracer on PIV measurements:

As already explained the emitted fluorescence signal is reflected by beam splitter and only Mie scattering signal in the visible range is passing through it and captured by CCD camera. Also, the wavelength range of emission of anisole vapor is around $270 - 350\ nm$, which is below than visible range so the interference of anisole vapor on PIV signal could be insignificant. In order to confirm this point, we have measured the level of Mie scattering signal for different equivalence ratios. But there has been no appreciable difference in the signal with increase of anisole tracer which means there is no perturbation of LIF tracer on PIV measurements.

Interference of PIV seeding on LIF measurements:

Next, the perturbation of micro-metric olive oil particles on the LIF signals is carried out by comparing the background and reference images with and without seeding particles. The perturbation of seeding particles on fluorescence signal level is clearly observed (shown in Fig. 6.7). There is a rise in fluorescence level with seeding particles and the level of increase is not uniform

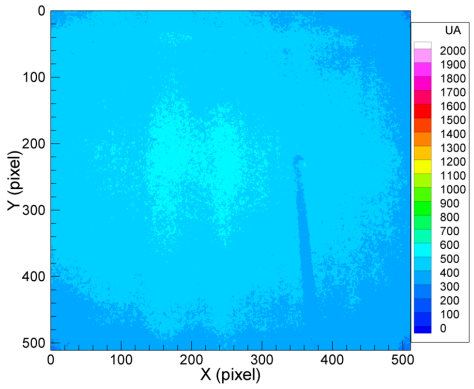

(a) Background image without PIV seeding.

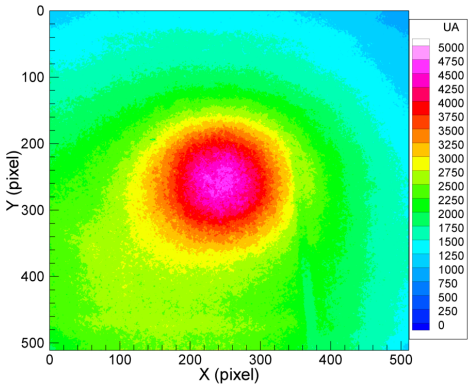

(b) Background image with PIV seeding.

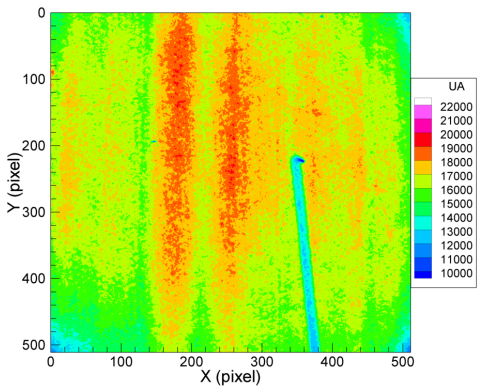

(c) Reference image without PIV seeding.

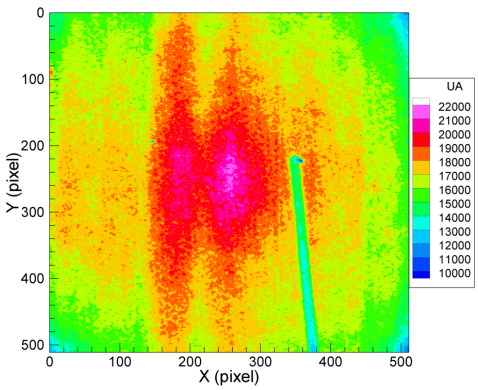

(d) Reference image with PIV seeding.

Figure 6.7: Interference of PIV seeding on LIF images.

throughout the image. The augmentation of signal in the center of image could be related to the optical collection system. The commercial filter placed inside the UV objective is not able to filter those signals. But for the unbiased measurements, the perturbation of seeding particles must be eliminated from LIF images.

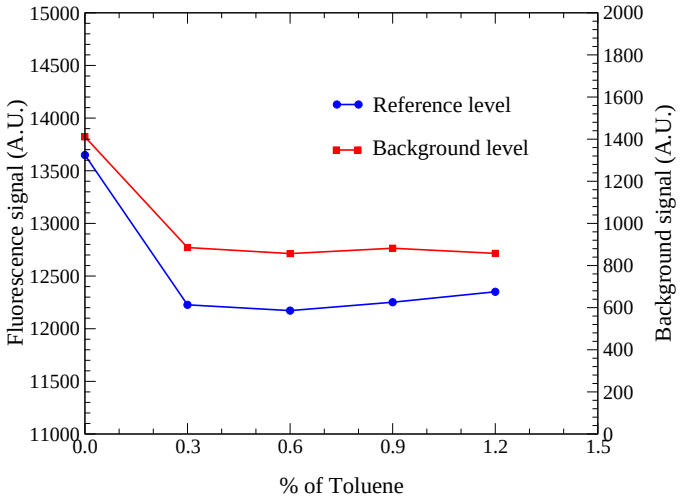

Figure 6.8: Fluorescence signal level as a function of percentage of Toluene in the liquid filter.

The residual signals from olive oil particles can be filtered out by using a liquid filter filled with toluene. In our work, the liquid filter is filled with mixture of iso-octane and toluene. The liquid filter is placed in between the dichroic sheet and ICCD objective [Pasquier-Guilbert (2004)]. Toluene is very effective in absorbing the residual signals. However, the higher concentration of toluene may decrease the fluorescence signal. So we optimized the concentration by measuring the fluorescence signal level with different toluene percentage as shown in Fig. 6.8. The variation of signal level for more than 0.6% of toluene becomes constant. So the optimum toluene concentration is taken as 0.6 % of total mixture of iso-octane and toluene.

The improvement in the equivalence ratio measurement due to the introduction of liquid filter in the PLIF system is shown in Fig. 6.9. The augmentation of signal in the center of image is eliminated and the equivalence ratio of mixtures are uniform throughout the image.

Technique	**PIV**	**PLIF**
Seeder / Tracer	$Olive\ oil$	$Anisole$
Laser excitation wavelength	$532\ nm$	$266\ nm$
Laser sheet thickness	$800\ \mu m$	$400\ \mu m$
Camera	$CCD\ (12\ bits)$	$ICCD\ (16\ bits)$
Image size (pixel)	2048×2048	512×512
Image size (mm)	45×45	45×45
Uncertainty ($\pm\ \sigma$)	$\pm\ 0.04\ m/s$	$\pm\ 2\ \%\ @\ \phi = 1.0$
Spatial resolution	$160\ \mu m$	$444\ \mu m$

Table 6.1: Important parameters of simultaneous PIV/PLIF measurement techniques.

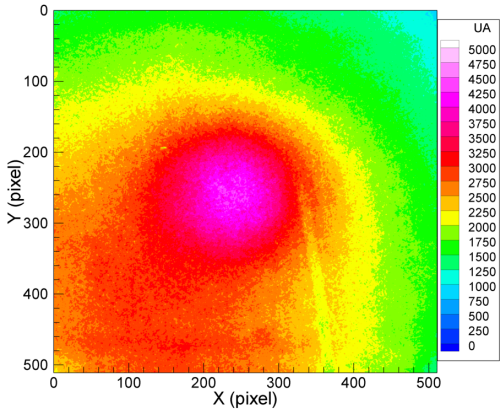

(a) Background image without liquid filter.

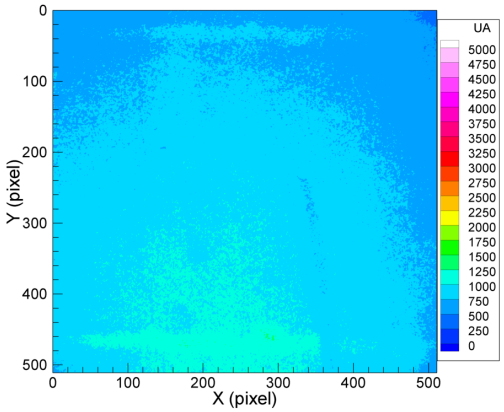

(b) Background image with liquid filter.

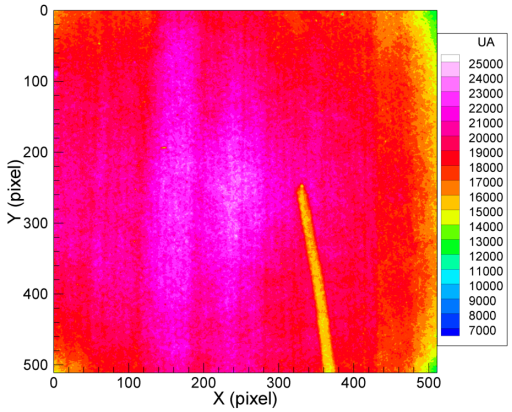

(c) Reference image without liquid filter.

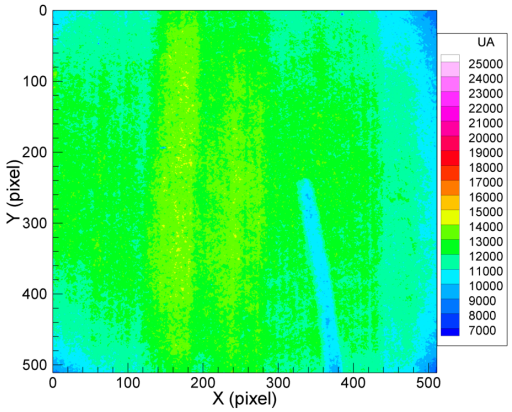

(d) Reference image with liquid filter.

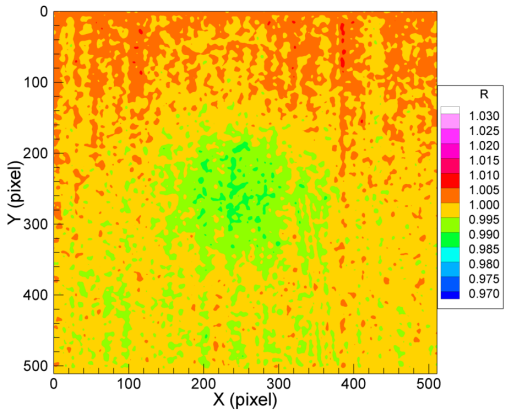

(e) Corrected image without liquid filter.

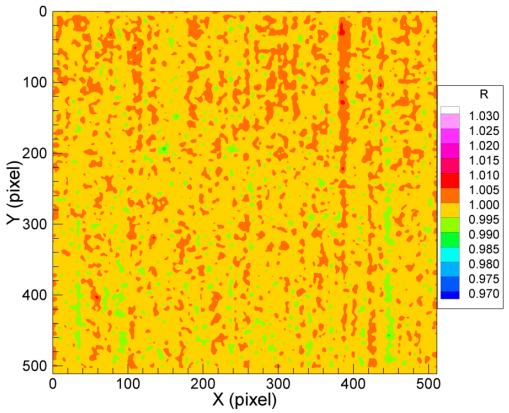

(f) Corrected image with liquid filter.

Figure 6.9: Effect of liquid filter on LIF signal.

Few important parameters are listed in the table 6.1. The combined PIV/PLIF techniques can measure simultaneous velocity and equivalence ratio field with an investigation area of $45 \times 45\ mm^2$. The velocity field can be measured with an uncertainty of $\pm 0.04\ m/s$ and equivalence ratio field can be measured with an uncertainty of $\pm\ 2\ \%\ @\ \phi = 1.0$. The spatial resolution of velocity measurement is $160\ \mu m$ whereas the spatial resolution of equivalence ratio measurement is $444\ \mu m$ which is around 2.78 times that of velocity measurements.

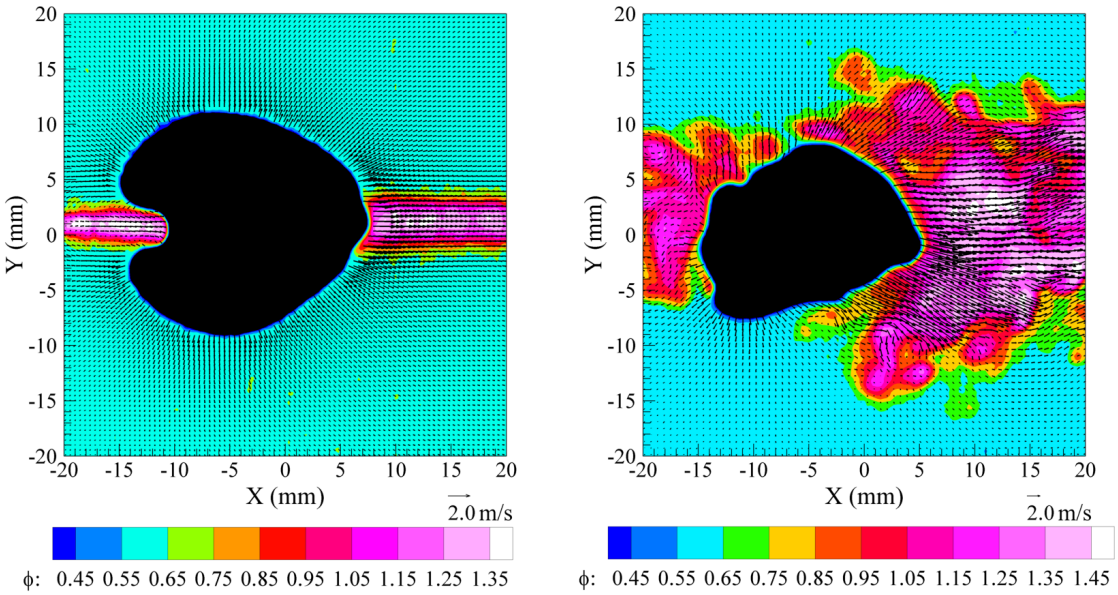

(a) Laminar stratified flame propagation.

(b) Turbulent stratified flame propagation.

Figure 6.10: Combined velocity and equivalence ratio field of flame propagation.

Examples of combined velocity and equivalence ratio fields of flame propagation are shown in Fig. 6.10. They clearly show the superposition of velocity field with equivalence ratio field in both laminar and turbulent flow conditions. So by the application of simultaneous PIV/PLIF measurement, we can able to measure combined local velocity and local equivalence ratio around the flame fronts for the investigation of stratified combustion.

6.6 Summary and conclusions

This chapter has explained the way of combining PIV/PLIF techniques in order to measure simultaneous velocity and equivalence ratio field. The synchronization of various units such as lasers, CCD and ICCD cameras with flow or combustion events are established. The perturbations between the two techniques due to their usage of particle seeding and fluorescent tracer are verified. We found no problem for PIV measurement but a strong perturbation for LIF measurement. We eliminated the perturbation of seeding particles by using a liquid filter. In conclusion, the simultaneous measurement of PIV/PLIF is successfully established for the stratified combustion studies.

Part II

Stratified Combustion

Chapter 7

Turbulent stratified mixture preparation

Abstract. *The velocity and equivalence ratio field of unsteady turbulent stratified jet injected into a constant volume chamber are measured by using simultaneous PIV/PLIF techniques. To create stratification of equivalence ratio, the combustion chamber is initially filled with lean propane-air mixture, and then a rich mixture is injected into the chamber in a controllable way. The evolution of turbulent stratified jet is analyzed in order to find the optimum location and time to ignite the mixture for the investigation of flame propagation through stratified mixture field. This chapter explains the injection unit to create turbulent stratified jet, synchronization of flow event with laser diagnostics and analyses of turbulent stratified mixture field.*

7.1 Introduction

The turbulent flame propagation through stratified mixture field is an important research area for both fundamental science of combustion and practical applications like direct injection spark ignition (DISI) engines. In DISI engines, stratified mode of operation yields high fuel efficiency and low emissions [Zhao et al. (1999)]. The improvement is attributed to the enhancement of flame propagation through stratified mixture. However, stratified flames are not well understood at a fundamental level, and there is a need for more complete experimental data sets on well-defined stratified flames that may be compared with numerical modeling and used to test the validity of modeling approaches.

The aim of the present work is to perform the measurements of unsteady flame propagation through stratified mixture field and to compare them with equivalent homogeneous cases. This chapter explains the way of achieving the stratified mixture field by using axi-symmetrical injection setup. Simultaneous PIV/PLIF techniques are utilized to measure velocity and equivalence ratio field of stratified mixture formation inside a constant volume combustion chamber. The experimental setup, axi-symmetrical injection unit and synchronization between injection unit and PIV/PLIF systems are given. Finally, mean values and fluctuations of velocity and equivalence ratio of stratified mixture at the position and time of ignition are given.

7.2 Experimental set-up

The stratified flame propagation is investigated in a constant volume combustion chamber (Fig. 7.1). The combustion chamber was designed and built by the LCD laboratory Poitiers in 1986 as a part of ARC (Action de Recherche Concertée). It is a rectangular chamber with a dimension of $60 \times 60 \times 160\ mm^3$, which is equipped with three quartz windows especially suitable for the UV range of laser diagnostics. It has a pressure sensor for dynamic pressure measurement and it can withstand maximum pressure of 20 bars. At the center of combustion chamber, two thin electrodes of diameter $300\ \mu m$ are placed to ignite the mixture.

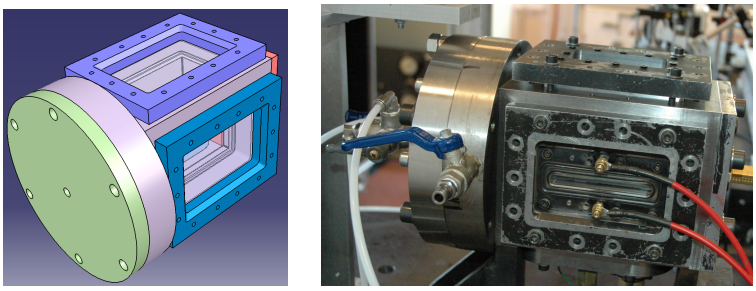

Figure 7.1: Constant volume combustion chamber.

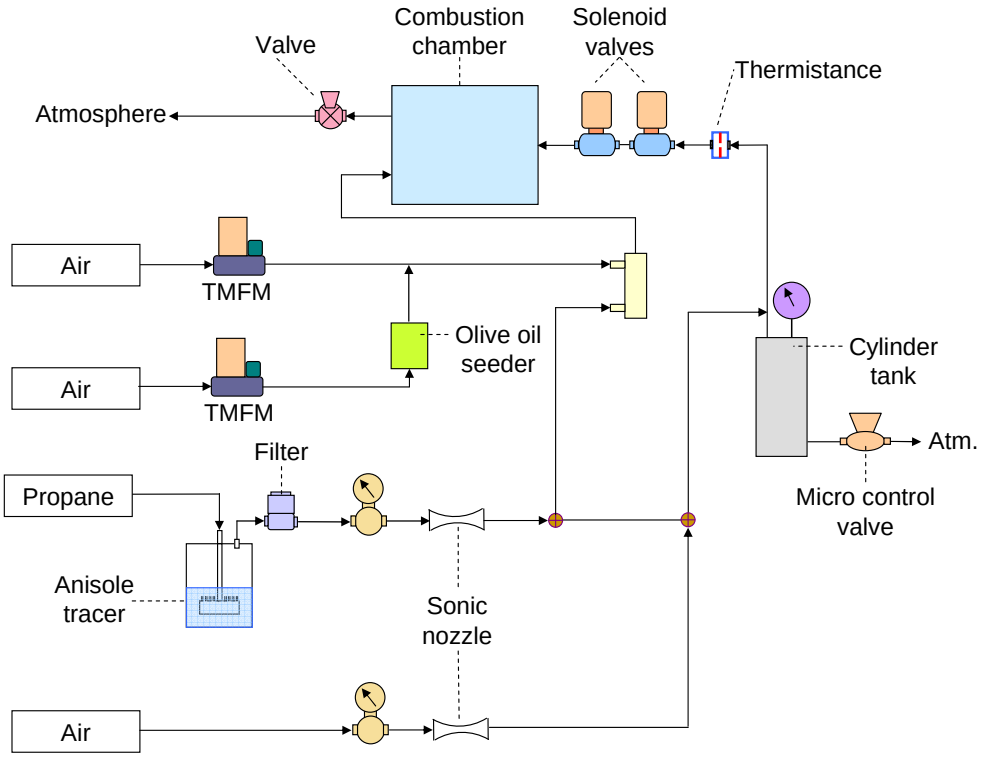

Figure 7.2: Schematic diagram of the flow set-up.

The schematic representation of flow setup is shown in Fig. 7.2. It consists of flow circuits of propane-air mixture and an injection unit. The flow rate of propane is regulated by the upstream pressure of sonic nozzle. The fluorescence tracer (anisole) is added to the propane flow proportional to its flow rate by a bubbler system. The flow rate of air is measured and regulated with less than 0.5% of error by thermal mass flow controllers (Bronkhorst EL-Flow series). Olive oil particles are generated by a seeder unit and added to the air flow. A secondary air circuit is used for the stratified mixture preparation and its flow rate is controlled by a sonic nozzle.

The procedure followed to create the turbulent stratified mixture field consists of two steps. First, the combustion chamber is filled with lean homogeneous mixture ($\phi = 0.6$) at atmospheric pressure. Next, inlet and outlet valves are closed and a rich mixture is injected into the chamber to produce stratification. More details of the injection setup are given in the next section.

7.3 Axi-symmetric injection

The main objective of axi-symmetrical injection unit is to realize turbulent stratified mixture field inside the chamber with following conditions at the location and time of ignition:

- Mean equivalence ratio at the point of ignition: $\phi = 1.1\ to\ 1.2$.
- Mean velocity at the point of ignition: $1.0\ to\ 1.2\ m/s$

Those above parameters are selected to be close to the conditions used in the experimental studies of Pasquier-Guilbert (2004), who investigated the stratified flame propagation on this same combustion chamber with stoichiometric condition at the location of ignition, but in this work we planned to investigate with slightly rich mixture at the ignition point.

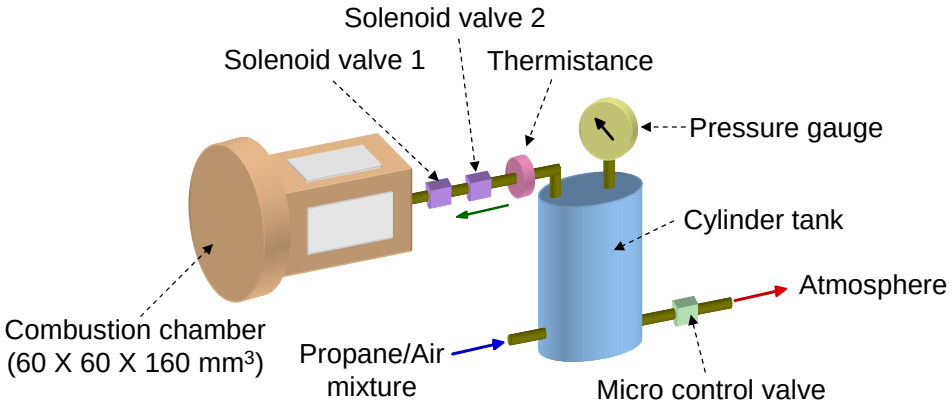

Figure 7.3: Axisymmetric injection set-up.

Injection setup:

The schematic diagram of axi-symmetrical injection unit is shown in Fig. 7.3. It comprises of two solenoid valves (Lucifer-Direct operated E133 K04), thermistance, cylinder tank and a micro control valve. In this configuration, cylinder tank is used to keep the pressure of rich mixture constant during the injection period. The tank pressure is measured by using piezoelectric pressure transducer (Keller series $33S$) and maintained by controlling the flow rate of rich mixture to atmosphere through micro-control valve. The solenoid valves are fixed to the side block of combustion

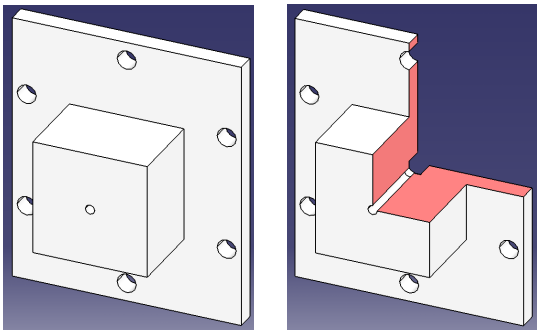

(a) Side block. (b) Cut section.

Figure 7.4: Cut section of side block of combustion chamber.

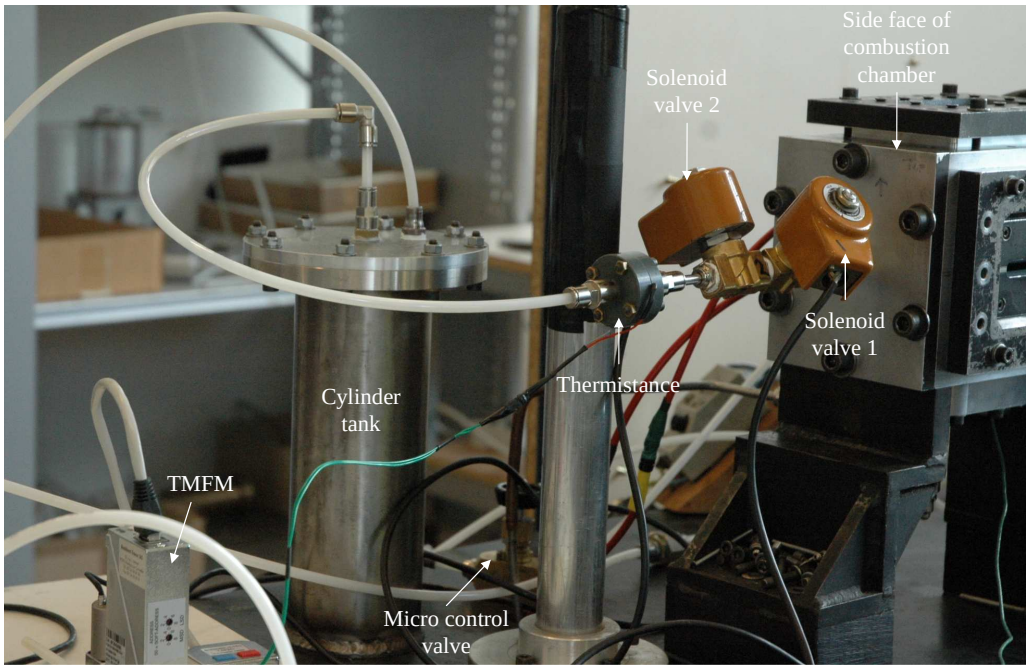

Figure 7.5: Photograph of axisymmetric injection set-up.

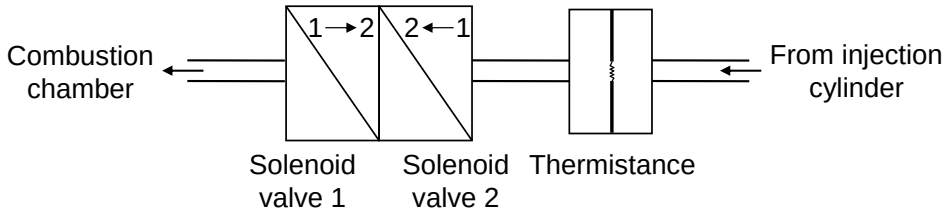

Figure 7.6: Flow direction of solenoid valves and thermistance.

chamber and thermistance unit is fixed in between second solenoid valve and cylinder tank for accurate synchronization of the injection event with acquisition events. The side block is having a straight circular hole at its center with diameter of $5\ mm$ and length of $60\ mm$ as shown in Fig. 7.4. This constant diameter circular hole helps to realize axi-symmetrical injection. The photograph of axisymmetric injection setup is shown in Fig. 7.5. The inlet and outlet direction of two solenoid valves with respect to the chamber is shown in Fig. 7.6. The solenoid valve close to the combustion chamber is fixed in the opposite way to the other solenoid valve in order to protect the solenoid valves from combustion pressure and to prevent the combustion waves entering into the cylinder tank.

Stratified jet:

The start and duration of injection are controlled by valve timings of two solenoid valves. The solenoid valves used in our configuration takes around 10 to $20\ ms$ to open completely, so we kept the opening of first valve around $96\ ms$. The duration and time of opening of second valve determines the velocity of turbulent jet and quantity of mixture injected. The duration of opening command of second valve is set to $5\ ms$ in order to keep the injection very short. The start of opening of second valve is fixed to $91\ ms$ so that both valves will be in closed position before ignition. The valve timings are shown in Fig. 7.7. The axi-symmetrical injection starts with opening

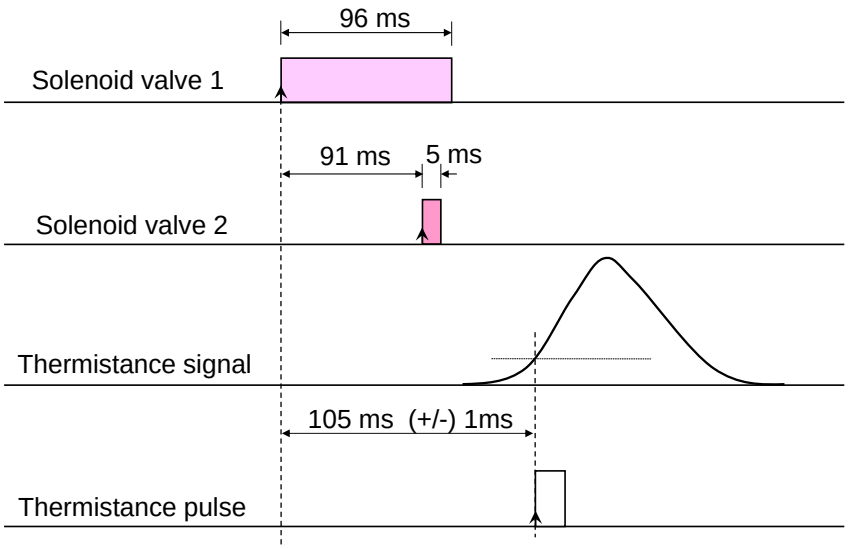

Figure 7.7: Solenoid valve timings and thermistance signal.

of second valve. The duration and time of opening of both solenoid valves are affected by the valve jitter effect. So it is not possible to know exactly the start of injection due to variation of valve timing which is around $\pm\ 1\ ms$. To solve this problem, a thermistance unit is utilized which consists of thermistance and electronic unit. After the start of injection, an electric signal is produced by thermistance based on hot wire principle and one example of such signal is shown in Fig. 7.7. This signal is processed by an electronic unit in order to generate a TTL pulse after the signal reaches the minimum threshold limit. The timing of TTL pulse is based on the thermistance signal which is related to flow characteristics and because of that we can find the exact timing of start of injection irrespective of variation of valve opening caused by the jitter effect. So this TTL pulse is

used to synchronize the injection event with ignition of mixture and laser diagnostics.

Controlling parameters:

The important parameters of axi-symmetrical injection that controls the characteristics of turbulent stratified mixture field are time of opening of second solenoid valve, duration of injection, pressure of injection and equivalence ratio of injection. Out of them, pressure of injection and equivalence ratio of injection need to be fixed to achieve the desired mixture conditions given in the start of this section. For that, the injection pressure is fixed to $150\ mbar$ above atmospheric pressure. Then, velocity of jet is measured at different timings from start of injection. After few trials, we found that $42\ ms$ after start of injection is the good timing to realize velocity field close to the ignition point initially located at the center of image zone shown in Fig. 7.8. We ignited the mixture at

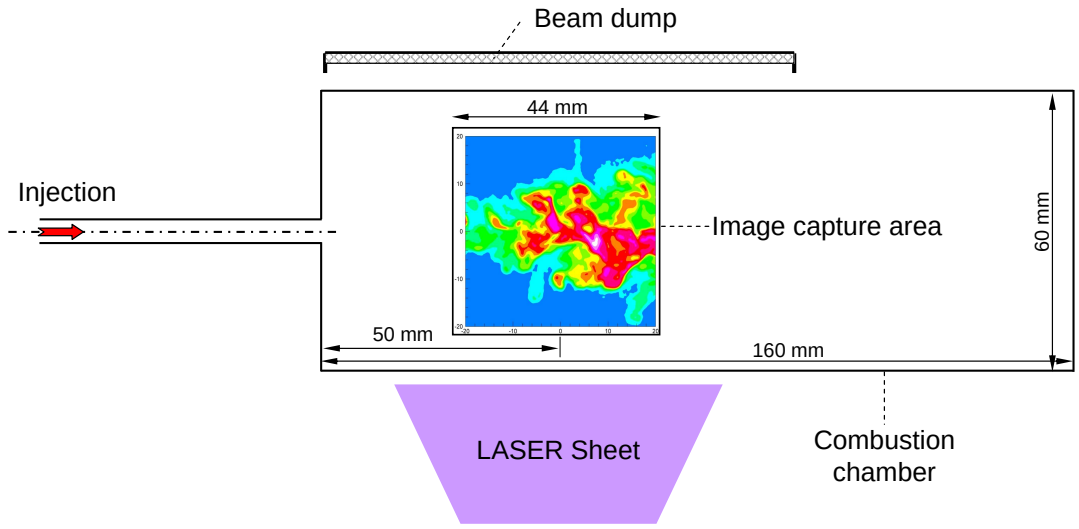

Figure 7.8: The dimensions of combustion chamber and the position of image capturing area.

that point and observed a global shift of flame front to the right side of image due to the velocity of jet. In order to compensate this shift and keep the flame front within image area, we decided to relocate the ignition point slightly on the left side with respect to the center of image. We tried different ignition positions and compared the flame front positions of the turbulent homogeneous combustion cases at different timings. Finally, we fixed the ignition location at $X = -8.5\ mm$, $Y = -0.5\ mm$ relative to the center of image which allow us to observe the flame propagation up to $5\ ms$ with a size of image area around $45 \times 45\ mm^2$. Next, we varied the equivalence ratio of rich mixture from $\phi = 6.0\ to\ 15.0$ in order to realize slightly rich condition at the ignition location and found that $\phi = 10.0$ is optimum to achieve the desired conditions at the time and location of ignition.

The optimized parameters of axisymmetrical injection are given in the table 7.1. In that, the quantity of injection is measured using soap bubble column. The global equivalence ratio of combustion chamber before injection is $\phi = 0.6$ and after injection is $\phi = 0.77$.

Injection pressure	$150\ mbar\ (g)$
Injector hole diameter	$5\ mm$
Injector hole length	$60\ mm$
Injection duration	$5\ ms$
Equivalence ratio of injection	$\phi_{inj} = 10.0$
Quantity of injection	$6.5\ cm^3$
Time of ignition	$42\ ms$

Table 7.1: Optimized injection and ignition parameters.

7.4 Synchronization

The axi-symmetrical injection of rich mixture into the combustion chamber is initiated by a TTL pulse to the first solenoid valve. Approximately $105 \pm 1\ ms$ after that, thermistance unit generates a TTL pulse representing the start of injection and this pulse is used to synchronize all other events. As already explained, LIF laser is a fixed frequency ($10\ Hz$) laser. We can synchronize the initiation of the first solenoid valve with the timing of LIF laser. But we cannot synchronize the timing of start of injection with LIF laser due to the valve jitter effect. The maximum uncertainty of injection timing is around $\pm 2\ ms$. So we need a system to synchronize the variable injection event with the LIF laser that can be operated with a small shift of $\pm 10\ \%$ of its operating frequency. This operating window can allow us to synchronize the laser with injection event.

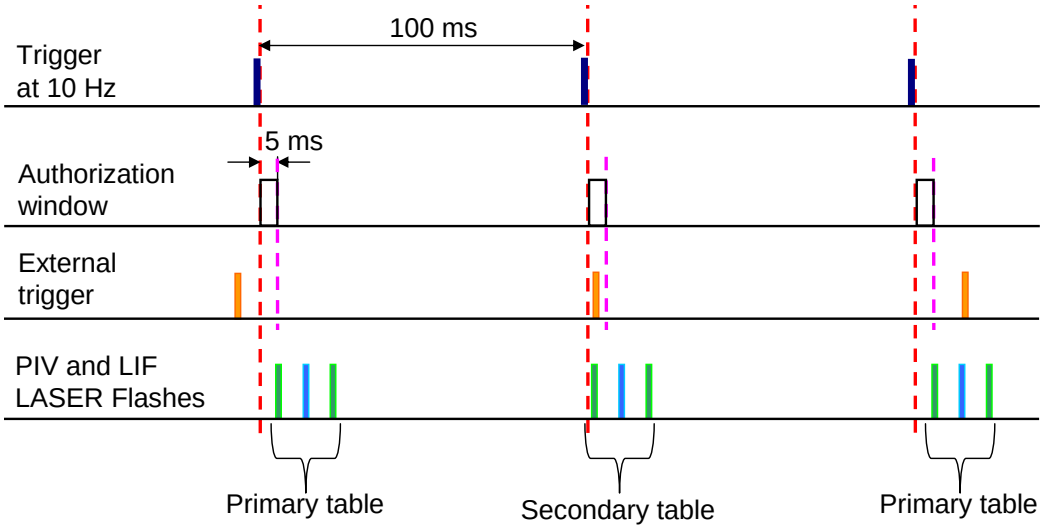

Figure 7.9: Normal and acquisition cycles.

An electronic control box with two different timings of operation has been utilized for this purpose. The principle of operation is to use two different tables, primary and secondary in that the events in the primary table are cyclic whereas the events in secondary table occur at only one time. In our case, the primary table controls the timings of PIV and LIF laser flashes and the secondary table controls laser flash timings and acquisition timings of CCD and ICCD cameras. The shifting of primary to secondary table needs an external trigger placed within authorization

window of $5\ ms$ as shown in Fig. 7.9. The normal cycle is operated at a fixed frequency of $10\ Hz$. The acquisition cycle starts when the external trigger is placed inside the authorization window that shifts the operation of control box to secondary table which immediately shifts the flash timings of PIV and LIF lasers and acquires two PIV images and one LIF image in between them. After $100\ ms$, the operation of control box shifted again to primary table.

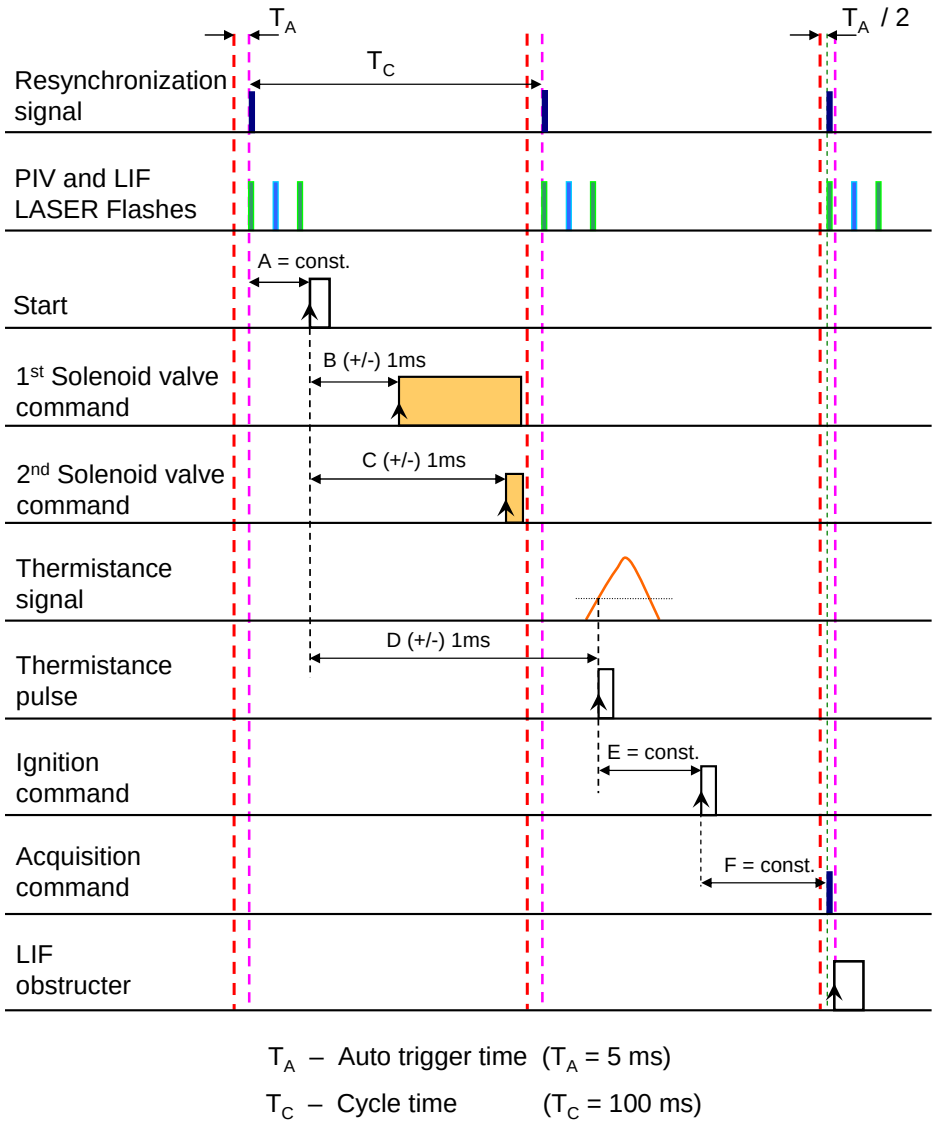

Figure 7.10: Synchronization timetable.

The synchronization of PIV with PLIF systems is discussed already in the previous chapter. In this section, the synchronization of injection event with PIV/PLIF systems is given. The various injection events with ignition and acquisition trigger is shown in Fig. 7.10. In that figure, B and C represent the first and second solenoid valve timings, D represents the start of injection, E represents the time of ignition ($42\ ms$) and F represents the acquisition time after ignition

$(1, 2, 3, 4, 5\ ms)$. The timing of A is adjusted to place the acquisition trigger within operating window. Examples of images acquired after $9\ ms$ from the start of injection are shown in Fig. 7.11. We are able to capture the flow event at the same location irrespective of valve jitter effect.

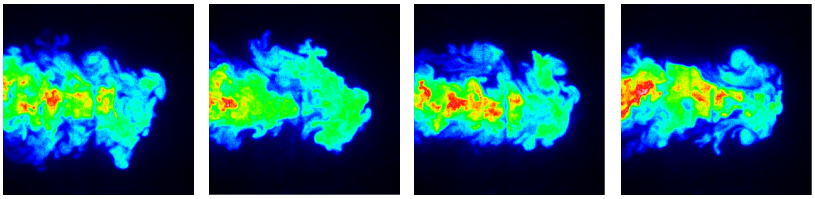

Figure 7.11: Symmetry and reproducibility of jet captured after 9 ms from start of injection.

7.5 Measurement of turbulent stratified flow condition

To define the initial condition of our unsteady injection, the time history of flow condition at the exit of the injector is needed additionally to the velocity and mixture field at the time of ignition. The velocity evolution during injection is an essential data, especially for numerical modeling for which the flow properties at ignition time is not sufficient to simulate the flame propagation. So in order to provide the time history of flow conditions at the exit of injector hole inside the combustion chamber, we have utilized the hot wire measurement technique.

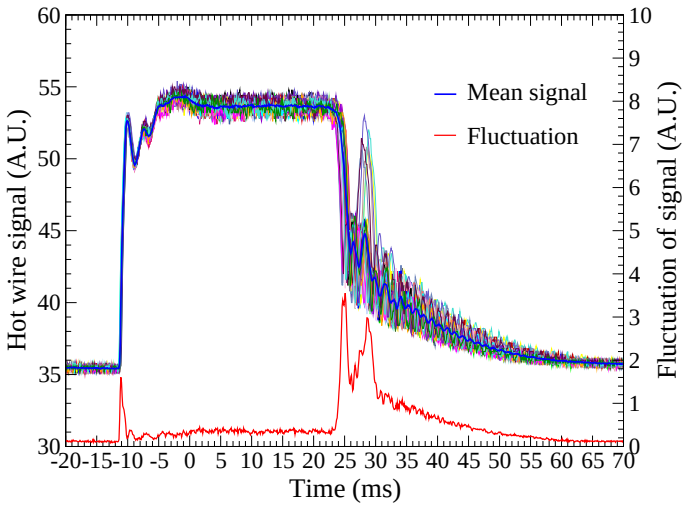

Figure 7.12: Hot wire signals of turbulent stratified jet at the entrance of combustion chamber.

Hot wire anemometry is the most common method used to measure instantaneous fluid velocity with high temporal resolution. This technique depends on the convective heat loss to the fluid from an electrically heated sensing element or probe placed in that fluid flow [Bruun (1995)]. In this work, a cylindrical sensor is placed at the exit of injector hole. Then, rich mixture is injected into the combustion chamber by the axi-symmetrical injection unit. The hot wire signal and thermistance signal are simultaneously acquired for each injection. We have collected signals of 50 cycles for the statistical analysis. After that, the hot wire signals are resynchronized based on

the thermistance signal which marks the start of injection and the mean and standard deviation of signals are measured which are shown in Fig. 7.12. It clearly shows a perfect synchronization of each cycle which confirms the accuracy of thermistance unit to predict the start of injection for each cycle. Due to the higher temporal resolution of hot wire sensor, we are able to measure the velocity of jet $12\ ms$ ahead of start of injection predicted by the thermistance unit. The hot wire signals show higher fluctuations at start of injection and almost constant flow velocity during middle of injection period and oscillations at the end of injection. The total duration of injection seems to be around $35\ ms$.

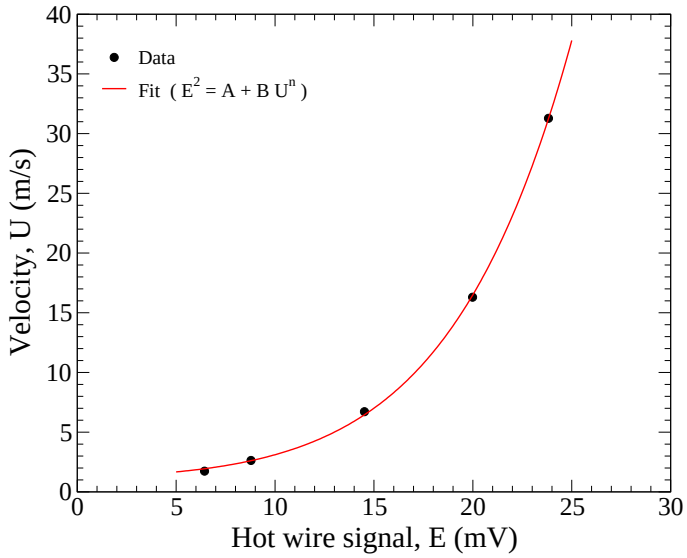

Figure 7.13: Calibration of hot wire signals.

In order to measure the flow velocity, the hot wire signal must be calibrated with known flow conditions under same fluid properties. In our case, we need to calibrate the sensor with rich propane-air mixture condition. For that, we have utilized the PIV measurement technique to measure the fluid velocity at the exit of injector hole, providing an in-situ calibration with the same mixture and pressure conditions. First, we measured the mean velocity of laminar jet at different flow conditions by using PIV technique and then we reproduced the same flow conditions and measured the hot wire signals from sensor placed at the exit of injector hole. At each flow condition, twenty cycles are performed for PIV and hot wire measurements and from that mean value of flow velocity and the corresponding mean value of hot wire signal are calculated. Then a non-linear fit is applied to them based on the relationship of modified King's law [Al-Garni (2007)]:

$$E^2 = A + BU^n \tag{7.1}$$

where A, B, n are constants, E is the hot wire signal and U is the flow velocity. The calibration curve is shown in Fig. 7.13. It clearly shows good agreement between the measurements and the non-linear fit applied to them.

Finally, the hot wire signals of turbulent stratified jet at the entrance of combustion chamber are calibrated which are shown in Fig. 7.14. The maximum velocity of jet reaches around $15\ m/s$ and the maximum fluctuation is around $3\ m/s$ occurs around the end of injection. The end of

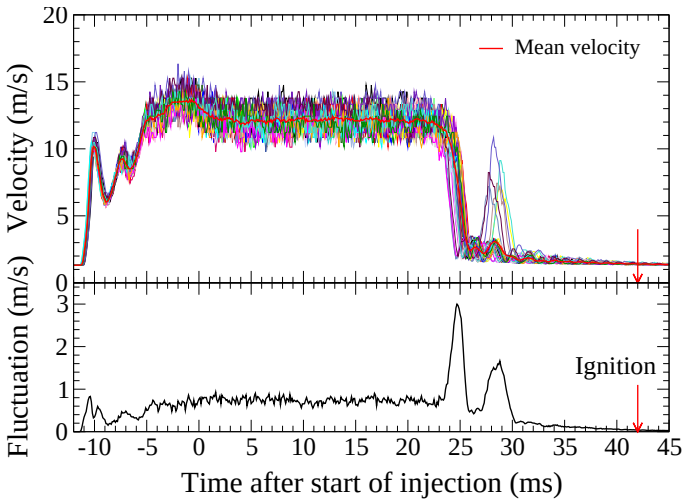

Figure 7.14: Variation of flow velocity of turbulent stratified jet at the entrance of combustion chamber as a function of time.

injection is around $25\ ms$ from start of injection with duration of injection around $35\ ms$. The next section focuses on the analysis of mixture field at the time of ignition.

7.6 Analysis of mixture field at the time of ignition

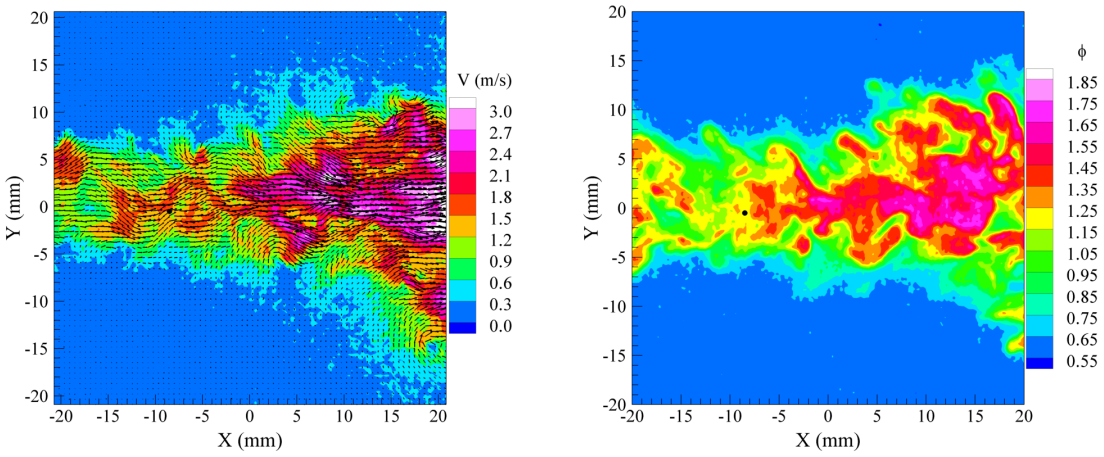

(a) Velocity field.

(b) Equivalence ratio field.

Figure 7.15: Instantaneous velocity and equivalence ratio field of turbulent stratified jet.

The combined velocity and equivalence ratio of turbulent stratified mixture field at the time of ignition ($42\ ms$ after start of injection) are measured from acquired PIV and PLIF images. The time delay between PIV image pair is fixed to $60\ \mu s$ after considering the range of velocities and the magnification of image. At this time delay, the spurious vectors are minimal (less than 1%) in the velocity vector field. One example of instantaneous and simultaneous velocity and equivalence ratio fields of axi-symmetrical jet is shown in Fig. 7.15. The ignition point is represented by a black

circle. Globally, the velocity field and the spread of mixture are symmetric with respect to the jet axis. We can also observe the similarity between flow structures and mixture distributions.

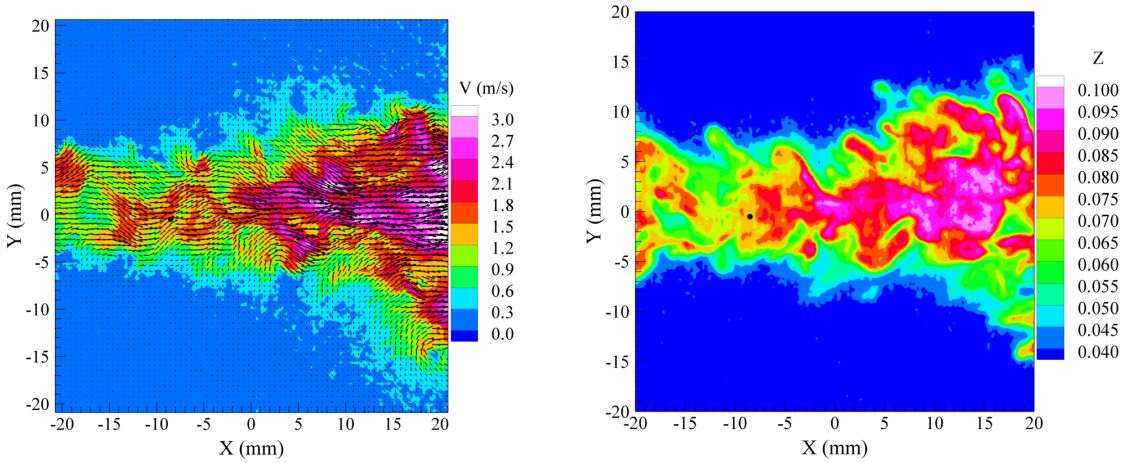

(a) Velocity field.

(b) Mixture fraction field.

Figure 7.16: Instantaneous velocity and mixture fraction field of turbulent stratified jet.

The mixture fraction Z can be expressed as a function of equivalence ratio ϕ [Peters (2000)]:

$$\phi = \frac{Z}{1-Z}\frac{1-Z_{st}}{Z_{st}} \tag{7.2}$$

where Z_{st} is the stoichiometric mixture fraction. This relationship can be further simplified as:

$$Z = \frac{\phi}{\phi + s} \tag{7.3}$$

where s is the mass stoichiometric coefficient ($s = 15.57$ for propane/air). The instantaneous mixture fraction field calculated from the equivalence ratio field is shown in Fig. 7.16.

7.6.1 Mean flow and scalar field

In order to determine minimum number of images required for good statistical analysis, the mean values and fluctuations of velocity at the center of mixture field is measured from one hundred cycles. Figure 7.17 shows the convergence of mean and fluctuations of velocity around ninety images. So, one hundred cycles are performed for the calculation of mean flow and scalar field of turbulent stratified mixture field.

The mean velocity vector field and mean scalar field of stratified mixture calculated from one hundred cycles are shown in Fig. 7.18. The center of jet is slightly shifted from the center of the image due to the small misalignment of injection hole in the side block of the combustion chamber. The mean velocity is around $1.2\ m/s$, the mean equivalence ratio is around $\phi = 1.1$ and the mean mixture fraction is around 0.07 at the point of ignition.

The transverse profiles of mean scalar field at the time of ignition are shown in Fig. 7.19. The profiles are almost symmetric and their variation with distance shows that the instance of ignition is very close to the tail of rich mixture jet. The width (FWHM) of profiles increases from $10\ mm$ in

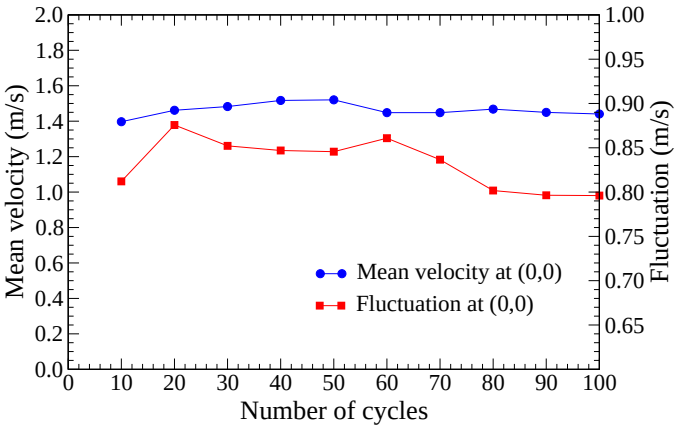

Figure 7.17: Determination of number of cycles.

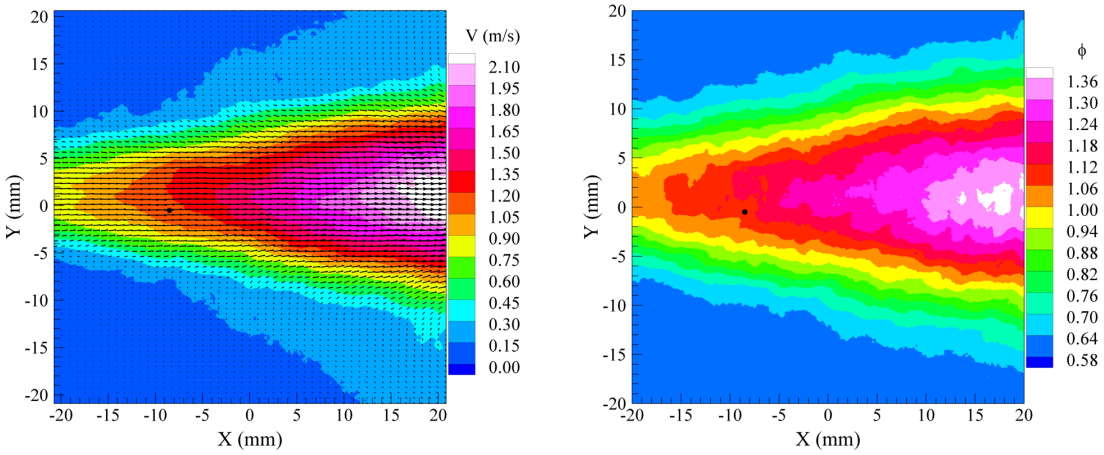

(a) Mean velocity vector field.

(b) Mean scalar field.

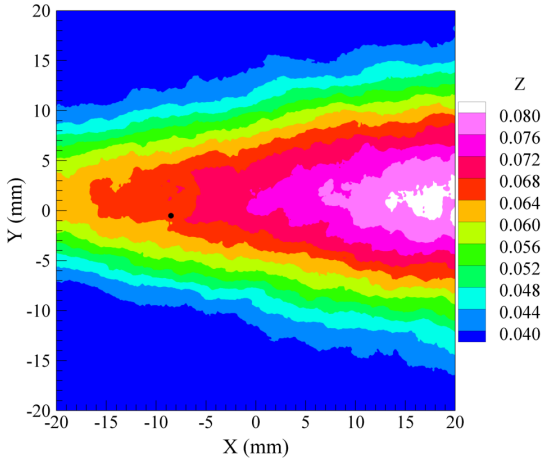

(c) Mean mixture fraction field.

Figure 7.18: Mean flow and scalar field of 100 injections.

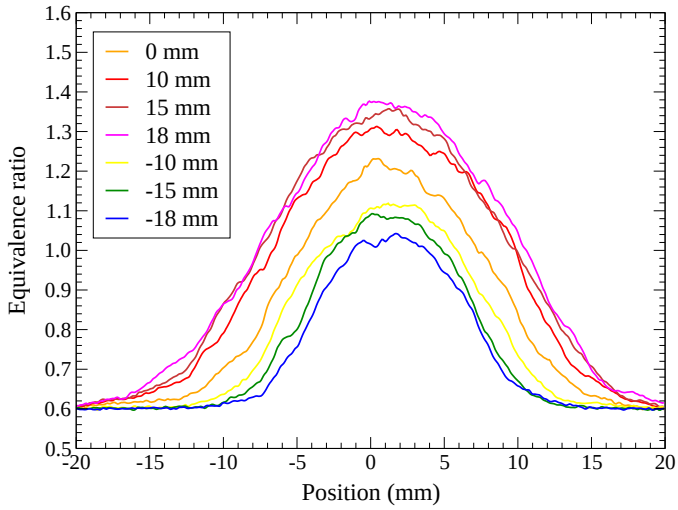

Figure 7.19: Transverse profiles of equivalence ratio at different positions of the combustion chamber.

the left side of image to $20\ mm$ in the right side of image. The mean equivalence ratio around the ignition point is around $\phi = 1.1$.

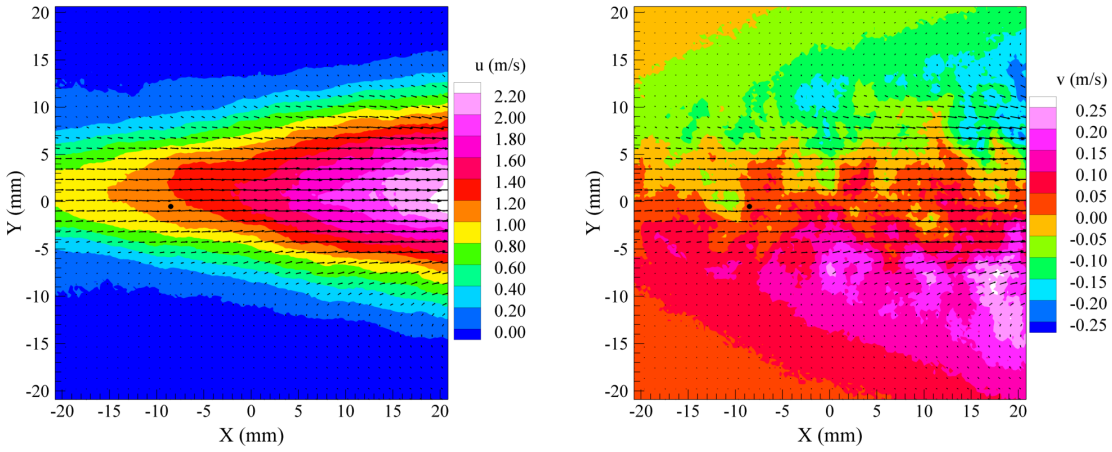

(a) Velocity vector field of U component.

(b) Velocity vector field of V component.

Figure 7.20: Mean velocity vector field of 100 injections.

The mean velocity fields of U and V components are shown in Fig. 7.20. The U component velocities are 10 times higher than the V component velocities. The mean transverse and longitudinal profiles of U and V components at the point of ignition are shown in Fig. 7.21. In transverse direction, U component varies from $1.0\ m/s$ to $1.3\ m/s$ around the ignition point. In the longitudinal direction, U component varies progressively from $0.8\ m/s$ to $2.3\ m/s$. The velocities of V component along transverse and longitudinal directions are very low as expected. Transverse and longitudinal profiles of ϕ and Z at the point of ignition are shown in Fig. 7.22. The equivalence ratio along the transverse direction is more than $\phi = 1.0$ around the ignition point. In the longitudinal direction, equivalence ratio varies progressively from $\phi = 1.0$ to $\phi = 1.4$.

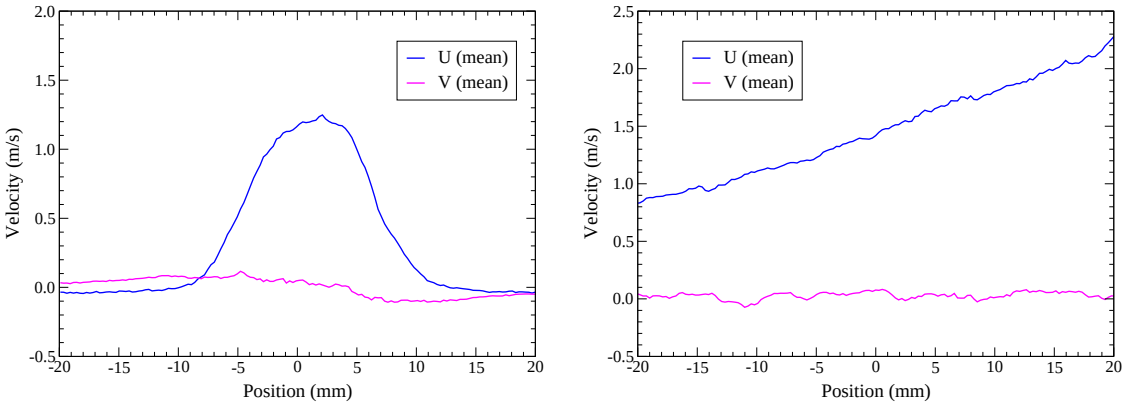

(a) Transverse profiles at X=-8.5 mm.

(b) Longitudinal profiles at Y=-0.5 mm.

Figure 7.21: Mean velocity profiles at ignition point.

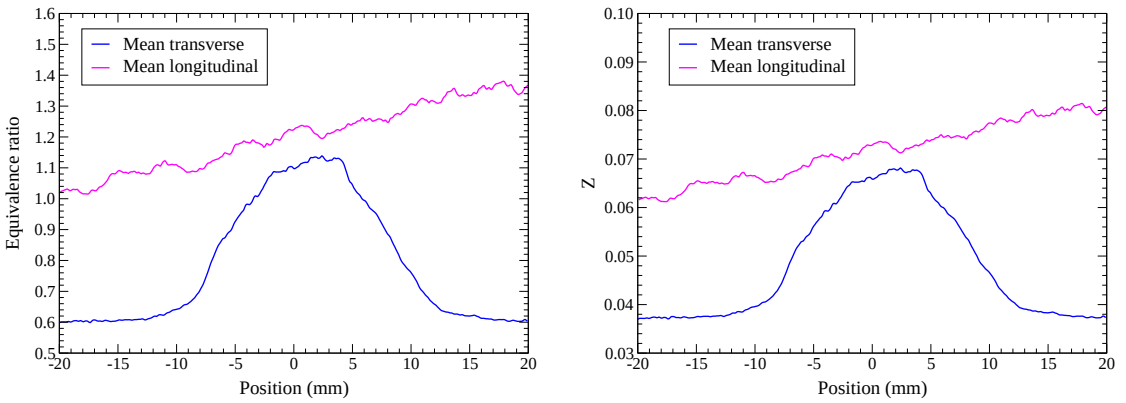

(a) Transverse and longitudinal profile of equivalence ratio.

(b) Transverse and longitudinal profile of mixture fraction.

Figure 7.22: Mean equivalence ratio and mixture fraction profiles at X=-8.5 mm,Y=-0.5 mm (ignition point).

7.6.2 Fluctuations

The fluctuations of U and V velocity components, equivalence ratio and mixture fraction are shown in Figs. 7.23 and 7.24. The fluctuations of U and V components around the ignition point are almost same. The fluctuations of equivalence ratio around the ignition point are smaller than surrounding region.

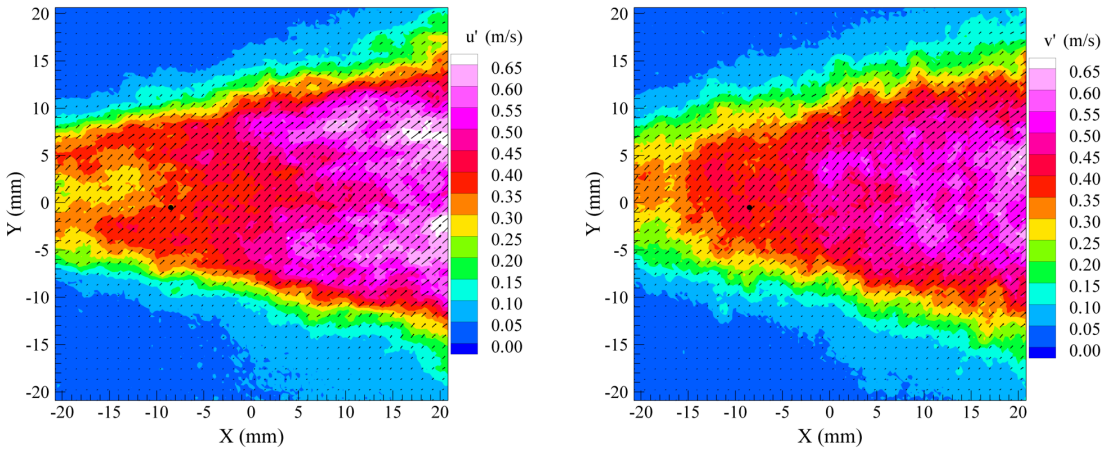

(a) Fluctuations of U component of velocity field.

(b) Fluctuations of V component of velocity field.

Figure 7.23: Fluctuations of velocity field.

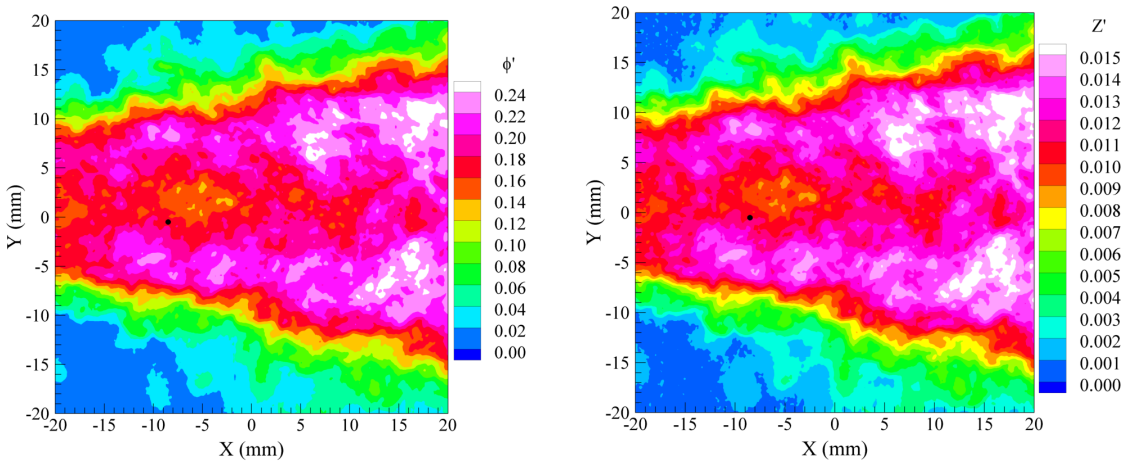

(a) Fluctuations of equivalence ratio.

(b) Fluctuations of mixture fraction.

Figure 7.24: Fluctuations of equivalence ratio and mixture fraction field.

From the fluctuations, we calculated the turbulent kinetic energy (TKE) of velocity and mixture field. Turbulent kinetic energy can be expressed as :

$$k_{vit} = \frac{1}{2}(u'^2 + v'^2 + w'^2) \tag{7.4}$$

with an assumption of $v' = w'$ because of symmetric of jet, TKE becomes,

$$k_{vit} = \frac{1}{2}(u'^2 + 2v'^2) \tag{7.5}$$

The calculated turbulent kinetic energy fields of velocity and equivalence ratio are shown in Fig. 7.25. TKE of equivalence ratio is the fluctuation of equivalence ratio field. TKE of velocity field at the ignition point is around $0.25\ m^2/s^2$ and the equivalence ratio field is around 0.18. The lower value of TKE is due to the position of ignition located close to the tail of jet at the end of injection.

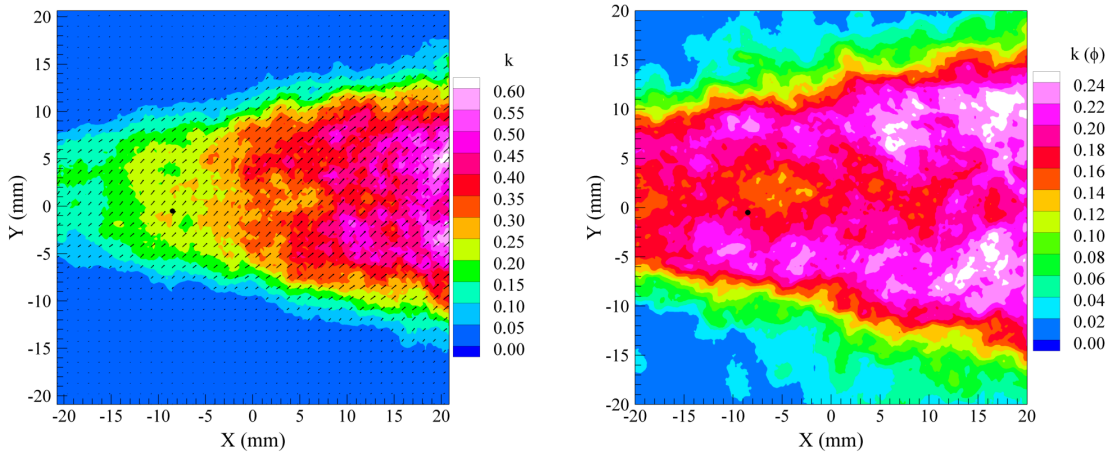

(a) Turbulent kinetic energy of velocity field.

(b) Turbulent kinetic energy of equivalnce ratio field.

Figure 7.25: Turbulent kinetic energy.

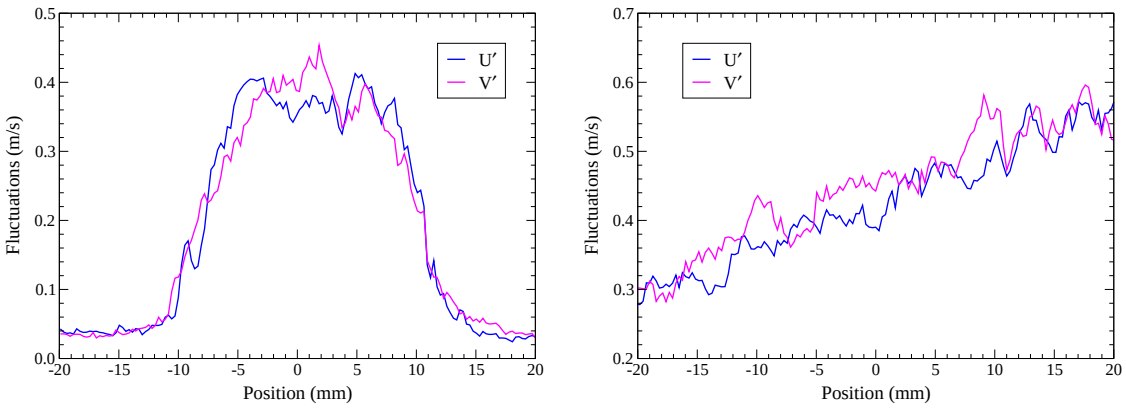

(a) Transverse profiles at X=-8.5 mm.

(b) Longitudinal profiles at Y=-0.5 mm.

Figure 7.26: Fluctuations of velocity field at ignition point.

Transverse and longitudinal fluctuations of velocity components, equivalence ratio and mixture fraction are shown in Figs. 7.26 and 7.27. The intensity of fluctuations in both U and V components are similar and varies around $0.3\ to\ 0.4\ m/s$ at the vicinity of ignition point. It also shows that one hundred injections are sufficient enough to calculate the characteristics of turbulent jet. Transverse fluctuation profile of equivalence ratio is having dual peaks and the ignition point is

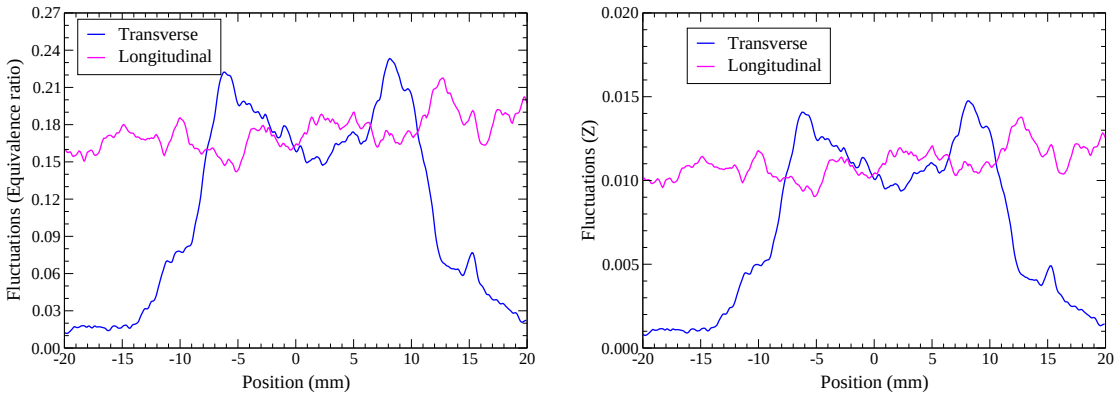

(a) Fluctions of equivalence ratio.

(b) Fluctions of mixture fraction.

Figure 7.27: Fluctuations of equivalence ratio and mixture fraction at X=-8.5 mm,Y=-0.5 mm (ignition point).

located around base of the peak. Table 7.2 summarizes the mixture conditions at the position and

Parameters	Mean	RMS
Velocity (m/s)	1.134	0.680
Equivalence ratio	1.074	0.171
Mixture fraction	0.065	0.011

Table 7.2: Injection parameters at the position and time of ignition.

time of ignition calculated from one hundred cycles. The velocity and equivalence ratio of mixture field at the time and location of ignition are closer to the desired conditions for the investigation of turbulent stratified flame propagations.

7.7 Conclusions

The turbulent stratified mixture formation inside a constant volume combustion chamber is analyzed by using simultaneous PIV/PLIF measurement techniques. The mixture stratification is achieved by injecting rich mixture inside the chamber which is already filled with lean propane-air mixture. An axi-symmetrical injection unit has been developed to control the characteristics of stratified mixture field. The synchronization of injection event with PIV/PLIF image acquisition event is explained. Examples of instantaneous velocity, equivalence ratio and mixture fraction field of stratified mixture at the time of ignition are provided. The mean fields of velocity, equivalence ratio and mixture fraction are discussed. The fluctuations of one hundred injections and the turbulent kinetic energy of mixture field are provided. The profiles of mean and fluctuations of velocity components of U and V, equivalence ratio and mixture fraction are given. At the time and point of ignition, mean velocity is $1.134\ m/s$ with fluctuation of $\pm\ 0.68\ m/s$ and mean equivalence ratio is $\phi\ =\ 1.074$ with fluctuation of $\pm\ 0.171$. So with this configuration, a slightly rich mixture condition is achieved around the point of ignition.

Chapter 8

Turbulent stratified flame propagation

Abstract. *The unsteady propagation of propane/air flame is analyzed through turbulent stratified mixture field by using simultaneous PIV/PLIF techniques. The constant volume combustion chamber is initially filled with lean mixture and then stratified mixture field is realized by an axisymmetrical injection of rich mixture. The mixture is then spark ignited in a region slightly richer than stoichiometric condition and the propagation of flame through stratified mixture is recorded by simultaneous PIV/PLIF techniques. To isolate the effect of turbulence, propagation of flame is recorded for the same aerodynamic jet conditions with six different homogeneous mixtures. From these measurements, the enhancement of flame propagation through stratified mixture condition is analyzed by comparing the results of stratified case with the results of homogeneous cases. Further analysis of local burning velocity conditioned on the local equivalence ratio is also performed to understand the stratification effect on the flame propagation with comparison of data obtained from equivalent homogeneous cases. These analyses of results revealed that the propagation of flame through stratified mixture is faster than their equivalent homogeneous mixtures.*

8.1 Introduction

In practical applications like direct injection gasoline engines and gas turbines, combustion takes place in partially premixed zone where rich stratified mixtures sustain the flame propagation through very lean mixture conditions. This stratified combustion increases the fuel efficiency and lowers CO_2 emissions [Alkidas (2007)]. However, the flame propagation through stratified mixture fields depends on various parameters such as local flow and mixture conditions and those parameters need to be optimized for the maximum benefits. For that, more fundamental understanding on the stratified flame propagation in simple configurations is essential. In that regard, few experimental and numerical investigations have been carried out and their results are often contradictory and need more studies on the stratified flame propagations.

So in this work, experimental investigation on unsteady flame propagation through stratified and homogeneous mixture fields are performed in order to understand the enhancement of flame propagation through stratified mixture field. In the previous chapter, we discussed about the way

of producing the stratified mixture field inside the combustion chamber. We also provided the velocity and equivalence ratio field around the ignition point at the time of ignition. This chapter focuses on the analysis of turbulent flame propagation through stratified and homogeneous mixture conditions.

Simultaneous PIV/PLIF techniques are used to measure combined velocity and equivalence ratio field of flame propagation. In order to isolate turbulence from the stratification effect, flame propagation through six different homogeneous conditions with same turbulent flow conditions are also performed. From the acquired PIV and PLIF images, flame fronts are extracted and their geometries are analyzed. The global parameters such as mean flame radius, mean flame propagation speed of stratified and homogeneous conditions are compared to know the stratification effect. Then from the measurements of simultaneous velocity and equivalence ratio fields, local burning velocities of stratified flames conditioned on the local equivalence ratios are calculated and then compared with equivalent homogeneous cases. Finally, we conclude our findings on the turbulent stratified flame propagation.

8.2 Flow and scalar fields of flame propagation

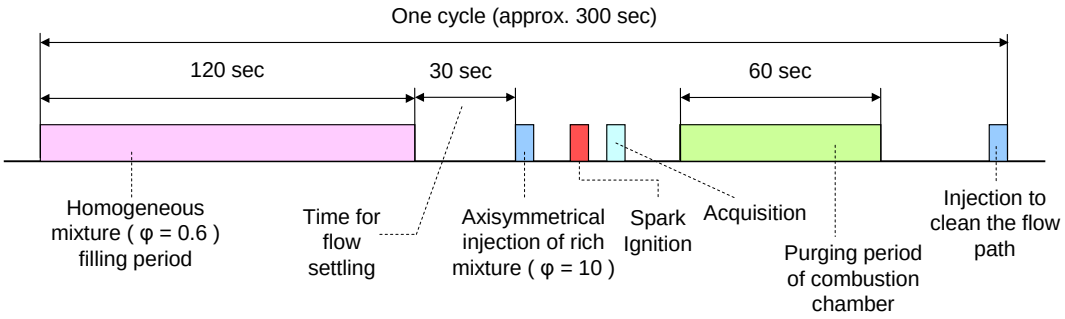

Figure 8.1: One cycle of experiment.

The experimental procedure for each cycle is schematically shown in Fig. 8.1. The combustion chamber is initially filled with continuous flow of lean propane-air mixture at atmospheric pressure. Then inlet and outlet valves are closed and the flow is allowed to come to rest. After that, axisymmetrical injection of rich mixture is commenced by injector unit. The stratified mixture is then spark ignited by applying a high voltage between two thin electrodes ($300\ \mu m$) placed inside the combustion chamber. Minimum spark ignition energy is utilized to ensure free propagation of flame in the initial phase of combustion. Then combustion images of unsteady flame propagation are acquired by using simultaneous PIV/PLIF techniques in the same way applied to the injection studies described in the previous chapter. Finally, the burned products are purged by using a vacuum pump and one more injection is delivered to the chamber to clean the injection line before the commencement of next cycle.

The same injection strategy is utilized for the homogeneous combustion cases in order to investigate the flame propagation through homogeneous mixtures subjected to the same level of turbulence. The flame propagations are observed starting from $1\ ms$ to $5\ ms$ with $1\ ms$ time

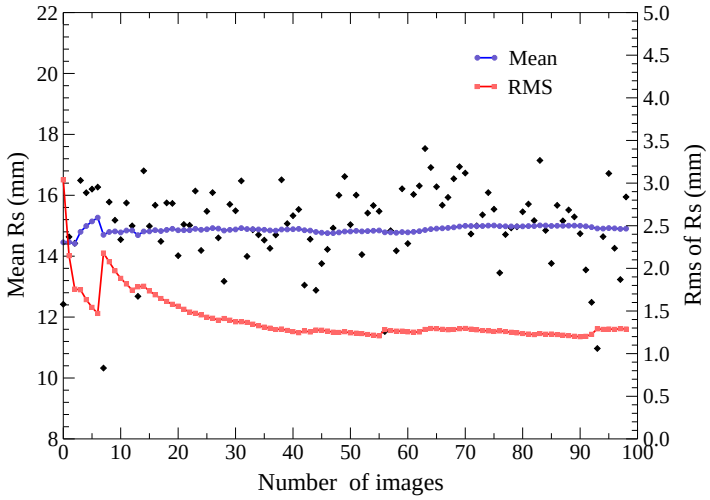

(a) Stratified case.

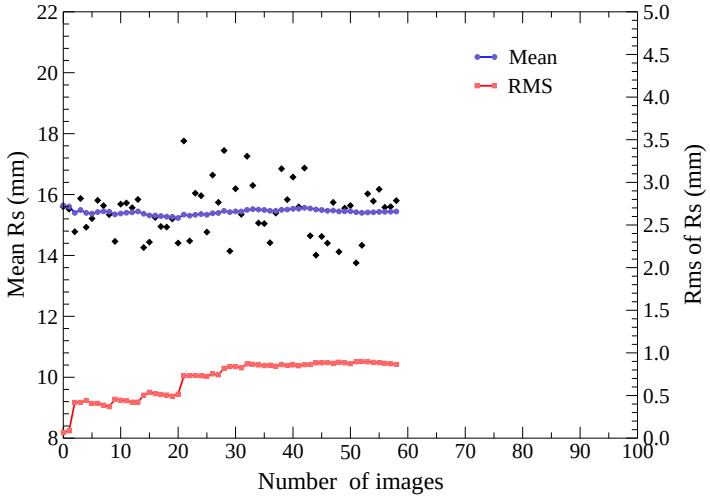

(b) Homogeneous case.

Figure 8.2: Determination of number of images required for statistical analysis.

Combustion mode	Stratified mode	Homogeneous mode
Acquisition time (ms)	1, 2, 3, 4, 5	1, 2, 3, 4, 5
Equivalence ratio of chamber (ϕ_{cc})	0.6	0.8, 0.9, 1.0, 1.1, 1.2, 1.3
Equivalence ratio of mixture (ϕ_{inj})	10.0	$\phi_{inj} = \phi_{cc}$
Total images	500	1560

Table 8.1: List of experimental studies carried out.

step. In order to determine minimum number of images required for good statistical analysis, the mean values and fluctuations of flame front radius are analyzed. Figure 8.2 shows convergence of fluctuations of flame radius at around one hundred images for stratified case and at around sixty images for homogeneous case. So for each timing, 100 images are acquired for the stratified case and 60 images are acquired for the homogeneous cases.

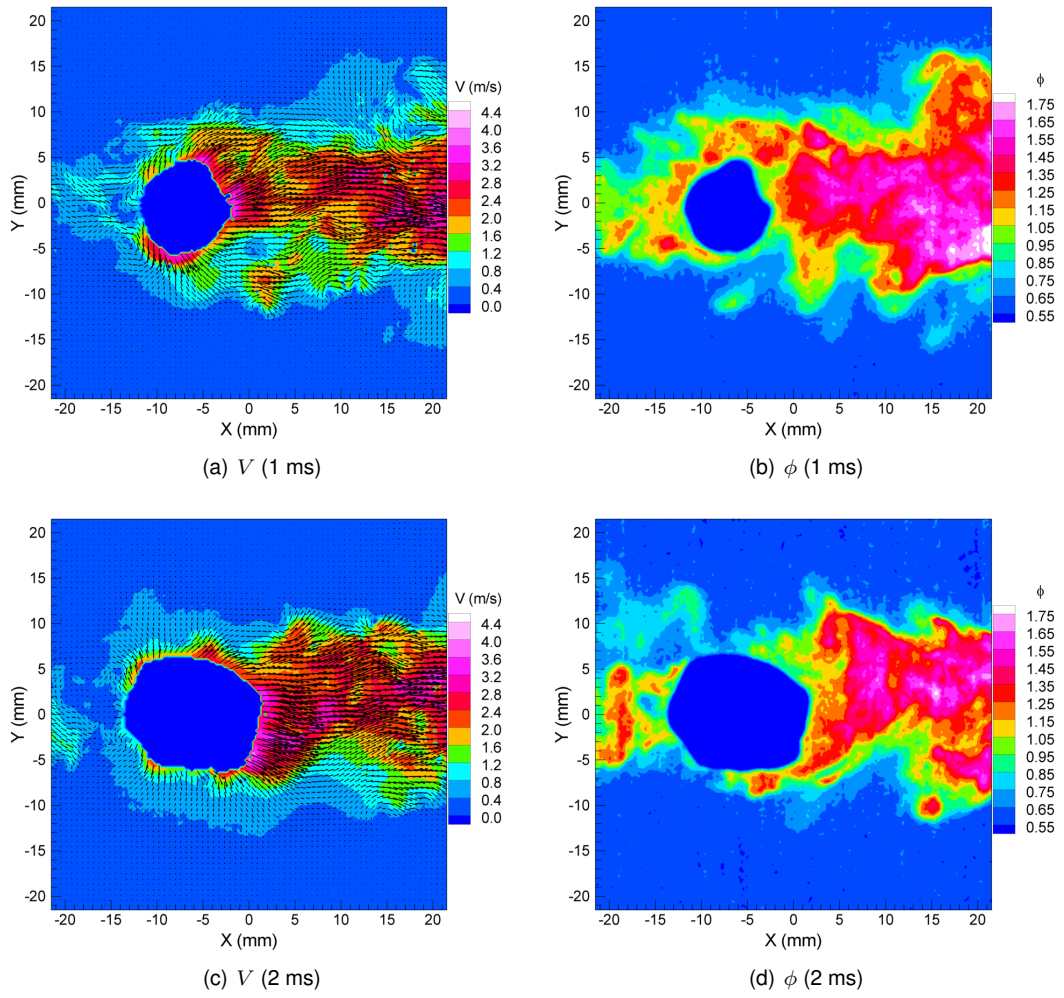

(a) V (1 ms) (b) ϕ (1 ms)

(c) V (2 ms) (d) ϕ (2 ms)

Figure 8.3: Instantaneous velocity and equivalence ratio field of stratified combustion

The instantaneous fields of velocity and equivalence ratio of flame propagation in the stratified mode of combustion are shown in Figs. 8.3 and 8.4. Those fields are calculated from different cycles. The flame front is almost spherical in shape at $1\ ms$ after ignition. Then it starts to elongate along with turbulent jet in the right side, but spreads laterally in the left side. The presence of rich mixtures surrounding the flame front declines over a period of time. Indeed, part of flame front starts to propagate through lean mixtures as early as $2\ ms$ after ignition. At $5\ ms$, the presence of rich mixtures around the flame front are very minimal and the spread of flame front is more in the X direction than Y direction. The wrinkling of flame front seems to be increasing with time due to the turbulence and stratified mixture field around the flame front. Generally, there are similarities between the flow structures and the distribution of equivalence ratio at each time.

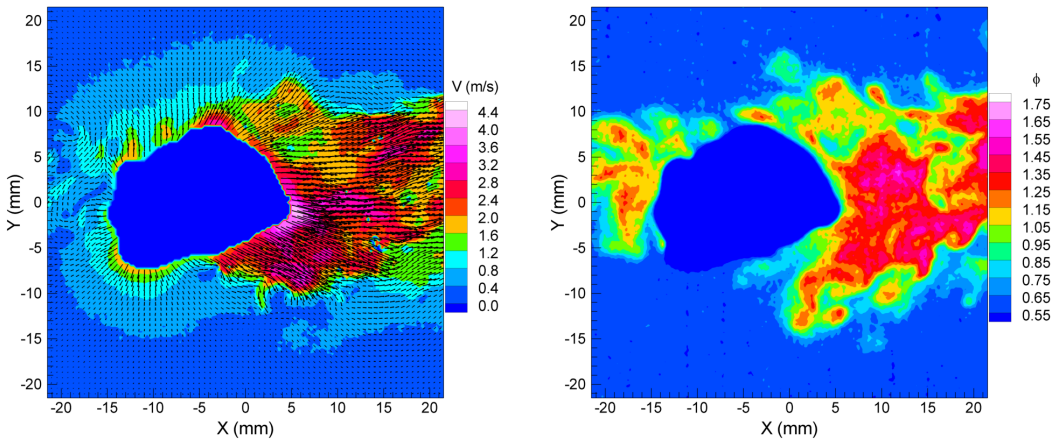

(a) V (3 ms)

(b) ϕ (3 ms)

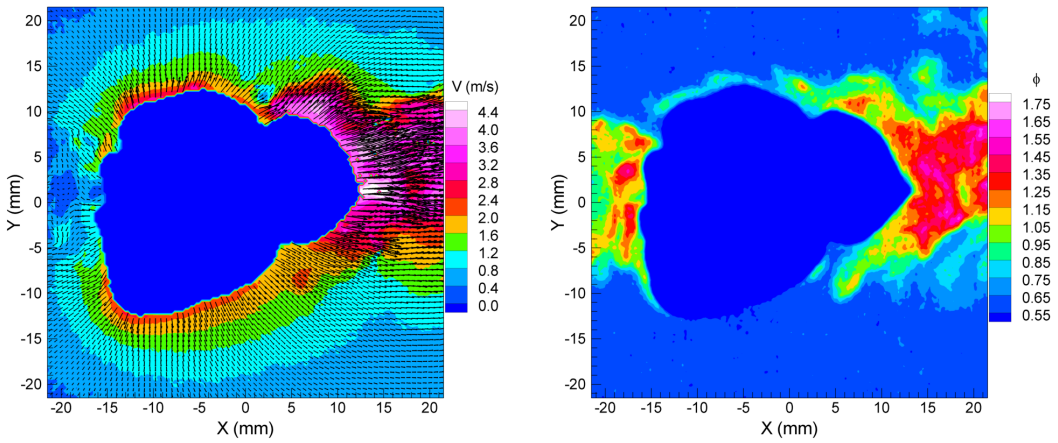

(c) V (4 ms)

(d) ϕ (4 ms)

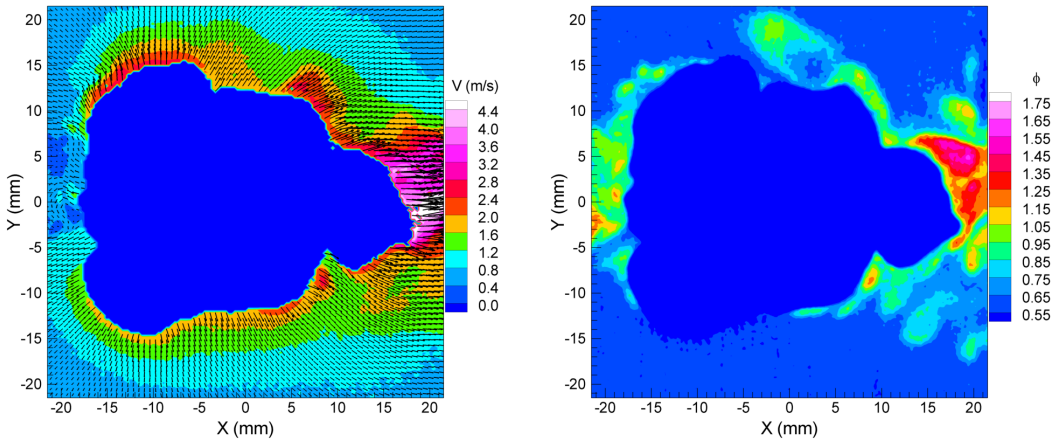

(e) V (5 ms)

(f) ϕ (5 ms)

Figure 8.4: Instantaneous velocity and equivalence ratio field of stratified combustion

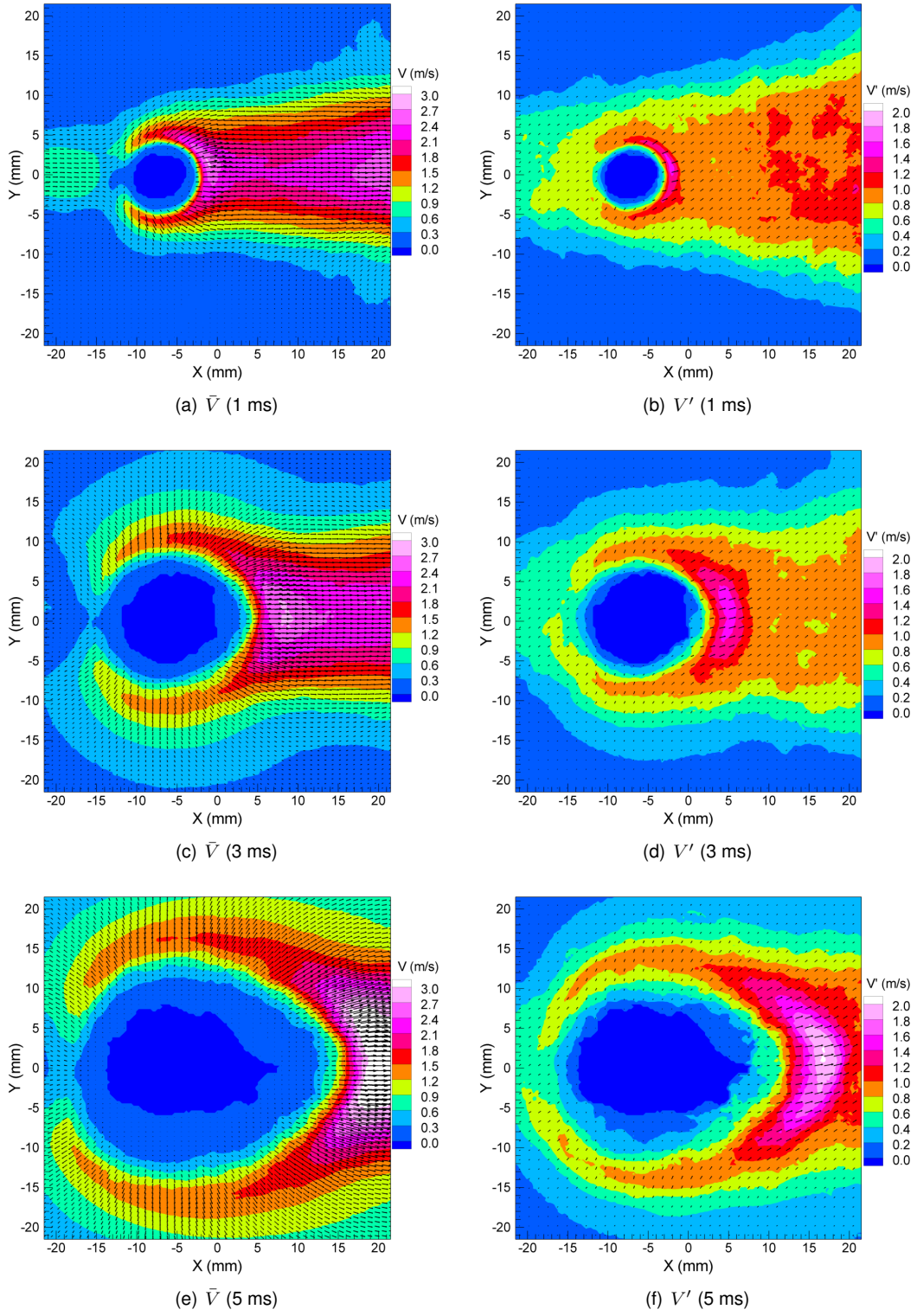

(a) $\bar{V}$ (1 ms)

(b) V' (1 ms)

(c) $\bar{V}$ (3 ms)

(d) V' (3 ms)

(e) $\bar{V}$ (5 ms)

(f) V' (5 ms)

Figure 8.5: Mean and fluctuations of velocity field of stratified combustion

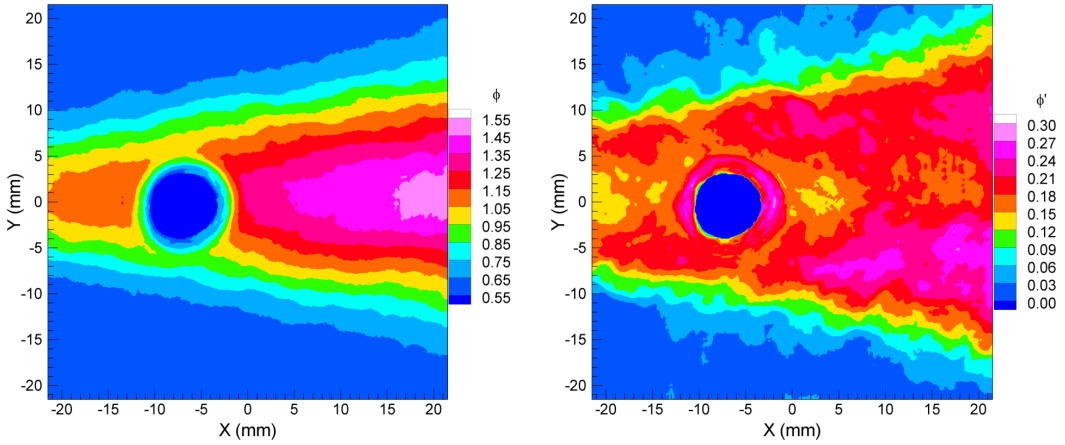

(a) $\bar{\phi}$ (1 ms) (b) ϕ' (1 ms)

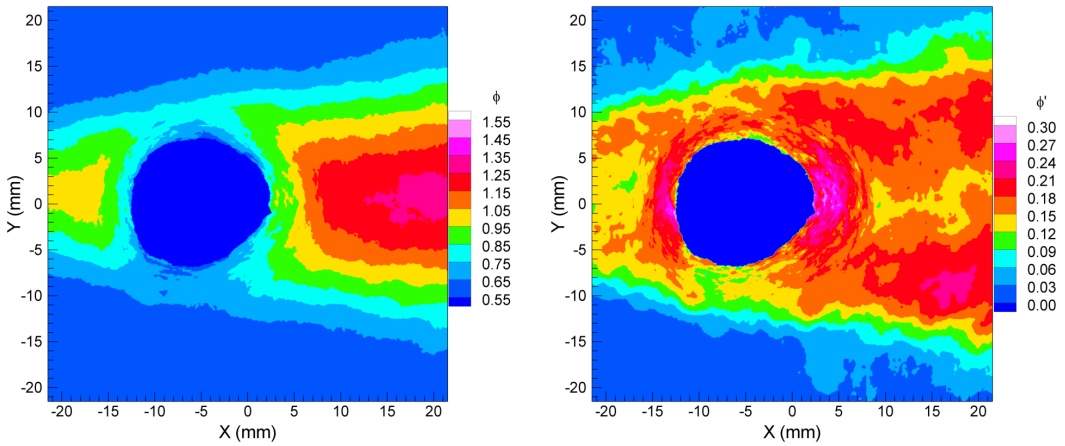

(c) $\bar{\phi}$ (3 ms) (d) ϕ' (3 ms)

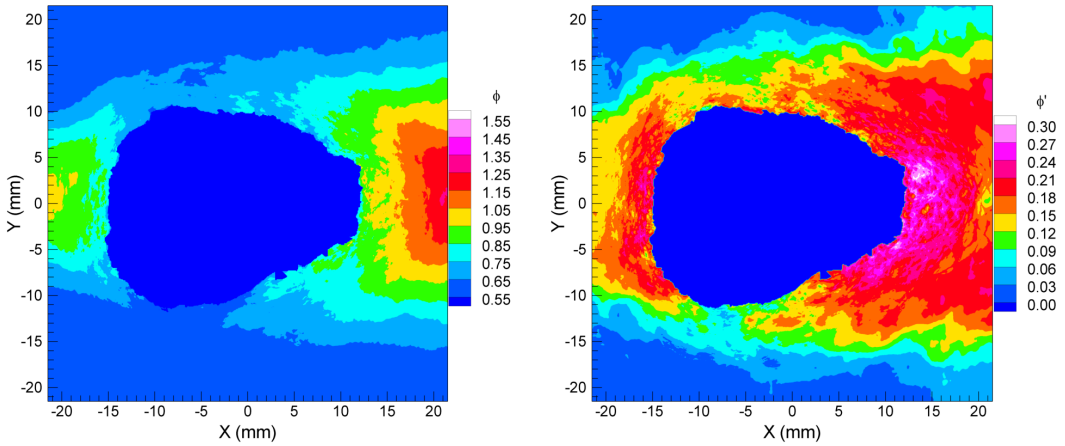

(e) $\bar{\phi}$ (5 ms) (f) ϕ' (5 ms)

Figure 8.6: Mean and fluctuations of equivalence ratio field of stratified combustion

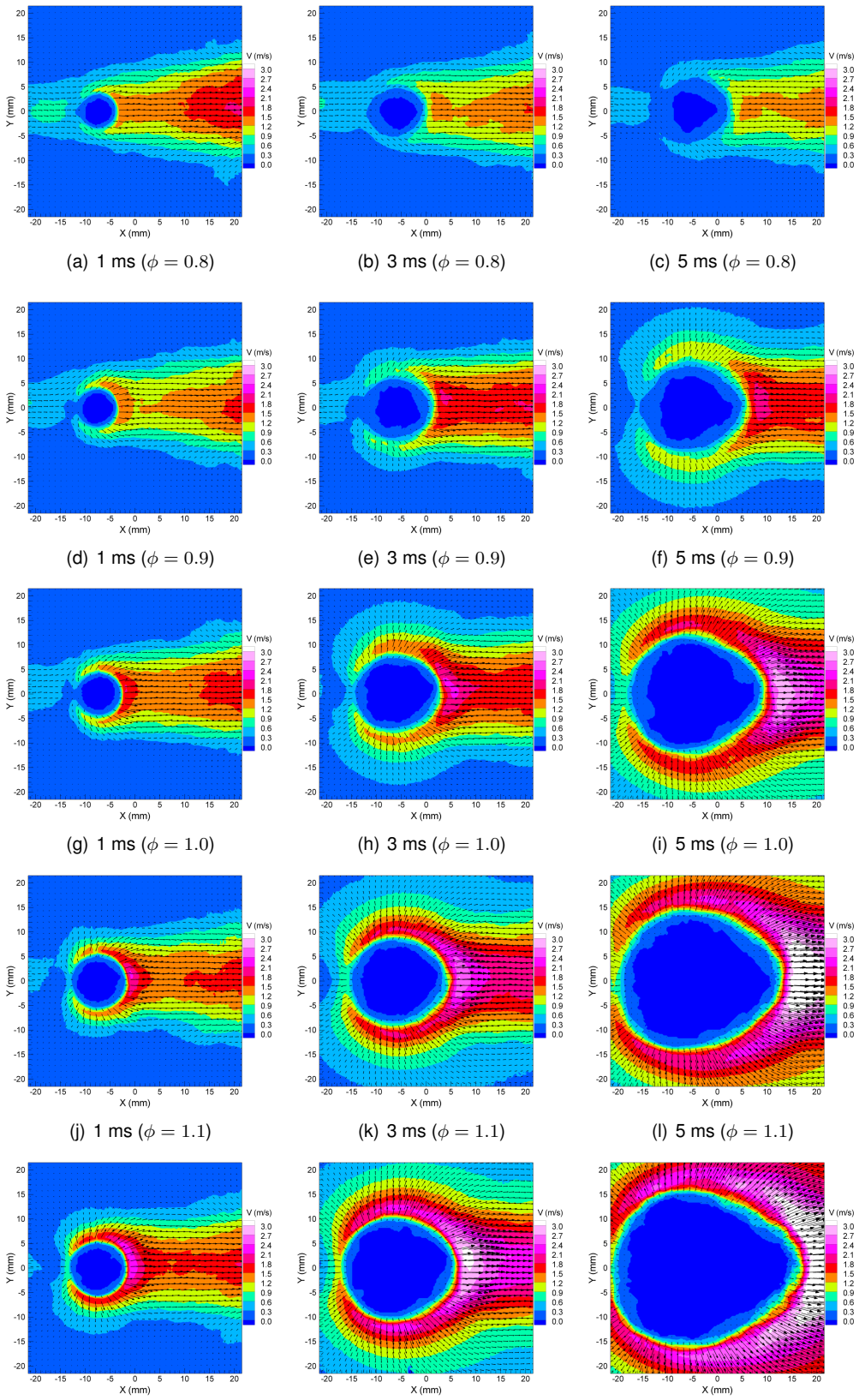

(a) 1 ms ($\phi = 0.8$) (b) 3 ms ($\phi = 0.8$) (c) 5 ms ($\phi = 0.8$)

(d) 1 ms ($\phi = 0.9$) (e) 3 ms ($\phi = 0.9$) (f) 5 ms ($\phi = 0.9$)

(g) 1 ms ($\phi = 1.0$) (h) 3 ms ($\phi = 1.0$) (i) 5 ms ($\phi = 1.0$)

(j) 1 ms ($\phi = 1.1$) (k) 3 ms ($\phi = 1.1$) (l) 5 ms ($\phi = 1.1$)

(m) 1 ms ($\phi = 1.2$) (n) 3 ms ($\phi = 1.2$) (o) 5 ms ($\phi = 1.2$)

Figure 8.7: Mean velocity field of homogeneous combustion

The mean velocity and equivalence ratio fields along with their fluctuations calculated from one hundred images at each time are shown in Figs. 8.5 and 8.6. Both the mean and fluctuations of velocity and equivalence ratio fields are almost symmetrical with respect to the jet axis. The mean velocity fields clearly show the progressive change of flame front shape from circular to oval. Both the mean and fluctuations of velocity field increases with time in the right side along the jet direction because of combined jet movement with flame propagation. The fresh gases pushed by the expansion of flame fronts almost covers the entire image area of $45 \times 45\ mm^2$ at $5\ ms$ after ignition. But the spread of equivalence ratios around that time is different where the mixtures are very lean at bottom and top of mean equivalence ratio field. Indeed, the flame fronts are initially surrounded by rich and stoichiometric mixtures and then the presence of rich mixtures reduces with time especially along the lateral side (Y direction) of flame fronts.

The mean velocity fields of turbulent homogeneous combustion at different equivalence ratios are shown in Fig. 8.7. For all the homogeneous cases at $1\ ms$ after ignition, flame fronts are almost spherical and their size increases with equivalence ratio. Also at $1\ ms$, the velocity of jet in the left side decreases with equivalence ratio whereas on the right side of ignition point, the velocity of jet increases with equivalence ratio. These patterns can be related to the increase of flame propagation speed with equivalence ratio of mixture.

In all the cases, the shape of flame front progressively changes from spherical to oval which is similar to the stratified case. Also, the velocity fields are symmetrical to the jet axis. The flame propagation seems to be very weak for $\phi = 0.8$ case where the mean velocity around the flame front is smaller than the velocity of jet which is clearly visible at $5\ ms$. The mean velocity fields of $\phi = 1.0$ look to be similar to the velocity fields of stratified case. Definitely, the flame propagation of $\phi = 1.2$ is more than all other homogeneous and stratified mixture conditions.

8.3 Global analysis

The influence of turbulence and the stratification effect on the flame propagation can be understood by analyzing the global parameters such as rise of combustion pressure, evolution of mean flame radius, mean flame propagation speed, flame front shape and so on. The flame fronts extracted from the PIV and PLIF images allow us to measure parameters related to the geometries of flame front for the homogeneous and stratified cases. In this section, the global analyses of parameters are presented to provide the insight of flow-flame interactions and the effect of stratification on flame propagation.

8.3.1 Pressure measurement

The analysis of pressure rise inside the constant volume combustion chamber can indicate the maximum time of free flame propagation, variation of pressure rise with different mixture conditions and the cycle-to-cycle variations of combustion pressure. In this work, the pressure rise during combustion is measured by using piezoelectric pressure pickup (KISTLER 601) with charge amplifier (KISTLER 5011) unit. The instantaneous pressure curves of homogeneous case of $\phi = 1.0$ and stratified combustion case are shown in Fig. 8.8. The rise of pressure is rapid in the homogeneous case compared to that of stratified case. But the pressure variations are high

for the stratified case. This higher cycle-to-cycle variations could be caused by the fluctuation of equivalence ratio of mixture around the electrodes at the time of ignition, similar to the observations from the direct injection gasoline engines [Aleiferis et al. (2004)].

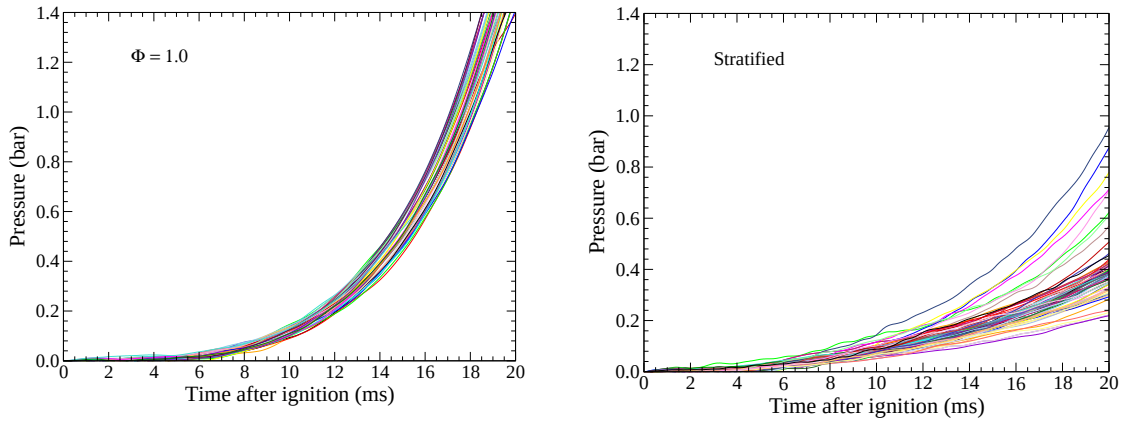

Figure 8.8: Instantaneous pressure curves after ignition.

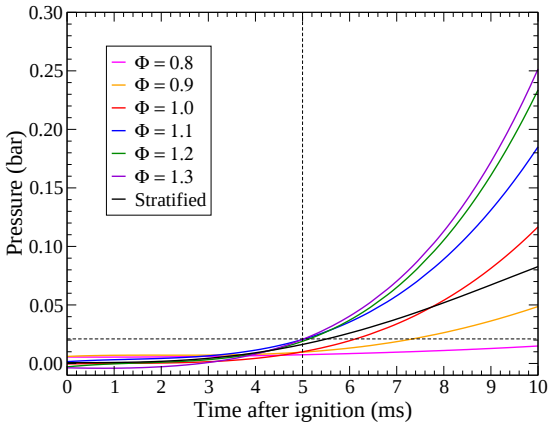

Figure 8.9: Mean pressure curves after ignition.

The mean pressure curves of various cases are shown in Fig. 8.9. First of all, the mean pressure rise is below 0.02 bar in all the cases up to 5 ms, which indicates the free propagation of flame front during the time of investigation. Indeed, the initial pressure rise is very small as well as same for all the cases up to $4\ ms$ from start of ignition. After that, pressure rises slowly for $\phi = 0.8$, moderately for $\phi = 0.9$ and rapidly for all other homogeneous mixtures conditions. The mean pressure of stratified case is more than $\phi = 1.0$ at $5\ ms$, becomes almost same at $7.7\ ms$ and after that its rate of pressure rise drops down and stays in between $\phi = 0.9$ and $\phi = 1.0$. The initial pressure rise of stratified case could be related to the availability of rich mixtures around the flame front and the later drop of pressure rise compared to $\phi = 1.0$ could be related to the propagation of flame front through lean mixture but still above than $\phi = 0.9$ could be due to the memory effect of stratified combustion. Further quantitative analysis of local variables can improve the understanding of this observation.

8.3.2 Analysis of flame front contours

The flame front is the boundary which separates the burned gas region from the fresh gas region and the coordinates of flame fronts need to be extracted from their PIV and PLIF images in order to analyze the flame front geometries and to measure local curvature, local velocity and local equivalence ratio around the flame fronts. In this work, the propane-air mixture is seeded with olive oil particles and anisole vapor for simultaneous PIV/PLIF measurements. The evaporation of olive oil particles through the flame front ensures the instantaneous position of flame front in the PIV images [Boyer (1980)]. Likewise the anisole vapor in the propane-air mixture burns through the flame front and by the way it marks the instantaneous position of flame front in the PLIF images [Pasquier et al. (2007)].

In this work, the coordinates of flame fronts are extracted with sub-pixel resolution by a new extraction tool which is described in the appendix (§ A). The extracted flame front contours are filtered in order to remove the small wrinkles superposed in to the contours due to the limited signal-to-noise ratio close to the flame front. The filtration method is explained in the appendix (§ C). One example of extracted and then filtered PIV and LIF contours are shown in Fig. 8.10. In general, the superposition of PIV contours with PLIF contour indicates that the PIV technique is well combined with PLIF technique for the simultaneous measurements of velocity and equivalence ratio. But there are few small differences between PIV and PLIF coordinates due to the difference in isothermal line marked by the olive oil particles and anisole vapor.

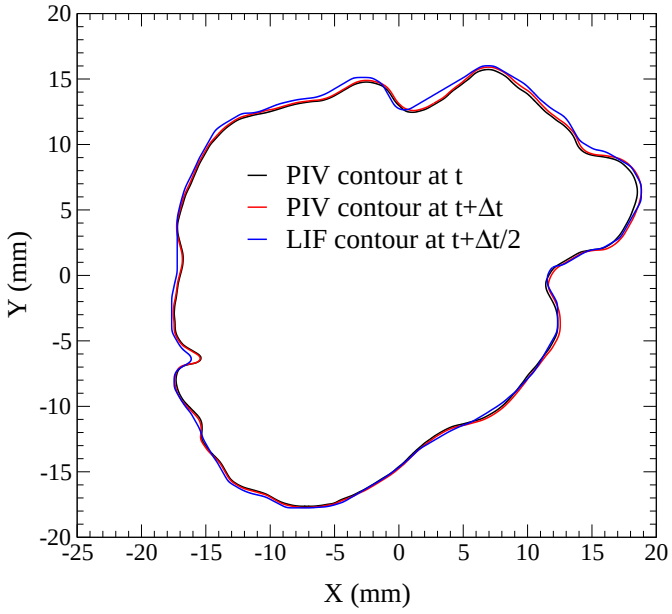

Figure 8.10: Superposition of PIV and LIF contours.

Figure 8.11 shows instantaneous flame front contours calculated from sixty PIV images taken for $\phi = 1.0$ at $5\ ms$ after ignition conditions. All the flame fronts are globally in oval shape. As discussed in the previous section, the shape of flame front changes from circular to oval and this change in shape can be well represented by the mean flame front at each condition for different cases. So for each condition, we calculated the mean flame front contour from their instantaneous contours using ignition point as center. The calculated mean flame front contour is shown in Fig.

8.11 as a thick black line. The evolution of mean flame front contours for different cases is shown in Fig. 8.12. The comparison of mean flame front contours of different cases with respect to the time after ignition is shown in Fig. 8.13.

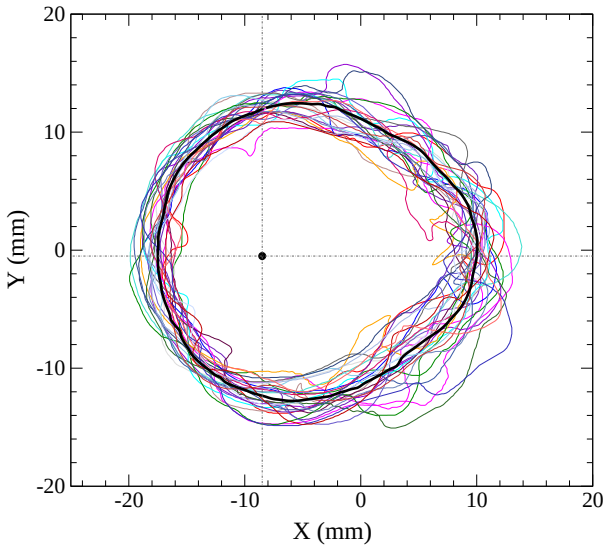

Figure 8.11: Instantaneous flame front contours and their mean contour.

Figure 8.12 clearly shows the evolution of flame shape from spherical to oval. The mean flame fronts are symmetrical with respect to the jet axis in all the cases. For the homogeneous cases, the size of mean flame fronts increases with equivalence ratios. The mean flame fronts of stratified case are more elongated along the X direction compared to the homogeneous cases due to the turbulence and the presence of rich and stoichiometric mixtures along the jet axis (Figs. 8.3 and 8.4).

From Fig. 8.13, the mean contours are spherical at $1\ ms$ after ignition for all the cases. Also, it shows difference in overlapping of mean contours due to the variation of flame propagation with equivalence ratio and the changes of position of ignition point during the acquisition of images. At $2\ ms$, the mean contours start to elongate on the right side of ignition point due to the combined movement of fresh gas and the turbulent jet. This elongation is clearly visible at $3\ ms$. The mean contour of stratified case is almost in same size with that of $\phi = 1.0$ at $2\ ms$, slightly elongates more than that at $3\ ms$ and elongates further than that of $\phi = 1.1$ at $5\ ms$. But the mean contours of homogeneous cases are evolving with similar shapes and their sizes increase with equivalence ratios.

So from the analysis of mean flame front contours, we can draw the following conclusions:

- The mean flame front contours are initially spherical in shape and become oval at latter times.
- The size of mean contours of homogeneous flames increases with their equivalence ratio.
- At each time, the mean contour of stratified case is more elongated than that of homogeneous cases.

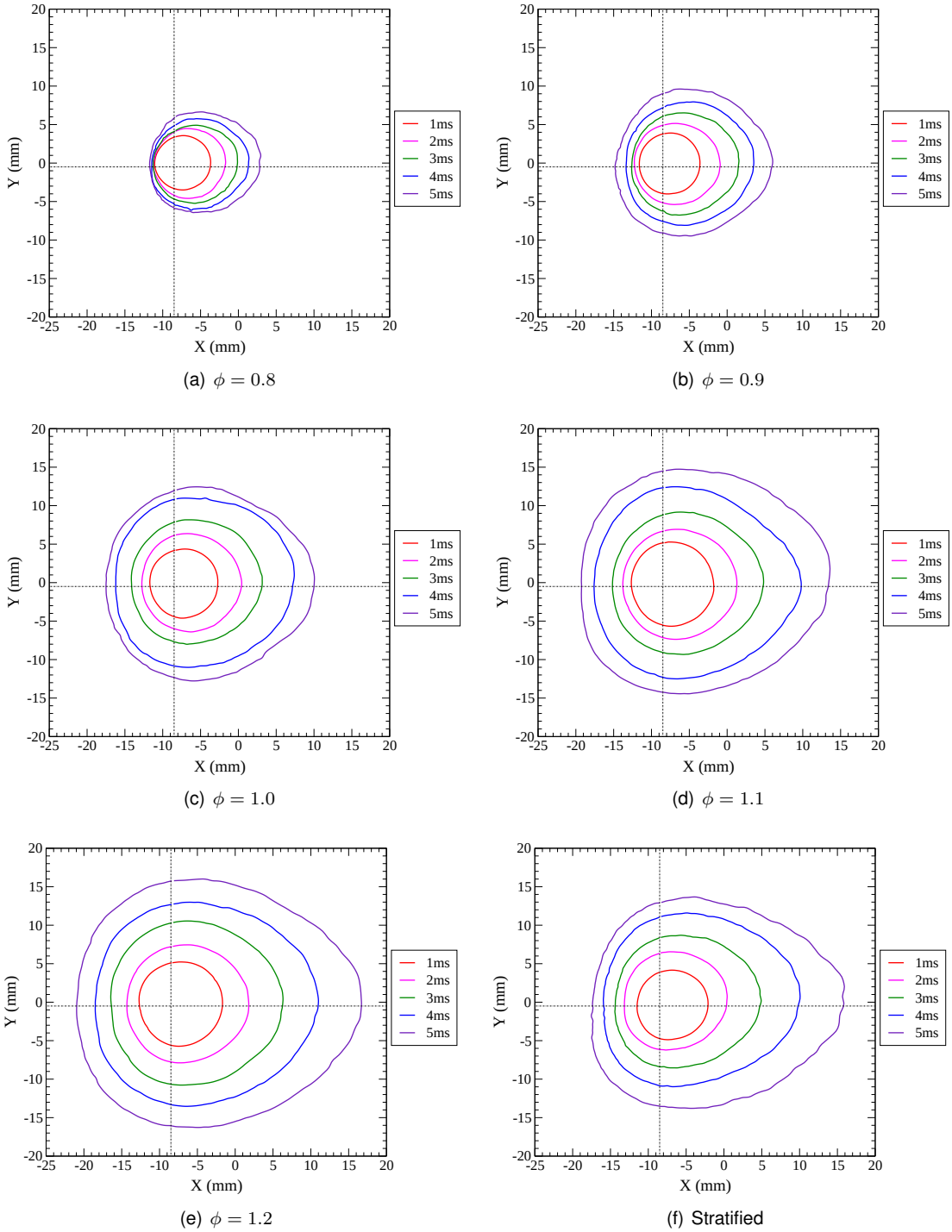

(a) $\phi = 0.8$ (b) $\phi = 0.9$

(c) $\phi = 1.0$ (d) $\phi = 1.1$

(e) $\phi = 1.2$ (f) Stratified

Figure 8.12: Mean flame front contours at different equivalence ratio.

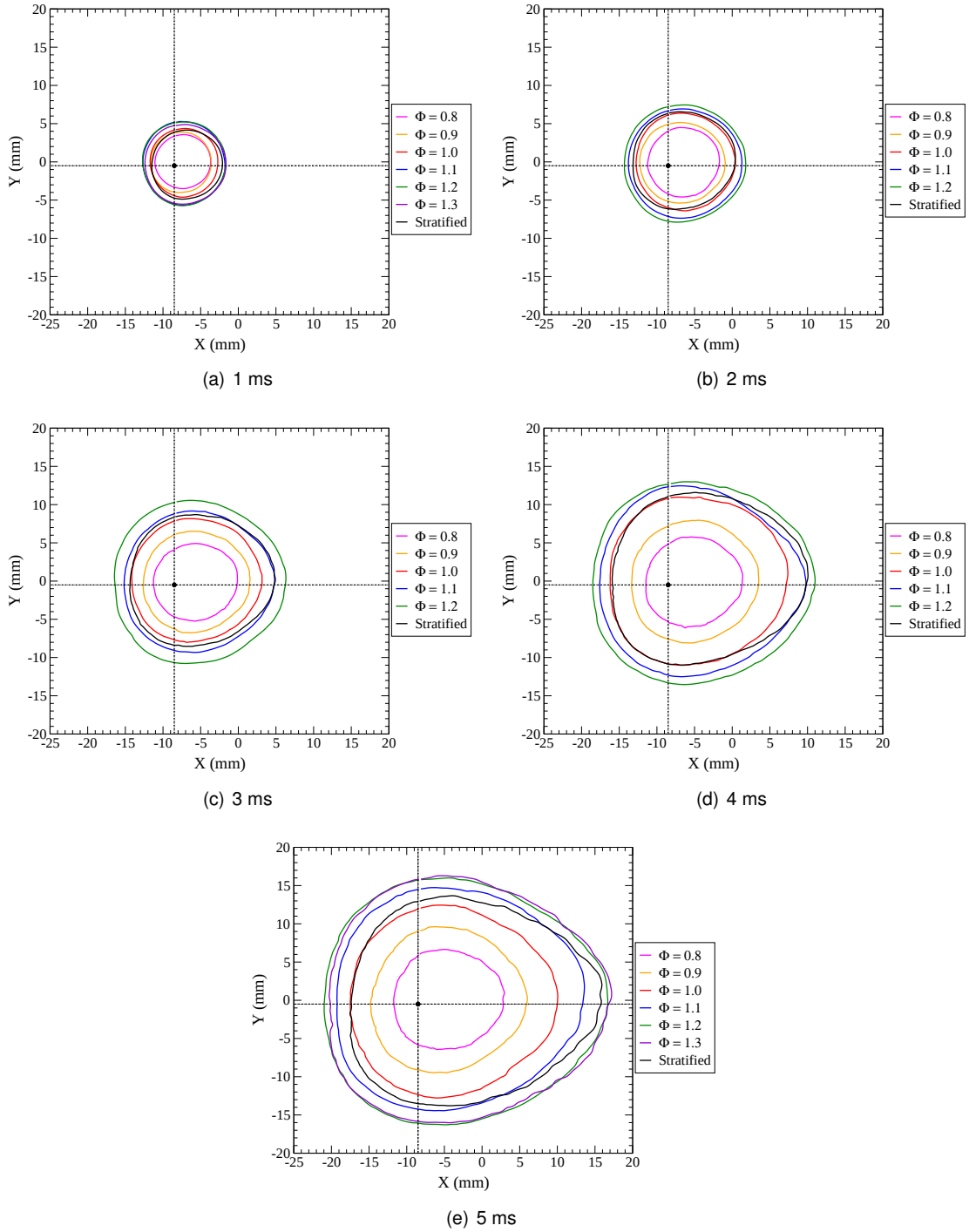

(a) 1 ms (b) 2 ms

(c) 3 ms (d) 4 ms

(e) 5 ms

Figure 8.13: Mean flame front contours at different timings.

8.3.3 Asymmetry

The flame propagation is subjected to the flow turbulence in homogeneous cases and also subjected to the local variation of mixture field in stratified case. Indeed, the equivalence ratio of stratified mixture varies mainly in the transverse direction of jet and because of that the propagation of stratified flame could be different in this transverse direction of jet compared to that of homogeneous flames. So by comparing the spread of flame fronts of homogeneous and stratified cases in transverse and longitudinal direction of jet, we can discriminate the stratification effect from the turbulence effect. For that, the maximum spread of flame front in X and Y directions are measured as shown in Fig. 8.14. The ratio of Lx/Ly is asymmetry coefficient which is equal to one for the perfect spherical flame front. The evolution of mean values of asymmetry coefficient is shown in Fig. 8.15, in that the vertical bars represent the standard deviation. The mean

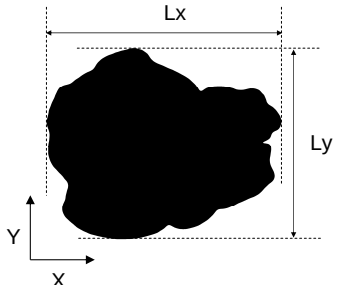

Figure 8.14: Measurement of Lx and Ly.

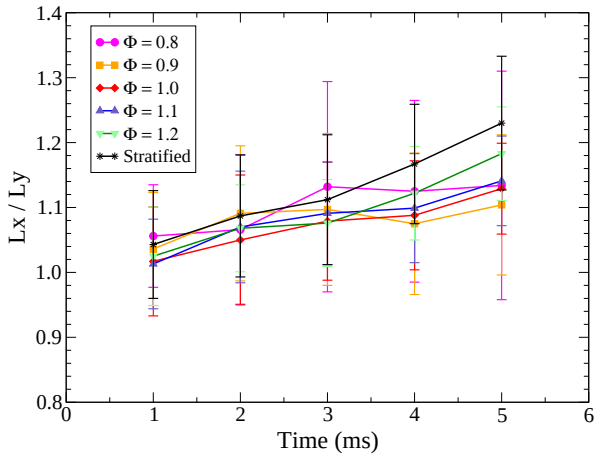

Figure 8.15: Asymmetry coefficient as a function of time.

values of asymmetry coefficients are higher than one for all the cases and continuously increase with time for stoichiometric and rich homogeneous mixture cases and also for stratified case. The strong longitudinal flow of turbulent jet coupled with flame propagation could be the reason for the increase of asymmetry ratio for stoichiometric and rich homogeneous cases. But there is no clear trend of evolution of asymmetry coefficient for lean homogeneous cases and that could be related to their slow flame propagation which could be affected more by the turbulence of flow field. Among the different cases, asymmetry coefficient of stratified case is always higher especially

after $3\ ms$. This can be due to the weaker flame propagation along normal to the jet compared to the propagation along the jet due to the availability of favorable mixtures along the jet axis for longer time. So this asymmetry analysis indicates that the shape of flame front is influenced more by mixture stratification than that of flow turbulence.

8.3.4 Analysis of mean flame radius

The analysis of mean flame front contours showed that the mean flame fronts are almost spherical at $1\ ms$ and then later become oval due to the turbulence and stratification effects. This evolution of flame shape can be well understood by analyzing the mean flame radii based on the surface area (R_s) and the circumference (R_l) of flame fronts. The definition of flame radius R_s and R_l are:

$$R_s = \sqrt{S_f/\pi} \tag{8.1}$$

$$R_l = L/2\pi \tag{8.2}$$

where S_f is the cross-sectional area of flame surface in the laser sheet and L is the circumference of flame front.

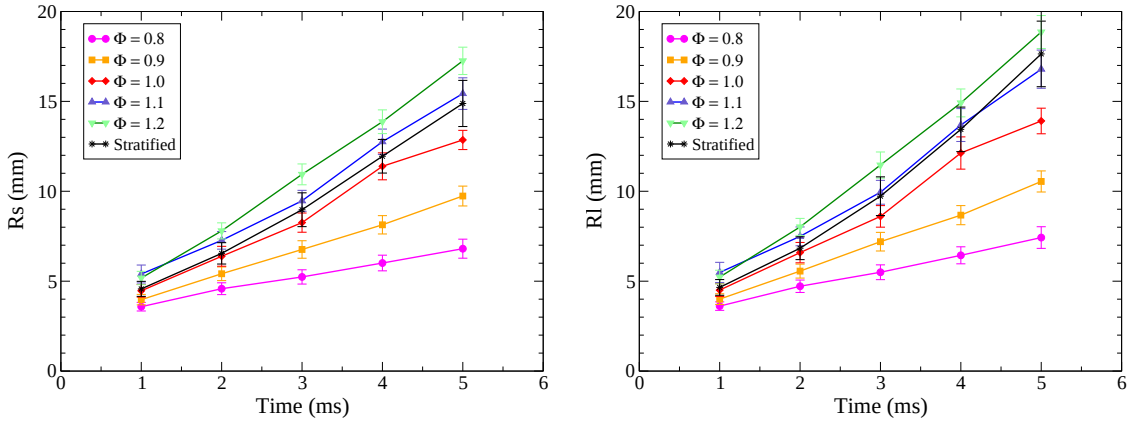

(a) R_s as a function of time.

(b) R_l as a function of time.

Figure 8.16: Time evolution of flame radius .

The evolution of flame radii R_s and R_l are shown in Fig. 8.16. The mean flame radii continuously increases with time for all the cases as expected. Also at each time, mean flame radius of homogeneous cases increases with equivalence ratio. For the stratified case, mean of R_s and R_l are slightly higher than that of $\phi = 1.0$ at $1\ ms$, and then start to increase more than mean values of $\phi = 1.0$ and become closer to mean values of $\phi = 1.1$ at later stages. The standard deviation of both R_s and R_l of stratified case are more than homogeneous cases due to the high cyclic variations as observed in the combustion pressure measurements. So from the evolution of mean flame radii, we observed that the stratified flames are bigger than that of $\phi = 1.0$ case and their variation of flame surface area is higher than that of homogeneous cases.

The ratio of R_l/R_s indicates the deviation of shape of flame front from perfectly spherical shape and also characterizes the degree of wrinkling of flame front due to the turbulence and

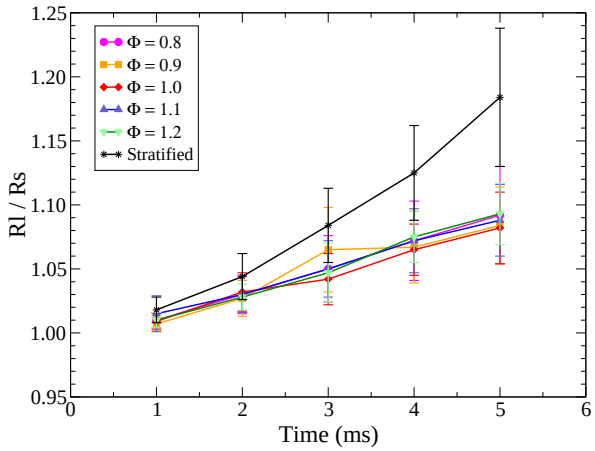

Figure 8.17: Variation of wrinkling rate as a function of time.

stratification effects. So the comparison of R_l/R_s of homogeneous cases with stratified case can show the effect of stratification on flame propagation. Figure 8.17 shows the mean and standard deviation of ratios for different cases. For the homogeneous cases, the variation of wrinkling rate with time is almost linear and almost independent on equivalence ratio. For the stratification case, the mean and standard deviation of wrinkling rate increases rapidly with time. Actually, R_l/R_s ratio is influenced by the global variation of flame front shape from spherical to oval over a period of time and also by the local wrinkling structure which increases the circumference of flame front. So in order to know the contribution of evolution of shape on wrinkling rate, we calculated the ratios Lx/Ly and R_l/R_s for the mean flame front contours of homogeneous and stratified flames and the results are shown in Fig. 8.18. The ratio of Lx/Ly of mean flame fronts

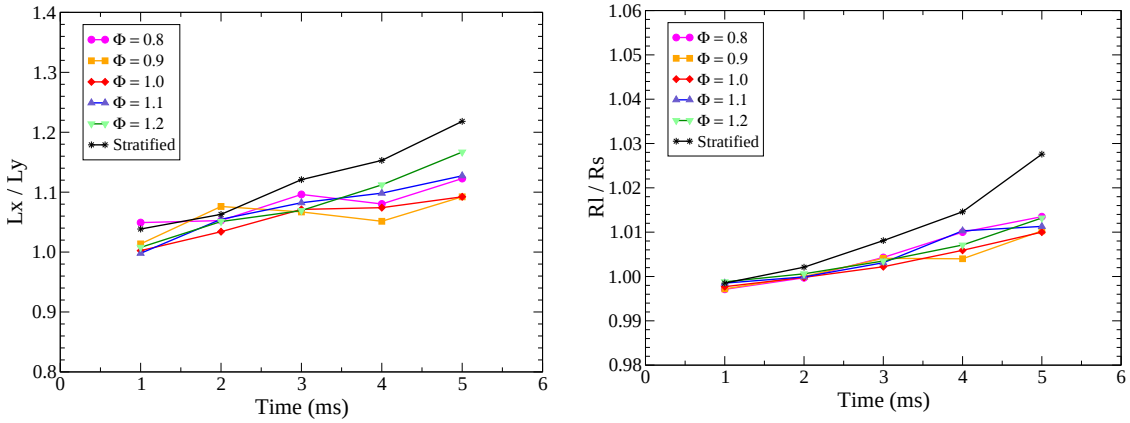

(a) Asymmetry coefficient of mean flame fronts.

(b) Wrinkling rate of mean flame fronts.

Figure 8.18: Variation of asymmetry coefficient and wrinkling rate of mean flame fronts as a function of time.

are almost similar with results obtained from instantaneous flame front contours. But the ratio of R_l/R_s of mean flame fronts are different from the results obtained from instantaneous flame fronts. Indeed, the ratio obtained from mean flame fronts are very small compared to the results

of instantaneous flame fronts for all the cases and this clearly indicates that the contribution of variation of flame front shape is small on evolution of R_l/R_s of instantaneous flame fronts. That means, the stratified flame fronts are more wrinkled than homogeneous flames. This observation supports the conclusion of Jiménez et al. (2002) that the stratification of mixture field enhances the wrinkling of flame front and this increase of wrinkling rate can further increase the flame propagation through stratified mixture field compared to the propagation through homogeneous mixtures.

8.3.5 Analysis of mean propagation speed

The mean flame radius R_s is the representation of cumulative volume of burned gases at a given instant of time and its derivative can be considered as the mean propagation speed [Pasquier et al. (2007)]. The definition of mean propagation speed is:

$$S_{Rs} = \frac{Rs_2 - Rs_1}{\Delta t} \tag{8.3}$$

where R_{s_1} and R_{s_2} are the mean flame radius of first and second flame fronts extracted from the PIV image pairs and Δt is the time delay between them ($\Delta t = 60\mu s$).

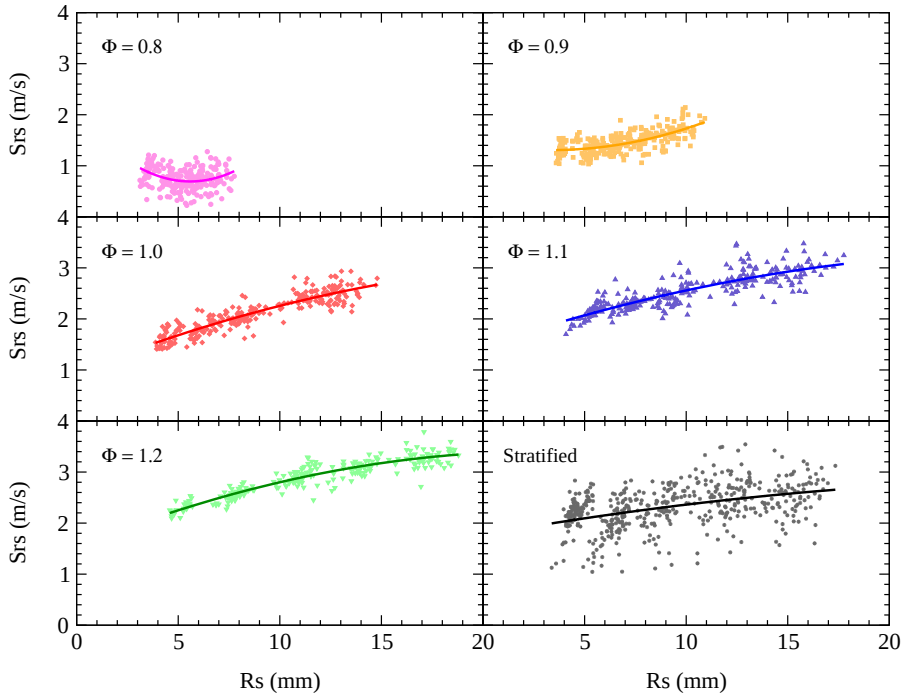

Figure 8.19: S_{Rs} as a function of Rs.

The analysis of variation of mean propagation speed as a function of mean flame radius for different cases can indicate the stratification effect on similarly stretched flame fronts. The variation of S_{Rs} as a function of R_s for different cases are shown in Fig. 8.19. A second order polynomial fit is applied to all the cases (continuous line) to know the slope. First of all, the slopes are different for lean mixtures compared to that of stoichiometric and rich homogeneous mixtures as well as

stratified case. At a particular R_s value, the mean propagation speed increases with equivalence ratio of mixture as expected. The mean propagation speed of stratified case is more than that of $\phi = 1.0$ up to $12\ mm$ and maintains that speed for larger flame fronts and also its slope is less sensitive to the mean radius compared to the slopes of homogeneous cases. That means, the initial flame propagation of stratified case is faster than the propagation of stoichiometric condition because of the availability of rich mixtures around the flame at the time of ignition and its later propagation is likely sustained by the memory effect [Ra (1999)]. The scattering of stratified case is wider than that of homogeneous cases due to the influence of variation of equivalence ratio around the ignition point. So this comparison of mean propagation speeds clearly indicates the effect of stratification on the enhancement of flame propagation.

8.4 Analysis of local variables

The global measurements revealed difference between the flame propagation through stratified and homogeneous mixtures. To analyze further in a quantitative way, we need to know the local parameters such as equivalence ratio, flame speed, fresh gas velocity and the burning velocity near the flame front. We already discussed about the measurement of velocity and equivalence ratio field and shown some examples of instantaneous cases. In this section, we explore more about the local turbulent burning velocity together with the local equivalence ratio and the local curvature in order to gain more insight of the stratified combustion.

8.4.1 Extraction of local variables

In order to extract the local variables around the flame front, we first calculated the local normal and tangential vector components along the flame front from the flame front coordinates. The flame front extracted from the first image of PIV image pair is used as a base to calculate the local velocity and equivalence ratio values. One example of the local normal and tangential velocity and the equivalence ratio extracted from the velocity and equivalence ratio fields are shown in Fig. 8.20.

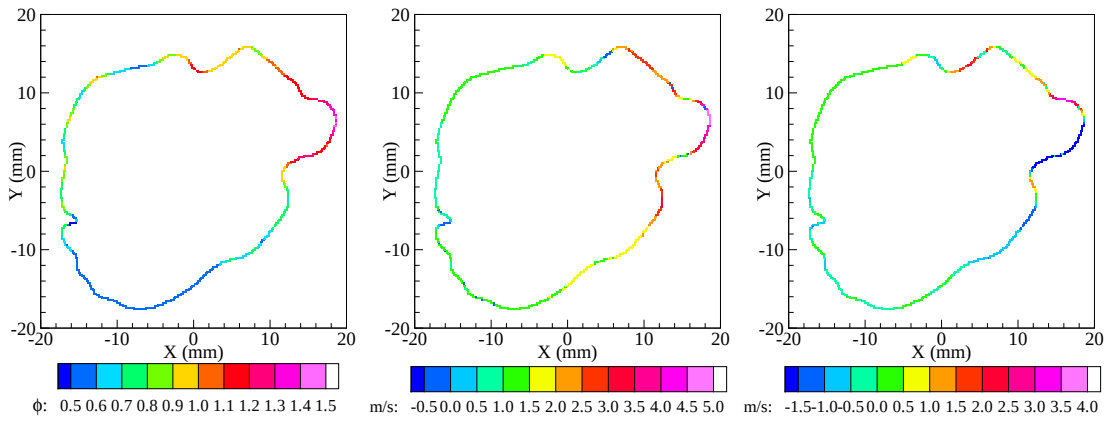

(a) Equivalence ratio ϕ (b) Normal velocity U_n (c) Tangential velocity U_t

Figure 8.20: Local values of velocity and equivalence ratio around the flame front contour.

The local velocities are measured at $0.3\ mm$ from the first flame front and the local equivalence ratio is measured at $0.9\ mm$ from the first flame front. These normal distances from the first contour for the measurement of velocity and equivalence ratio are fixed after analyzing the variation of local variables with respect to normal distance which varied from 0.1 to $1.2\ mm$ and the optimum distance is fixed where the mean of local variables reaches 95% of its maximum value. The difference in normal distances between velocity and equivalence ratio measurement is due to the difference in the influence of temperature on the olive oil particles and the anisole vapor closer to the flame front [Pasquier-Guilbert (2004)].

8.4.2 Analysis of local equivalence ratio

Analysis of distribution of local equivalence ratio around the flame front is very much essential to understand the memory effect of flame propagation. The distribution of equivalence ratio closer to stratified flame front at different timings is shown in Fig. 8.21. The mean and fluctuation of local equivalence ratio distribution at different timings are given in the table 8.2.

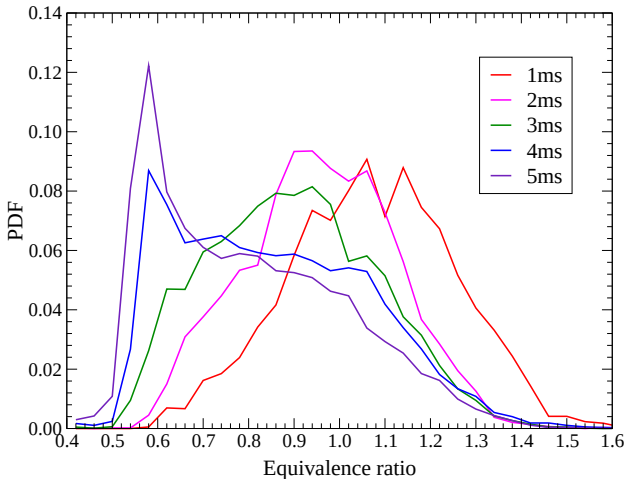

Figure 8.21: PDF of local equivalence ratio close to the flame front.

	1 ms	2 ms	3 ms	4 ms	5 ms
$\bar{\phi}$	1.07	0.96	0.90	0.86	0.80
ϕ'	0.18	0.16	0.18	0.21	0.21

Table 8.2: Mean and fluctuation of local equivalence ratio around the flame front.

At $1\ ms$, the flame fronts are surrounded by lean and rich mixtures with peak value of distribution is around $\phi = 1.0$. At $2\ ms$, the peak of distribution is shifted to around $\phi = 0.9$ with moderate distribution of rich mixtures and increased distribution of lean mixtures around the flame fronts. At $3\ ms$, the peak of distribution is shifted further to around $\phi = 0.85$ with clear reduction of presence of rich mixtures around the flames. At $4\ ms$, the distribution is slightly bimodal with a strong peak around $\phi = 0.6$ and at $5\ ms$, the peak becomes more visible and the flames are mainly surrounded by lean mixtures with very few rich mixtures around left and right side of flame fronts along the

stratified jet. The mean and fluctuations of distribution of local equivalence ratios shown in the table 8.2 also indicate that the flames are initially surrounded by rich mixtures and over a period of time, those mixtures are consumed and progressively the distribution is shifted from rich to lean mixtures. This observation of mixture distribution will be helpful to analyze the evolution of local velocities in the next section.

8.4.3 Analysis of local burning velocity

In this work, the local turbulent burning velocity is measured as local displacement speed ($S_{T,LD}$) which is the difference between the local flame propagation speed S_f and the local fresh gas velocity U_n in normal direction to the flame front [Driscoll (2008)]:

$$S_{T,LD_i} = (S_{f_i} - U_{n_i}) \tag{8.4}$$

The local flame propagation speed S_{f_i} is calculated for each coordinate (x_i, y_i) of flame front of the first image as:

$$S_{f_i} = \frac{1}{2K+1} \sum_{j=i-K}^{j=i+K} \Delta d_j / \Delta t \tag{8.5}$$

where, Δd_j is the local shortest distance between the two flame front contours of a couple of PIV images, Δt is the time delay between them and K the size of a local filter ($\Delta t = 60\mu s$ and $K = 2$ in our case). The local fresh gas velocity is measured from the instantaneous velocity field and its normal component of velocity (U_{n_i}) is measured by using the local normal vectors.

The distributions of local burning velocity for various cases are shown in Fig. 8.22. In those graphs, the unstretched laminar burning velocity (S_L^0) of corresponding homogeneous mixture is shown as black line. For all the cases, the distributions are almost symmetrical around the peak except the tail-ends. In the distributions, negative value is corresponding to the region where local flame speed is slower than local fresh gas velocity of turbulent jet or may be due to the strong flame propagation in third dimension (in Z plane), which is perpendicular to the laser sheet. In the homogeneous cases, there is no significant shift in distribution of local burning velocity over a period of time at each case. However, there is a global shift of distributions with equivalence ratios. But in the stratified case, the distribution shows faster burning velocity at $1\ ms$ compare to that of other timings. This shift in local burning velocity correlates well with shift in local equivalence ratio distribution from rich to lean mixtures.

The comparison of local burning velocities of different cases with respect to time is shown in Fig. 8.23. It clearly shows the shift in distribution with equivalence ratio of homogeneous mixtures. With the increase of equivalence ratio, the contribution of negative burning velocities in the distribution reduces due to the increase of flame propagation speed. The distribution of stratified case overlaps distribution of $\phi = 1.1$ to $\phi = 1.3$ cases at $1\ ms$ and later at $5\ ms$, it overlaps distribution of $\phi = 0.9$ and $\phi = 1.0$ cases. This clearly shows that the stratified flames are initially propagating faster than that of $\phi = 1.0$ case and later slows down due to the decrease of rich mixtures around the flame fronts. So the analysis of local turbulent burning velocities clearly shows the initial faster propagation of stratified flames compared to that of homogeneous cases. But the variation of distribution of local burning velocities over a period of time are almost constant for all the cases which is contradictory to the results observed in the analysis of mean

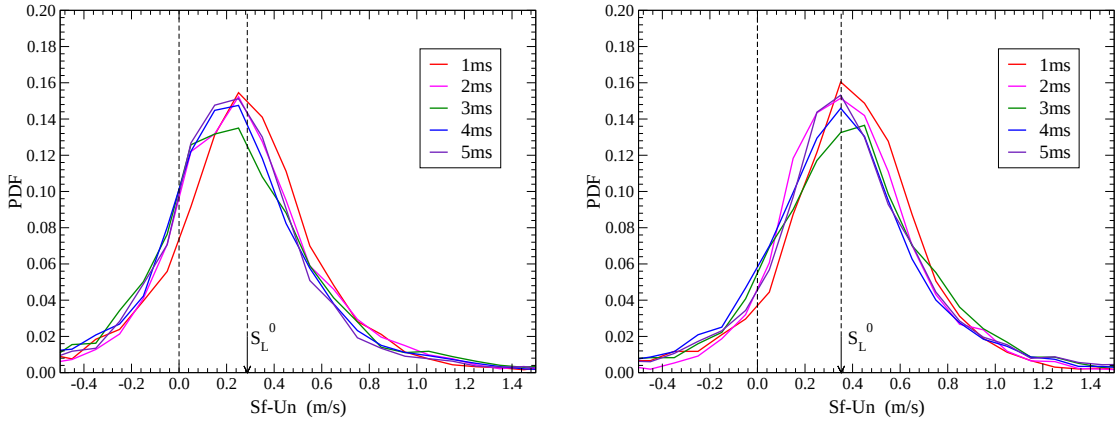

(a) $\phi = 0.8$

(b) $\phi = 0.9$

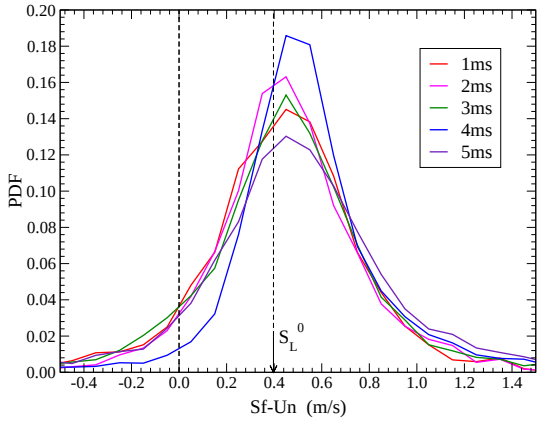

(c) $\phi = 1.0$

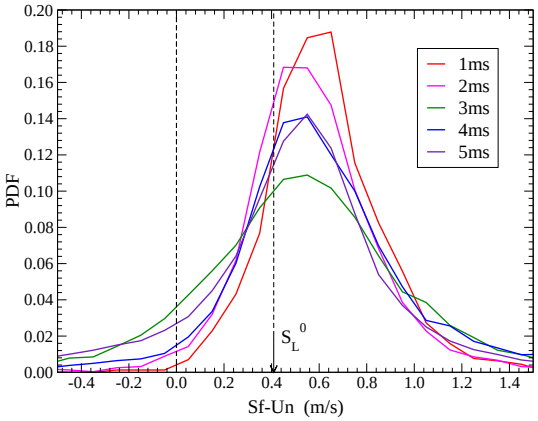

(d) $\phi = 1.1$

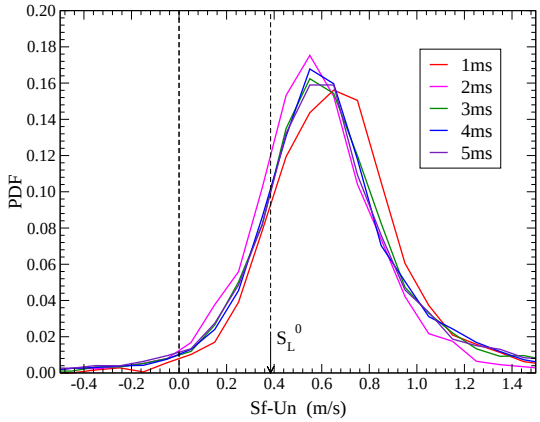

(e) $\phi = 1.2$

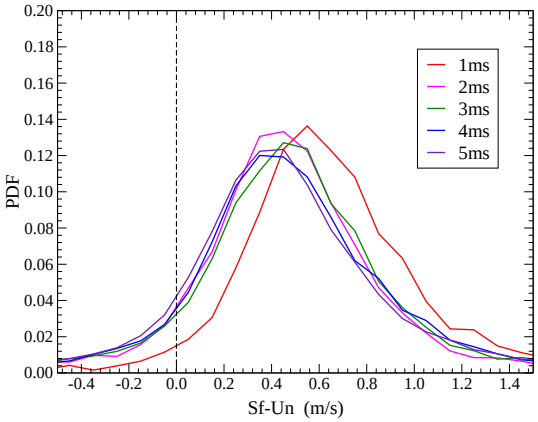

(f) Stratified

Figure 8.22: PDF of local burning velocity for homogeneous and stratified conditions.

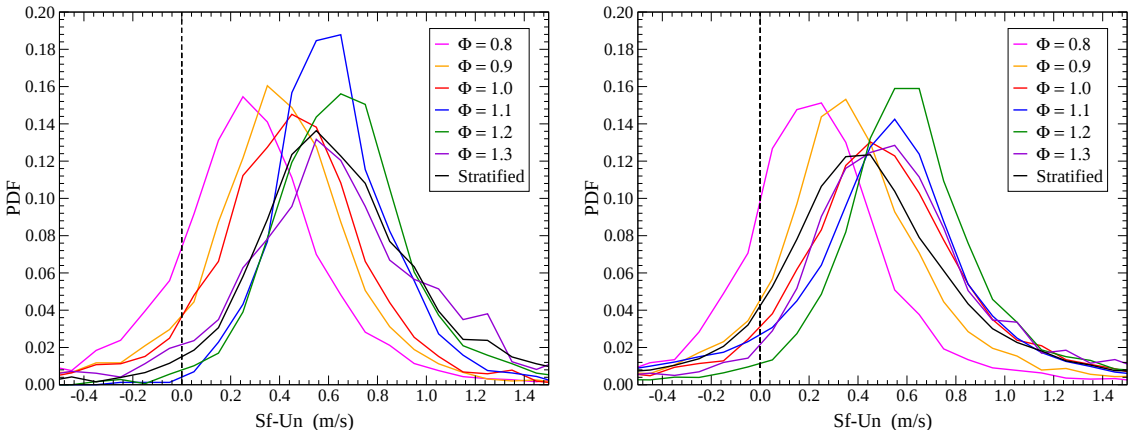

(a) 1 ms (b) 5 ms

Figure 8.23: PDF of local burning velocity at different timings.

propagation speed. Therefore, we can not draw any conclusions about the enhancement of flame propagation from this analysis alone.

8.4.4 Analysis of local curvature

We have already seen that the stratification of mixture field can enhance the wrinkling of flame fronts (§ 8.3.4). To understand that observation, an analysis of local curvature of homogeneous and stratified cases can be helpful. The local mean curvature of flame front is calculated using an expression given below [Mokhtarian and Mackworth (1986)]:

$$h_m = \frac{x'y'' - y'x''}{[(x')^2 + (y')^2]^{\frac{3}{2}}} \tag{8.6}$$

where x', y', x'', y'' are first and second order derivatives of equally spaced x and y coordinates of flame front.

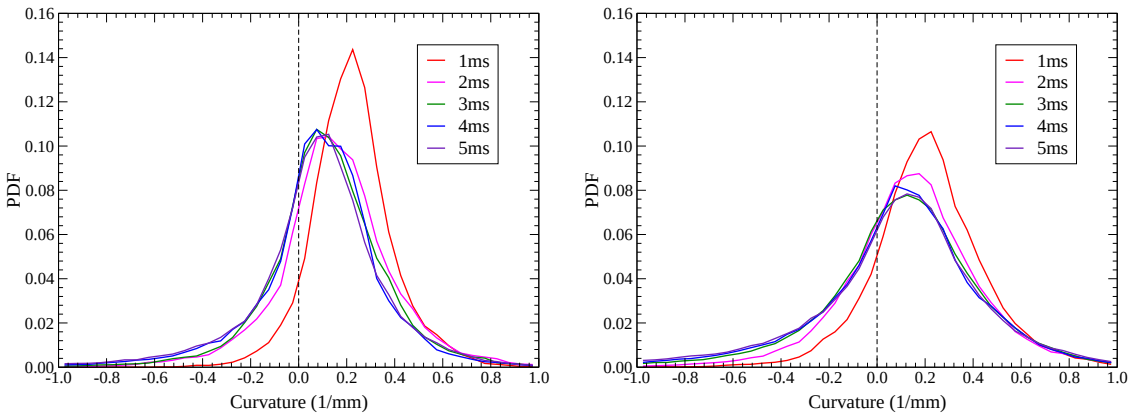

(a) $\phi = 1.0$ (b) Stratified case

Figure 8.24: PDF of curvature for different cases.

The distributions of local curvature for different cases and at different timings are shown in Figs. 8.24 and 8.25. The distributions are almost symmetrical with respect to their peak values, which are located in the positive side of curvatures. In both stoichiometric and stratified cases, the distribution at $1\ ms$ is different than the distribution of all other timings. The higher positive curvature at $1\ ms$ correlates well with initial spherical shape of mean flame front contours for all the cases observed in the previous section (§ 8.3.2). But after $1\ ms$, there is a gradual shift of distribution with peak of distribution moves towards zero curvature. Among homogeneous cases, the distribution widens with decrease of equivalence ratio because the shape of slowly propagating flames are more affected by the flow turbulence. At both $1\ ms$ and $5\ ms$, the distribution of curvature of stratified flames are wider than the distribution of homogeneous cases. But the stratified flames are propagating faster than that of $\phi = 1.0$ case (§ 8.4.3). So the distributions of curvature of stratified flames are widened due to the presence of stratified mixture field around the flame fronts and not by the flow turbulence alone. Therefore, the analysis of local curvature clearly indicates the increase of wrinkling by the stratified mixture field.

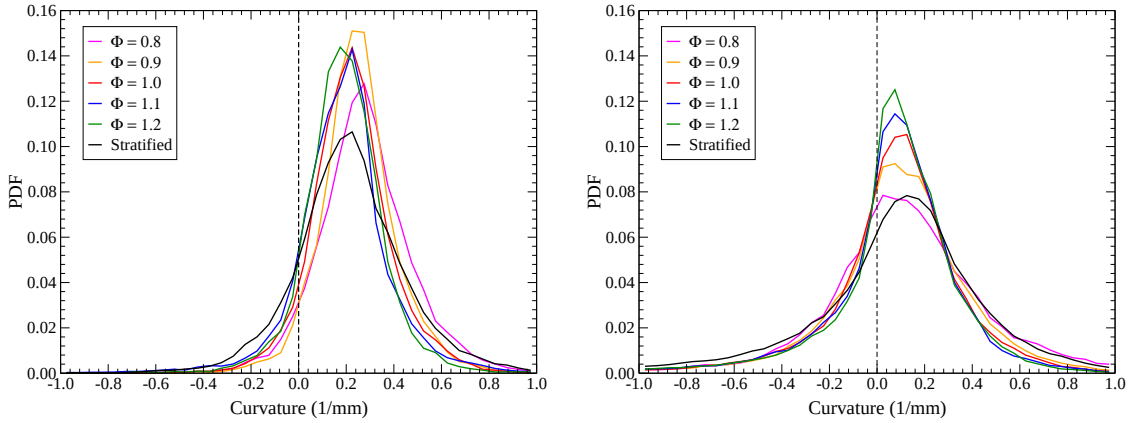

(a) 1 ms (b) 5 ms

Figure 8.25: PDF of curvature at different timings.

8.5 Influence of stratification

So far, the global and local analyses are clearly indicated the difference between homogeneous and stratified flames. But those results are not enough to show the quantitative difference between stratified and homogeneous flames. For that, we need to compare the conditioned local parameters of stratified flames with equivalent homogeneous conditions. The simultaneous measurement of velocity and equivalence ratio of flame propagation makes it possible to analyze the evolution of local burning velocity and local curvature as a function of local equivalence ratio around the flame front so that we can directly compare the stratified case with equivalent homogeneous cases.

8.5.1 Analysis of joint distribution

In this work, the joint pdf of local equivalence ratio and local curvature as well as local equivalence ratio and local turbulent burning velocity are calculated for stratified flames, thanks to the simul-

taneous measurement of flow and scalar field. The joint pdfs are shown in Figs. 8.26 and 8.27. In those figures, the modal and standard deviation of homogeneous flames are also provided as black lines with three dots for each case, where the center dot corresponds to the modal value and two other dots represent the standard deviation. These modal and standard deviation values for each homogeneous case are calculated from their pdf curves by using Gaussian interpolation fit.

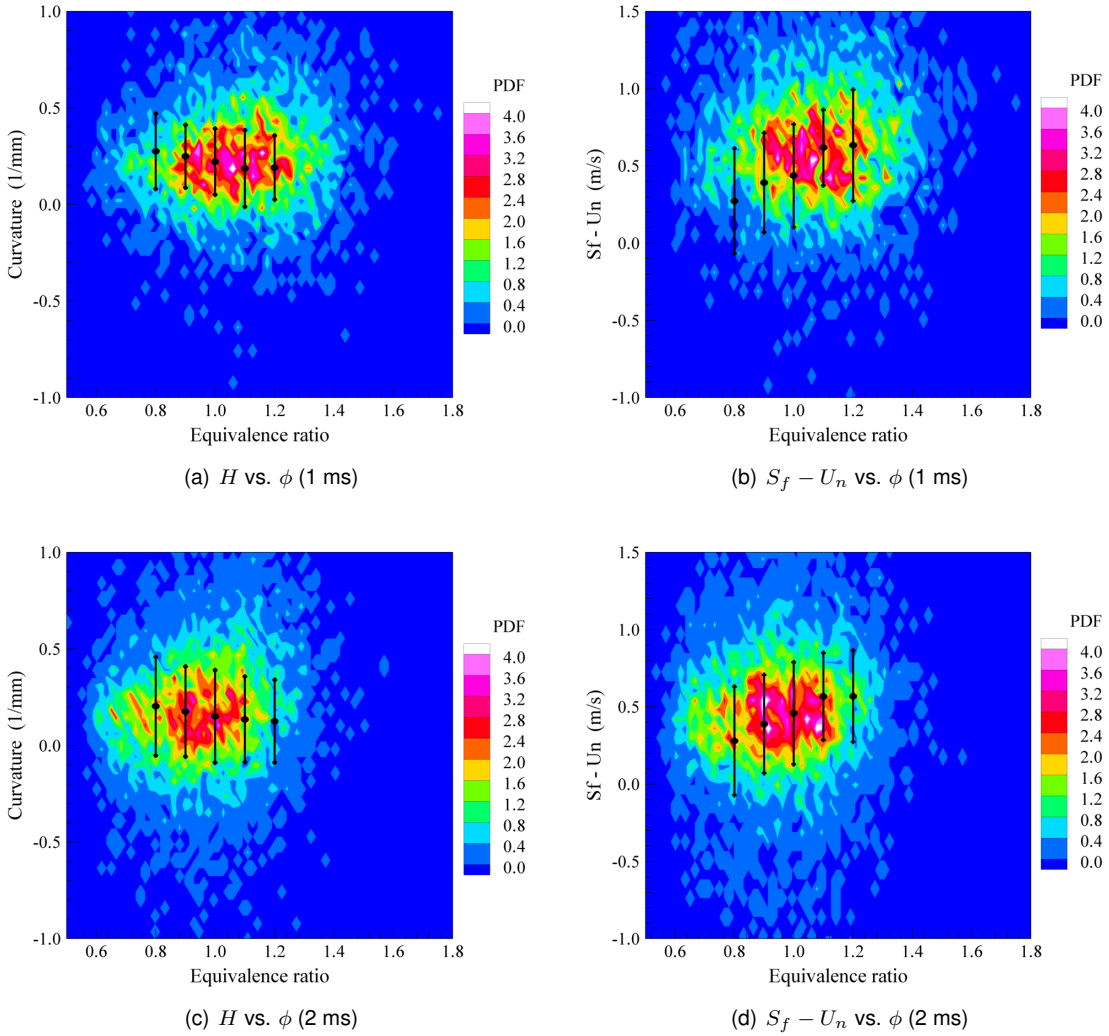

(a) H vs. ϕ (1 ms)

(b) $S_f - U_n$ vs. ϕ (1 ms)

(c) H vs. ϕ (2 ms)

(d) $S_f - U_n$ vs. ϕ (2 ms)

Figure 8.26: Joint PDF of local curvature and local burning velocity as a function of local equivalence ratio.

Globally, both joint distributions show the shifting of equivalence ratio from rich condition to very lean condition over a period of time. In the curvature versus equivalence ratio distribution, we can observe only slight variations between peak values of distribution of stratified flames with modal values of homogeneous flames. But in the case of joint distribution of local burning velocity and local equivalence ratio, we can notice clear difference between the peak values of distribution of stratified case compared to the modal values of homogeneous cases. At $1\ ms$, peak of local turbulent burning velocity of stratified case is around $0.53\ m/s$ which occurs around $\phi = 1.06$. The

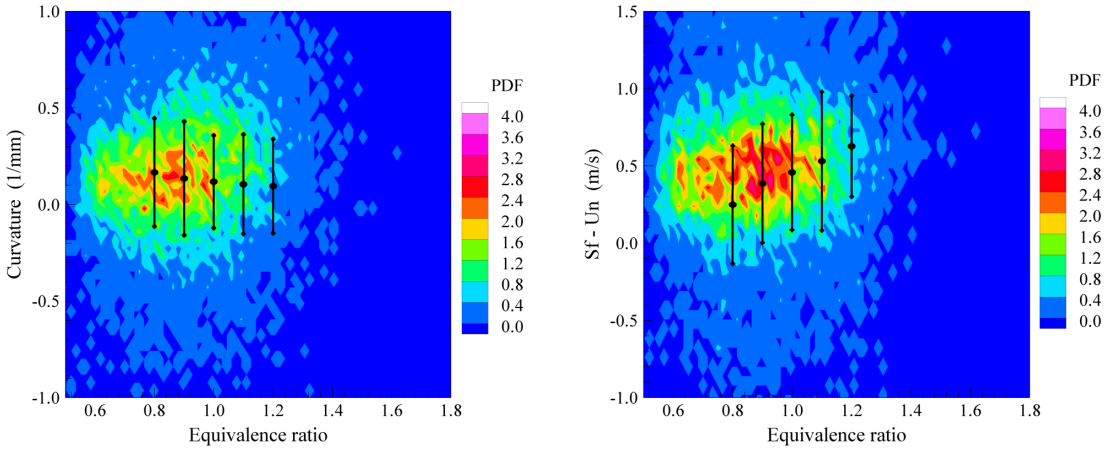

(a) H vs. ϕ (3 ms)

(b) $S_f - U_n$ vs. ϕ (3 ms)

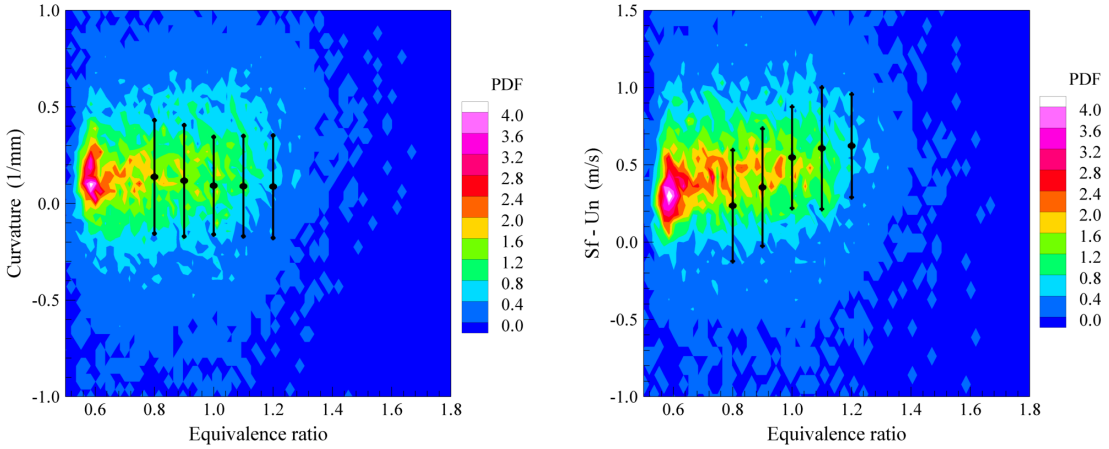

(c) H vs. ϕ (4 ms)

(d) $S_f - U_n$ vs. ϕ (4 ms)

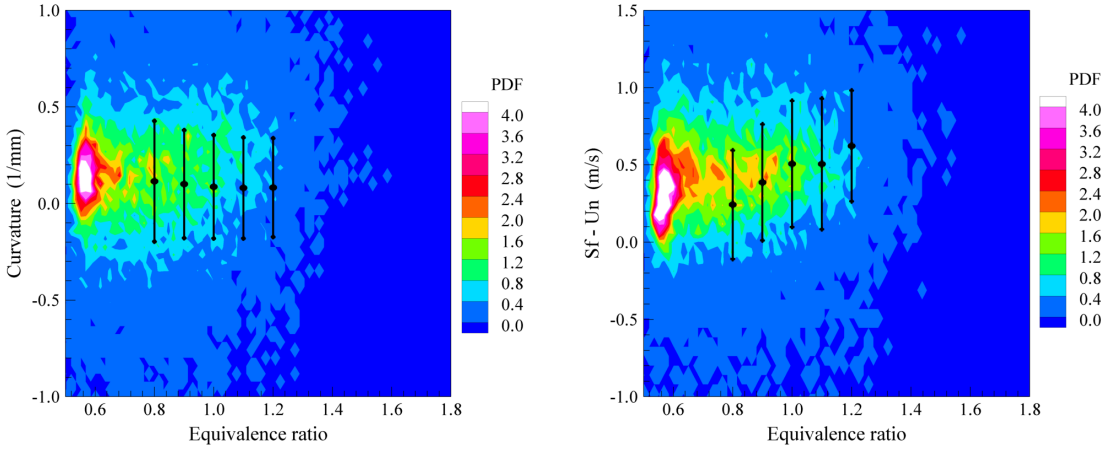

(e) H vs. ϕ (5 ms)

(f) $S_f - U_n$ vs. ϕ (5 ms)

Figure 8.27: Joint PDF of local curvature and local burning velocity as a function of local equivalence ratio.

local peaks of distribution of stratified flames are almost same with modal values of rich mixtures and higher than modal values of stoichiometric and lean mixture cases. This clearly indicates that the propagation of stratified flame is initially faster than stoichiometric case due to the presence of rich mixtures around the flame fronts. At $5\ ms$, both joint pdfs are converged around $\phi = 0.6$, indicate that the most of flame fronts are propagating through very lean mixtures. The local peaks of distribution of stratified case are higher than modal values of lean homogeneous mixture conditions. Indeed, the peak value of distribution of local burning velocity is around $0.35\ m/s$ occurs at $\phi = 0.6$. This clearly confirms the enhanced flame propagation through very lean mixtures supported by the rich and stoichiometric flame fragments of previous timings.

So from the analysis of joint pdfs, we have shown the close relationship of evolution of local curvature and local burning velocity with evolution of local equivalence ratio. Over a period of time of propagation, rich and stoichiometric mixtures around the flame fronts disappears and the peak of local burning velocity decreases from $0.53\ m/s$ to $0.35\ m/s$. In later stages, too, the local burning velocities of stratified flames propagating through lean mixtures are higher than equivalent unstretched laminar burning velocities of homogeneous mixture conditions.

8.5.2 Analysis of local conditioned burning velocity

The analysis of joint pdfs clearly showed the enhancement of flame propagation through stratified mixture field. But to quantify the enhancement, we have to isolate the mixture stratification effect from the turbulence effect. For that, we need to compare the local burning velocity conditioned on the local equivalence ratio of stratified flames with local burning velocity of equivalent homogeneous cases. Simultaneous measurements of velocity and equivalence ratio allow us to calculate the local burning velocities conditioned by the local equivalence ratios. The local conditioned velocities are measured at each equivalence ratios with a range of $\pm 0.02\ \phi$.

The distribution of conditioned local burning velocities of stratified flames as a function of time at different equivalence ratios are shown in Fig. 8.28. In lean mixture conditions, the distribution of local burning velocity at $1\ ms$ is different from the distributions of all other timings. But in stoichiometric and rich mixture conditions, there is no clear difference between the distributions over a period of time. Actually, the flame stretch rate varies with time and its influence on local burning velocity varies with equivalence ratio of mixtures. For $\phi = 0.9$, the stretch effect is very small on local burning velocity yet we can see clear shift of distribution between $1\ ms$ and $2\ ms$. Indeed, the joint distribution of local burning velocity versus local equivalence ratio has shown that the stratified flames are initially surrounded by rich and stoichiometric mixtures with very few lean mixtures and the adiabatic flame temperatures of rich mixtures are at least $200\ K$ higher than that of lean mixture conditions [Law (2006)]. So the enhanced flame propagation through lean mixtures at initial stage is due to the influence of hot burned gases of rich mixtures around the flame fragments of lean mixtures.

The comparison of conditioned local burning velocity distributions of stratified flames with distributions of local burning velocities of equivalent homogeneous flames are shown in Fig. 8.29. In that graphs, continuous lines represent the stratified case and dashed lines represent the homogeneous case. For each distribution, the modal value is calculated by using Gaussian interpolation fit. The modal values are also shown in that graphs as straight lines along X axis where black line represents the unstretched laminar burning velocity (S_L^0) of propane-air mixture for the

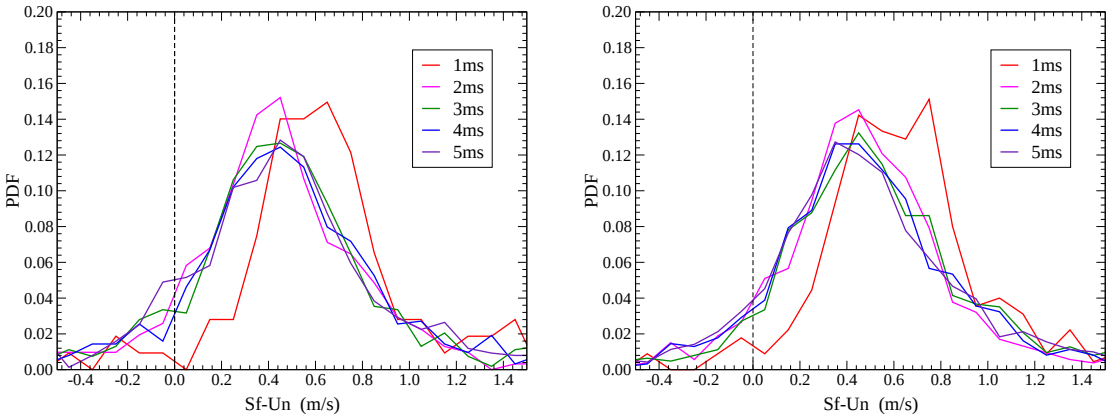

(a) $\phi = 0.8 \pm 0.02$

(b) $\phi = 0.9 \pm 0.02$

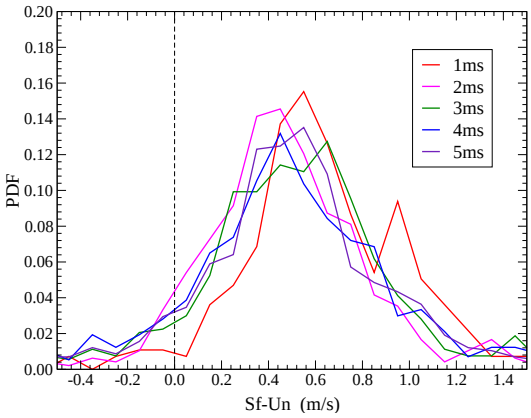

(c) $\phi = 1.0 \pm 0.02$

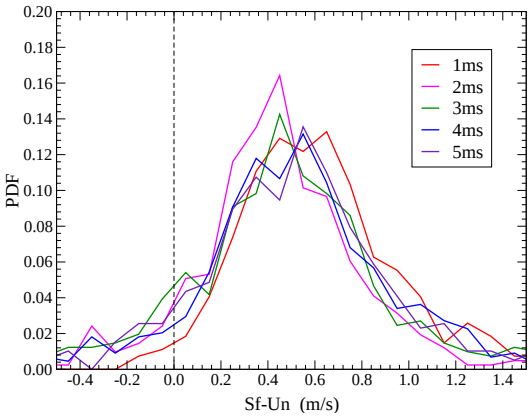

(d) $\phi = 1.1 \pm 0.02$

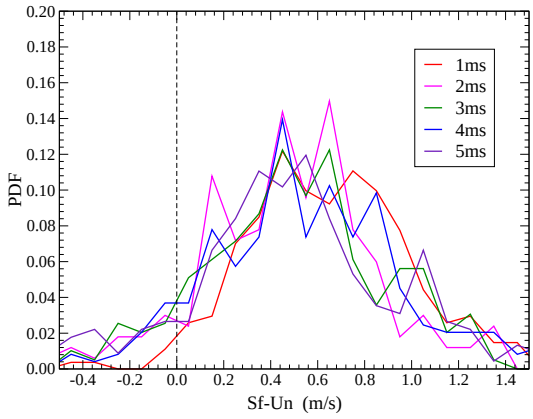

(e) $\phi = 1.2 \pm 0.02$

Figure 8.28: PDF of conditioned local burning velocity of stratified flames at different equivalence ratio.

corresponding equivalence ratio. These unstretched laminar burning velocities are taken from available literature results. The modal values for different mixture conditions are also listed in the table 8.3. For $\phi = 0.8$, the pdfs of stratified case are shifted to higher values of velocity than that of homogeneous case at early as well as later stage of propagation. The modal values of homogeneous case are lower than unstretched laminar burning velocity whereas the modal values of stratified case are almost two times more than that of homogeneous case. Also, the distribution of stratified case at $5\ ms$ is wider than the distribution of homogeneous case. For $\phi = 0.9$, the modal value of homogeneous case is more than unstretched laminar burning velocity at $1\ ms$ and almost equal at $5\ ms$. The distribution of stratified case at $1\ ms$ is shifted to higher velocity compared to the distribution of homogeneous case but almost same at $5\ ms$. Also the modal value of stratified case at $1\ ms$ is almost 1.5 times more than that of homogeneous case and later becomes 1.2 times that of homogeneous case. For $\phi = 1.0$, the distributions are almost same except stratified case at $1\ ms$. All the modal values are higher than unstretched laminar burning velocity. The modal value of stratified case is 1.2 times more than that of homogeneous case at $1\ ms$ and almost equal at $5\ ms$. For $\phi = 1.1$, the distributions are almost same except homogeneous case at $1\ ms$. The modal value of homogeneous case is 1.1 times more than that of stratified case at $1\ ms$ and almost equal at $5\ ms$. For $\phi = 1.2$, the distributions of stratified case are wider and shifted to lower values compared to the homogeneous case. The modal value of homogeneous case is almost same with stratified case at $1\ ms$ but 1.3 times more than that of stratified case at $5\ ms$.

ϕ	S_L^0 (cm/s)	Modal velocity (cm/s)			
		Conditioned		Homogeneous	
		1 ms	5 ms	1 ms	5 ms
0.8	28.7	59.4	44.0	27.2	21.5
0.9	35.2	59.3	40.9	40.1	34.0
1.0	39.7	55.5	47.8	45.3	48.2
1.1	40.9	53.8	50.4	59.1	53.8
1.2	38.5	62.0	44.3	63.3	58.5

Table 8.3: Modal values of local burning velocities of stratified and homogeneous cases.

So the comparison of conditioned data of stratified case with equivalent homogeneous case clearly quantified the enhancement of flame propagation through stratified mixture. Indeed, the propagations of stratified flame fragments through lean mixtures are around 1.2 to 2 times faster than the propagation of equivalent homogeneous flames. This experimental result clearly proved that stratified flames exhibit faster propagation through very lean mixtures when ignited around stoichiometric mixture due to the memory effect.

The enhancement of flame propagation by stratification can be further confirmed by analyzing the flame propagation through very lean mixture which is $\phi = 0.6$ in our work. The distribution of local curvature and local burning velocity of stratified flames conditioned for $\phi = 0.6$ are shown in Fig. 8.30. For $\phi = 0.6$, there are no sufficient data at $1\ ms$ and $2\ ms$ after the ignition. Both local curvature and local burning velocity distributions are not varying much over time. The modal values of distribution of local burning velocity are around $0.3\ m/s$ which is at least three

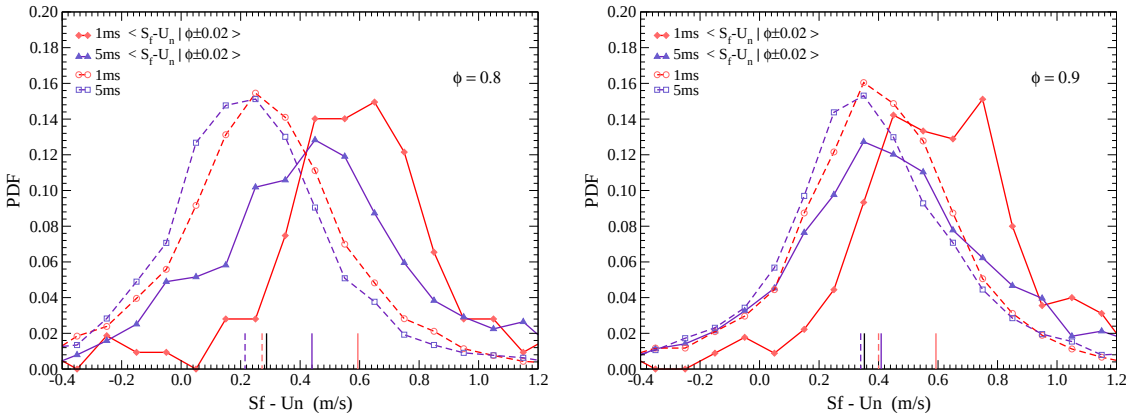

(a) $\phi = 0.8$

(b) $\phi = 0.9$

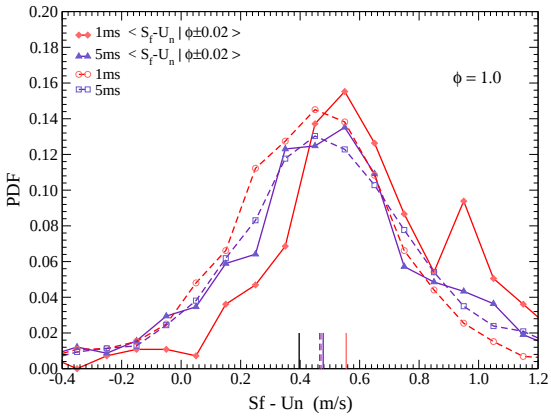

(c) $\phi = 1.0$

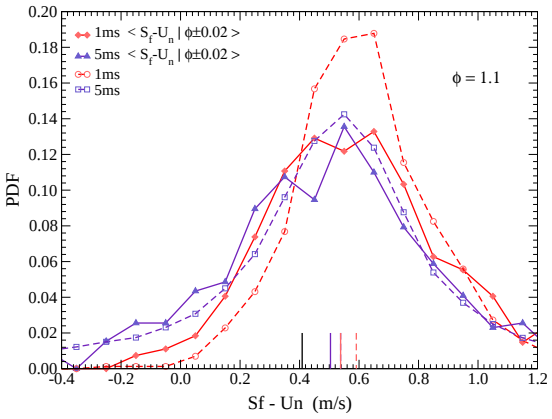

(d) $\phi = 1.1$

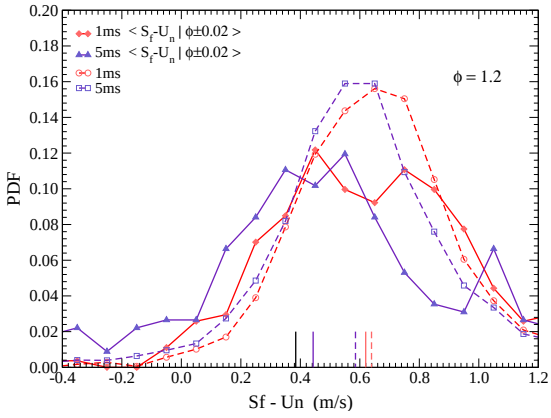

(e) $\phi = 1.2$

Figure 8.29: Comparison of conditioned local burning velocities of stratified case with equivalent homogeneous cases.

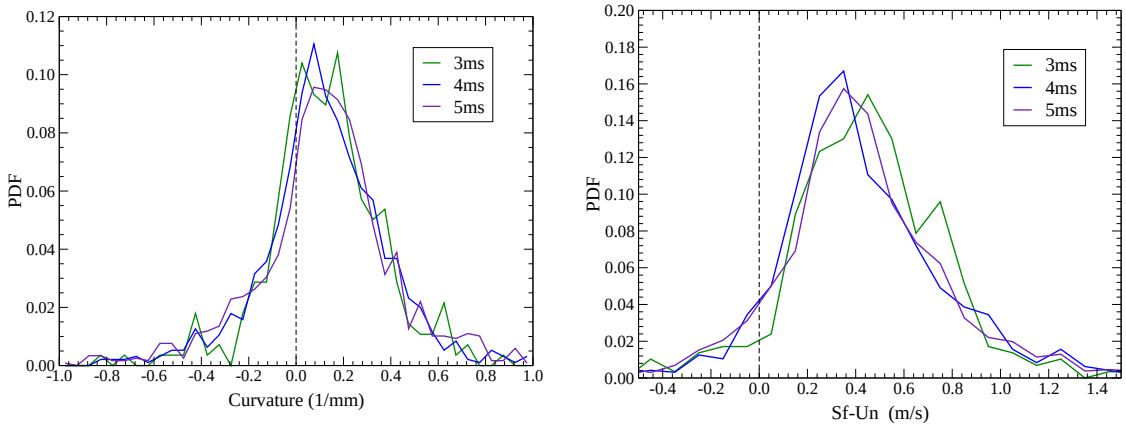

(a) Distribution of local curvature

(b) Distribution of local burning velocity

Figure 8.30: PDF of conditioned local burning velocity and local curvature of stratified flames at $\phi = 0.6$.

times more than unstretched laminar burning velocity of homogeneous flame. So this higher flame propagation of stratified flame through very lean mixture over a period of time confirms the memory effect of stratified flames. Actually, in this work, the mixture condition around ignition point is slightly rich ($\phi = 1.07$) whereas Pasquier-Guilbert (2004) previously carried out experiments in the same configuration with stoichiometric condition around ignition point at the time of ignition and the enhancement of propagation observed in this work is higher than that of their observation. So, the initial availability of rich mixtures around the flame front produces hot burned products and those hotter gases supports the flame propagation through very lean mixtures and also extends their flammability limits.

8.6 Conclusions

In this chapter, we discussed the results of turbulent flame propagation through homogeneous and stratified mixture fields. First, the instantaneous flow and scalar field of stratified combustion are discussed. Then mean flow and scalar field of stratified and homogeneous combustion cases are discussed. After that, the evolution of mean flame front contours for different cases are compared which shown more elongation of stratified flames compared to that of homogeneous flames. Next, the mean flame front radius and mean propagation speed are analyzed which indicated the enhancement of flame propagation through stratified mixture fields. Finally, the local parameters such as local curvature and local burning velocities are analyzed. For that, the extraction of local variables near the flame front is explained. Then the local curvatures for different cases are compared which showed that the stratified flames are wrinkled more than that of homogeneous flames. The local burning velocity is then measured as the difference between the local flame propagation speed and the local normal fresh gas velocity. The comparison of local burning velocities for different cases indicated the variation of propagation with equivalence ratio for homogeneous cases and high initial flame propagation for stratified case. Then local burning velocities are conditioned based on local equivalence ratios and compared with local burning velocities of homogeneous cases at $1\ ms$ and $5\ ms$ after ignition. The comparison revealed the

enhancement of flame propagation through stratified mixtures at lean conditions compared to the equivalent homogeneous conditions. In conclusion, the stratified mixture field increases the flame front wrinkling, enhances the flame propagation and supports the propagation through very lean mixtures.

Chapter 9

Local laminar burning velocity measurement

Abstract. *Two original methods have been developed for the accurate measurement of local flame speed and local fresh gas velocity near flame front from pair of particle images. The local laminar burning velocity is measured as a direct difference between the local flame speed and the local fresh gas velocity. The accuracy and reliability of new methods have been evaluated from two complementary approaches based respectively on synthetic images of particle and on the well-established configuration of outwardly propagating spherical flames. The measurements of the local laminar burning velocity of propane-air flames are compared in term of unstretched laminar burning velocity to the results available in the literature.*

9.1 Introduction

The experimental investigation on turbulent stratified combustion has revealed the importance of local measurements of flame propagation in order to understand those kinds of complex combustion phenomenon. Despite the moderate accuracy of prediction of local turbulent burning velocity due to the absence of third component of velocity vector in the calculation, we have successfully demonstrated the effect of mixture stratification on flame propagation compared to that of equivalent homogeneous cases. Indeed, the stratification effect on flame propagation can be analyzed with greater accuracy, if we investigate the stratified flames under laminar flow conditions where the influence of third component of velocity vector could be negligible. But the main challenge to that investigation is the requirement of suitable post-processing tools for the accurate measurement of local flame speed and local fresh gas velocity of laminar stratified flames. So in this work, we have developed two original methods for the accurate measurement of local flame speed and local fresh gas velocity near flame front from pair of particle images. Then local laminar burning velocity is measured as the difference between the local flame speed and the local fresh gas velocity at the entrance of the flame zone. The accuracy and reliability of two methods have been evaluated from two complementary ways based respectively on synthetic images of particle [Lecordier and Westerweel (2004)] and on the well-established configuration of outwardly propagating spherical flames [Bradley et al. (1996)]. For different equivalence ratios of propane-air

mixture, the local laminar burning velocity has been measured as a function of the local flame stretch and the local instantaneous measurements have been compared to the statistical results available in the literature. This chapter explains the newly developed methods and the experimental results obtained from the spherically propagating propane-air flames for the validation purpose.

9.2 Local instantaneous laminar burning velocity

The laminar burning velocity can be determined directly as the difference between the local flame speed S_b and the local fresh gas velocity u_g as a function of flame stretch rate [Bradley et al. (1996), Lecordier (1997)]

$$u_n(k) = S_b(k) - u_g(k) \tag{9.1}$$

This laminar burning velocity can be related to the flame stretch rate through a linear expression within the limit of moderate stretch and far from the extension limit as:

$$u_n(k) = u_n^0 - L^n \cdot k \tag{9.2}$$

where, u_n^0 is the unstretched laminar burning velocity at zero stretch and L^n is the Markstein length in the fresh gas region. This unstretched laminar burning velocity can also be obtained from the flame speed and fresh gas velocity measurements by using density ratio of burned and unburned gases as explained in the literature review chapter.

The measurement of local instantaneous laminar burning velocity needs accurate calculation of local flame speed and local fresh gas velocity near flame front. The flame speed can be calculated from the evolution of flame radius. But this approach cannot measure the local flame speed. So a new technique has been developed to directly measure the flame speed from the flame front contours. The measurement of local fresh gas velocity near the flame front is a challenging one due to the requirement of high spatial resolution. For that, a new PIV approach has been developed based on the adaptive interrogation scheme which takes into account the local topology as well as local fresh gas movement. The next sections explain the local flame speed and local fresh gas velocity measurements.

9.3 Measurement of local flame speed

One example of particle image pair of a spherically expanding laminar flame front captured after $4ms$ from ignition is shown in Fig. 9.1. The time delay between the two images is fixed as $\Delta t = 300\ \mu s$ based on the image magnification and the mean flame propagation speed. The fresh gas region is well represented by the Mie scattering of the seeding particles and the burned gas region is represented by the absence of seeding particles which are evaporated and completely burnt through the very sharp temperature gradient of the flame front [Boyer (1980)]. Due to the very thin flame thickness, the isothermal surface of particle evaporation can often be assimilated with very low errors to the flame front location. For the flame speed, that error becomes negligible because all the isothermal surfaces in the flame have almost the same velocity [Bradley et al.

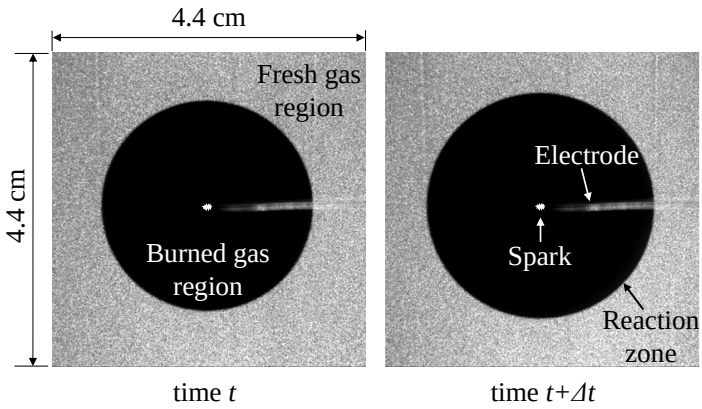

Figure 9.1: PIV image pair of spherically expanding laminar premixed propane-air flame.

(1996)]. The first step of flame speed measurement is the extraction of flame front coordinates from the PIV image pair. The coordinates of flame front are extracted with sub-pixel resolution by using the newly developed extraction tool which is explained in the appendix (§ A). A closer view of extracted flame front is shown in Fig. 9.2. Though the flame front is extracted with high accuracy,

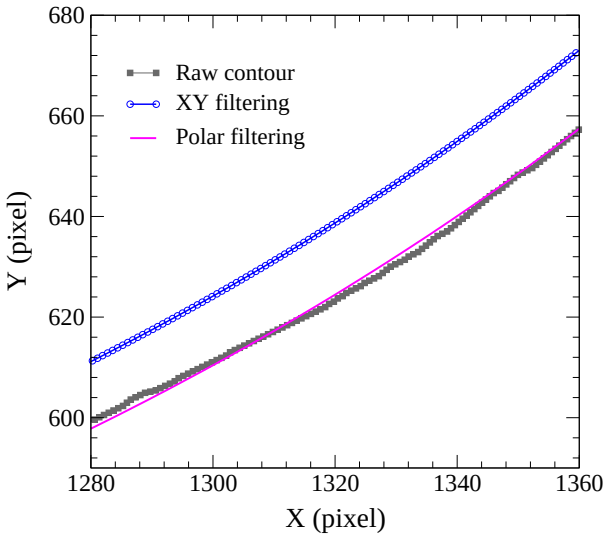

Figure 9.2: Extracted raw contour and filtered contours.

still the contour is affected by the limited signal to noise ratio close to the flame front. But for an accurate local measurement of flame speed, the contour has to be filtered. So after the extraction step, the flame front coordinates are sampled in Cartesian system at equal space as function of independent variables $s : x = f(s)$ and $y = f(s)$, where s corresponds to the curvilinear distance relative to the starting point on the contour. Then 1D low pass filter based on Gaussian weighted moving average scheme is applied to the independent variables. One example of extracted raw contour and the filtered contour (XY filtering) is shown in Fig. 9.2. The filtration technique has removed all the small wrinkles on the flame contour, but has a tendency to induce a spatial shift of the flame front position towards the center of flame front. We found that the magnitude of the shift is related with size of Gaussian filter and radius of flame front. So this filtering technique was

inappropriate to the accurate local flame speed measurement and an adapted filtration scheme has been developed. Its principle consists in applying the filtration step on the polar coordinates of contour rather than on Cartesian coordinates and projecting back the filtered coordinates to the Cartesian coordinates. The polar transformation of the flame front contour starts from the determination of the global center (x_c, y_c) and the mean radius of flame by using the least square circle (LSC) fit technique which is explained in the appendix (§ B). The local distance (d_{θ_i}) of each point of the flame front coordinate (x_i, y_i) to the center as a function of angle (θ) is then calculated by the following expression:

$$d_{\theta_i} = \sqrt{(x_c - x_i)^2 + (y_c - y_i)^2} \tag{9.3}$$

with $tan(\theta_i) = (y_i - y_c)/(x_i - x_c)$. Next, the local distance is filtered by 1D Gaussian weighted moving average scheme. One example of measured and filtered local distances as a function of angle is shown in Fig. 9.3.

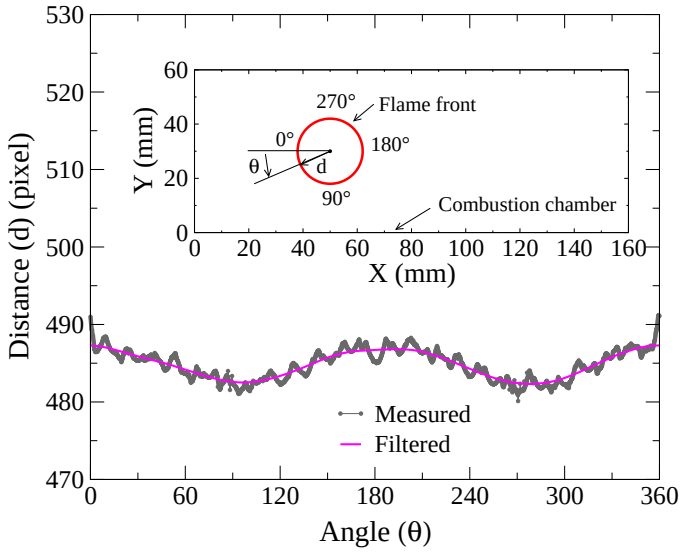

Figure 9.3: Measured and filtered local distances.

As expected, all the small wrinkles related to the seeding are well filtered and only a large oscillation due to the wall confinement persists. More discussion about this wall confinement effect is given in the later section (§ 9.7.3). Finally, the filtered distance is converted back to the Cartesian Coordinates. The filtered contour by the new method (Polar filtering) shows good agreement in mean position with the raw contour (Fig. 9.2).

Finally, the local flame speed S_{b_i} is calculated for each coordinate (x_i, y_i) of flame front of the first image as:

$$S_{b_i} = \frac{1}{2K+1} \sum_{j=i-K}^{j=i+K} \Delta d_j / \Delta t \tag{9.4}$$

where, Δd_j is the local shortest distance between the two flame front contours of a couple of PIV images, Δt is the time delay between them and K the size of a local filter ($\Delta t = 300\mu s$ and $K = 2$ in our case). The local flame stretch rate is then calculated based on the local flame speed and the mean radius of flame front calculated by the least square circle fit technique.

9.4 Measurement of local fresh gas velocity

The structure of laminar premixed flame consists of two main zones, namely the preheat zone which is chemically inert, and the reaction zone. A schematic representation of reaction and preheat zone for an outwardly propagating spherical flame is shown in Fig. 9.4. In that figure,

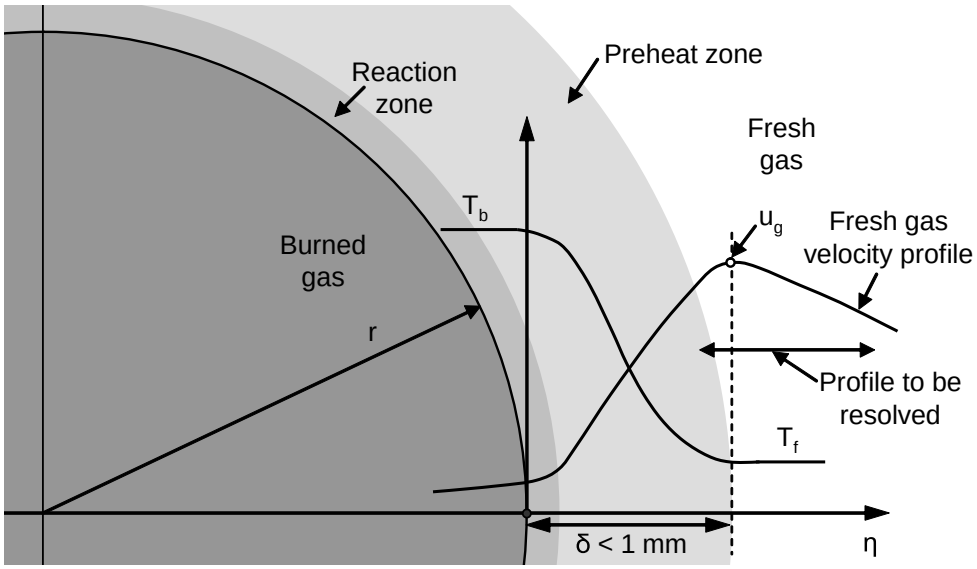

Figure 9.4: Conceptual fresh gas velocity profile near the flame front region.

the temperature profile along the direction normal (η) to the flame front is shown. The local temperature varies from ambient temperature ($T_f = 300\ K$) at the preheat zone to the flame temperature ($T_b \approx 2000\ K$) at the reaction zone. This sharp change in temperature causes variation of density through the flame front and influences the fresh gas velocity near the flame front. The fresh gas velocity profile near the preheat zone of flame front reaches maximum, which characterizes the beginning of the heat release influence on the fresh gas velocity [Groot and De Goey (2002)]. The challenging part of the measurement is to resolve the velocity profile closer to the flame front in order to find the maximum point corresponds to the local fresh gas velocity (u_g).

The standard cross-correlation PIV technique is initially applied to the particle pairs to optimize the various experimental parameters such as seeding concentration, time delay between image pair, laser energy, lens and so on. One example of velocity vector field calculated by the standard PIV technique with interrogation windows of 32 $\times$ 32 pixels is shown in Fig. 9.5. The predicted velocity vector field clearly shows the fresh gas expansion. But the velocity vectors are not well predicted near the flame front because of the sampling of interrogation areas in both burned and fresh gas regions close to the flame front as shown in Fig. 9.6. The use of solid particles could be a solution to solve the problem of seeding particle disappearance in the flame [Armstrong (1992)], but the large variation of seeding concentration due to the gas density change would lead to the similar problem for the standard PIV algorithm besides additional problem to the flame front localization. One solution to the sampling problem has been proposed by Lecordier et al. (1999). Their approach is to rotate and relocate the interrogation window to the flame front region by using the local normal vector as shown in Fig. 9.6. By this way, the interrogation windows will

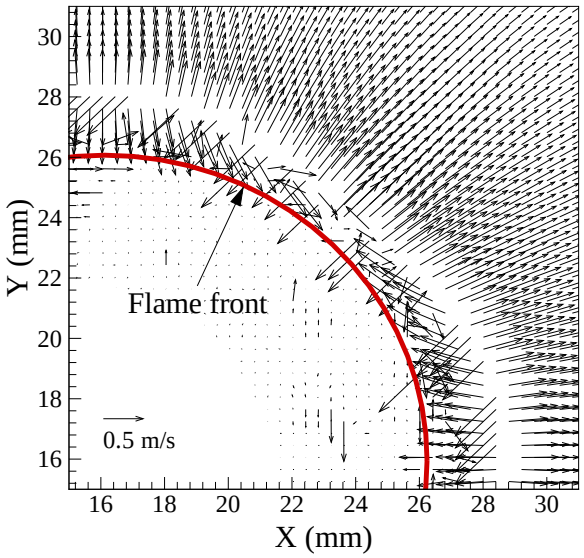

Figure 9.5: Velocity vector field calculated by the classical PIV technique.

be always sampled in the fresh gas region. Nevertheless, the sides of the interrogation window being not aligned with the streamlines induces by the gas expansion, large velocity variations within the interrogation window make reliable velocity measurements more or less inaccessible to that approach, especially for the smallest flame radius. In order to improve spatial resolution and accuracy of measurement of fresh gas velocity profile, an original interrogation window reshaping technique has been developed. The details of the new PIV algorithm are given in the following section.

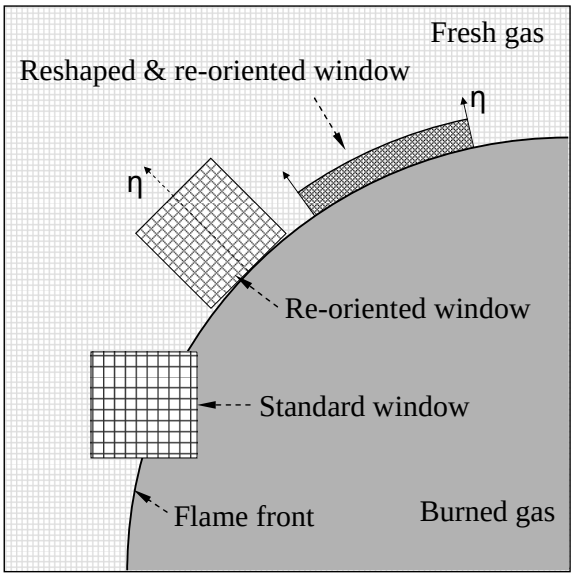

Figure 9.6: Reshaping and re-orienting the PIV interrogation window.

9.5 New PIV algorithm

The new algorithm has been developed based on the adaptive interrogation window scheme which considers both local topology of flame front and the gas expansion effect. The principle of the algorithm is depicted in the Fig. 9.7. In that figure, W_1 and W_2 are the interrogation windows sampled from first and second images captured at time t and $t + \Delta t$, respectively. The shape of the interrogation window is continuously modified to suit the local topology of the flame front. The row pixel values of interrogation window are sampled along the flame front coordinates and the column pixel values are sampled perpendicular to the flame front coordinates by using local normal vectors and the relative normal distance from the flame front coordinates. The pixel intensities within interrogation windows are interpolated from the 3 $\times$ 3 surrounding pixels of particle image by using a 2D polynomial interpolation of second order. The main advantages of this adaptive interrogation window sampling technique are, first to continuously compensate the particle pattern deformation induced by the gas expansion ahead the flame and second the possibility to use very thin interrogation windows in order to improve the measurement of the velocity gradient in the normal direction to the flame.

Particle matching:

Unlike standard PIV algorithm, the velocity measurement is extracted from a 1D correlation signal. This signal is constructed from a continuous shift along the normal between the two interrogation windows. For a single velocity measurement at a fixed position Δd ahead the flame, the first interrogation window W_1 is placed at a distance Δd relative to the flame position at time t (Fig. 9.8) and is sampled as previously described. The first interrogation contains the particle pattern which has to be found in the second image of particle. The matching procedure consists in shifting and stretching the second interrogation window W_2 in the image at $t + \Delta t$ as depicted in Fig. 9.8. This continuous window shift is performed by step of one pixel between the positions δ_{min} and δ_{max}. At each position $\Delta d + \delta$ of the second interrogation window, the product pixel-to-pixel $W_1(\Delta d) * W_2(\Delta d + \delta)$ is performed and the maximum is extracted. The variation of the maximum is then plotted as a function of the interrogation window shift δ as shown in Fig. 9.8. On that graph, the optimal shift between the interrogation windows which maximizes the particle matching between the particle image pair corresponds to the peak position. The particles displacement with sub-pixel accuracy is then evaluated using 1D Gaussian fit on three points centered on the maximum [Willert and Gharib (1991)].

Construction of fresh gas velocity profile:

In order to measure the velocity profile ahead the flame, the first interrogation W_1 is moved pixel by pixel in the direction normal to the flame front (Fig. 9.9). For each new position of W_1, the normal velocity is then calculated by the particle matching procedure described previously. The velocity measurement is carried out up to a maximum distance of $1.2\ mm$ to the flame front. One example of fresh gas velocity profile ahead the flame is shown in Fig. 9.9 as a function of flame distance Δd. The variation of the velocity profile and the magnitude of the velocity gradients are in accordance with those predicted by simulation in a comparable situation [Groot and De Goey (2002)]. The maximum of velocity, which corresponds to the heat release effect on fresh gas, is clearly observed and in this work is extracted by applying fourth degree polynomial fit on the velocity profile (Fig. 9.9). From that profile, we can notice that the first velocity measurement are located around $200\ \mu m$ ($\approx$ 10 pixels) ahead the flame and that the maximum is predicted

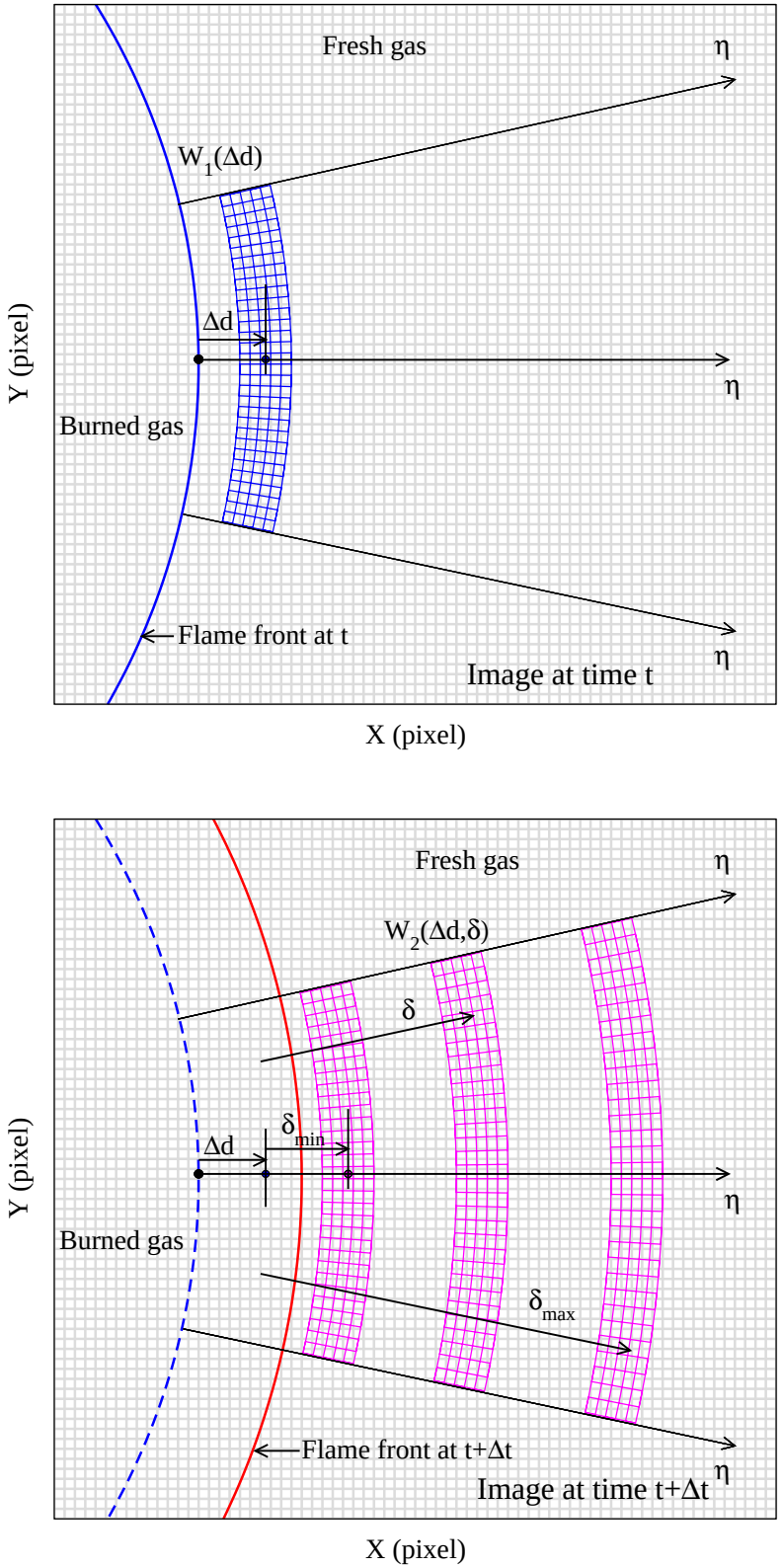

Figure 9.7: Principle of measuring the fresh gas velocity near preheat zone of flame front.

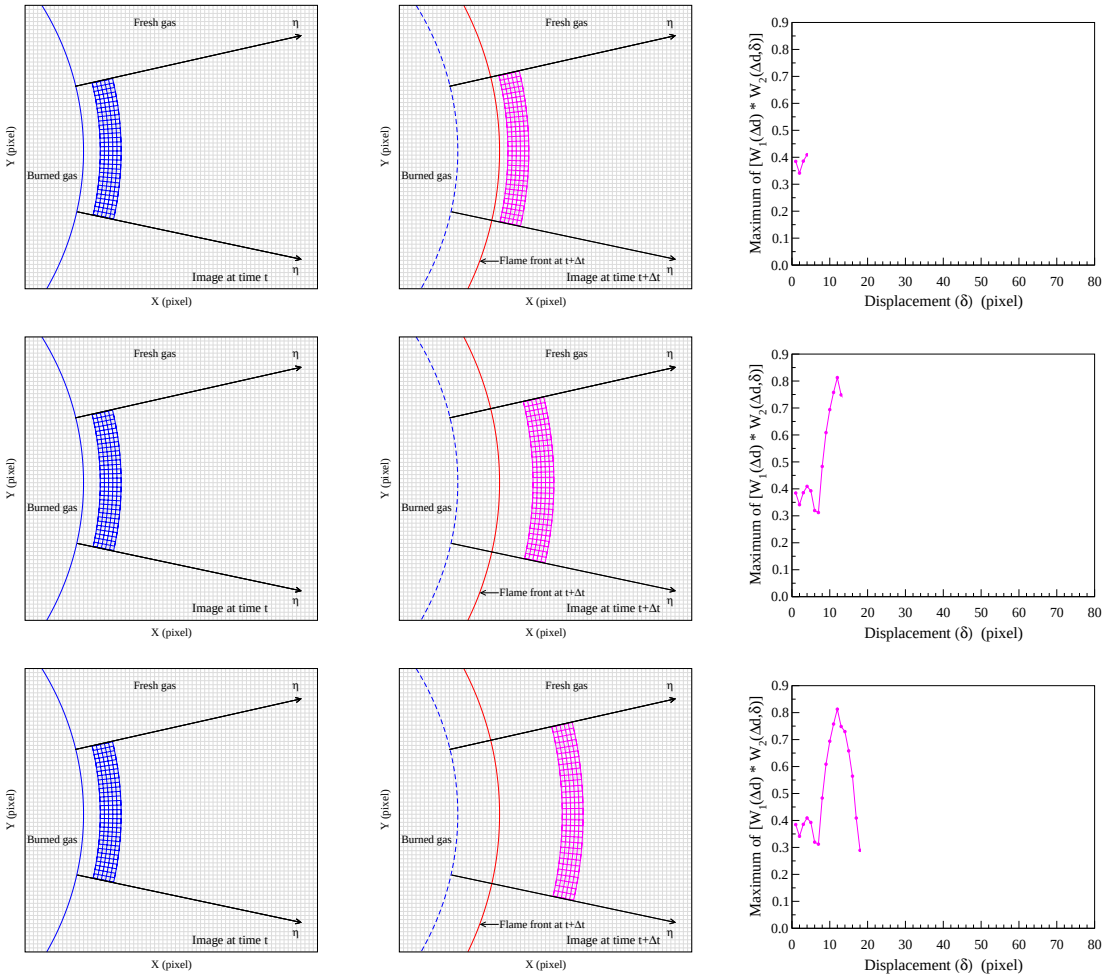

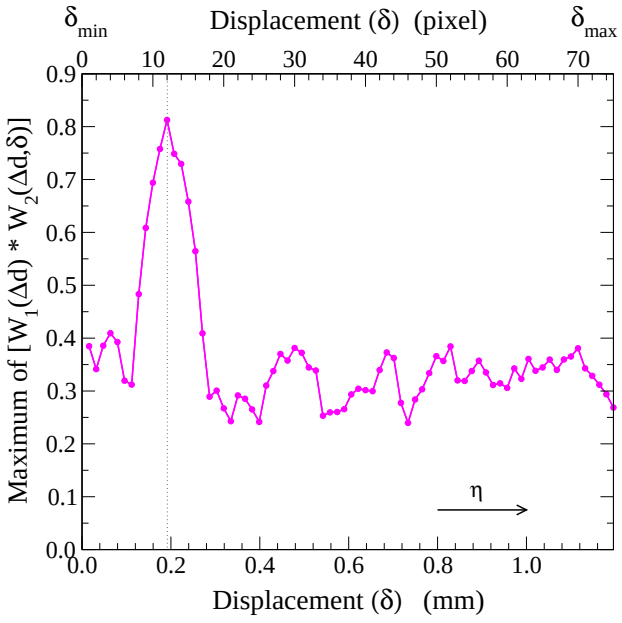

Figure 9.8: Particle matching algorithm

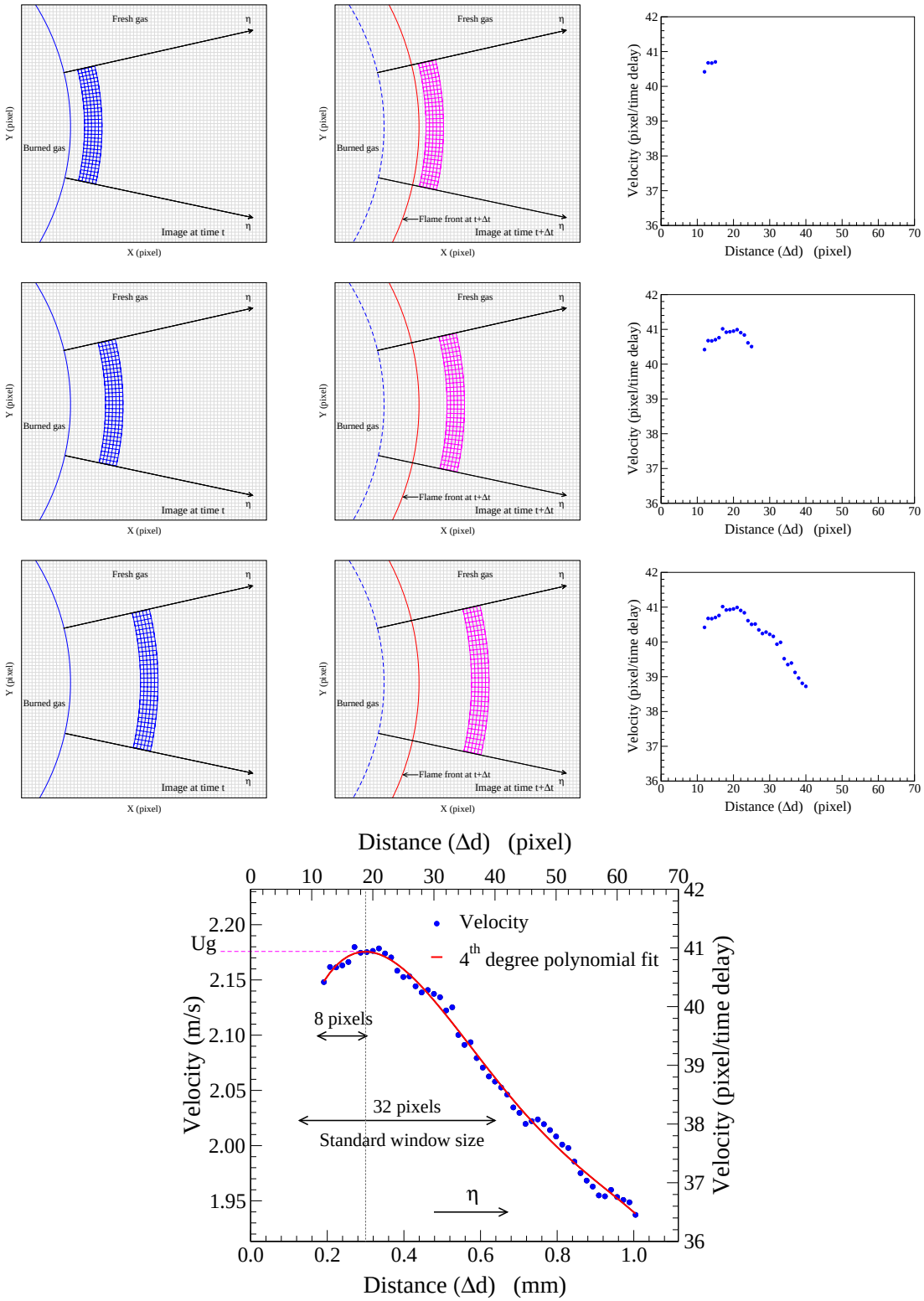

Figure 9.9: Calculation of normal fresh gas velocity profile

within $300\ \mu m$ (≈ 20 pixels). These distances are small compared to the characteristic size of interrogation window for the standard PIV approach (32×32 pixels $\sim 0.69 \times 0.69\ mm$). In our approach, even if we keep a large field of view (around $44\ mm$) to conserve a full visualization of the flame, we can resolve the velocity gradient ahead the flame over a distance of $0.5\ mm$. In this work, the high spatial resolution has been reached by using thin interrogation window of 32 pixels along the flame front and 8 pixels in the normal direction to the flame ($0.69\ mm \times 0.17\ mm$).

9.6 Validation of new methods

The accuracy and reliability of new methods developed for the local measurement of flame speed and fresh gas velocity have been validated by two complementary schemes based respectively on synthetic images of particles and well-established spherical outwardly propagating flame configuration. The following sections explains the validation of fresh gas velocity measurement by synthetic images and the experimental configuration of stretched premixed flame.

9.6.1 Validation of new PIV algorithm using SIG

The newly developed PIV algorithm has been validated by using synthetic images. The synthetic images are generated with the Synthetic Image Generator program which has been developed under the scheme of *EUROPIV 2* project [Lecordier and Westerweel (2004)]. The flow conditions on the synthetic images have been tuned to be comparable in terms of distribution, magnitude and gradient to those predicted by numerical simulation in similar conditions [Groot and De Goey (2002)].

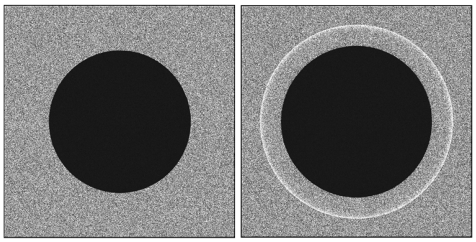

Figure 9.10: One example of synthetic images generated by SIG program.

The particle evaporation within the flame front has been simulated by removing all the particles located behind the flame radius (Fig. 9.10). The particle concentration and the particle image size on the synthetic image have been adjusted to be representative to those observed on real images. The flame front contours are then extracted from the synthetic images in order to calculate the local normal vectors. Then the synthetic images are processed by our new PIV technique. The constructed profiles from the synthetic images are then compared with imposed profile as shown in Fig. 9.11 and 9.12.

The influence of length (number of columns) and width (number of rows) of interrogation windows on the measurements are analyzed. In Fig. 9.11, the imposed profile is compared with instantaneous constructed profiles of different interrogation window sizes. Nice overlaps of constructed profiles are observed and a good agreement between imposed and constructed profiles

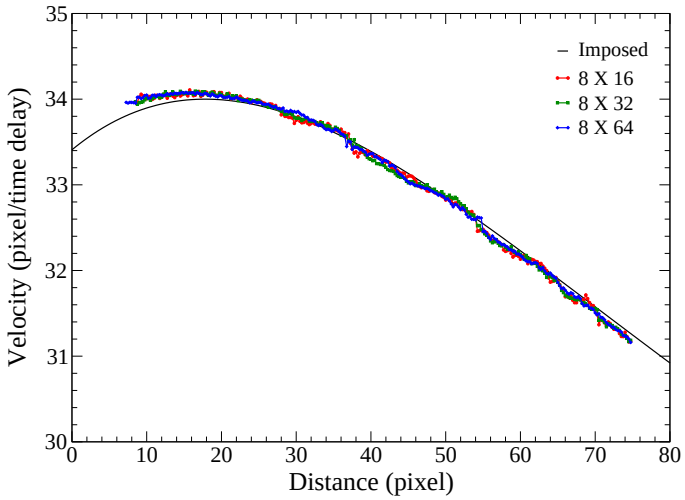

Figure 9.11: Influence of length of interrogation window.

is also observed even very close to the flame front. From that figure, it becomes clear that the influence of number of columns of interrogation window on the velocity measurement is negligible. But the size of length of interrogation window could be a concern when the flame propagation is not uniform along the flame front. In Fig. 9.12, the imposed profile is compared with instantaneous constructed profiles of different width of interrogation windows. It clearly shows the influence of width size on the prediction of velocity profile. The difference between the imposed and constructed profile increases with size of width of interrogation window. The peak values of profiles are around 34 pixels/time delay for up to 16 pixels and 33.9 pixels/time delay for 32 pixels. The differences between the imposed and constructed profiles increases with distance from the flame front and the deviation from the imposed profile start to increase with width of interrogation window. This result emphasizes the importance of using very thin interrogation windows otherwise

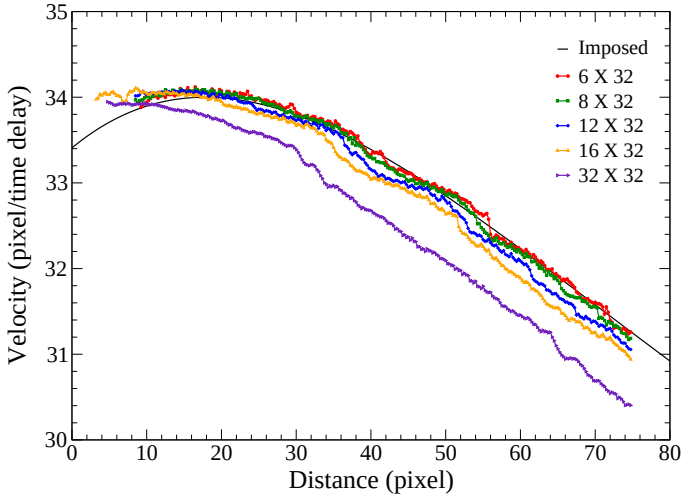

Figure 9.12: Influence of width of interrogation window.

we would lose the gradient of the velocity profile. It also confirms that standard and reoriented interrogation window technique cannot resolve the velocity profile with standard window size (32

$\times$ 32 pixels) due to the requirement of high resolution close to the flame front. So from the validation of new PIV algorithm using synthetic images, we have shown the significant improvement of spatial resolution obtained by the new PIV algorithm to accurately resolve the velocity profile very near to the flame front.

9.6.2 Experimental configuration

The experimental setup is based on the PIV technique alone. The schematic representation of experimental set-up is shown in Fig. 9.13. Experiments are conducted in the same constant volume chamber which is used for the turbulent studies. In this study, the combustion chamber is initially filled with known equivalence ratio of propane-air mixture and then spark-ignited at the center of chamber. After that particle images of freely propagating flame front is captured using PIV technique for local flame speed and fresh gas velocity measurements.

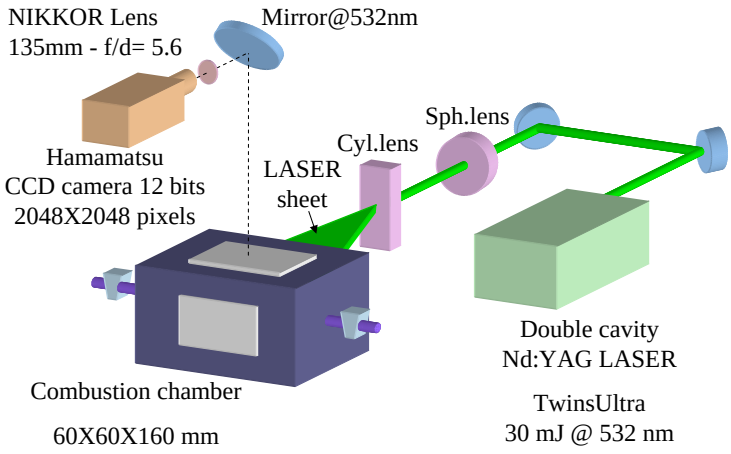

Figure 9.13: Experimental set-up.

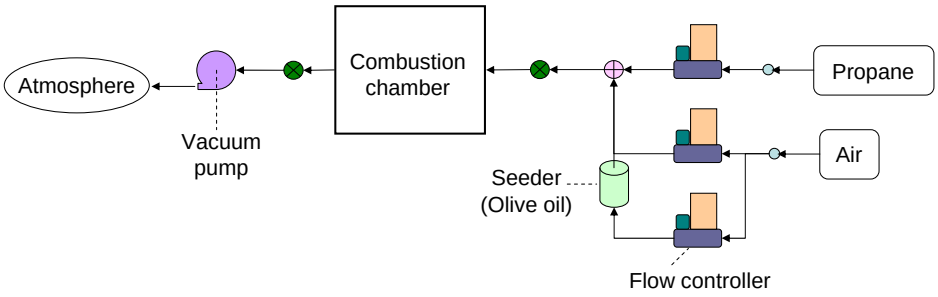

Figure 9.14: Flow set-up.

The flow circuit is shown in Fig. 9.14. The flow rates of propane and air are measured and regulated with less than 0.5% of error by thermal mass flow controllers (Bronkhorst EL-Flow series) and gases and seeding particles are mixed prior to entering the combustion chamber. At

the start of each cycle, the combustion chamber is filled with mixture of known equivalence ratio at atmospheric pressure for two minutes. Then the chamber is closed and the flow is allowed to settle. Next the mixture is spark-ignited by energizing the centrally located electrodes by standard capacitive ignition system. Minimum spark energy is supplied to ensure free propagation from the initial phase of combustion. For capturing Mie scattered images, the air flow rate is seeded with micro-metric olive oil droplets. The mass fraction of olive oil added is kept very low to ensure there has no effect on the combustion process, and this point has been verified from comparisons of pressure rise in the combustion chamber in the case of mixtures with and without particles [Lecordier (1997)]. At the end of cycle, the burned products are purged using vacuum pump.

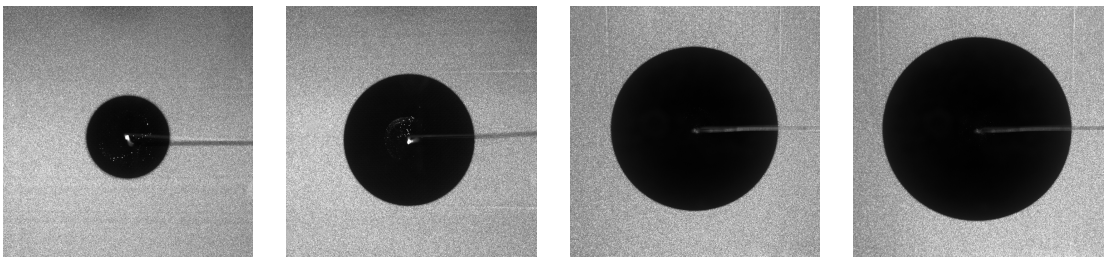

(a) $\phi = 0.80$, $t = 5.5\ ms$ (b) $\phi = 0.90$, $t = 5.6\ ms$ (c) $\phi = 1.00$, $t = 5.4\ ms$ (d) $\phi = 1.10$, $t = 5.4\ ms$

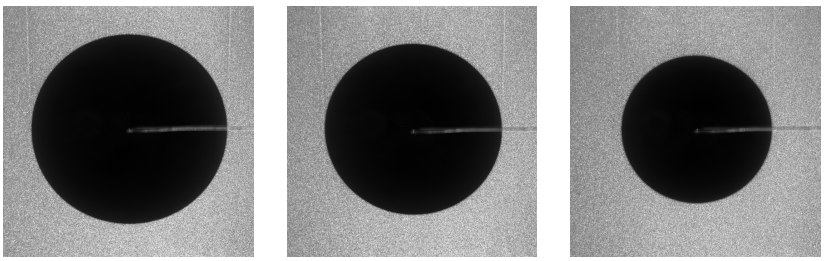

(e) $\phi = 1.21$, $t = 5.6\ ms$ (f) $\phi = 1.32$, $t = 5.5\ ms$ (g) $\phi = 1.43$, $t = 5.5\ ms$

Figure 9.15: Example of spherical flame: propane-air, $T = 298\ K$ and $P = 1\ bar$.

The PIV system is the same one used for the turbulent studies. It consists of a double cavity Nd:YAG laser (TwinsUltra, Quantel) delivering pulses of $30\ mJ$ at $532\ nm$ and an full frame interline CCD camera (Hamamatsu $C9300$) providing a $12\ bit$ image pair of 2048×2048 pixels. The laser sheet is created by the association of one spherical lens of $1\ m$ focal length and one cylindrical lens of $-25\ mm$ focal length. The camera is mounted with a Nikkor lens of $135\ mm$ focal length ($f/d_{max} = 2$)which provided $4.45 \times 4.45\ cm^2$ field of view. Flame chemiluminescence is rejected by an interferential pass-band $(532 \pm 5\ nm)$ filter.

In this work, PIV images of combustion flame fronts of propane-air mixture with a range of equivalence ratios, $\phi = 0.8 - 1.43$, are captured which includes both thermo-diffusively stable and unstable conditions. For each mixture, around one hundred PIV image pairs are taken covering the duration of flame propagation, free from ignition energy effects and pressure influences. Examples of PIV images taken for different equivalence ratios at different acquisition time after ignition are shown in Fig. 9.15. The flame fronts are spherical in shape and their sizes vary with equivalence ratios.

9.7 Results

The newly developed methods have been validated on the outwardly propagating spherical flames through propane-air mixture with a range of equivalence ratios, $\phi = 0.8 - 1.43$, which includes both thermo-diffusively stable and unstable conditions. For each mixture, around 100 PIV image pairs are taken covering the duration of flame propagation. For each time after ignition, 10 image pairs are taken. The spherical laminar flames are captured with diameters above $5mm$ to avoid spark influences and then consider only free propagation condition [Bradley et al. (1996)]. The maximum flame diameter has been adjusted for each case to keep the pressure rise below 0.1 bar in the combustion chamber during the recording. That ensure the data are within constant-pressure combustion regime but also avoid any appearance of thermo-diffusive instabilities which arise at larger flame radius for our mixture conditions. For each image pair, local flame speeds and local fresh gas velocities are calculated by the newly developed algorithms at more than 100 positions all around the flame.

9.7.1 Evolution of flame radius

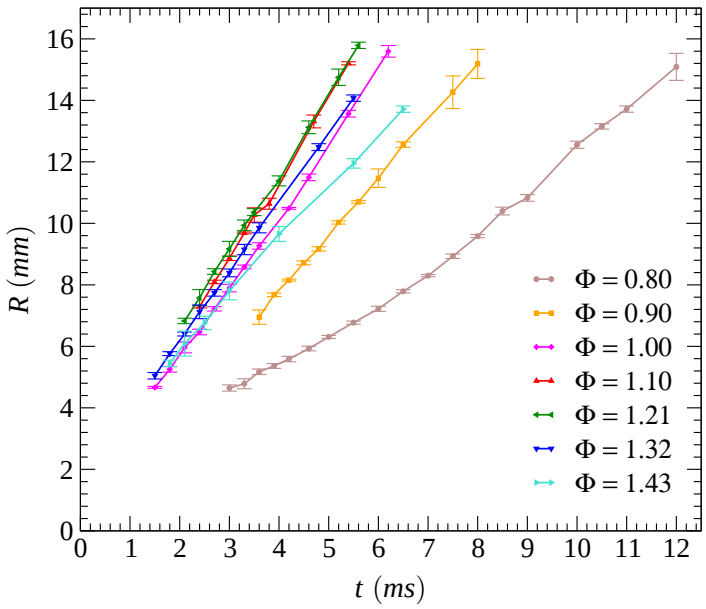

Figure 9.16: Evolution of flame radius for different equivalence ratio.

For each PIV image pair, the mean flame radius is calculated by using least square circle fit technique. Then, for each time after ignition (t), we have calculated the mean and standard deviation of mean flame radius of 10 image pairs. The evolution of mean flame radius (mean values $\pm$ standard deviations) for different equivalence ratios are shown in Fig. 9.16. It varies significantly with equivalence ratios and their variation is more pronounced in the lean mixture conditions. In all the cases, the mean flame front size varies from one sixth to half of characteristic size of combustion chamber.

9.7.2 Evolution of flame speed

The local flame speed is measured from the distance between the two flame fronts multiplied by the time delay between the two acquisitions ($\Delta t = 300\mu s$). Then, for each time after ignition, we have measured the mean and standard deviation of local flame speed. The evolution of flame speed (mean values $\pm$ standard deviations) as a function of time after ignition is shown in Fig. 9.17. Also, the evolution of flame speed (mean values $\pm$ standard deviations) as a function of mean flame radius is shown in Fig. 9.18. First of all, the evolutions of flame speeds are non linear

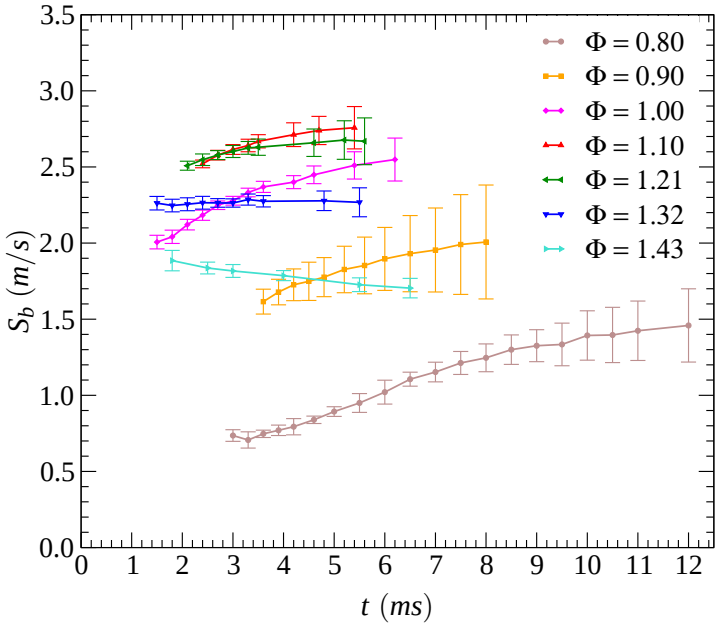

Figure 9.17: Evolution of flame speed as a function of time for different equivalence ratio.

and differs with equivalence ratios. For lean to stoichiometric mixtures, the flame speed increases continuously with time and with flame radius. For rich mixtures, up to $\phi = 1.32$, the flame speed increases with time, becomes steady at $\phi = 1.32$ and start to fall at $\phi = 1.43$. The evolutions of flame speeds clearly indicate the interconnection between the equivalence ratio of mixture and the flame front stability.

The standard deviations of measurements are increasing with radius in all the cases and we can notice very high deviation for $\phi = 0.9$ case. For $\phi = 0.8$ and $\phi = 0.9$ cases, the dimension of combustion chamber is $60 \times 60 \times 160mm^3$. The reason for the higher standard deviation is related to the non-symmetrical distances to the walls around the flame front with respect to the ignition location. In order to minimize this non-symmetrical shape, we have reduced the length of combustion chamber from $160mm$ to $100mm$ so that the combustion chamber is more symmetrical with respect to the ignition location than previous dimension. Then we have carried out measurements for the stoichiometric and rich mixture conditions with modified combustion chamber. Therefore, even though the flame propagation is faster for $\phi = 1.0$, the deviations are smaller for $\phi = 1.0$ compared to $\phi = 0.9$. The next section explains the wall confinement effect on flame propagation and their local measurements.

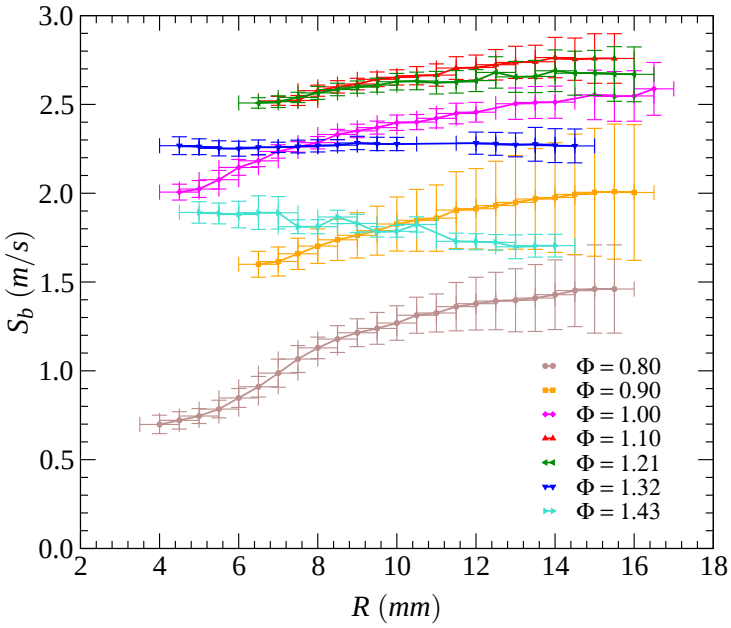

Figure 9.18: Evolution of flame speed as a function of radius for different equivalence ratio.

9.7.3 Wall confinement

The geometry of our combustion chamber is non-spherical as depicted in the Fig. 9.19. This rectangular shape of combustion chamber could disrupt the flow field induced by the gas expansion, which can affect the local flame propagation. Indeed, Burke et al. (2009) examined the wall confinement effect using non-spherical (cylindrical) configuration and they concluded that the interaction of flame propagation with wall starts after the flame front reaches one third of characteristic size of chamber. They also shown that flame speed calculated neglecting wall confinement effect can be underestimated by $\sim$15 $\%$ even within constant pressure condition.

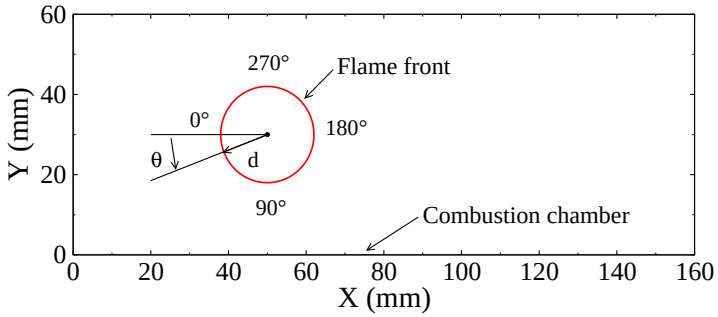

Figure 9.19: Flame front position relative to the combustion chamber.

In our case, by the implementation of two new methods, we are able to measure the local instantaneous distance (d), flame speed (S_b), fresh gas velocity (u_g) and laminar burning velocity (u_n). One example of local variables as a function of angle is shown in Fig. 9.20. We can clearly notice the similarities of variation of local distance with flame speed and fresh gas velocity with respect to the angle. All three parameters reaches local minimum at 90° and 270°, which

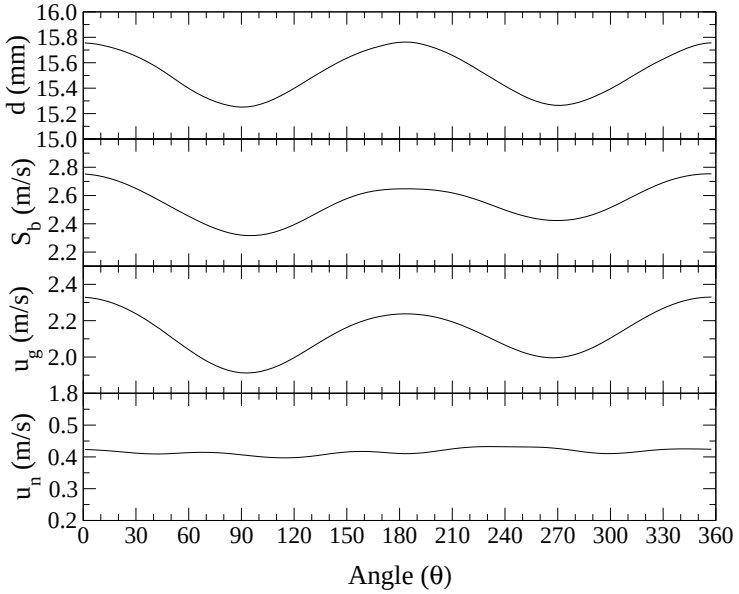

Figure 9.20: Variation of local distance and instantaneous velocities.

correspond to the portions of the flame closest to the walls as depicted in Fig. 9.19. So the local variations are due to the effect of wall confinement on the flame propagation because the heat losses to the walls are negligible. The flame radius in this example is approximately 0.25 times the characteristic width (60mm) of combustion chamber yet we can notice the effect of wall confinement. This effect occurs as soon as the fresh gas pushed by the flame expansion reaches the wall and is then slowed down. The important point to be mentioned here is that the local flame speed and the local fresh gas velocity are measured independently yet the variations are similar. So, the calculated laminar burning velocity as a direct difference between the flame speed and the fresh gas velocity is completely free from the wall confinement effect as shown in Fig. 9.20, indicates the great potential of this direct measurement technique.

9.7.4 Planar flame speed and fresh gas velocity

The variation of mean values of flame speed and fresh gas velocity as a function of stretch for different equivalence ratios are shown in Figs. 9.21 and 9.22. For each equivalence ratios, a linear fit is applied between the velocity and the stretch rate [Markstein (1964), Clavin (1985), Bradley et al. (1996)]. The linear fits are represented by the dotted lines. The unstretched flame speeds (S_b^0) and fresh gas velocities (u_g^0) are then extracted from the linear extrapolation to zero stretch. For each mixture conditions, we have similar slopes for both flame speed and fresh gas velocity as expected because of the outwardly flame propagation which induces the fresh gas flow. In case of lean mixtures, propagation of flame increases with time. Similarly, for the stoichiometric case, the propagation increases with decrease of stretch rate. But for the rich cases, influence of stretch rate is moderate up to $\phi = 1.21$, becomes zero at $\phi = 1.32$ and influences oppositely $\phi = 1.43$ condition compared to lean cases. That means, $\phi = 1.43$ is thermo-diffusively unstable condition and Markstein length changes its sign around $\phi = 1.32$, indicates the start of thermo-diffusive instability effect.

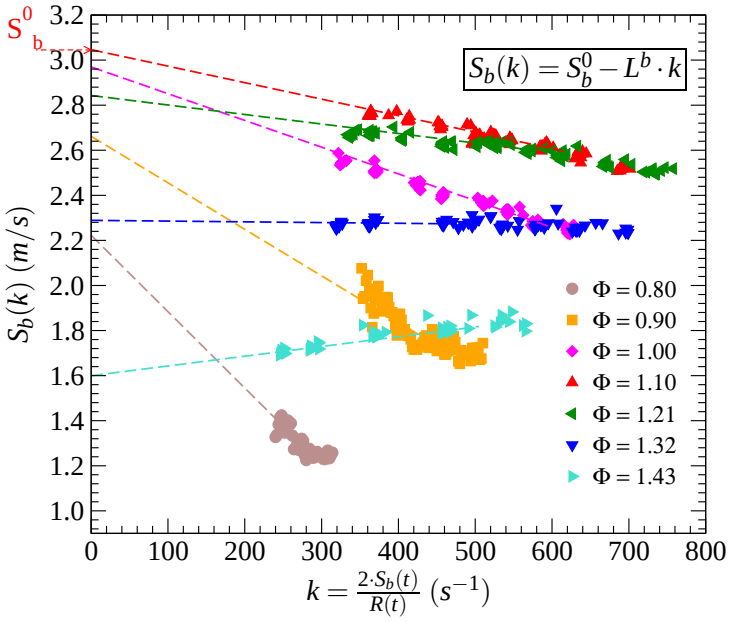

Figure 9.21: Variation of flame speed as a function of flame stretch for different equivalence ratio.

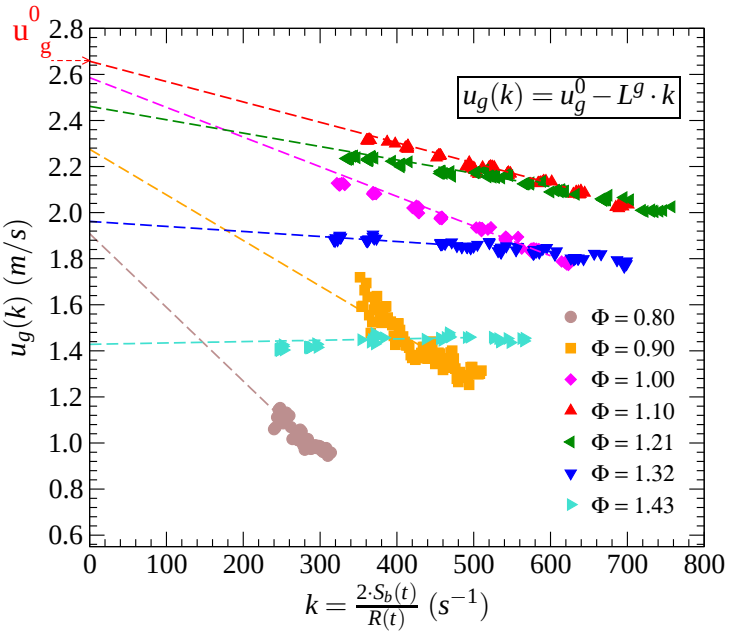

Figure 9.22: Variation of fresh gas velocity as a function of flame stretch for different equivalence ratio.

9.7.5 Laminar burning velocity

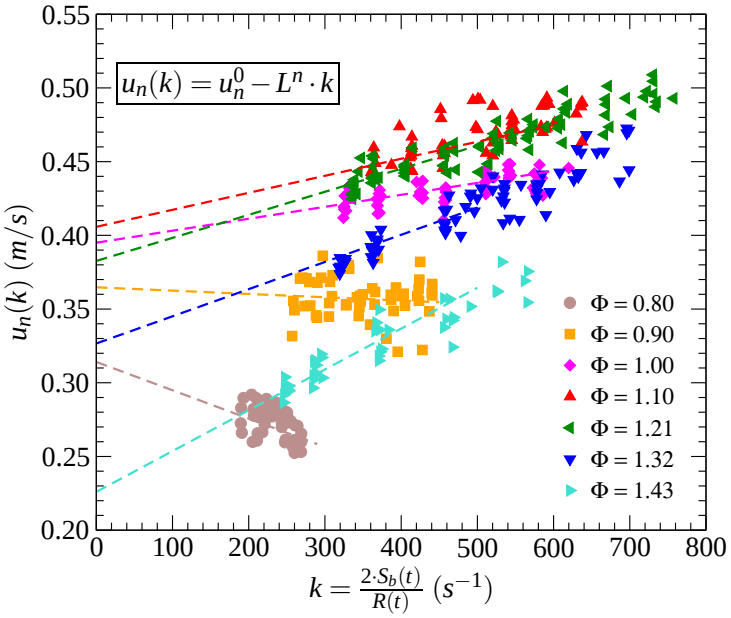

Figure 9.23: Laminar burning velocity u_n as a function of flame stretch.

The variation of local instantaneous laminar burning velocities (mean values) obtained by the direct method is shown in Fig. 9.23. The unstretched laminar burning velocities (u_n^0) are then obtained by linear extrapolation to zero stretch. The influence of stretch rate on the local laminar burning velocities are completely different for lean mixture conditions compared to other equivalence ratio conditions. This direct laminar burning velocities are compared with the velocities obtained from the flame speed and fresh gas velocity by using density ratios (Fig. 9.24). In this work, the density ratios have been taken from the Davis et al. (2002). The slopes of each curve are different, because the measurements being relative to different isotherms in the flame zone. The extrapolated laminar burning velocities from the flame speed (u_{Sb}^0)and the fresh gas velocity (u_{nr}^0) are in good convergence at zero stretch but differing with the direct method (u_n^0). Also, the unstretched laminar burning velocities calculated from the flame speeds and fresh gas velocities by using density ratios are under predicted compared to the direct values (Fig. 9.25). Indeed, the direct measurements are in good agreement with available results as shown in Fig. 9.26. This comparison shows clearly the consistency of our local direct instantaneous measurement of laminar burning velocity. So the underestimation of u_{nr}^0 and u_{Sb}^0 is certainly induced by the confinement effect, which tends to reduce the flame speed and the fresh gas velocity for the larger flame radius. In contrast, the good agreement of planar laminar burning velocities from the local instantaneous laminar burning velocities (Fig. 9.26) shows the potential of this new direct measurement technique.

The extrapolated values of unstretched flame speed, fresh gas velocity and laminar burning velocity together with density ratios used are given in the table 9.1.

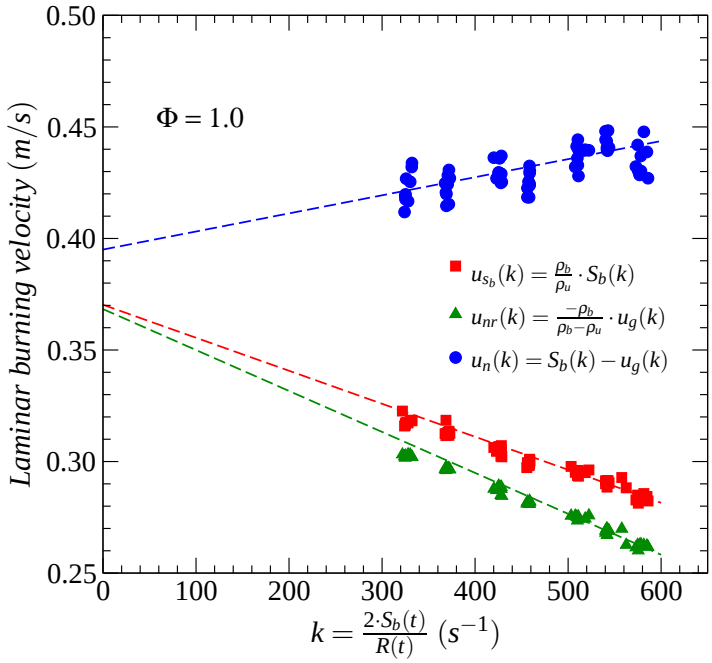

Figure 9.24: Comparison of different laminar burning velocities ($\phi = 1.0$).

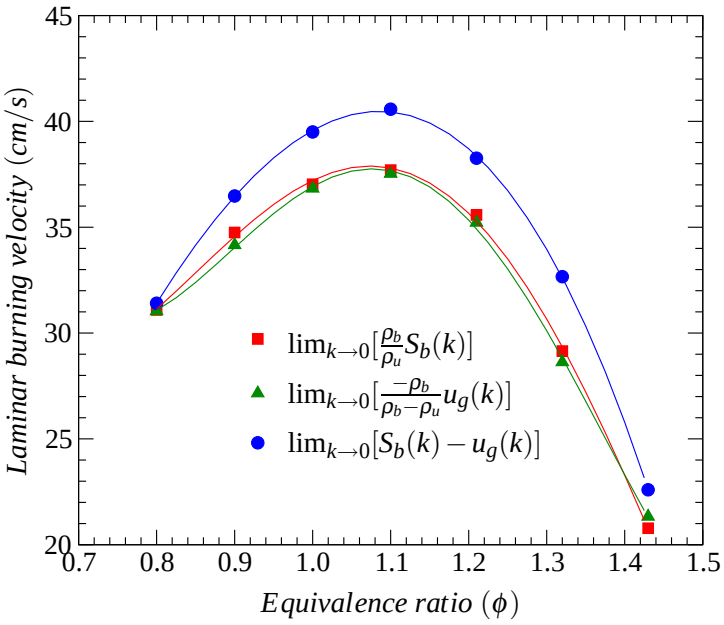

Figure 9.25: Variation of unstretched laminar burning velocities as a function of equivalence ratio.

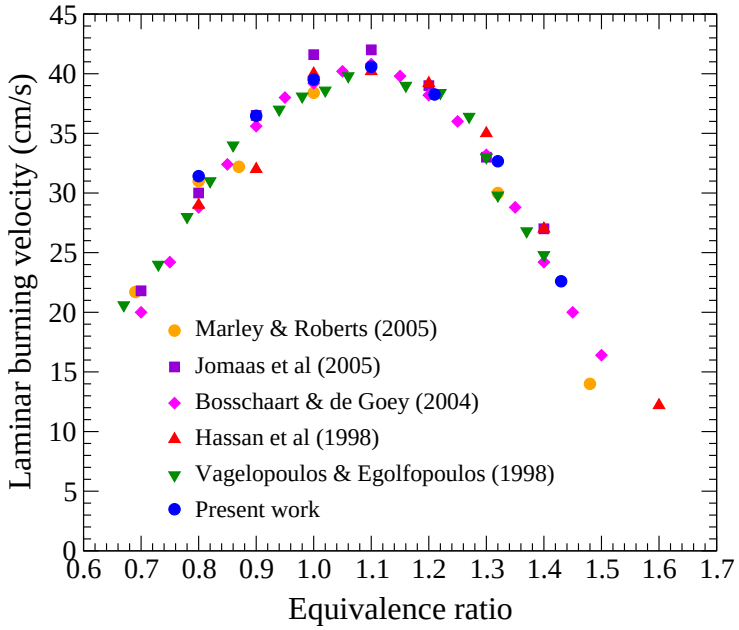

Figure 9.26: Comparison of measured unstretched laminar burning velocities.

ϕ	ρ_u/ρ_b	$S_b^0\ (m/s)$	$u_g^0\ (m/s)$	$u_n^0\ (cm/s)$	$u_{s_b}^0\ (cm/s)$	$u_{nr}^0\ (cm/s)$
0.80	7.15	2.22	1.91	31.4	31.1	31.0
0.90	7.66	2.66	2.28	36.5	34.8	34.2
1.00	8.02	2.97	2.59	39.5	37.0	36.8
1.10	8.08	3.05	2.66	40.6	37.7	37.5
1.21	7.99	2.84	2.46	38.3	35.6	35.2
1.32	7.85	2.29	1.96	32.7	29.1	28.6
1.43	7.70	1.60	1.43	22.6	20.8	21.3

Table 9.1: Unstretched laminar burning velocities of propane-air flames at atmospheric conditions.

9.7.6 Markstein length and number

The Markstein numbers represents the effect of flow curvature and flow field strain on the flame propagation [Bradley et al. (1996)]. The Markstein numbers for the burned region can be calculated from the flame speed and for the fresh gas region can be calculated from the laminar burning velocity.

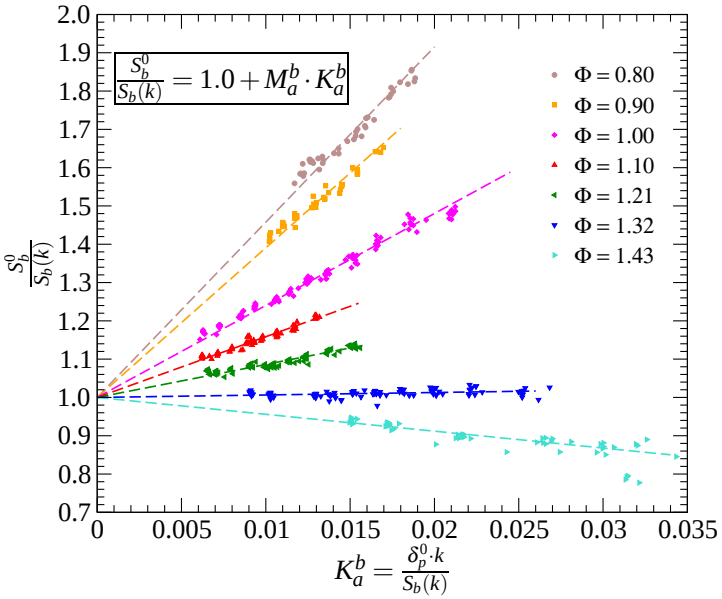

Figure 9.27: Normalized flame speed as a function of Karlovitz number for different equivalence ratio.

The variations of normalized flame speed (mean values) as a function of Karlovitz number for different mixture conditions are shown in Fig. 9.27. The flame thickness (δ_p^0) values have been taken from the Davis et al. (2002). The Markstein numbers are then calculated from the linear relationship as given in the same figure. The variation of normalized flame speed with Karlovitz number is almost zero at $\phi = 1.32$ where the Markstein number changes its sign from positive to negative. The negative Markstein number indicates the unsteady flame propagation that means the flame speed decreases with stretch rate.

The Markstein lengths and numbers are shown in Fig. 9.28 as a function equivalence ratio. Globally, the Marktein length and number varies linearly with equivalence ratio. Also, the comparison of Markstein numbers with available literature results shows agreement at rich mixture conditions (Fig. 9.29).

The Markstein number for the fresh gas region is measured from the linear relationship between the normalized laminar burning velocity and the Karlovitz number which is calculated as the ratio of flame thickness to the local laminar burning velocity (Fig. 9.30). The variations of slope are entirely different for lean and rich mixtures conditions. The calculated Markstein length and number are shown in Fig. 9.31. The Markstein numbers are positive for the lean mixtures and become negative for the rich mixture conditions. The variation of Markstein numbers in the fresh gas region is not linear unlike the variation in the burned gas region.

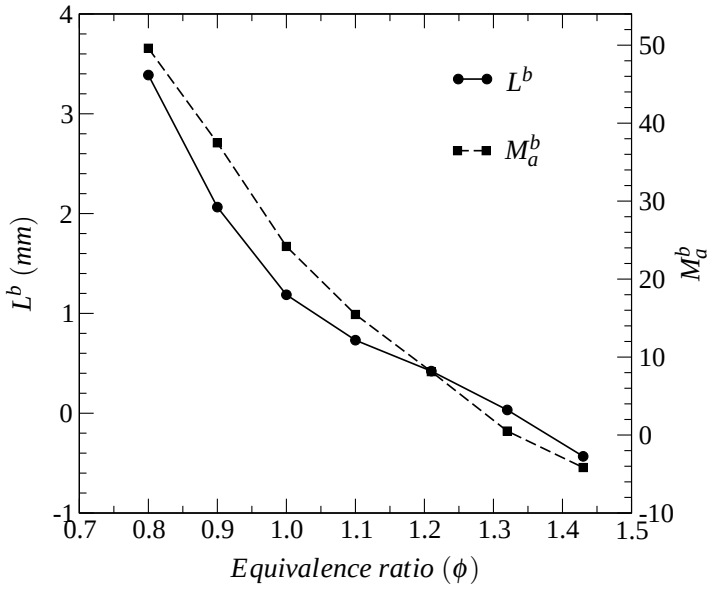

Figure 9.28: Markstein length and Markstein number as a function of equivalence ratio.

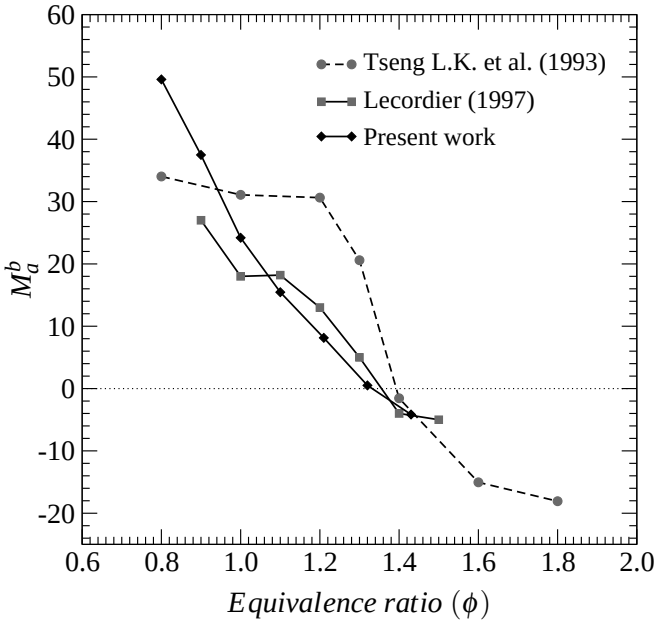

Figure 9.29: Markstein number as a function of equivalence ratio.

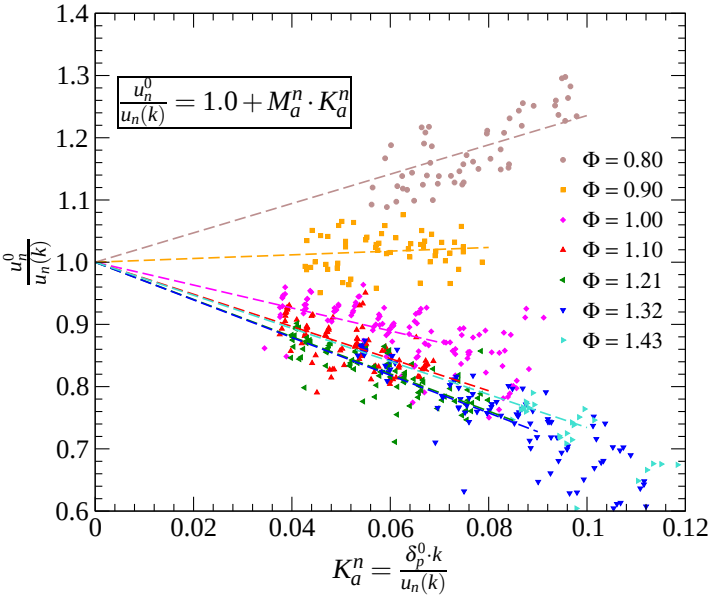

Figure 9.30: Normalized laminar burning velocity as a function of Karlovitz number for different equivalence ratio.

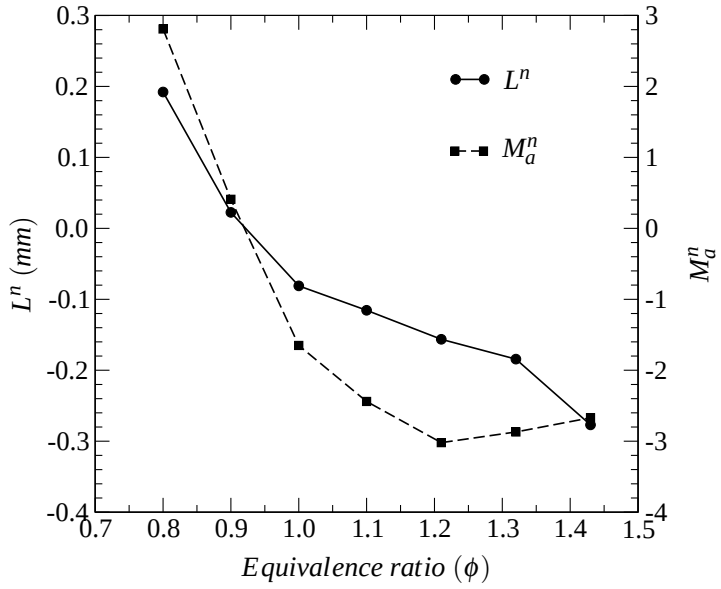

Figure 9.31: Markstein length and Markstein number in the fresh gas region as a function of equivalence ratio.

ϕ	$\delta_p^0\ (\mu m)$	$L^b\ (mm)$	$L^n\ (mm)$	Ma^b	Ma^n
0.80	68.32	3.39	0.19	49.60	2.81
0.90	55.08	2.06	0.02	37.48	0.41
1.00	49.04	1.19	-0.08	24.19	-1.65
1.10	47.32	0.73	-0.12	15.46	-2.44
1.21	51.85	0.42	-0.16	8.13	-3.02
1.32	64.19	0.03	-0.18	0.51	-2.87
1.43	103.60	-0.43	-0.28	-4.17	-2.67

Table 9.2: Markstein lengths and Markstein numbers of propane-air flames at atmospheric conditions.

9.8 Conclusions

A direct experimental measurement of local instantaneous laminar burning velocity is developed based on the PIV technique. The main focus is to measure the local flame speed and the local fresh gas velocity near the flame front in order to obtain the local laminar burning velocity as their direct difference. The local measurement of flame speed is greatly improved by a new extraction tool, which extracts the flame front with sub-pixel accuracy and eliminates noises superposed on the flame front. The local fresh gas velocity near the flame front is achieved successfully by a new PIV approach. The accuracy and reliability of new tools have been evaluated from two complementary approaches based respectively on synthetic images of particle and on the well established configuration of outwardly propagating spherical flames of propane-air mixtures at atmospheric pressure conditions. The measured laminar burning velocities are compared with existing experimental results and satisfactory agreement is observed. So this new PIV approach can be extended to the laminar stratified flame configurations to measure the local laminar burning velocity of stratified flames which would be otherwise not possible to measure by any of the global measurement techniques because of the variation of local equivalence ratio in those configurations.

Chapter 10

Laminar stratified flame propagation

Abstract. *The laminar flame propagation through three different stratified mixture fields are analyzed by using simultaneous PIV/PLIF techniques. The mixture stratification is realized inside a constant volume combustion chamber by a laminar jet of rich propane-air mixture. The flame is then spark ignited and the propagation of flame through stratified mixture is acquired by simultaneous PIV/PLIF techniques. The flame propagations through three different stratified levels are investigated in order to know the effect of degree of stratification on flame propagation. The local flame speed, local fresh gas velocity and local laminar burning velocity of stratified flames are measured by using the new PIV approach. The local conditioned variables of different stratified cases are calculated and then compared to each other. Finally, the enhancement of flame propagation by mixture stratification and the memory effect are discussed.*

10.1 Introduction

Our experimental investigation on turbulent stratified combustion has successfully confirmed the enhancement of flame propagation by stratification of mixture field. The combined measurement of velocity and equivalence ratio field of turbulent stratified flame propagation has proved very useful to understand the fundamentals of stratified combustion. We have also improved the accuracy of local measurements of flame propagation and successfully validated our new methods using synthetic images and experimental configurations, which are explained in the previous chapter. By taking advantage of improved local measurements, we have decided to investigate the laminar stratified flame propagation in order to provide valuable data for numerical simulations. So far very few experimental and numerical investigations have been carried out on laminar stratified combustion, but the outcomes are small and sometimes contrary, emphasize the need of more studies in order to understand the fundamentals of laminar stratified combustion. So in this work, the laminar flame propagation through stratified mixture field is investigated by using simultaneous PIV/PLIF techniques. For that, a unique injection setup has been developed to generate laminar stratified mixture field of low velocity with high degree of stratification inside a constant volume chamber in a controllable way. Then simultaneous PIV/PLIF images of laminar flame propaga-

tions are acquired for three different stratified mixture configurations. From the PIV images, the local flame speed, local fresh gas velocity and local laminar burning velocity are measured by using the new methods explained in the previous chapter. Then global parameters such as asymmetry and mean flame front contours of three different stratified cases are analyzed. After that, the local conditioned variables are calculated thanks to the combined measurement of flow and scalar fields of propagation. The local conditioned variables of three stratified cases are then compared in order to understand the effect of degree of stratification on flame propagation. From that comparison, the memory effect of stratified flames and their relaxation times are analyzed.

10.2 Experimental setup

The schematic diagram of experimental setup is shown in Fig. 10.1. It mainly consists of a constant volume combustion chamber, injector unit, electrical valves (EV1, EV2, EV3), vacuum pump (VP), mass flow controllers (TMFM), mechanical valves and pressure sensor (PS). The setup can be divided into three sections; propane-air mixture preparation, injection unit and vacuum unit.

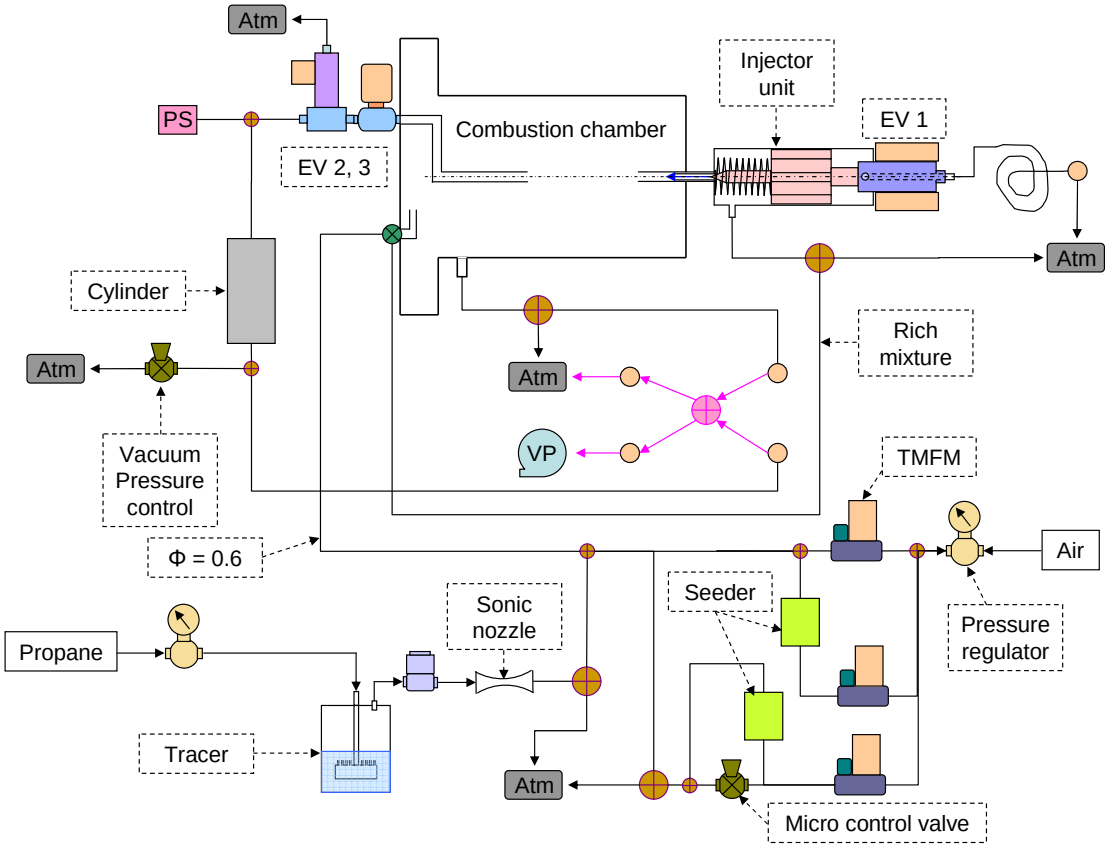

Figure 10.1: Schematic diagram of experimental set-up.

The objective of propane-air mixture unit is to control the flow rate and equivalence ratio of mixture as well as to seed the flow with anisole vapor and olive oil particles. The flow rate of propane is controlled by a sonic nozzle and mixed with air prior to filling the combustion chamber. The flow of propane is traced with anisole vapor for PLIF measurement. The air flow rate is

controlled by TMFM units. Two separate olive oil particle generators are used to seed air flow for PIV measurement, one generator seeds the air flow of lean mixture and another one seeds the air flow of laminar stratified jet. The lean propane-air mixture is prepared by mixing total air flow with propane flow and the rich mixture is prepared by diverting part of the air flow to atmosphere prior to mixing air and propane flows. With the help of two PIV seeders, the olive oil particle density is kept same in both lean mixture filled inside the combustion chamber and the rich stratified mixture injected into the combustion chamber. The principle of injection and vacuum units are given in the next section. The laser illumination and image acquisition units are same as used in the turbulent stratified flame investigation (§8).

10.3 Laminar stratified jet

The few investigations carried out so far have indicated the memory effect of stratified flames [Ra (1999), Pires Da Cruz et al. (2000), Kang and Kyritsis (2007a)]. Actually, those investigations have shown that the flame fragments propagated previously through rich mixtures back supported the flame propagation through very lean mixtures. That means the degree of stratification could play an important role in enhancing the flame propagation. So the objective of this study is to understand the effect of degree of stratification by analyzing the flame propagation through three different stratified mixture fields which are given below:

- Case 1: Rich mixture to very lean mixture.
- Case 2: Stoichiometric mixture to very lean mixture.
- Case 3: Lean mixture to very lean mixture.

A unique injection setup has been developed to realize those stratified cases with low velocity flow inside a constant volume chamber. Figure 10.2 shows the injection setup, which consists of injection unit and vacuum unit.

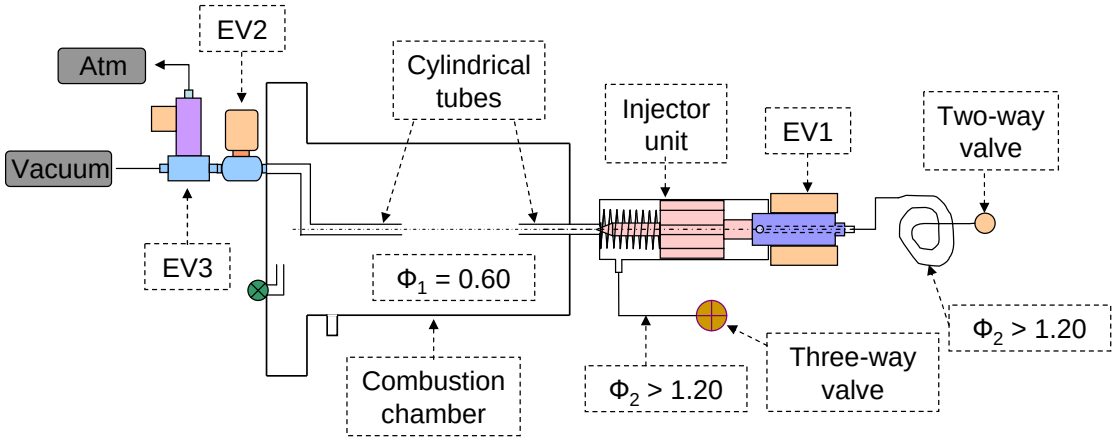

Figure 10.2: Stratified mixture injection setup.

The main role of injection and vacuum units are the realization of controllable and reproducible stratified jet inside a constant volume chamber. This has been achieved by introducing a controlled

vacuum inside the combustion chamber that sucks the rich mixture from a closed volume through the injection unit. The quantity of mixture and the velocity of jet are controlled by vacuum pressure and duration of injection. The injection unit controls the start and duration of injection whereas the vacuum unit controls and maintains the vacuum pressure.

Injection unit:

The injection unit mainly consists of an axisymmetrical injector, one electrical solenoid valve (EV1), a wire mesh placed inside the injector, a cylindrical tube and a small volume made up of tube (shown in Fig. 10.2 as a spiral connected with solenoid valve). Inside the injector, a small needle is blocking its opening against spring force which can be released by energizing the electrical solenoid valve. So the timing of solenoid valve controls the start and duration of injection. When the injector opens, rich mixture in the tube starts to flow to the combustion chamber through a wire mesh which imposes a small pressure drop to the flow and also prevents the flame propagation through injector during combustion. A small copper tube is fixed inside the side block of combustion chamber in order to provide sufficient length to the developing region of laminar flow. Just before the injection, rich mixture is circulated through small volume of tube and injector unit for few seconds and then closed by two-way and three-way valves shown in Fig. 10.2. This unique injection method ensures the mixture with same equivalence ratio in every cycle. The injector unit has been fixed very close to the side block of combustion chamber to reduce the dead volume, which would otherwise decrease the mixture gradient due to the very low quantity of injection in each cycle.

Vacuum unit:

The vacuum unit comprises of a vacuum pump, two-way and three-way electrical solenoid valves, a small cylinder tank, a piezoelectric pressure transducer (Keller series 33S), a small copper tube and a micro control valve. The function of this unit is to maintain a constant vacuum pressure during the injection in order to realize a reproducible laminar stratified jet. Otherwise variation in vacuum pressure will lead to random start of injection and fluctuations in the quantity of mixture injected in each cycle. Therefore, a constant vacuum pressure is maintained by feeding air to the inlet pipe of vacuum pump and the flow rate of air is controlled by a micro control valve (shown in Fig. 10.1). By balancing the vacuum and air flow rate, we are able to control and maintain the vacuum pressure in the flow line. But the electrical solenoid valve (EV2) used in this work is not suitable for vacuum and that introduced some fluctuation to the vacuum pressure. In order to eliminate this pressure fluctuation, a three-way electrical solenoid valve (EV3) is used which decouples EV2 valve from vacuum line as shown in Fig. 10.2. In switched-off condition, EV3 valve connects the EV2 valve to atmosphere and when switched-on, it connects the vacuum line to EV2 valve. This unique arrangement ensures constant vacuum in the line, no leak through solenoid valve and repeatable vacuum condition at each cycle. A small copper cylindrical tube is used to connect the vacuum line to the investigation zone of combustion chamber as shown in Fig. 10.2 in order to control the jet direction to be parallel with axis of combustion chamber.

Controlling parameters:

The main factors that control the velocity and equivalence ratio of stratified mixture field are vacuum pressure, equivalence ratio of mixture inside the injector unit and duration of injection. Among them, the valve timings of EV1, EV2 and EV3 control the start of injection and duration of injection. First, the equivalence ratio of lean mixture inside the combustion chamber is fixed to $\phi = 0.6$

and then vacuum pressure is optimized to 150mbar. After that, different solenoid valve timings are tried to achieve the mean velocity of jet as low as possible at the time of ignition by using combined velocity and equivalence ratio field of stratified jet. The optimized valve timings after a lot of experimental iterations are shown in Fig. 10.3. The opening of EV2 and EV3 are delayed in order to provide sufficient time to balance the pressure between combustion chamber and injector volume. The duration of opening of EV3 is extended more than 20ms than EV2 to avoid leak through EV2 to combustion chamber. The injection process is initiated by a TTL pulse to the first solenoid valve (EV1). The opening of other two valves, ignition of mixture by energizing two thin electrodes and image acquisition events are synchronized with TTL pulse of EV1. Unlike turbulent jet, the fluctuation of laminar jet is very minimal, so that ignition and image acquisition events are directly synchronized with injection event.

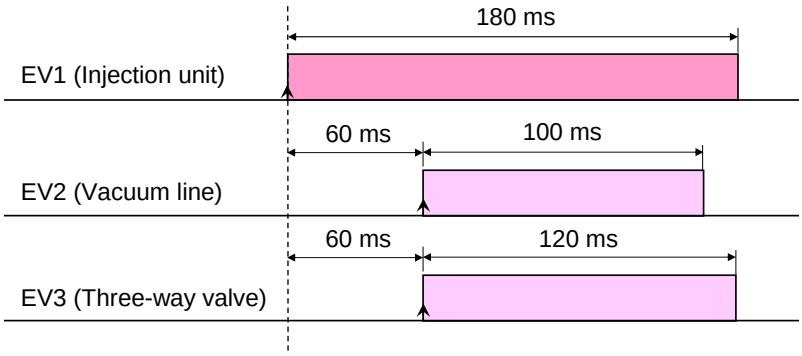

Figure 10.3: Solenoid valve timings.

Optimized conditions:

The optimized values of various parameters of injection setup are given in the table 10.1. The equivalence ratio of injection is $\phi = 2.2$ for case 1, $\phi = 1.4$ for case 2 and $\phi = 1.2$ for case 3. The time of ignition is set to $215\ ms$ after start of injection. The location of ignition is set at $X = -5.95\ mm, Y = 1.2\ mm$ with respect to the center of acquired image.

Vacuum pressure	150 mbar (g)
Equivalence ratio of chamber	0.6
Equivalence ratio of injection	2.2, 1.4, 1.2
Time of ignition from start of injection	215 ms
Location of ignition	X=-5.95 mm, Y=1.2 mm

Table 10.1: Injection and ignition parameters.

10.4 Analysis of mixture field at the time of ignition

The mean flow and scalar field of laminar stratified mixture at the time of ignition are shown in Fig. 10.4. The mean field is calculated from 10 consecutive cycles. The time delay between the

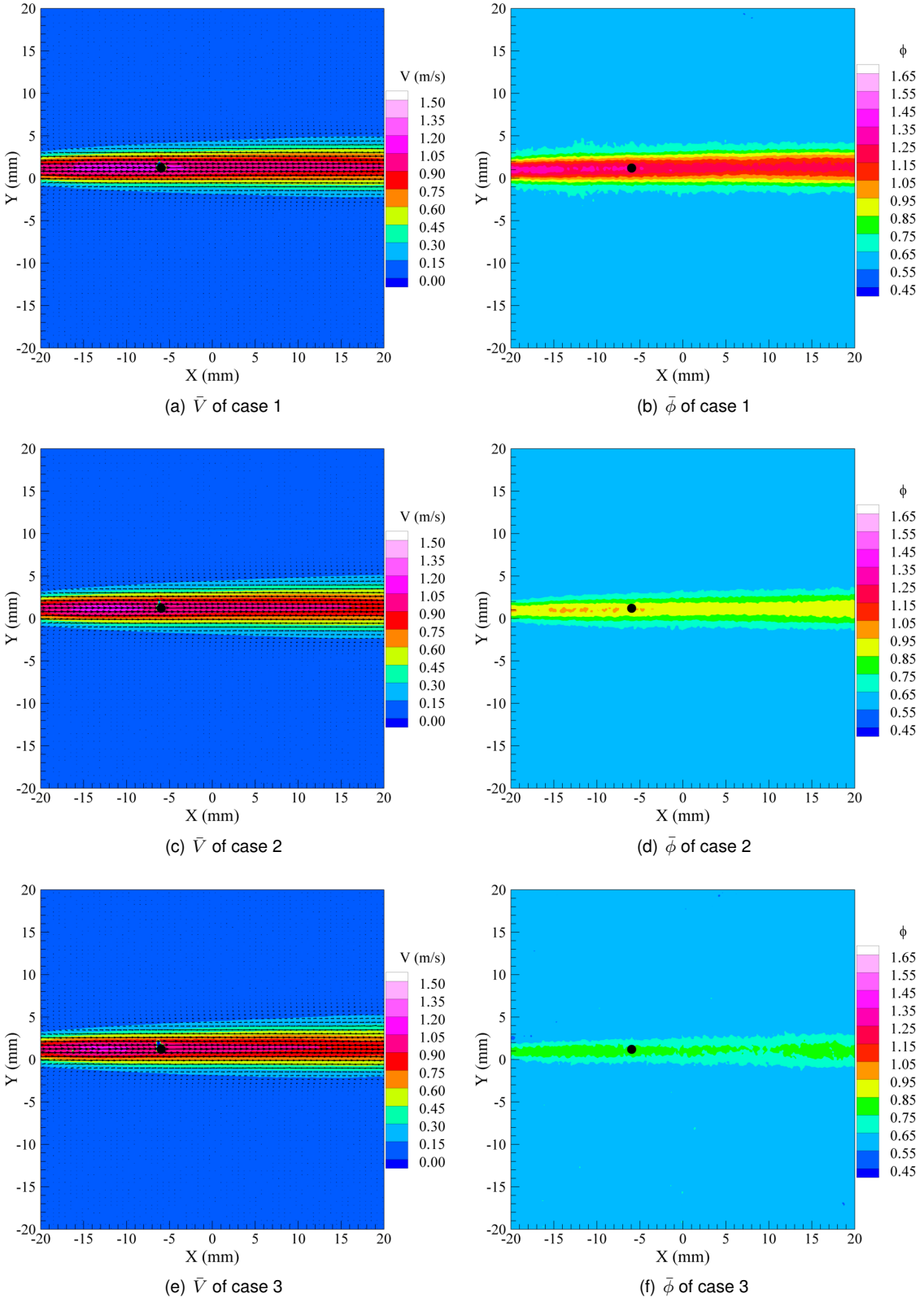

(a) $\bar{V}$ of case 1

(b) $\bar{\phi}$ of case 1

(c) $\bar{V}$ of case 2

(d) $\bar{\phi}$ of case 2

(e) $\bar{V}$ of case 3

(f) $\bar{\phi}$ of case 3

Figure 10.4: Mean flow and scalar field of different cases.

PIV image pair is fixed to 200 μs in order to keep the percentage of spurious vectors less than 1% in the velocity vector field before validation. The mean velocity vector field is almost same in all three cases. The position of ignition is indicated by a black circle. The mean scalar field is symmetric with respect to the jet axis which is slightly above the center of combustion chamber because of small shift of injection hole in the side block with respect to the center of chamber. The stratification along the axis of jet is uniform and varies along normal to the axis. The thickness of distribution of equivalence ratio shrinks with decrease of mixture stratification, whereas there is no variation of thickness of jet in the velocity vector field.

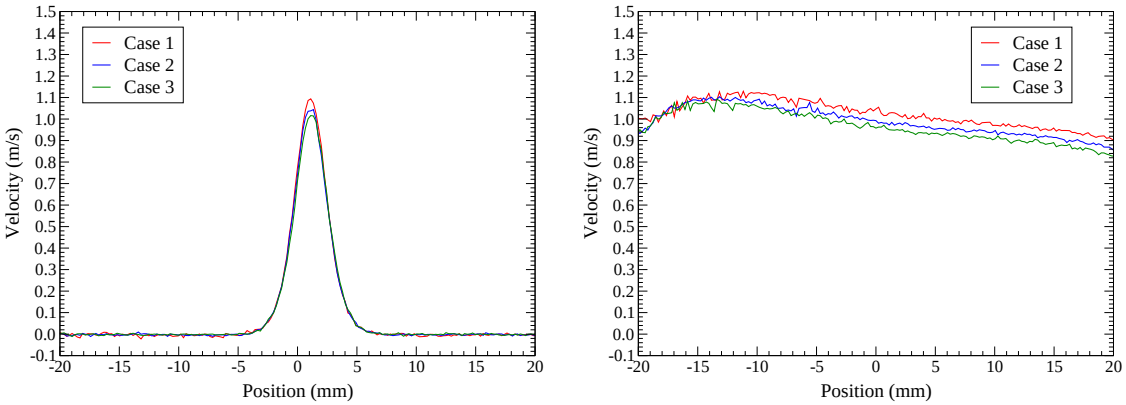

(a) Transverse profiles at X=-5.95 mm

(b) Longitudinal profiles at Y=1.2 mm

Figure 10.5: Mean profiles of U component of velocity field at ignition location.

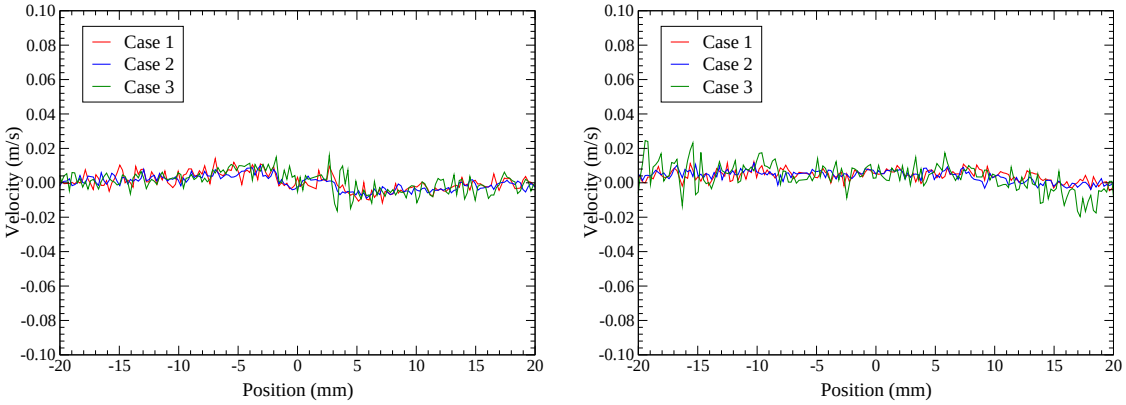

(a) Transverse profiles at X=-5.95 mm

(b) Longitudinal profiles at Y=1.2 mm

Figure 10.6: Mean profiles of V component of velocity field at ignition location.

The transverse and longitudinal profiles of U and V components of mean velocity field of three cases are shown in Figs. 10.5 and 10.6. Good agreements between the velocity profiles of three different cases are observed except the longitudinal profiles of U component. The transverse profiles of U component of velocity field clearly show that the laminar jet is symmetrical with respect to the jet axis. The difference in agreement between the longitudinal profiles of U component is due to the small variation in flow conditions induced by the difference in balance between the vac-

uum pressure and mass flow rate of injected mixture which varies slightly with equivalence ratio of mixture. Both transverse and longitudinal profiles of V component are closer to zero velocity indicate that the streamlines are almost parallel to the flow direction.

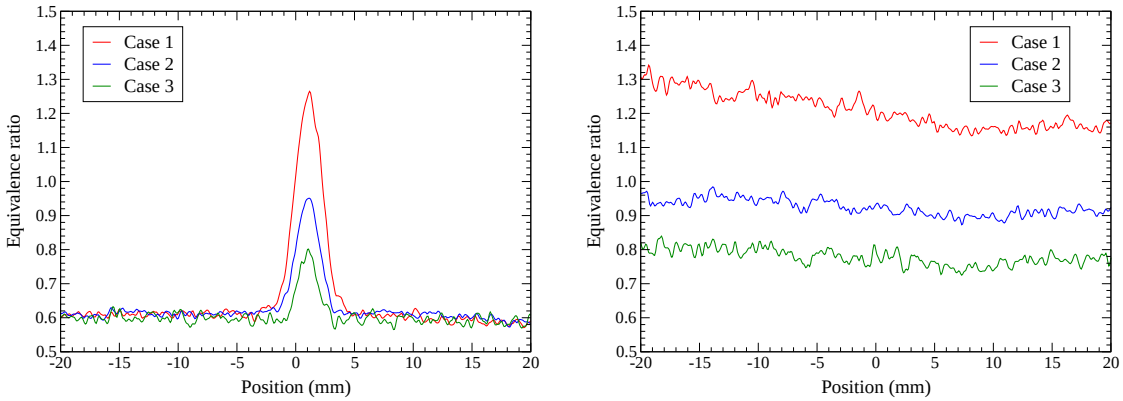

(a) Mean transverse profiles at X=-5.95 mm

(b) Mean longitudinal profiles at Y=1.2 mm

Figure 10.7: Mean profiles of equivalence ratio field at ignition location.

The transverse and longitudinal profiles of equivalence ratio field at the position of ignition are shown in Fig. 10.7. The width of jet is around $5\ mm$ for all the cases. The transverse profiles indicate that the equivalence ratios of mixture fields are symmetrical along normal to the jet axis. The longitudinal profiles indicate that the equivalence ratio of rich mixture case varies slightly along the jet. The other two cases are not varying much along the jet axis.

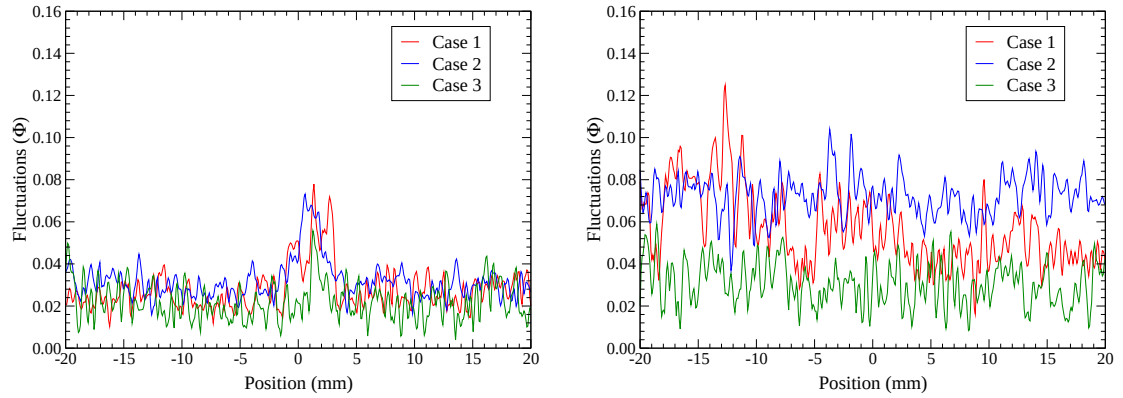

(a) Fluctuations in transverse direction

(b) Fluctuations in longitudinal direction

Figure 10.8: Fluctuations of equivalence ratio field at ignition location.

The transverse and longitudinal profiles of fluctuations of equivalence ratio field at the position of ignition are shown in Fig. 10.8. The local increase of fluctuation of equivalence ratio in transverse direction is due to the presence of electrodes in the acquired images. The fluctuations in the longitudinal direction varies around ϕ=0.02 to 0.1. This smaller fluctuation in the equivalence ratio field indicates the good repeatability of laminar stratified mixture.

The fluctuations of velocity and scalar field are shown in Fig. 10.9. It clearly shows very low fluctuations of velocity field in all three cases. Also, in both velocity and equivalence ratio field,

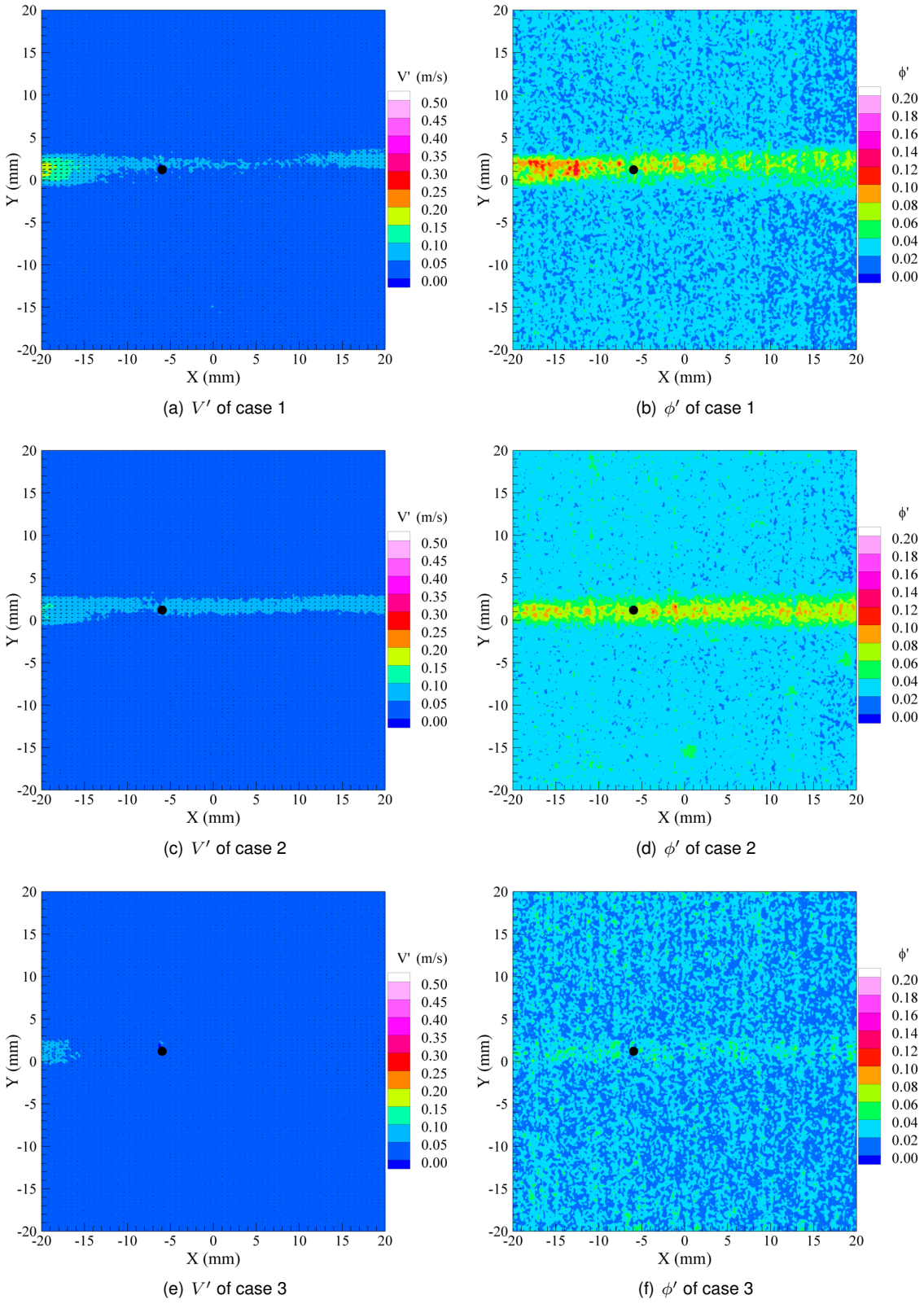

(a) V' of case 1

(b) ϕ' of case 1

(c) V' of case 2

(d) ϕ' of case 2

(e) V' of case 3

(f) ϕ' of case 3

Figure 10.9: Fluctuations of flow and scalar field of stratified cases.

we can observe the decrease of fluctuations with decrease of mixture stratification. This effect is linked to the delicate balance between the vacuum at the start of injection and the mass flow rate of mixture which varies slightly with equivalence ratio of mixture.

Parameters	Case 1		Case 2		Case 3	
	Mean	RMS	Mean	RMS	Mean	RMS
Velocity (m/s)	1.08	0.06	1.04	0.05	1.01	0.02
Equivalence ratio (ϕ)	1.24	0.06	0.95	0.06	0.79	0.03
Mixture fraction (Z)	0.074	0.004	0.058	0.004	0.048	0.002

Table 10.2: Mixture field conditions at the position and time of ignition.

The mean and rms of velocity, equivalence ratio and mixture fraction field at the position and time of ignition are given in the table 10.2. The mean velocity is around 1 m/s for all three cases. The mean equivalence ratio at the ignition point is rich for case 1, near stoichiometric for case 2 and lean for case 3.

10.5 Flow and scalar fields during flame propagation

The various steps of one cycle of experiment are shown in Fig. 10.10. The combustion chamber is initially filled with lean propane-air mixture of equivalence ratio ϕ=0.6 at atmospheric pressure. Then inlet and outlet valves of combustion chamber are closed and the flow is allowed to come to rest, meanwhile rich mixture is circulated inside the injector unit. After 30 seconds, injection is commenced, followed by ignition and acquisition of combustion images. Finally, the burned products are purged by using a vacuum pump. This sequence of steps completes one cycle of experiment within 240 seconds. For each time after ignition, 20 cycles are carried out.

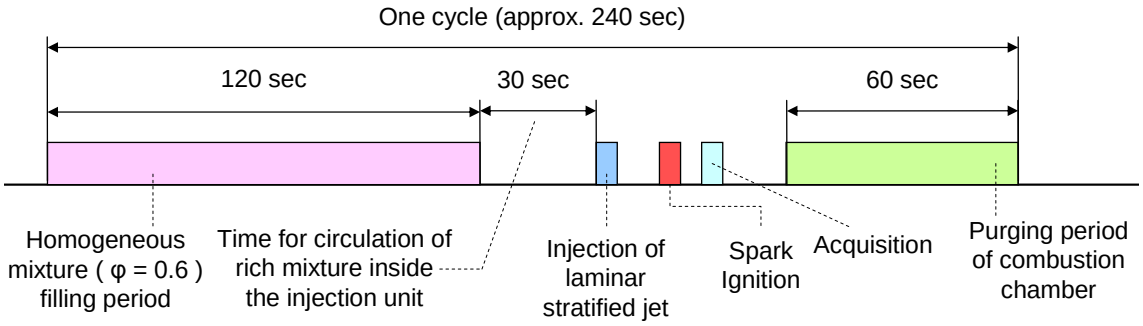

Figure 10.10: One cycle of laminar stratified flame propagation experiment.

The instantaneous flow and scalar field of flame propagation through three different stratified mixture fields are shown in Figs. 10.11 and 10.12. Generally, the flow and scalar fields are symmetrical with respect to the jet axis. At $1\ ms$, the flame propagation of stoichiometric case seems to be faster than the propagation of other two cases. The flame fronts are elongated in the right side of ignition point and slightly flattened in the left side due to the movement of laminar jet.

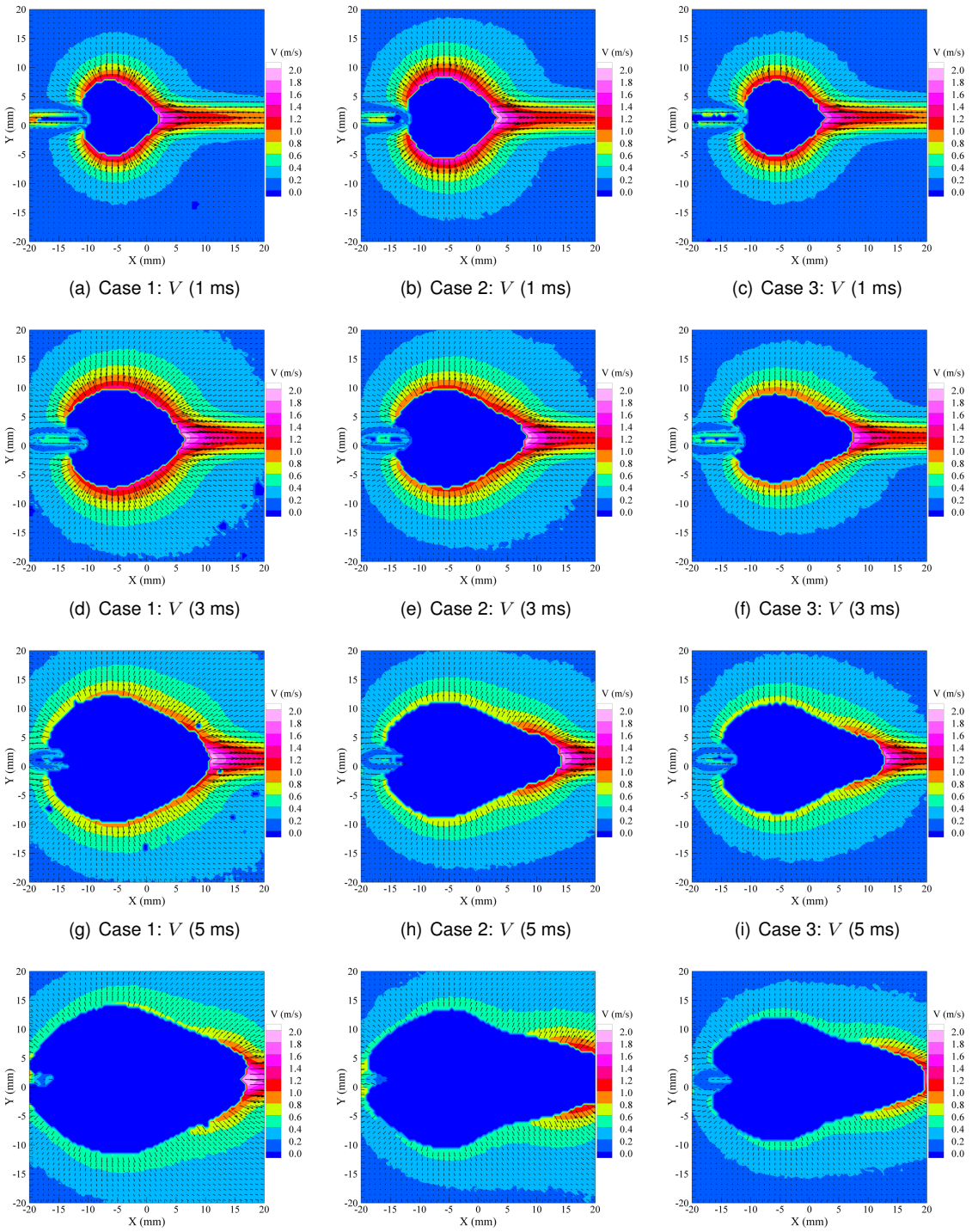

(a) Case 1: V (1 ms) (b) Case 2: V (1 ms) (c) Case 3: V (1 ms)

(d) Case 1: V (3 ms) (e) Case 2: V (3 ms) (f) Case 3: V (3 ms)

(g) Case 1: V (5 ms) (h) Case 2: V (5 ms) (i) Case 3: V (5 ms)

(j) Case 1: V (8 ms) (k) Case 2: V (8 ms) (l) Case 3: V (8 ms)

Figure 10.11: Instantaneous flow field of stratified flame propagation at different time after ignition.

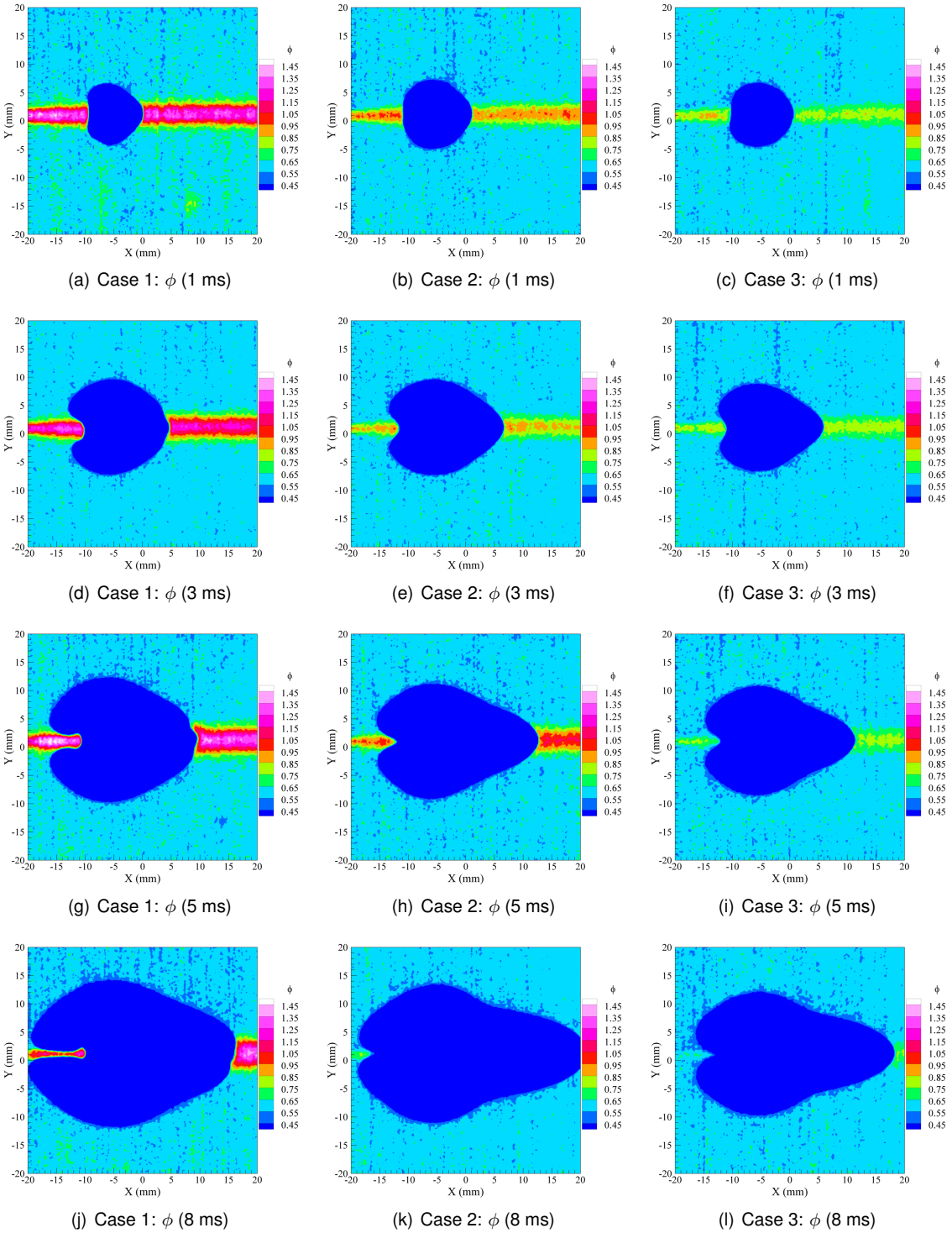

(a) Case 1: ϕ (1 ms) (b) Case 2: ϕ (1 ms) (c) Case 3: ϕ (1 ms)

(d) Case 1: ϕ (3 ms) (e) Case 2: ϕ (3 ms) (f) Case 3: ϕ (3 ms)

(g) Case 1: ϕ (5 ms) (h) Case 2: ϕ (5 ms) (i) Case 3: ϕ (5 ms)

(j) Case 1: ϕ (8 ms) (k) Case 2: ϕ (8 ms) (l) Case 3: ϕ (8 ms)

Figure 10.12: Instantaneous scalar field of stratified flame propagation at different time after ignition.

In all the cases, parts of flame fronts are already propagating through very lean mixtures. Indeed, the spread of flame fronts in Y direction is more than twice the thickness of stratified jet. At $3\ ms$ after ignition, the flame propagation of rich case seems to be faster than in other two cases. The flame fronts are elongated along the axis in the right side of ignition point and on the left side, the flame fronts are started to propagate along the boundaries of stratified jet. At $5\ ms$, the fresh gas expansion shrinks with decrease of stratification. The spread of flame propagation through very lean mixture is more for rich case compared with other two cases. At $8\ ms$, the elongation of flame front along the jet axis increases with decrease of stratification. The part of laminar stratified jet is still visible in rich case but not visible in other two cases.

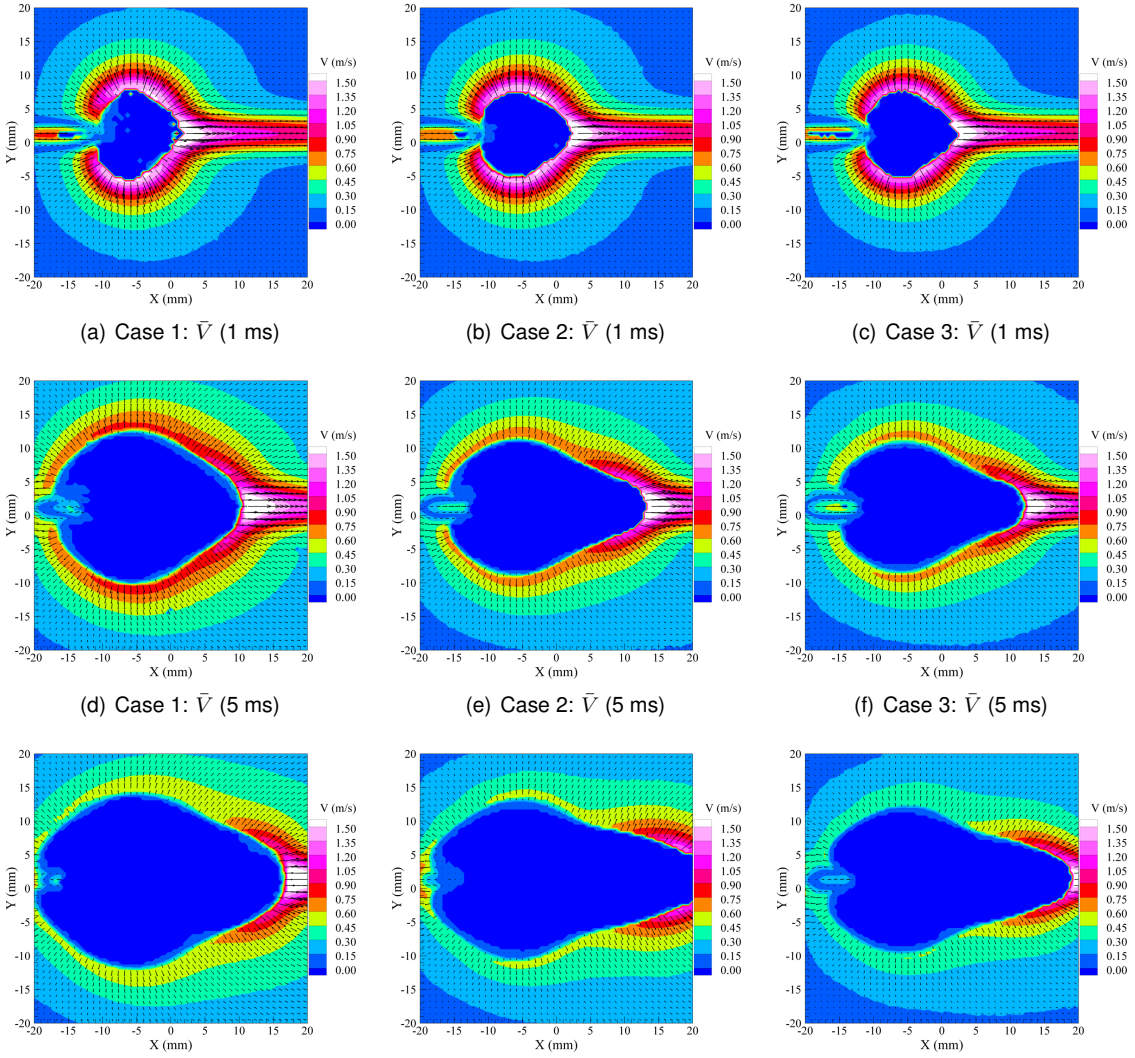

(a) Case 1: $\bar{V}$ (1 ms) (b) Case 2: $\bar{V}$ (1 ms) (c) Case 3: $\bar{V}$ (1 ms)

(d) Case 1: $\bar{V}$ (5 ms) (e) Case 2: $\bar{V}$ (5 ms) (f) Case 3: $\bar{V}$ (5 ms)

(g) Case 1: $\bar{V}$ (8 ms) (h) Case 2: $\bar{V}$ (8 ms) (i) Case 3: $\bar{V}$ (8 ms)

Figure 10.13: Mean flow field of stratified flame propagation at different time after ignition.

The mean flow and scalar fields of flame propagation of three different stratified cases are shown in Figs. 10.13 and 10.14. In all the cases, at $1\ ms$ after ignition, flame propagation seems to be uniform all around the flame front except the left side of ignition point where the laminar jet impinges on the flame front. The burned gas region is symmetrical and almost spherical for

stoichiometric and lean cases but irregular for rich case. At $5\ ms$, the velocity field of rich case clearly shows the faster flame propagation compared to the propagation in other cases. Indeed, rich stratified case propagated more on the lean mixture region than in other two cases. The mean scalar field is almost symmetrical for all the cases. Also, the burned regions of stoichiometric and lean cases are almost identical in shape, which are more elongated along the jet axis compared to that of rich case. At $8\ ms$, the presence of rich mixtures are still visible in case 1 because those mixtures are yet to be consumed by combustion. The velocity fields clearly show the difference among the cases where the flame fronts are propagating faster in rich case compared to that of stoichiometric case.

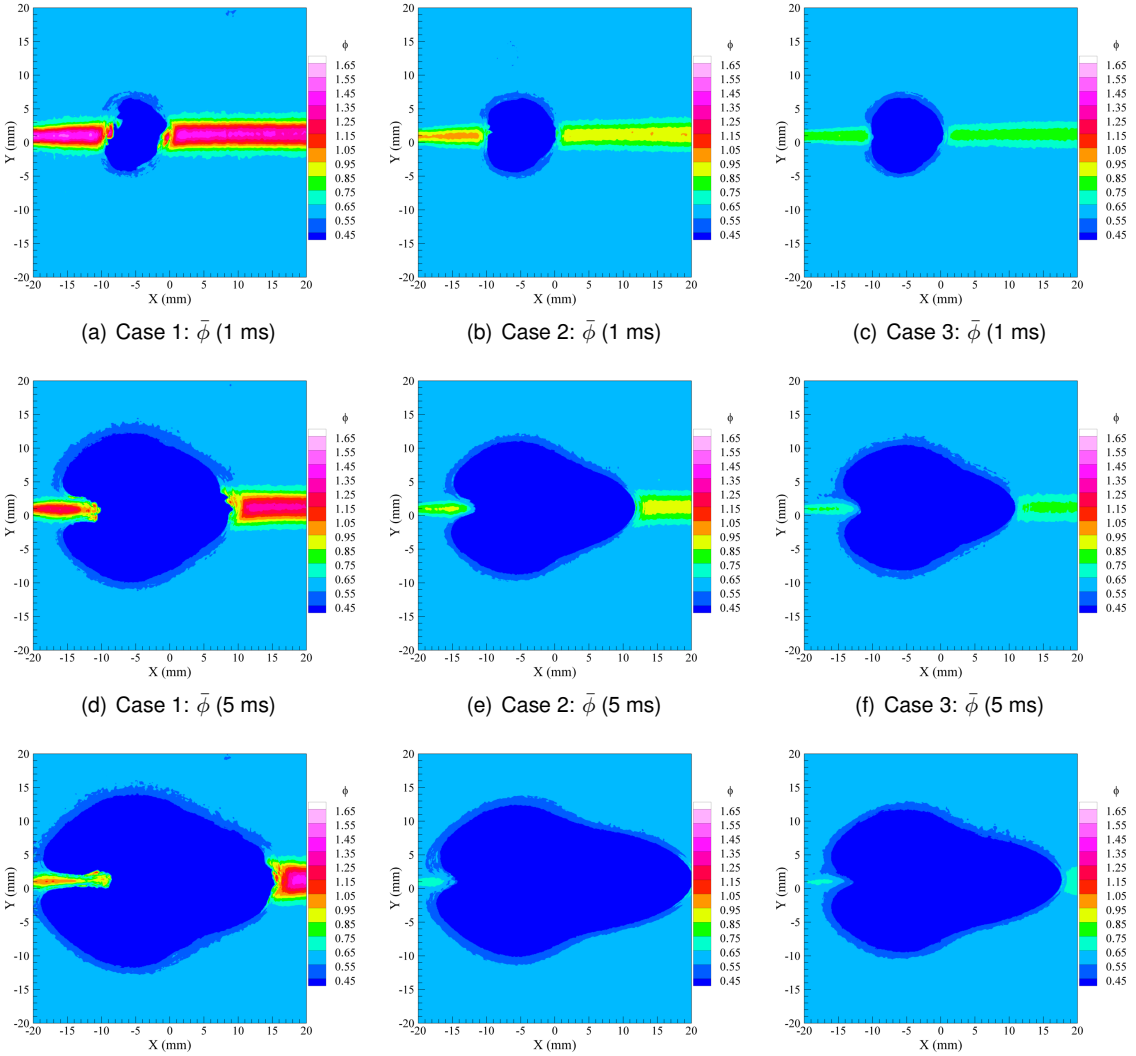

(a) Case 1: $\bar{\phi}$ (1 ms) (b) Case 2: $\bar{\phi}$ (1 ms) (c) Case 3: $\bar{\phi}$ (1 ms)

(d) Case 1: $\bar{\phi}$ (5 ms) (e) Case 2: $\bar{\phi}$ (5 ms) (f) Case 3: $\bar{\phi}$ (5 ms)

(g) Case 1: $\bar{\phi}$ (8 ms) (h) Case 2: $\bar{\phi}$ (8 ms) (i) Case 3: $\bar{\phi}$ (8 ms)

Figure 10.14: Mean scalar field of stratified flame propagation at different time after ignition.

The fluctuations of flow and scalar field at 1 and 8 ms after ignition are shown in Fig. 10.15. At $1\ ms$, the fluctuations of rich case in both velocity and equivalence ratio fields are higher than in other two cases. The similar trend is observed at $8\ ms$ after ignition shows that the variation of equivalence ratio around the ignition point at the time of ignition could be the reason

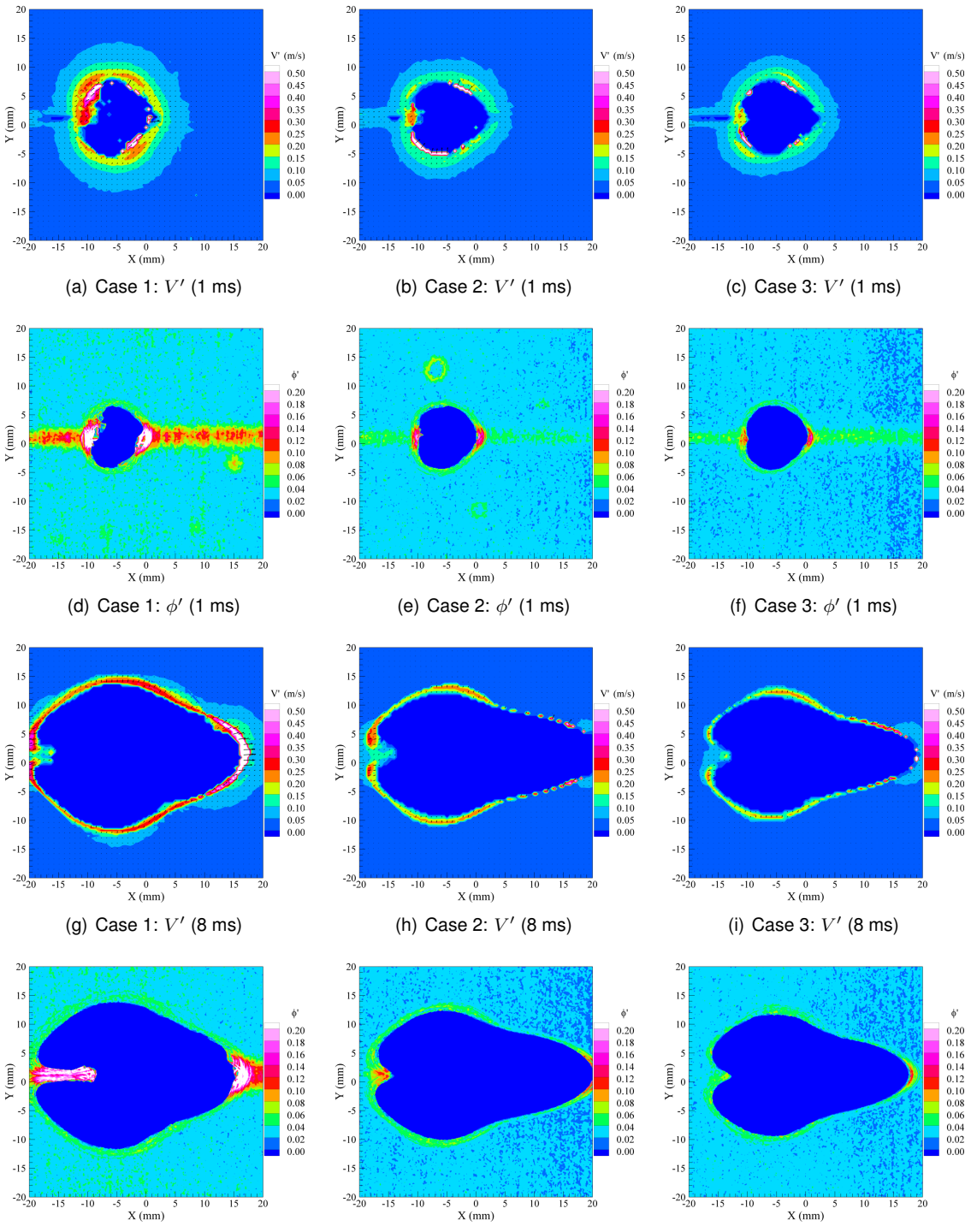

(a) Case 1: V' (1 ms) (b) Case 2: V' (1 ms) (c) Case 3: V' (1 ms)

(d) Case 1: ϕ' (1 ms) (e) Case 2: ϕ' (1 ms) (f) Case 3: ϕ' (1 ms)

(g) Case 1: V' (8 ms) (h) Case 2: V' (8 ms) (i) Case 3: V' (8 ms)

(j) Case 1: ϕ' (8 ms) (k) Case 2: ϕ' (8 ms) (l) Case 3: ϕ' (8 ms)

Figure 10.15: Fluctuations of stratified flame propagation at different time after ignition.

of increased fluctuation for rich stratified case than in other two cases. Nevertheless, in all the cases, fluctuations are very low indicating that 20 images acquired at each time seem to be sufficient for statistical data analysis. The localized fluctuations in the scalar fields are due to the deposit of oil droplets on the top window of combustion chamber.

10.6 Global analysis

The effect of degree of stratification on the flame propagation can be understood by analyzing the global parameters such as evolution of mean flame fronts and their spreads. So in this section, the global parameters of three different stratified cases are compared in order to gain some information on the effect of stratification.

10.6.1 Mean flame front contours

The flow and scalar fields of flame propagation indicated that the shape of flame fronts is changing from almost spherical to oval over a period of time. This evolution of flame front shape can be observed from the analysis of mean flame front contours. In this work, the instantaneous flame fronts are extracted from PIV and PLIF images by using new flame front extraction algorithm which is explained in the appendix (§ A). One example of flame fronts extracted from PIV image pair and PLIF image are shown in Fig. 10.16. It shows a good superposition of PIV contours with PLIF contour which confirms that both PIV and PLIF cameras are acquiring images from the same image zone.

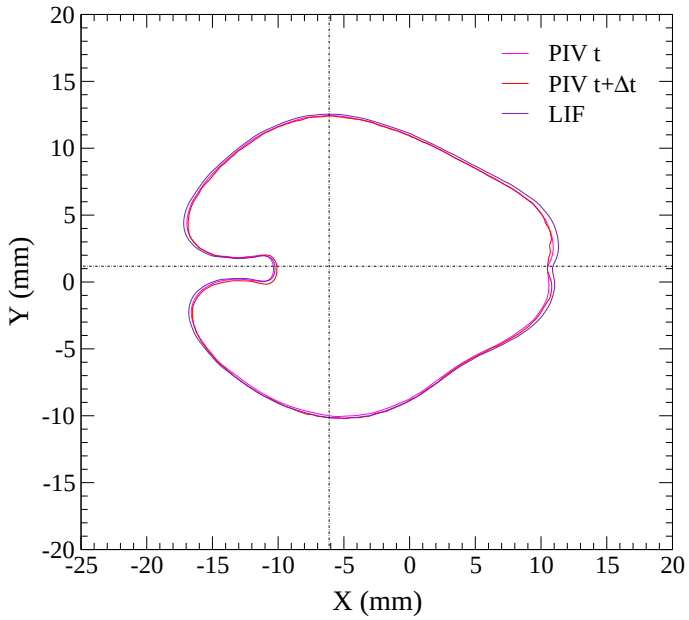

Figure 10.16: Superposition of LIF contour with PIV contours.

For each case, at a given time after ignition, mean flame fronts are calculated from their instantaneous flame front contours. The evolution of mean flame fronts for three stratified cases is shown in Fig. 10.17. First of all, the flame fronts are almost symmetrical with respect to the

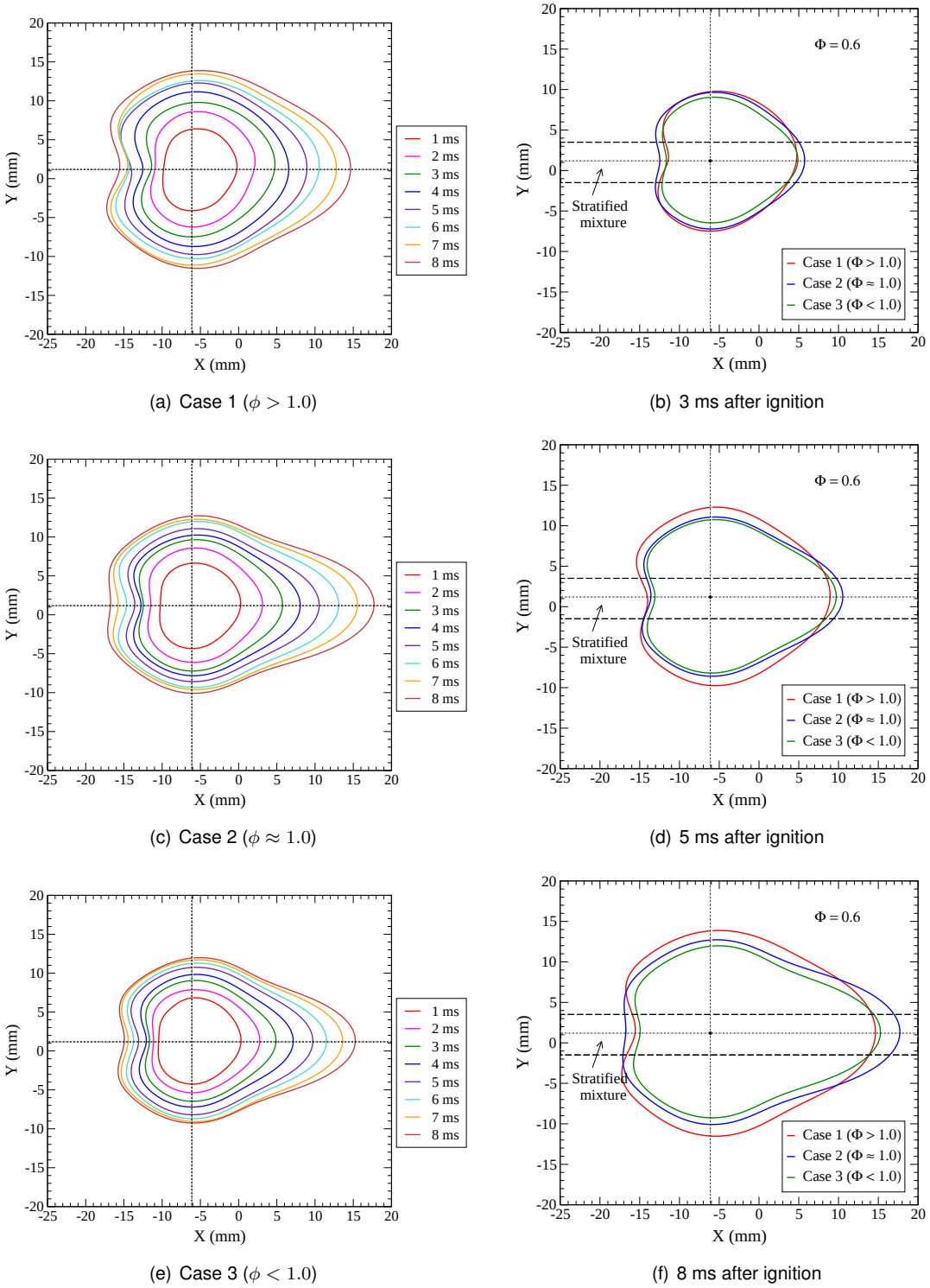

(a) Case 1 ($\phi > 1.0$)

(b) 3 ms after ignition

(c) Case 2 ($\phi \approx 1.0$)

(d) 5 ms after ignition

(e) Case 3 ($\phi < 1.0$)

(f) 8 ms after ignition

Figure 10.17: Evolution of mean flame front contours.

jet axis. In all the cases, the rate of flame front expansion along normal to the jet axis decreases over a period of time whereas the expansion along the jet axis increases with time. At $3\ ms$ after ignition, the spreads of mean flame fronts in Y direction are more than twice the thickness of stratified jet for all the cases. We can notice only a small difference between three different cases at this time. But the difference in shape between three cases becomes quite visible at $5\ ms$ after ignition where the flame front of rich case propagated more in the very lean side compared to that of other cases. Also the mean flame front shapes of stoichiometric and lean cases are almost identical with small variation in size of flame surface. At $8\ ms$ after ignition, the mean flame front of rich case propagated further in to very lean mixture than in other two cases. But the stoichiometric and lean cases are elongated more in the X direction than in rich case. So this analysis of mean flame fronts roughly indicates that the rich stratified case increases the rate of flame propagation through very lean mixture than in other two cases.

10.6.2 Asymmetry

The mean flame fronts clearly showed the difference in flame propagation between X and Y direction. This asymmetry in flame front shape can be analyzed by measuring the maximum spread of flame propagation in X and Y directions. So we calculated the maximum spread of flame fronts and their ratio (Lx/Ly) as a function of time for different cases (shown in Fig. 10.18).

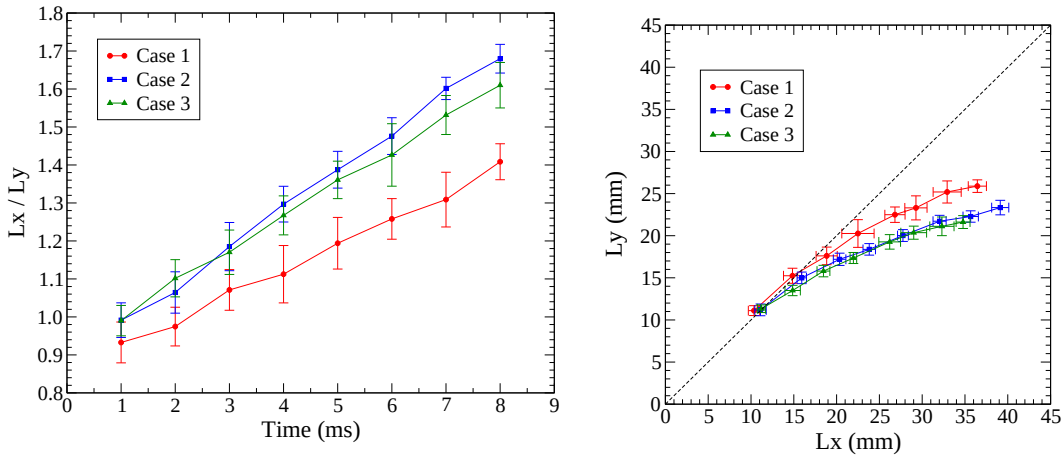

(a) Variation of asymmetry coefficient as a function of time.

(b) Ly as a function of Lx

Figure 10.18: Analysis of flame front geometry.

At $1\ ms$ after ignition, the mean values of asymmetry coefficient of rich case is smaller than one indicates that the flame propagation along jet axis is smaller than normal to the jet because of presence of higher equivalence ratio mixtures ($\phi > 1.2$) along the jet axis. But the mean value of asymmetry coefficients for stoichiometric and lean cases are equal to one indicates that the flame fronts of these cases are almost spherical at this time. The asymmetry coefficient of all the cases continuously increases with time and the rate of increase is smaller for the rich case than in other two cases. After $4\ ms$, the asymmetry coefficient of stoichiometric case is more than in other two cases. This comparison confirms that the flame front originated from rich mixture condition is spreading faster into very lean mixture compared with the spread of flame fronts of

other two cases. Among the stoichiometric and lean case, the flame fronts of stoichiometric case are more elongated along the jet axis than lean case but both cases are having same variation of Ly as a function of Lx (Fig. 10.18). This observation points out that the increased elongation of stoichiometric case is due to its faster flame propagation along the jet axis compared to that of lean case.

10.7 Analysis of conditioned local variables

So far global analysis indicated that the flame propagation increases with degree of stratification. However, those observations cannot reveal the quantitative difference between three different stratified cases and their relaxation time because those global data are affected by the variation of local equivalence ratios and local stretch rates. So we have to isolate those factors from the local measurements in order to quantitatively know the effect of degree of stratification on flame propagation. This can be achieved by measuring the local flame speed, local fresh gas velocity, local laminar burning velocity and local stretch rate along with local equivalence ratio. In this work, the local equivalence ratio around the flame front is measured from the instantaneous scalar field of flame propagation. The local flame speed is measured from the displacement between two successive flame fronts extracted from PIV image pair. But the local laminar burning velocity cannot be measured from the instantaneous flow field of flame propagation because the spatial resolution of velocity field is not sufficient to measure the local fresh gas velocity near preheat zone of flame front. So in order to measure the local fresh gas velocity and local laminar burning velocity, we have utilized the newly developed PIV approach explained in the previous chapter. After that, to compare the stratified cases, the measured local variables are sampled from the regions where the flame fronts are propagating through lean mixture of $\phi = 0.6$ within moderate stretch range.

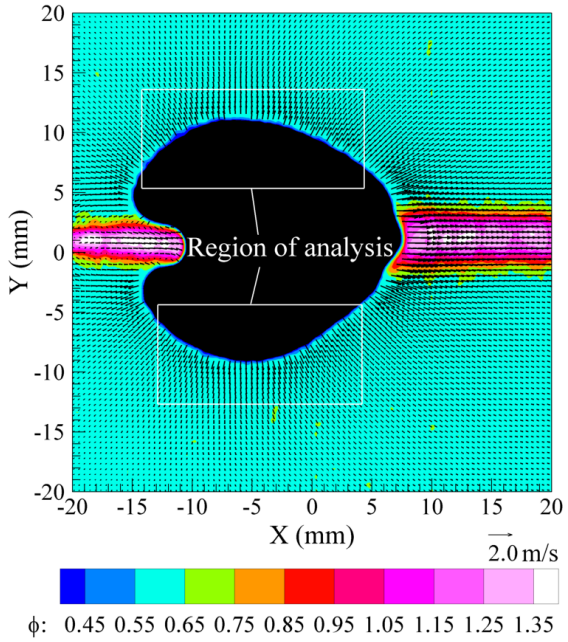

Figure 10.19: Selection of region of analysis for conditional measurements.

One example of superimposed velocity and equivalence ratio field of flame propagation is shown in Fig. 10.19. The approximate region of analysis used for sampling the local variables is also indicated in that figure as rectangular in white color where the flame front propagates through mixture of equivalence ratio $\phi = 0.6$ and the flame fragments are almost spherical in shape in that region. The flame fragments propagating through lean homogeneous mixture ($\phi = 0.6$) and low stretch rate conditions are selected with the following criteria:

- Equivalence ratio: 0.55 $< \phi <$ 0.65
- Flame stretch rate (1/s): K $<$ 1000
- Laminar burning velocity (m/s): $u_l <$ 0.60
- Tangential velocity (m/s): -0.1 $< u_t <$ 0.1

Two additional criterions have been added to remove the measurement still affected by the energy deposit of ignition and by tangential strain rate. One example of datasets with and without conditioning is shown in Fig. 10.20. The complete dataset on the left shows a large dispersion due to various conditions of flame propagation. The conditioning of measurements induces a narrower dispersion (right plot) with a high sampling.

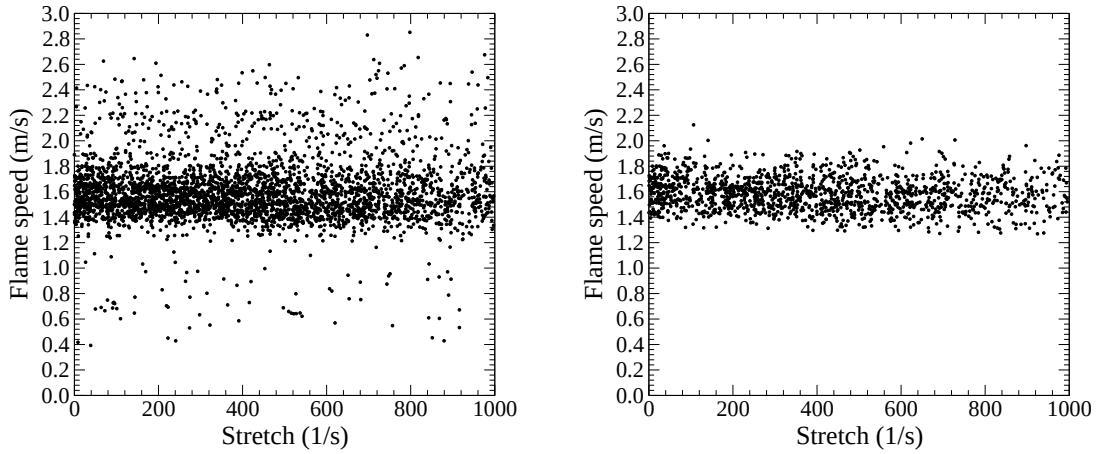

(a) Complete dataset

(b) Conditioned dataset

Figure 10.20: Local flame speed as a function of stretch rate for case 1 at 2 ms.

In first approximation, the local flame stretch has been estimated only from in-plane local curvature and the transverse curvature has not been considered. So, the response of the measurement as a function of stretch cannot be analyzed and then in Figs. 10.21 and 10.22, only the extrapolation to zero stretch will be considered to estimate the laminar burning velocity. The unstretched values are provided in the tables 10.3 and 10.4. The comparisons of unstretched values of three cases are shown in Fig. 10.23. Generally, the difference between the values of rich and stoichiometric case are more than difference between the stoichiometric and lean case in all the timings. For example at $1\ ms$ after ignition, the difference between the conditioned planar flame speed of rich and stoichiometric case is around $0.29\ m/s$ whereas the difference between

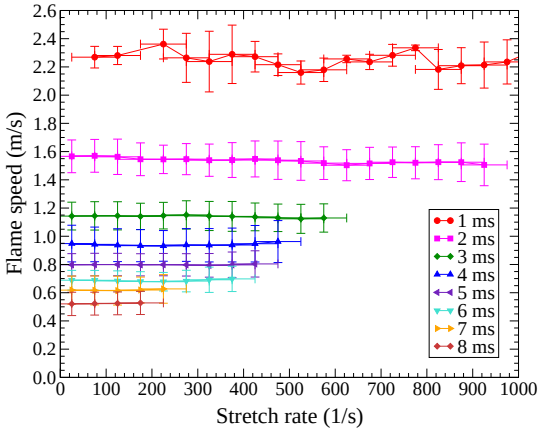

(a) Case 1: S_b Vs. K

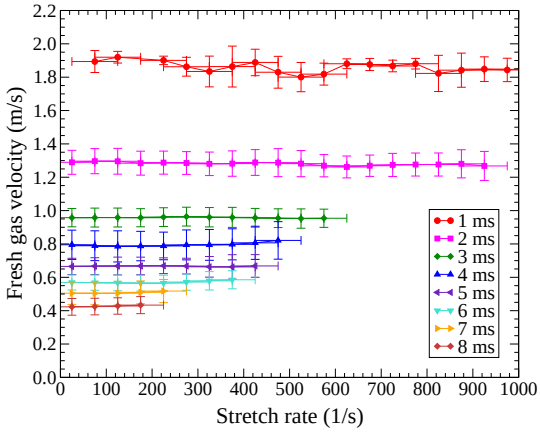

(b) Case 1: u_g Vs. K

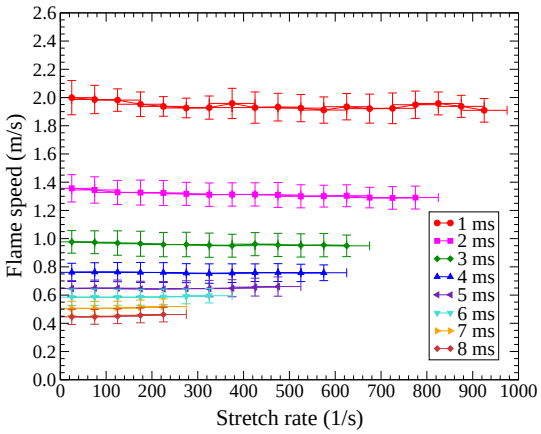

(c) Case 2: S_b Vs. K

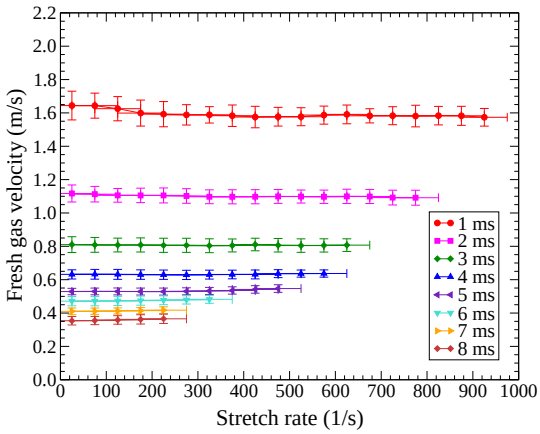

(d) Case 2: u_g Vs. K

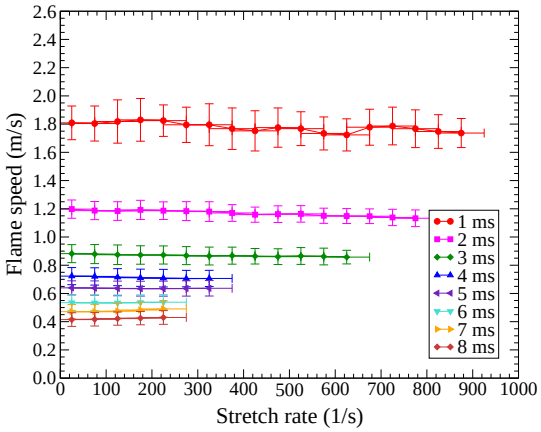

(e) Case 3: S_b Vs. K

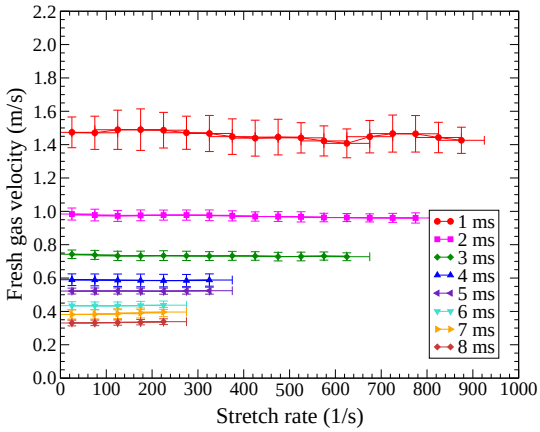

(f) Case 3: u_g Vs. K

Figure 10.21: Variation of flame speed and fresh gas velocity as a function of stretch rate for different cases.

Time (ms)	S_b^0 (m/s) at $\phi = 0.6$			u_g^0 (m/s) at $\phi = 0.6$		
	Case 1	Case 2	Case 3	Case 1	Case 2	Case 3
1	2.28	1.97	1.82	1.89	1.62	1.48
2	1.56	1.35	1.20	1.29	1.11	0.98
3	1.15	0.97	0.88	0.96	0.81	0.74
4	0.94	0.76	0.72	0.78	0.63	0.59
5	0.80	0.64	0.64	0.67	0.52	0.52
6	0.68	0.58	0.53	0.56	0.47	0.43
7	0.61	0.50	0.47	0.50	0.41	0.38
8	0.52	0.44	0.41	0.42	0.35	0.33

Table 10.3: Unstretched values of conditioned flame speed and fresh gas velocity of three cases.

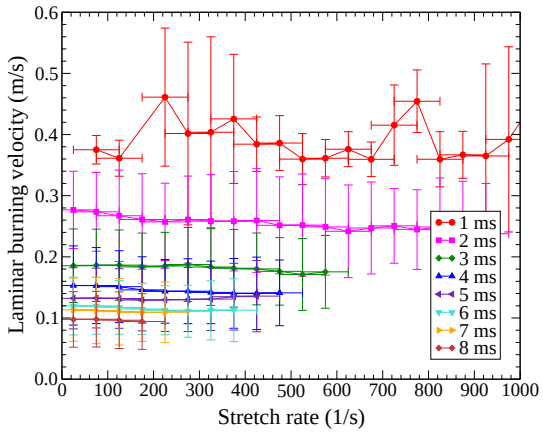

(a) Case 1: u_n Vs. K

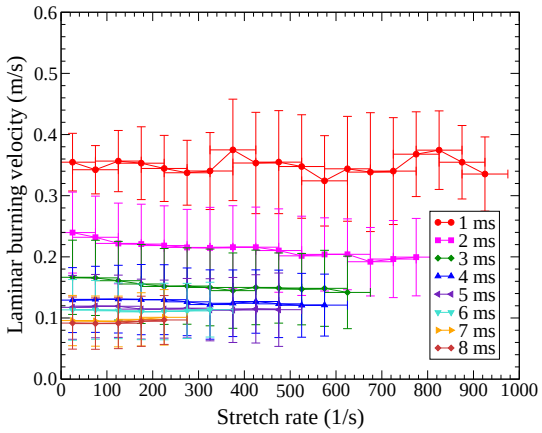

(b) Case 2: u_n Vs. K

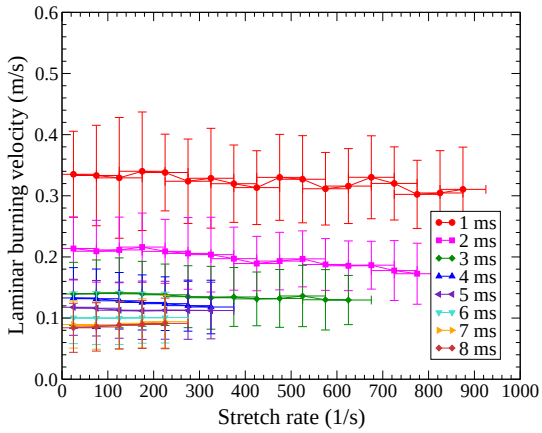

(c) Case 3: u_n Vs. K

Figure 10.22: Variation of laminar burning velocity as a function of stretch rate for different cases.

Time (ms)	u_n^0 (cm/s) at $\phi = 0.6$		
	Case 1	Case 2	Case 3
1	39.2	34.9	33.8
2	27.1	23.3	21.9
3	18.9	16.4	14.1
4	15.3	13.2	13.5
5	13.0	11.9	11.7
6	12.0	11.3	10.0
7	11.4	9.3	8.7
8	9.9	9.0	8.3

Table 10.4: Unstretched values of conditioned laminar burning velocity of three cases.

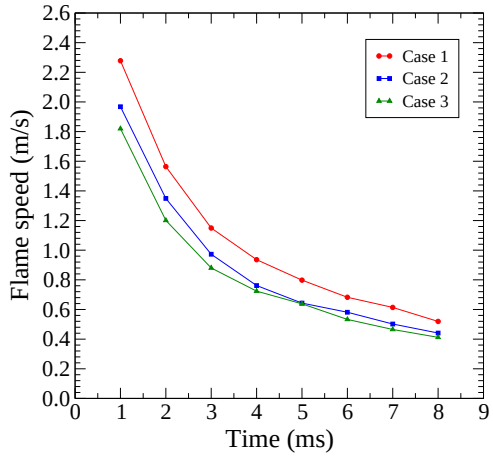

(a) Evolution of unstretched flame speed

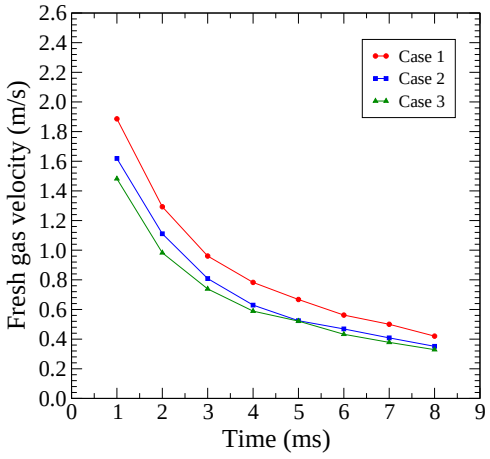

(b) Evolution of unstretched fresh gas velocity

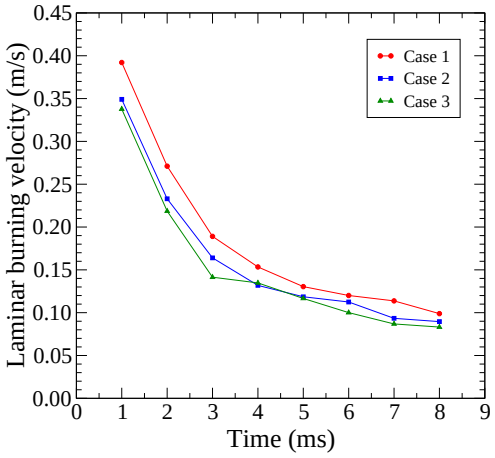

(c) Evolution of unstretched laminar burning velocity

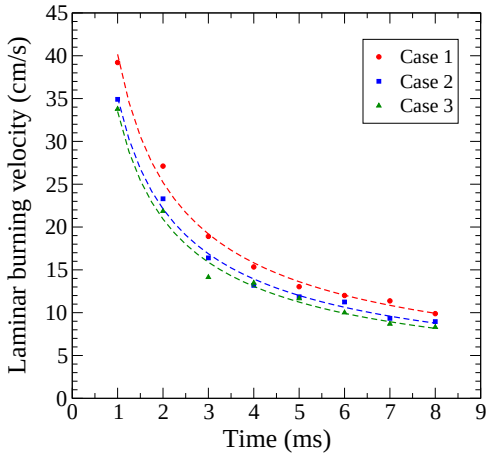

(d) Power law fit to the evolution of laminar burning velocity

Figure 10.23: Unstretched values of conditioned velocities for different cases.

stoichiometric and lean case is around $0.13\ m/s$. The similar kinds of variations between the cases are observed for fresh gas velocities and laminar burning velocities.

In all the cases, the unstretched velocities at $1\ ms$ after ignition are around 4.2 times greater than their corresponding values at $8\ ms$ after ignition. It shows that the propagation of flame through very lean homogeneous mixture of equivalence ratio $\phi = 0.6$ slows down over a period of time in all the cases. Also the evolutions of unstretched velocities are almost similar for all the stratified cases. Indeed, the variations of unstretched values show a power law relationship with time for all the cases. Therefore, power law fit is applied to the unstretched laminar burning velocity which is shown in Fig. 10.23 as dashed line for each case. Those power law fits indicate that the unstretched conditioned laminar burning velocity is proportional to the $Time^{-\alpha}$, where the scaling parameter α is varying between 0.66 to 0.67 for three cases. This small difference of scaling parameter between three cases indicates that time to relax is independent of degree of stratification. But the magnitude of local laminar burning velocity is not independent to the degree of stratification. Indeed, at each time after ignition, the unstretched laminar burning velocity of rich stratified case is around 1.14 times higher than that of stoichiometric stratified case and almost 1.2 times higher than that of lean stratified case. This clearly confirms the effect of degree of stratification on flame propagation. At $6\ ms$, the unstretched laminar burning velocity of rich stratified case is almost equal with that of homogeneous mixture of equivalence ratio $\phi = 0.6$ which is around $12.5\ cm/s$ [Razus et al. (2010)]. So in our configuration, the relaxation time is around $5\ ms$ to $6\ ms$ from start of ignition. The quantitative analysis of local conditioned velocities of three cases clearly shown that the flame fronts initially propagate at faster rate due to the availability of favorable mixture conditions around the ignition point at the time of ignition as proposed in literature [Ra (1999), Pires Da Cruz et al. (2000), Kang and Kyritsis (2007a)]. Then flame propagation gradually decelerates during its propagation through very lean mixture and at later stages, the rate of propagation is almost equal to the local homogeneous combustion. The degree of stratification greatly influences the flame propagation through very lean mixture which back supports the flame propagation by hotter gases temperature and excess of fuel in burned gases.. So our quantitative analysis of laminar stratified flame propagation clearly confirmed the memory effect of stratified flames.

10.8 Conclusions

In this chapter, we have discussed the experimental setup to create controllable laminar stratified mixture field inside a constant volume chamber. We analyzed the flow and scalar fields of stratified mixture at the position and time of ignition for three different stratified cases. Then laminar flame propagations through stratified mixture fields are analyzed. From that, we compared the global parameters such as evolution of mean flame fronts, flame front geometries and observed the enhancement of flame propagation by the increase of degree of stratification level. Then local instantaneous flame speeds, fresh gas velocities and laminar burning velocities are measured by using the newly developed algorithms explained in the previous chapter. Finally, we computed the conditioned local variables based on local equivalence ratio, local stretch rate and local tangential velocity of flame propagation and compared the results of three different stratified cases. The comparison of results clearly proved the enhancement of flame propagation by stratification of

mixture field and increase of enhancement with increase of degree of stratification. The average relaxation time of stratified flame propagation is $5\ ms$ in our configuration. In conclusion, the stratification of mixture field enhances the propagation of flame front through very lean mixture field back supported by the rich and stoichiometric flame fragments of previous timings of stratified combustion.

Chapter 11

Conclusions and Perspectives

The automobile manufacturers are developing new technologies to reduce fuel consumption as well as emissions. One such technology is the direct injection gasoline engine which offers more fuel efficiency than conventional petrol engines [Zhao et al. (1999)]. The potential of direct injection gasoline engine is realized by utilization of stratified combustion mode where the overall mixture is lean but the mixture around the spark plug is rich enough to ensure flame propagation through lean mixtures. This strategy results in less fuel consumption and lower CO_2 emissions. But this stratified mode introduces cycle-to-cycle variations and difficulties in controlling the combustion. In that regard, numerical modeling can be very helpful to optimize engine parameters but the modeling process requires deep fundamental understanding of stratified combustion. So it becomes important to study the stratified flame propagation in simple configurations to gain knowledge and to provide data for the numerical simulations. Therefore, in this work, flame propagation through stratified mixture field under laminar and turbulent flow conditions have been investigated by using simultaneous PIV/PLIF measurement techniques. The experimental investigations are supported by the ANR (*A*gence *N*ationale de la *R*echerche) and the CNRS through the MESOPTI-CO2 program, in collaboration with the GSM (*G*roupement *S*cientifique *M*oteurs).

The experiments are conducted in a constant volume combustion chamber under atmospheric pressure and ambient temperature conditions. Simultaneous PIV/PLIF measurement techniques are utilized in order to measure combined flow and scalar field of flame propagations with an investigation area of $45 \times 45\ mm^2$. In this work, propane flow is seeded with fluorescent tracer to measure the equivalence ratio by FARLIF technique [Reboux et al. (1996)]. Anisole is selected as fluorescent tracer for propane-air mixture based on the investigations carried out by Pasquier-Guilbert (2004). The air flow rate is seeded with micro-metric olive oil particles to measure the velocity field by PIV technique. The area under investigation is illuminated by the combined PIV/PLIF laser sheets and the emitted fluorescence signal in the UV range is collected by ICCD camera and emitted Mie scattering signal in the visible range is collected by CCD camera and all the systems are synchronized by a special control unit. From the acquired CCD and ICCD images, combined velocity and equivalence ratio fields are measured by using post-processing schemes. A new LIF image correction scheme has been developed to remove the noises in the fluorescence images, which also improved the accuracy of equivalence ratio measurement. The velocity field is measured from particle images by using post-processing scheme developed by Lecordier (1997). The two-dimensional velocity field is measured with an uncertainty of $\pm\ 0.04\ m/s$ and equivalence

ratio field is measured with an uncertainty of $\pm$ 2% @ $\phi = 1.0$. The spatial resolution of velocity measurement is $160\ \mu m$ whereas the spatial resolution of equivalence ratio measurement is $444\ \mu m$.

The first task of this work is the investigation of turbulent stratified flame propagation in a constant volume combustion chamber by using simultaneous PIV/PLIF techniques. For that, an axisymmetrical injection setup has been developed to realize turbulent stratified mixture field inside the combustion chamber. The evolution of velocity of turbulent jet at the entrance of combustion chamber is measured by hot wire anemometry technique in order to provide data for numerical simulation. From the analysis of mixture field, the optimal ignition location is selected and the mixture is spark-ignited at slightly richer than stoichiometric condition. Then unsteady flame propagation through stratified mixture field is acquired by using simultaneous PIV/PLIF techniques. Also, flame propagation through six different homogeneous mixtures is acquired with same injection strategy in order to isolate the influence of flow turbulence from the effect of stratification of mixture field. In all the cases, the flame propagations are acquired starting from $1\ ms$ to $5\ ms$ after ignition with $1\ ms$ time duration. At each cycle of experiment, one PIV image pair simultaneously one PLIF image of flame propagation is acquired. At each acquisition time, one hundred cycles are performed for stratified case and sixty cycles are performed for homogeneous cases. From those images, the combined velocity and equivalence ratio fields of flame propagations are calculated using post-processing tools. A new extraction method has been developed to extract the flame front contours with sub-pixel resolution. From the extracted flame front contours, mean flame front radius and mean flame propagation speed of different cases are calculated. The analysis of those global parameters indicated the increased wrinkling rate of stratified flames and their higher cycle-to-cycle variations compared to that of homogeneous flames. The local variables such as equivalence ratio, flame speed, normal component of fresh gas velocity all around the flame fronts are then calculated for all the cases. The local curvature and the local turbulent burning velocity of stratified flames are conditioned based on the local equivalence ratio. The local conditioned values of stratified flames are then compared with that of equivalent homogeneous cases. The comparison revealed that the stratified flames are always faster than lean and stoichiometric homogeneous cases and at least twice faster than lean homogeneous cases at initial propagation period. Indeed, the turbulent burning velocity of stratified flame through $\phi = 0.6$ mixture is around $0.3\ m/s$ which is at least three times faster than the unstretched laminar burning velocity of equivalent premixed flame. So our quantitative analysis has confirmed the effect of mixture stratification on flame front wrinkling, enhancement of flame propagation and widening of flammability limits. Our observations significantly contributed to the understanding of fundamentals of turbulent stratified combustion.

The second task of this work is the development of new technique to accurately measure the local flame speed and the local fresh gas velocity in order to investigate the laminar stratified flame propagation. For that, two original methods have been developed to deduce the local flame speed and local fresh gas velocity from pair of PIV images. The local flame speed is measured from the distance between two successive flame positions. For the flame localization, a new extraction tool combined with a filtering technique has been developed to access to the flame front coordinates with sub-pixel accuracy. The local fresh gas velocity near the flame front is extracted from the maximum of the normal velocity profile, located within $1\ mm$ ahead of the flame front. To achieve

the required spatial resolution, a new algorithm based on adaptive interrogation window scheme has been developed by taking into account the flow and flame front topologies. The accuracy and reliability of new methods have been evaluated from two complementary approaches based respectively on synthetic images of particle and on the well-established configuration of outwardly propagating spherical flames. The directly measured unstretched laminar burning velocities of propane-air premixed flames are then compared with literature results and satisfactory agreement is observed. The two newly developed approaches have improved the accuracy of measurement of local flame speed and local fresh gas velocity and they greatly improved the accuracy of direct measurement of local laminar burning velocity of stretched flames which would be otherwise not possible to measure by available global measurement techniques.

The final task is the investigation of laminar stratified flame propagation by using simultaneous PIV/PLIF techniques. For that, a unique injection setup has been developed to achieve controllable as well as repeatable laminar stratified mixture field inside a constant volume combustion chamber. The injection system is optimized to realize very low flow with very high degree of stratification. The laminar stratified mixture is then spark-ignited and the propagation of flame through stratified mixture field is acquired by using simultaneous PIV/PLIF measurement techniques. The flame propagations through three different stratified fields with same aerodynamics are analyzed in order to understand the effect of degree of stratification on combustion. In all the cases, the flame propagations are acquired starting from $1\ ms$ to $8\ ms$ after ignition with $1\ ms$ time duration. At each cycle of experiment, one PIV image pair simultaneously one PLIF image of flame propagation is acquired. At each acquisition time, twenty cycles are performed for each case. From the particle images, the local flame speed, local fresh gas velocity and local laminar burning velocity are calculated by using new PIV algorithms developed in this work. From the measurements, local conditioned variables are calculated for flame fragments propagating through lean mixture with moderate stretch after ignition in three different stratified mixture cases. Then, local conditioned flame speed, fresh gas velocity and laminar burning velocity of three different stratified cases are compared in order to know the memory effect and relaxation time of stratified flames. Our results has clearly shown that at early stage, the stratified flames are propagating around three to four times faster through very lean mixture field compared to unstretched laminar burning velocity of equivalent homogeneous flame and decelerates over a period of time and eventually losses its memory effect. Our quantitative analysis has confirmed the enhanced flame propagation through lean mixtures when back supported by rich and stoichiometric flame fragments of previous timings and also quantitatively shown that the enhancement of propagation increases with increase of degree of stratification of mixture field.

From our experimental investigations, we have observed some interesting results of stratified combustion. The analysis of turbulent stratified flame propagation showed that igniting flame at slightly rich mixture condition is advantageous than igniting at stoichiometric condition. The analysis can be extended to study the importance of mixture strength at the location of ignition and their role in cycle-to-cycle variation. Another interesting possibility is to find the link between lower flammability limit and initial mixture strength. The analysis of laminar stratified flame propagation confirmed the enhancement of flame propagation with degree of stratification. So it could be interesting and worthwhile to investigate the flame propagation through maximum possible degree of stratification obtainable in order to know the effect of excess chemical species on stratified

flame propagation. Also, this experimental setup could be extended to find the lower flammability limits of stratified flames and their behavior at near flammability limits. In this work, we have also developed an interrogation window reshaping technique, which is able to resolve the velocity gradient with high spatial resolution and offers interesting potentials to improve the measurement of the normal and tangential components of fluid velocity very near to flat or curved surfaces. Our direct local instantaneous burning rate measurement from PIV images opens new potentials for investigating the local properties of flame interacting for instances with flow structures, mixture fluctuations and walls.

Part III

Appendices

Appendix A

Flame front extraction tool

The flame front characteristics such as mean flame radius, local curvature can be calculated from the flame front coordinates. For that, we need a tool to extract the flame front accurately from the PIV and PLIF images. This appendix explains the new extraction tool developed in this work.

A.1 Edge detection algorithm

One example of particle image of a spherically expanding laminar flame front captured at $4ms$ after ignition is shown in Fig. A.1. The bright zone is the fresh gas region, represented by the Mie scattering signal of seeding particles. The dark zone is the burned gas region, represented by the absence of seeding particles which are completely burnt through the very sharp temperature gradient of the flame front. A closer observation of the flame front region shows irregularities in the seeding particle distribution and that could introduce small artificial wrinkles in the extracted flame front coordinates.

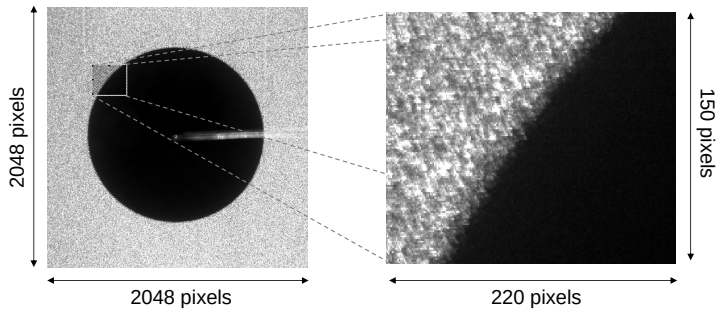

Figure A.1: A closer view of flame front region in PIV image.

In this work, the PIV images are 12 bit images and the PLIF images are 16 bit images. So each pixel may have a value between 0 to 4095 in the PIV images and have a value between 0 to 65535 in the PLIF images. One example of histogram of PIV image is shown in Fig. A.2. It clearly shows two peaks corresponding to the burned and fresh gas region. We can find an optimum threshold which separates the fresh gas region from the burned gas region. This has been achieved by using Otsu algorithm [Otsu (1979)]. Then the coordinates of flame front at the

interface between fresh and burned region are located by the edge detection algorithm based on the optimum threshold value [Lecordier (1997)]. One example of extracted flame front contour is shown in Fig. A.3.

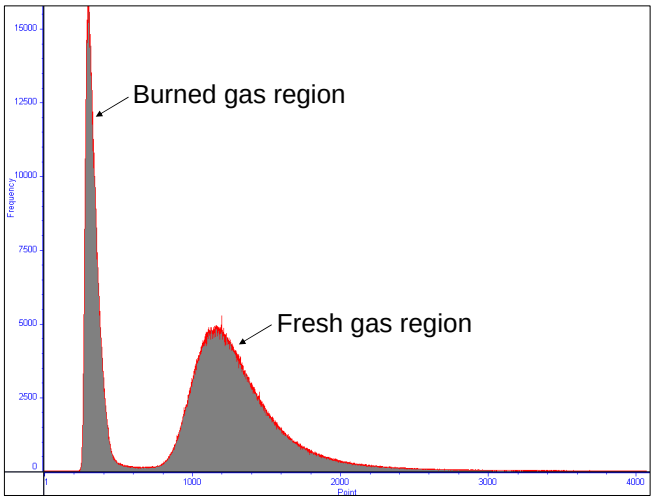

Figure A.2: Histogram of PIV image.

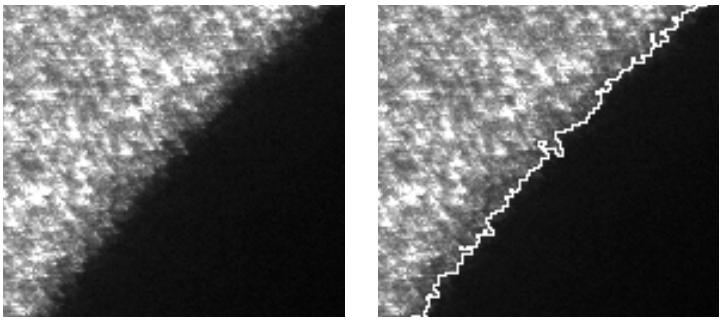

Figure A.3: A closer view of coordinates of flame front extracted by edge detection algorithm.

A simple visual impression of flame front seems to be smooth whereas the extracted flame front shows lot of small wrinkles. These artificially superposed noises are due to the irregularities in the seeding particle distribution closer to the flame front. In order to measure the local curvature and flame front displacement, it is very important to extract the flame front without superposed noises. So we have developed a new extraction tool which is explained in the next section.

A.2 Novel extraction algorithm

The new algorithm extracts the flame front coordinates with sub-pixel resolution in three steps. The first step determines the optimum threshold I_{otsu} which differentiates the burned gas region from the fresh gas region by using Otsu algorithm applied on the top left quarter area (512×512 pixels) of images, which always contains both fresh and burned gas region. The next two steps are depicted in the Fig. A.4.

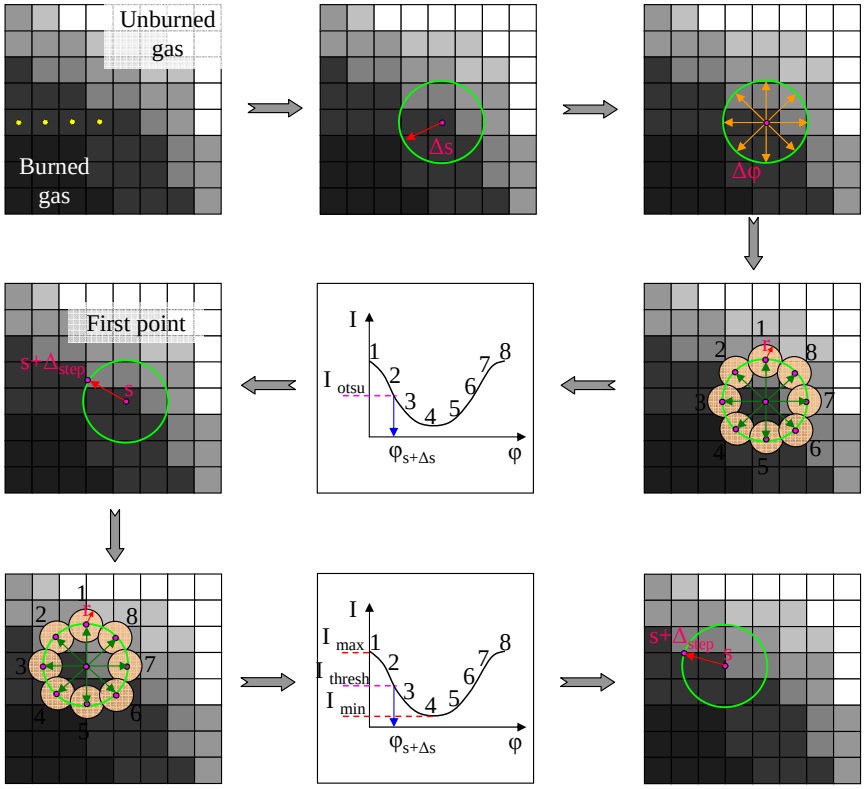

Figure A.4: The principle of novel extraction algorithm with sub-pixel resolution.

The second step starts to find the first flame front coordinate from the initial coordinate location given as input to the algorithm. The principle of this step is developed by Weißet al. (2008). The first six sequences in the Fig. A.4 are the second step. The first frame is the small portion of an image of size 8×8 pixels close to the flame front. In that frame, dark region is the burned gas region and bright region is the fresh gas region. The yellow points are the failed coordinates that means they are not belong to the flame front contour. The second of the sequence shows the center point and a virtual circle of radius Δs. The third shows the segments of virtual circle with an angle $\Delta\varphi$. The fourth one shows small circles centered on the circumference of virtual circle with a radius r. The mean intensities of the area covered by the small circles are calculated at this stage. The fifth one shows the variation of mean intensities as a function of angle φ. Here the values of mean intensities are compared with optimum intensity (I_{otsu}) and the angle ($\varphi_{s+\Delta s}$) of matching intensity level is calculated. The final of the second step locates the first flame front coordinate in the direction ($\varphi_{s+\Delta s}$) with a normal distance (Δ_{step}) from the present location (s).

The third step extracts the whole flame front coordinates starting from the first point. The rest of the sequences (7 to 9) are the third step. In this step, the criterion to find the flame front location is not based on the optimum threshold but rather based on the local threshold value (I_{thresh}). The local threshold value is calculated from the local minimum (I_{min}) and maximum threshold values (I_{max}) by the following expression:

$$I_{thresh} = I_{min} + 2 * (I_{max} - I_{min}) / 5 \tag{A.1}$$

The sequences of this step are repeated until it reaches the final point of the flame front contour. At the end of each repetition, shortest distance between the first and current point is calculated and if it is below a predefined value then the current point is taken as final point. The variables in this new algorithm are radius of virtual circle Δs, radius of small circle r, angle φ and step-size Δ_{step}. The final optimized values of those variables for the PIV images are given below: Δs = 5.0; r = 5.0; φ = 15°; Δ_{step} = 0.6;

As mentioned earlier, this new algorithm extracts the flame front contour with sub-pixel resolution which is fixed by the step size.

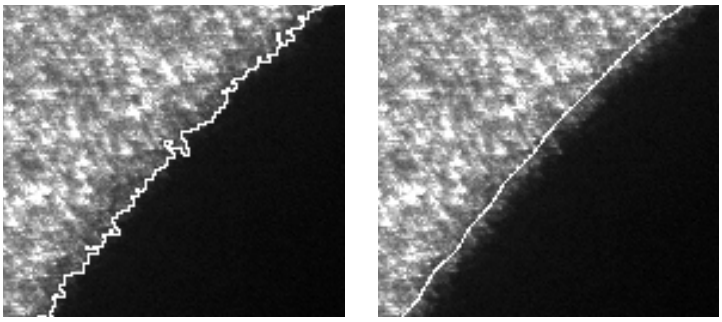

(a) Edge detection algorithm. (b) New algorithm.

Figure A.5: Extracted flame front contours.

A comparison of extracted flame front contours by the edge detection algorithm and by the new algorithm is shown in Fig. A.5. The flame front extracted by the new algorithm is far superior to the edge detection algorithm. Also the extracted flame front is not affected by the variation of seeding particles density closer to the flame front.

The same new algorithm is also utilized for the extraction of flame front from the PLIF image whose size is 512×512 pixels. The variables of the algorithm are again optimized for the PLIF images. The only difficulty is the finding of first point of contour. The histogram of PLIF image is not a bi-model like PIV image and the Otsu algorithm cannot find the optimum threshold. So we initially presumed the value of threshold and extracted the contour. We then compared the superposition of PLIF contour with PIV contours and by that way we optimized the initial threshold value. The final optimized values for the PLIF images are given below: $I_{thresh} = 0.41$; Δs = 1.5; r = 1.5; φ = 20°; Δ_{step} = 0.6;

A.3 Conclusion

Flame front contours are very much important to characterize the flame front geometry. In this work, we initially applied the edge detection algorithm and found more noises in the extracted flame front contours. So we developed a new extraction tool which extracts the flame front coordinates with sub-pixel resolution without superposed noises. We successfully implemented the new algorithm for both PIV and PLIF images.

Appendix B

Least square circle fit technique

The local flame propagation speed can be measured from the shortest distance between the two flame front coordinates extracted from the PIV image pairs. The accuracy of this local measurement can be improved by applying the filtration to the extracted flame front contours. So we developed a filtration technique which requires the global center and radius of given flame front coordinates and that is achieved by the least square technique explained in this appendix.

B.1 Least square circle

The least square fit is a well known technique to solve set of equations in order to find equal number of unknowns. The technique will produce direct solutions for the unknowns if the equations are in linear form otherwise requires initial guess for the unknowns. The least square technique can be used to fit a curve to the given data set. The principle of least square fit is to minimize the mean square distance from the fitting curve to the given data points. The least square circle fit technique finds the global center for the given coordinates. The technique can be applied for the linear or nonlinear form of circle equations. In this work, linear form of least square circle fit technique is utilized.

B.2 Linear method

A circle can be defined as:

$$(x - x_0)^2 + (y - y_0)^2 = r^2 \tag{B.1}$$

where, (x_0, y_0) is the center of the circle, (x, y) is the coordinate of the circle and r is the radius of the circle.

For a given set of coordinates, it is possible to find a best fitting circle by minimizing the square of the distance between the coordinates defining the circle and the radius of circle.

$$\sum_i \left[(\sqrt{(x_i - x_0)^2 + (y_i - y_0)^2} - r)^2 \right] \rightarrow 0 \tag{B.2}$$

This can be achieved by using the least square circle fit technique [Chernov and Lesort (2005)].

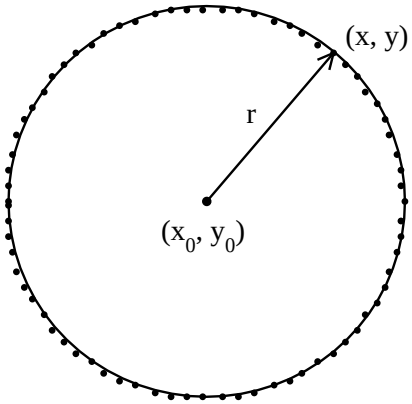

The equation of a circle can be expressed in the linear form as:

$$A(x^2 + y^2) + Bx + Cy = 1 \tag{B.3}$$

where

$$A = \frac{1}{r^2 - x_0^2 - y_0^2}; \quad B = \frac{-2x_0}{r^2 - x_0^2 - y_0^2}; \quad C = \frac{-2y_0}{r^2 - x_0^2 - y_0^2} \tag{B.4}$$

The relationship between the unknowns A, B, C and the circle parameters are given below:

$$x_0 = \frac{-B}{2A}; \quad y_0 = \frac{-C}{2A}; \quad r = \frac{\sqrt{4A + B^2 + C^2}}{2A} \tag{B.5}$$

The unknowns A, B, C can be related to the coordinates of the circle by the following way [Manthey (1999)]:

$$\begin{bmatrix} A \\ B \\ C \end{bmatrix} = \begin{bmatrix} \sum\left((x_i^2 + y_i^2)^2\right) & \sum\left((x_i^2 + y_i^2)x_i\right) & \sum\left((x_i^2 + y_i^2)y_i\right) \\ \sum\left((x_i^2 + y_i^2)x_i\right) & \sum\left(x_i^2\right) & \sum\left(x_i y_i\right) \\ \sum\left((x_i^2 + y_i^2)y_i\right) & \sum\left(x_i y_i\right) & \sum\left(y_i^2\right) \end{bmatrix}^{-1} \begin{bmatrix} \sum\left(x_i^2 + y_i^2\right) \\ \sum x_i \\ \sum y_i \end{bmatrix} \tag{B.6}$$

Finally, the center and radius of the best fitting circle will be obtained by solving the Eqns. B.6 and B.5. Few examples are given in the next section.

B.3 Examples

In this work, the flame fronts are mostly closed curves. However in some cases the flame fronts are semi circles so the least square circle fit technique must provide accurate results for both closed and open curves. This is verified by applying the least square circle fit technique to the known circle with different size of data points as shown in Fig. B.1. In that figure, data points are represented by the black dots and the fitted curves are represented by the red line.

The global center of the imposed curve is $x_0 = 200, y_0 = 200$ with radius $r = 100$ pixels. The measured global center and radius by the least square circle fit technique are given in the following table. B.1.

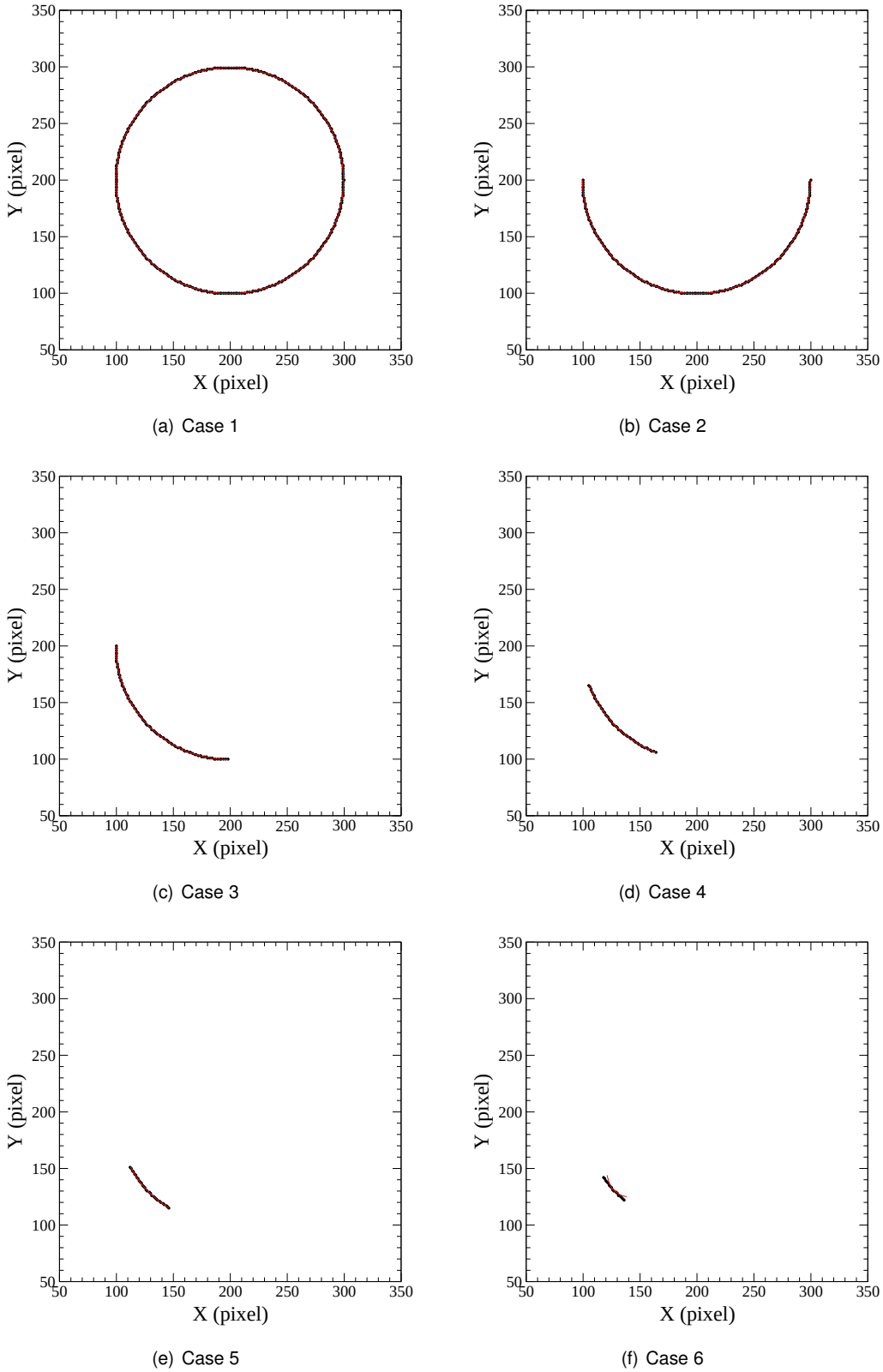

(a) Case 1

(b) Case 2

(c) Case 3

(d) Case 4

(e) Case 5

(f) Case 6

Figure B.1: Least square circle fit.

Case	X_0 (pixel)	Y_0 (pixel)	Radius (pixel)
1	199.497	199.501	99.936
2	199.500	199.511	99.944
3	199.370	199.317	99.748
4	201.297	201.123	102.280
5	191.303	191.432	88.492
6	175.494	175.657	66.324

Table B.1: Least square circle fit results.

The method predicts the global center and radius perfectly for the full circle, half circle and quarter of circle. After that it starts to fluctuate and predicts less and less accurate results with reduction of data points. So the method can measure the global center and radius accurately of the data points which contains at least quarter the size of circle.

B.4 Conclusion

The global center and radius of flame front can be measured by the least square circle fit technique. This appendix explained the linear form of the least square circle fit technique. We applied the technique to data sets ranging from full circle to arcs and the method predicts the global center and radius for the data points up to quarter of circle. So this method is quite accurate to measure the flame front radius and the flame front global center for the given flame front coordinates.

Appendix C

Filtration of flame front contour

In this work, flame front contours are extracted from PIV and PLIF images by using new extraction tool which extracts the flame front coordinates with sub-pixel resolution. But the extracted flame fronts are still affected by limited signal-to-noise ratio closer to the flame front zone. So the flame front contours need to be filtered for accurate measurements. This appendix explains the filtration technique applied to the flame front coordinates.

C.1 Raw flame front contours

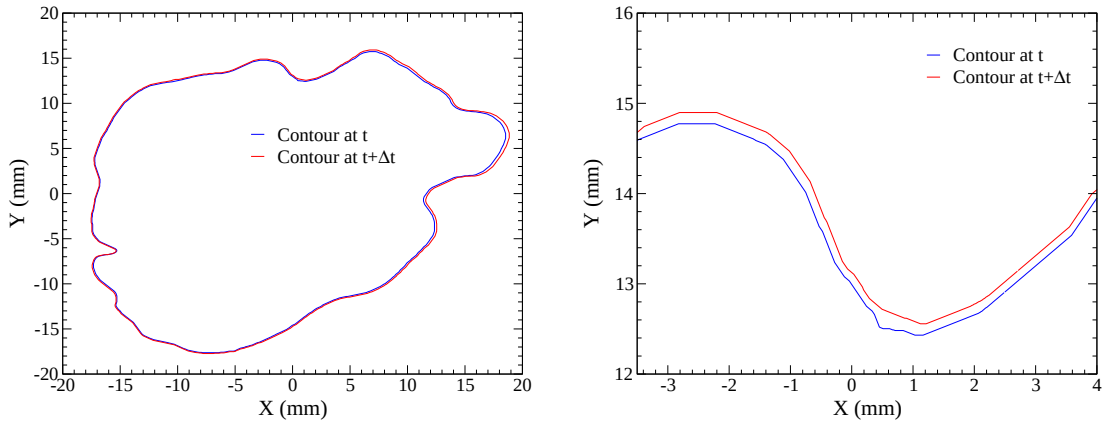

(a) Raw contours

(b) Closer view

Figure C.1: One example of extracted PIV contours.

One example of extracted flame front contours from a pair of PIV images is shown in Fig. C.1. These flame front contours are extracted by using newly developed extraction tool explained in the appendix § A. Though flame front coordinates are extracted with sub-pixel resolution, still they are affected by limited signal-to-noise ratio that imposes small artificial wrinkles to the extracted coordinates clearly visible in the closer view of flame fronts shown in Fig. C.1.

In this work, the local flame speed is measured for each flame front coordinate as a shortest distance between two flame front coordinates divided by the time delay (Δt) between them. The

accuracy of this local measurement is very sensitive to the extracted flame fronts and any artificial noises imposed on to the contours during extraction step affects the flame speed measurement [Balusamy et al. (2009)]. So the extracted flame front contours need to be filtered before the flame speed measurement.

C.2 Optimization of filter size

Gaussian filter is an effective tool to remove artificial noises added to the flame front coordinates. In this filtration process, first the flame front coordinates are sampled at equal space as a function of independent variables $s : x = f(s)$ and $y = f(s)$, where s corresponds to the curvilinear distance relative to the starting point of contour. Then low pass filter based on Gaussian weighted moving average scheme is applied to the independent coordinates. Here, the important parameter is the size of filter which needs to be optimized; otherwise the filtration process will remove small structures in the flame front. For that, laminar spherically outward propagating flame fronts are utilized. Their mean radius based on surface area (Rs) and circumference (Rs) are used to find the optimum filter size. The definition of flame radius Rs and Rl are given below:

$$R_s = \sqrt{S_f/\pi} \tag{C.1}$$

$$R_l = L/2\pi \tag{C.2}$$

where S_f is the flame surface area and L is the circumference of flame front. In the laminar premixed flame configuration, the ratio of Rl/Rs is related to the artificial wrinkles superposed on the circumference of contour and its value close to the one indicates the smoothness of contour without any artificial wrinkles. Figure C.2 shows the ratio of Rl/Rs of filtered flame fronts taken

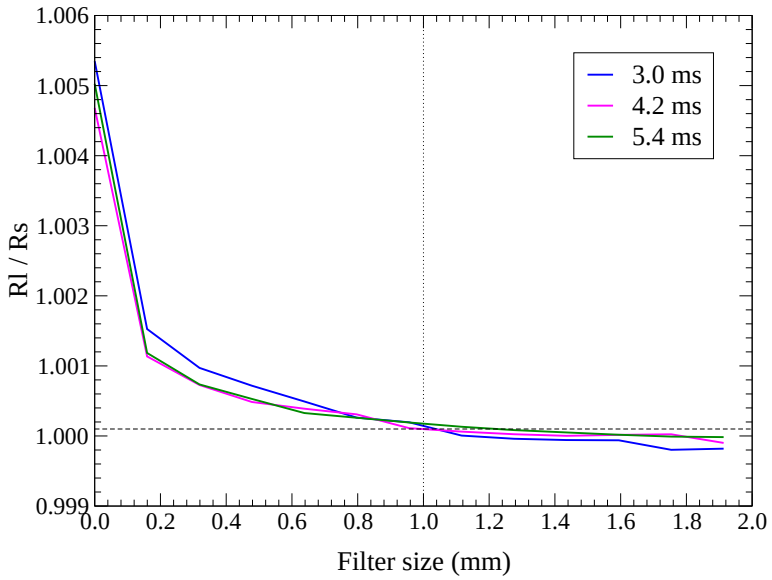

Figure C.2: Influence of filter size on Rl/Rs.

at different time after ignition as a function of size of filter. For a filter size of $1\ mm$, the ratio of Rl/Rs of filtered contours at various timings reaches value around unity, which indicates that all artificial noises are removed by the filtration process. So the optimum filter size is taken as $1\ mm$ for both PIV and PLIF images. Figures C.3 and C.4 shows the comparison of raw and filtered

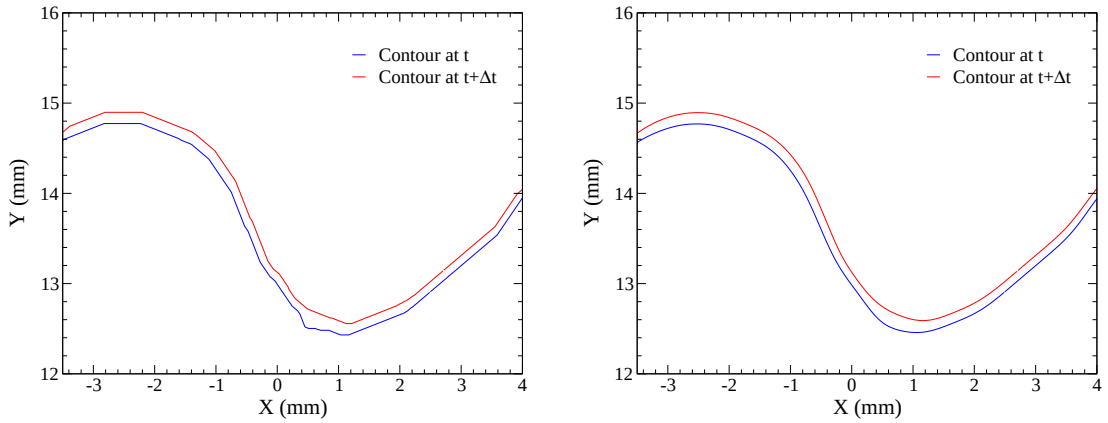

(a) Raw contours (b) Filtered contours

Figure C.3: Closer view of raw and filtered PIV contours.

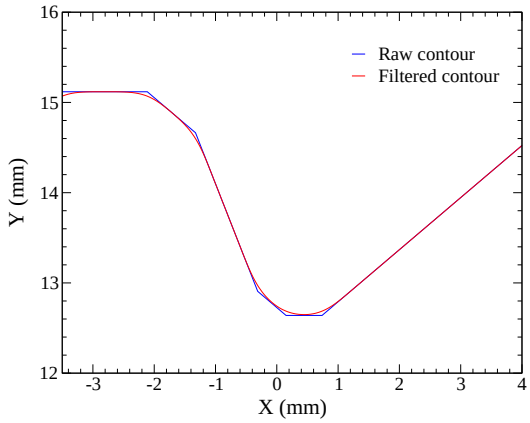

Figure C.4: Closer view of raw and filtered PLIF contours.

PIV and PLIF contours. The filtration process removed all the artificial noises superposed to the raw contour by extraction step but conserves the small scale structures of flame fronts in both PIV and PLIF cases.

C.3 Conclusion

In this appendix, the need of filtration of flame front contour is discussed. The filtration process based on Gaussian moving average scheme is explained. The size of filter is optimized by using laminar premixed flame configuration. The optimized filtration scheme is applied to the PIV and PLIF flame fronts and compared to their respective raw flame fronts. The filtration process successfully removed all the artificial noises superposed to the contour by the extraction step.

Bibliography

Abdel-Gayed, R., D. Bradley, and F.-K. Lung, 1989: Combustion regimes and the straining of turbulent premixed flames. *Combustion and Flame*, **76**(2), 213–218.

Adrian, R. J., 2005: Twenty years of particle image velocimetry. *Experiments in Fluids*, **39**(2), 159–169.

Al-Garni, A. M., 2007: Low speed calibration of hot-wire anemometers. *Flow Measurement and Instrumentation*, **18**(2), 95–98.

Aleiferis, P. G., A. M. K. P. Taylor, K. Ishii, and Y. Urata, 2004: The nature of early flame development in a lean-burn stratified-charge spark-ignition engine. *Combustion and Flame*, **136**(3), 283–302.

Alkidas, A. C., 2007: Combustion advancements in gasoline engines. *Energy Conversion and Management*, **48**(11), 2751–2761.

Anselmo-Filho, P., S. Hochgreb, R. Barlow, and R. Cant, 2009: Experimental measurements of geometric properties of turbulent stratified flames. *Proceedings of the Combustion Institute*, **32**(2), 1763–1770.

Armstrong, N. W. H., 1992: *Planar Flowfield Measurement in Premixed Turbulent Combustion*. PhD thesis, Department of Engineering, University of Cambridge.

Balusamy, S., A. Cessou, and B. Lecordier, 2009: Direct experimental determination of laminar burning velocity using a new piv approach. *8th International Symposium on Particle Image Velocimetry*.

Barlow, R. S., 2007: Laser diagnostics and their interplay with computations to understand turbulent combustion. *Proceedings of the Combustion Institute*, **31**(1), 49–75.

Barrere, M., 1974: Modeles de combustion turbulente. *International Journal of Thermal Sciences*, **13**(148), 295–308.

Berlman, I. B., 1971: *Handbook of fluorescence spectra of aromatic molecules*. Academic Press (New York), second edition.

Bignell, N., 2000: Using small sonic nozzles as secondary flow standards. *Flow Measurement and Instrumentation*, **11**(4), 329–337.

Boer, H., J., 1995: Mass flow controlled evaporation system. *J. Phys. IV France*, **05**(C5), C5–961–C5–966.

Borghi, R., 1984: Mise au point sur la structure des flammes turbulentes. *Journal de chimie physique*, **81**, 361–370.

Bosschaart, K. J. and L. De Goey, 2004: The laminar burning velocity of flames propagating in mixtures of hydrocarbons and air measured with the heat flux method. *Combustion and Flame*, **136**(3), 261–269.

Boyer, L., 1980: Laser tomographic method for flame front movement studies. *Combustion and Flame*, **39**(3), 321–323.

Bradley, D., P. Gaskell, and X. Gu, 1996: Burning velocities, markstein lengths, and flame quenching for spherical methane-air flames: a computational study. *Combustion and Flame*, **104**(1-2), 176–198.

Bray, K. N. C., 1980: *Turbulent Reacting Flows*. Springer- Verlag, 115 – 183.

Brown, L. R., 2006: *Plan B 2.0: Rescuing a Planet Under Stress and a Civilization in Trouble*. NY: W.W. Norton & Co.

Bruun, H. H., 1995: *Hot-wire anemometry, principles and signal analysis.* New York: Oxford University Press.

Burke, M. P., Z. Chen, Y. Ju, and F. L. Dryer, 2009: Effect of cylindrical confinement on the determination of laminar flame speeds using outwardly propagating flames. *Combustion and Flame*, **156**(4), 771–779.

Bychkov, V. V. and M. A. Liberman, 2000: Dynamics and stability of premixed flames. *Physics Reports*, **325**(4-5), 115–237.

Cessou, A., 2006: Diagnostics lasers en combustion: mesures de concentration et de temperature. In *Ecole thématique de combustion*.

Cessou, A., U. Meier, and D. Stepowski, 2000: Applications of planar laser induced fluorescence in turbulent reacting flows. *Measurement Science and Technology*, **11**(7), 887–901.

Chernov, N. and C. Lesort, 2005: Least squares fitting of circles. *Journal of Mathematical Imaging and Vision*, **23**(3), 239–252.

Cho, Y. S. and D. A. Santavicca, 1993: The effect of incomplete fuel-air mixing on spark-ignited flame kernel growth. *SAE 932715*.

Clavin, P., 1985: Dynamic behavior of premixed flame fronts in laminar and turbulent flows. *Progress in Energy and Combustion Science*, **11**(1), 1–59.

Davis, S., J. Quinard, and G. Searby, 2002: Markstein numbers in counterflow, methane- and propane- air flames: A computational study. *Combustion and Flame*, **130**(1-2), 123–136.

Dégardin, O., B. Renou, and A. Boukhalfa, 2006: Simultaneous measurement of temperature and fuel mole fraction using acetone planar induced fluorescence and rayleigh scattering in stratified flames. *Experiments in Fluids*, **40**(3), 452–463.

Driscoll, J. F., 2008: Turbulent premixed combustion: Flamelet structure and its effect on turbulent burning velocities. *Progress in Energy and Combustion Science*, **34**(1), 91–134.

Duclos, J.-M., M. Zolver, and T. Baritaud, 1999: 3d modeling of combustion for di-si engines. *Revue de l'Institut Francais du Petrole*, **54**(2), 259–264.

Eckbreth, A. C., 1998: *Laser Diagnostics for Combustion Temperature and Species*, volume 7 of *Energy and Engineering Sciences*. Taylor & Francis, Inc.

Egolfopoulos, F. N., P. Cho, and C. K. Law, 1989: Laminar flame speeds of methane-air mixtures under reduced and elevated pressures. *Combustion and Flame*, **76**(3-4), 375–391.

Ferrier, A. J., D. R. Funk, and P. J. W. Roberts, 1993: Application of optical techniques to the study of plumes in stratified fluids. *Dynamics of atmospheres and oceans*, **20**, 155–183.

Foucaut, J., J. Carlier, and M. Stanislas, 2004: Piv optimization for the study of turbulent flow using spectral analysis. *Measurement Science and Technology*, **15**(6), 1046–1058.

Frank, J. H., K. M. Lyons, and M. B. Long, 1996: Simultaneous scaler/velocity field measurements in turbulent gas-phase flows. *Combustion and Flame*, **107**(1-2), 1–4.

Galizzi, C. and D. Escudie, 2006: Experimental analysis of an oblique laminar flame front propagating in a stratified flow. *Combustion and Flame*, **145**(3), 621–634.

Glassman, I., 1987: *Combustion*. Academic Press, Inc., second edition.

Groot, G. and L. De Goey, 2002: A computational study on propagating spherical and cylindrical premixed flames. *Proceedings of the Combustion Institute*, **29**(2), 1445–1451.

Gu, X. J., M. Z. Haq, M. Lawes, and R. Woolley, 2000: Laminar burning velocity and markstein lengths of methane-air mixtures. *Combustion and Flame*, **121**(1-2), 41–58.

Hanson, R. K., J. M. Seitzman, and P. H. Paul, 1990: Planar laser-fluorescence imaging of combustion gases. *Applied physics. B, Photophysics and laser chemistry*, **50**(6), 441–454.

Hassan, M. I., K. T. Aung, O. C. Kwon, and G. M. Faeth, 1998: Properties of laminar premixed hydrocarbon/air flames at various pressures. *Journal of Propulsion and Power*, **14 (4)**, 479–488.

Haworth, D., R. Blint, B. Cuenot, and T. Poinsot, 2000: Numerical simulation of turbulent propane-air combustion with nonhomogeneous reactants. *Combustion and Flame*, **121**(3), 395–417.

Haworth, D. C. and T. J. Poinsot, 1992: Numerical simulations of lewis number effects in turbulent premixed flames. *Journal of Fluid Mechanics Digital Archive*, **244**(-1), 405–436.

Hélie, J. and A. Trouvé, 1998: Turbulent flame propagation in partially premixed combustion. *Symposium (International) on Combustion*, **1**, 891–898.

Hélie, J. and A. Trouvé, 2000: A modified coherent flame model to describe turbulent flame propagation in mixtures with variable composition. *Proceedings of the Combustion Institute*, **28**(1), 193–201.

Hentschel, W., 2000: Optical diagnostics for combustion process development of direct-injection gasoline engines. In *Symposium (International) on Combustion*, volume 28, Combustion Institute, Edinburgh, United kingdom, 1119–1135.

Iwamoto, Y., 1997: Development of gasoline direct injection engine. *SAE 970541*.

Jiménez, C., B. Cuenot, T. Poinsot, and D. Haworth, 2002: Numerical simulation and modeling for lean stratified propane-air flames. *Combustion and Flame*, **128**(1-2), 1–21.

Jomaas, G., X. Zheng, D. Zhu, and C. Law, 2005: Experimental determination of counterflow ignition temperatures and laminar flame speeds of c2-c3 hydrocarbons at atmospheric and elevated pressures. *Proceedings of the Combustion Institute*, **30**(1), 193–200.

Kang, T. and D. C. Kyritsis, 2007a: A combined experimental/computational investigation of stratified combustion in methane-air mixtures. *Energy Conversion and Management*, **48**(11), 2769–2774.

Kang, T. and D. C. Kyritsis, 2007b: Departure from quasi-homogeneity during laminar flame propagation in lean, compositionally stratified methane-air mixtures. *Proceedings of the Combustion Institute*, **31**(1), 1075–1083.

Kang, T. and D. C. Kyritsis, 2009: Phenomenology of methane flame propagation into compositionally stratified, gradually richer mixtures. *Proceedings of the Combustion Institute*, **32**(1), 979–985.

Lavoie, P., G. Avallone, F. De Gregorio, G. Romano, and R. Antonia, 2007: Spatial resolution of piv for the measurement of turbulence. *Experiments in Fluids*, **43**(1), 39–51.

Law, C., 1989: Dynamics of stretched flames. *Symposium (International) on Combustion*, **22**(1), 1381–1402.

Law, C. K., 2006: *Combustion Physics*. Cambridge University Press, Cambridge.

Law, C. K., 2007: Combustion at a crossroads: Status and prospects. *Proceedings of the Combustion Institute*, **31**(1), 1–29.

Lecordier, B., 1997: *Etude de l'interaction de la propagation d'une flamme prémélangée avec le champ aérodynamique, par association de la tomographie laser et de la vélocimetrie par images de particules*. PhD thesis, l'Université de Rouen.

Lecordier, B., D. Demare, L. Vervisch, J. Réveillon, and M. Trinité, 2001: Estimation of the accuracy of piv treatments for turbulent flow studies by direct numerical simulation of multi-phase flow. *Measurement Science and Technology*, **12**, 1382 – 1391.

Lecordier, B., M. Mouquallid, and M. Trinité, 1999: Simultaneous 2d measurements of flame front propagation by high speed tomography and velocimetry field by cross-correlation. In *7th International Symposium on Applications of Laser Techniques to Fluid Mechanics, Lisbon Portugal*.

Lecordier, B. and M. Trinité, 2003: Advanced piv algorithms with image distortion validation and comparison using synthetic images of turbulent flow. *Particle Image Velocimetry: recent improvements, Springer*.

Lecordier, B. and J. Westerweel, 2004: *The EUROPIV Synthetic Image Generator (S.I.G). In: Stanislas, M., Westerweel, J., Kompenhans, J. (Eds.) Particle Image Velocimetry: Recent Improvements*. Springer, 145–161.

Li, B., E. Baudoin, R. Yu, Z. Sun, Z. Li, X. Bai, M. Aldén, and M. Mansour, 2009: Experimental and numerical study of a conical turbulent partially premixed flame. *Proceedings of the Combustion Institute*, **32**(2), 1811–1818.

Manthey, D., 1999: General least-squares - direct solutions and bundle adjustments. Technical report.

Markstein, G., 1964: *Non steady Flame Propagation*. Oxford Pergamon.

Marley, S. and W. Roberts, 2005: Measurements of laminar burning velocity and markstein number using high-speed chemiluminescence imaging. *Combustion and Flame*, **141**(4), 473–477.

Marzouk, Y., A. Ghoniem, and H. Najm, 2000: Dynamic response of strained premixed flames to equivalence ratio gradients. *Proceedings of the Combustion Institute*, **28**(2), 1859–1866.

Mokhtarian, F. and A. Mackworth, 1986: Scale-based description and recognition of planar curves and two-dimensional objects. *IEEE Trans. Pattern Anal. Mach. Intell.*, **8**(1), 34–43.

Moriyoshi, Y. and M. Morita, 2003: Effects of fuel and diluents on stratified charge turbulent combustion in simplified conditions. *SAE 2003-01-1807*, **01**.

Otsu, N., 1979: A threshold selection method from grey-level histograms. *IEEE Trans Syst Man Cybern*, **9**, 62–66.

Pasquier, N., B. Lecordier, M. Trinité, and A. Cessou, 2007: An experimental investigation of flame propagation through a turbulent stratified mixture. *Proceedings of the Combustion Institute*, **31**(1), 1567–1574.

Pasquier-Guilbert, N., 2004: *Mesures couplées de richesse et de vitesse pour la combustion instationnaire en écoulement stratifié.* PhD thesis, l'Université de Rouen.

Peters, N., 1988: Laminar flamelet concepts in turbulent combustion. *Symposium (International) on Combustion*, **21**(1), 1231–1250.

Peters, N., 1999: The turbulent burning velocity for large-scale and small-scale turbulence. *Journal of Fluid Mechanics*, **384**(-1), 107–132.

Peters, N., 2000: *Turbulent Combustion*. Cambridge University Press, Cambridge.

Pires Da Cruz, A., A. Dean, and J. Grenda, 2000: A numerical study of the laminar flame speed of stratified methane/air flames. *Symposium (International) on Combustion*, **28**(2), 1925–1932.

Poinsot, T. and D. Veynante, 2005: *Theoretical and Numerical Combustion*. R.T.Edwards.

Pope, S. B., 1988: The evolution of surfaces in turbulence. *International journal of engineering science*, **26**, 445–469.

Ra, Y., 1999: *Laminar Flame Propagation in a Stratified Charge*. PhD thesis, Massachusetts Institute of Technology.

Raffel, M., E. W. Christian, T. W. Steve, and J. Kompenhans, 2007: *Particle Image Velocimetry A Practical Guide*. Springer Berlin Heidelberg, second edition.

Razus, D., D. Oancea, V. Brinzea, M. Mitu, and C. Movileanu, 2010: Experimental and computed burning velocities of propane-air mixtures. *Energy Conversion and Management*, **51**(12), 2979–2984.

Reboux, J., D. Puechberty, and F. Dionnet, 1996: Study of mixture inhomogeneities and combustion development in a s.i. engine using a new approach of laser induced fluorescence (farlif). *SAE 961205*, **105**, 1678–1691.

Robin, V., A. Mura, M. Champion, O. Degardin, B. Renou, and M. Boukhalfa, 2008: Experimental and numerical analysis of stratified turbulent v-shaped flames. *Combustion and Flame*, **153**(1-2), 288–315.

Samson, E., 2002: *Etude experimentale de la propagation de flammes en expansion dans un milieu a richesse stratifiee*. PhD thesis, INSA de ROUEN.

Santavicca, D., 1995: Spark ignited turbulent flame kernel growth. Technical report, Pennsylvania State University, University Park, PA (US).

Schulz, C. and V. Sick, 2005: Tracer-lif diagnostics: Quantitative measurement of fuel concentration, temperature and fuel/air ratio in practical combustion systems. *Progress in Energy and Combustion Science*, **31**(1), 75–121.

Shan, J. W., D. B. Lang, and P. E. Dimotakis, 2004: Scalar concentration measurements in liquid-phase flows with pulsed lasers. *Experiments in Fluids*, **37**(2), 310–310.

Smith, S. W., 1997: *The Scientist and Engineer's Guide to Digital Signal Processing*.

Stone, R., A. Clarke, and P. Beckwith, 1998: Correlations for the laminar-burning velocity of methane/diluent/air mixtures obtained in free-fall experiments. *Combustion and Flame*, **114**(3-4), 546–555.

Takagi, Y., 1998: New era in spark-ignition engines featuring high-pressure direct injection. *Symposium (International) on Combustion*, **2**, 2055–2068.

Vagelopoulos, C. M. and F. N. Egolfopoulos, 1998: Direct experimental determination of laminar flame speeds. *Symposium (International) on Combustion*, **1**, 513–519.

Weiß, M., N. Zarzalis, and R. Suntz, 2008: Experimental study of markstein number effects on laminar flamelet velocity in turbulent premixed flames. *Combustion and Flame*, **154**(4), 671–691.

Wereley, S. T. and C. D. Meinhart, 2001: Second-order accurate particle image velocimetry. *Experiments in Fluids*, **31**(3), 258–268.

Westerweel, J., 1993: *Digital particle image velocimetry - Theory and application*. PhD thesis, Technische Universiteit Delft.

Westerweel, J., 1994: Efficient detection of spurious vectors in particle image velocimetry data. *Experiments in Fluids*, **16**(3), 236–247.

Willert, C. and M. Gharib, 1991: Digital particle image velocimetry. *Experiments in Fluids*, **10**, 182–193.

Williams, F., 1985: *Combustion Theory*. Perseus Books Reading, second edition.

Zhao, F., T. N. Asmus, D. N. Assanis, J. E. Dec, J. A. Eng, and P. M. Najt, 2003: *Homogeneous Charge Compression Ignition (HCCI) Engines*. SAE International, 646.

Zhao, F., M. C. Lai, and D. L. Harrington, 1999: Automotive spark-ignited direct-injection gasoline engines. *Progress in Energy and Combustion Science*, **25**(5), 437–562.

Zhou, J., K. Nishida, T. Yoshizaki, and H. Hiroyasu, 1998: Flame propagation characteristics in a heterogeneous concentration distribution of a fuel-air mixture. *SAE 982563*.

List of Figures

List of Tables

Résumé:

Pour mieux comprendre la combustion en mode stratifié, la propagation de flammes au sein de stratifications de richesse laminaire ou turbulente a été étudiée par des mesures simultanées de richesse et de vitesse effectuées par couplage de la PIV et de la PLIF. L'accent a été mis sur le développement de méthodes permettant d'améliorer la qualité des mesures locales. En particulier, un nouvel algorithme de PIV permettant la mesure locale de la vitesse des gaz frais véritablement à l'entrée de la zone de préchauffage a été développé. Pour améliorer la résolution, les mailles de calcul s'adaptent localement à la topologie de la flamme, pour tenir compte de la forme du front de flamme et de l'expansion des gaz. L'analyse statistique des mesures conditionnée sur la richesse locale a permis de caractériser les propriétés de la flamme soumise à une stratification de richesse dans un écoulement laminaire et turbulent, en particulier en mettant en évidence un effet mémoire.

Mots Clés:

combustion stratifiée, flamme turbulente, flamme laminaire, PIV, PLIF, vitesse de combustion laminaire

Abstract:

In order to better understand the stratified combustion, the propagation of flame through stratified mixture field in laminar and turbulent flow conditions has been studied by using combined PIV/PLIF techniques. A great emphasis was placed on developing methods to improve the accuracy of local measurements of flame propagation. In particular, a new PIV approach has been developed to measure the local fresh gas velocity near preheat zone of flame front. To improve the resolution of measurement, the shape of interrogation window has been continuously modified based on the local flame topology and gas expansion effect. Statistical analysis of conditioned local measurements by the local equivalence ratio of flames allows the characterization of the properties of flame propagation subjected to the mixture stratification in laminar and turbulent flows, especially the highlight of the memory effect.

Keywords:

stratified combustion, turbulent flame, laminar flame, PIV, PLIF, laminar burning velocity